PHOTOPRODUCTION OF K° MESONS FROM CARBON
A FREON BUBBLE CHAMBER EXPERIMENT

Thesis by

Ethan Davidson Alyea, Jr.

In Partial Fulfillment of the Requirements

For the Degree of

Doctor of Philosophy

California Institute of Technology

Pasadena, California

1962

ACKNOWLEDGMENTS

This work was carried out with the guidance and participation of Drs. J. H. Mullins and J. M. Teem. I should like to thank them not only for aid in the experiment reported herein, but also for generous counsel during my graduate residence.

Many people have been associated with the bubble chamber program. Among the students, Messrs. D. G. Coyne and L. F. Fretwell contributed to this experiment. The crew of the Synchrotron Laboratory, under the direction of Mr. L. B. Loucks, has rendered many services; in particular, Mr. W. H. Traver has devoted much effort to the operation of the bubble chamber. The Laboratory's Administrative Secretary, (Mrs.) B. Hall, has often given assistance. Valuable engineering advice has been obtained from Messrs. C. L. Friswold and D. D. Sell.

Of the Technical Aides, Mrs. S. D. Alyea, Miss W. C. Kogan, and Miss S. M. Laitinen performed most of the film scanning and event analysis. Mrs. T-H. Chang, Mrs. L. M. Coyne, and Mr. and Mrs. L. R. Gallagher donated time to several analysis projects.

I extend my thanks to Professor R. L. Walker for his comments on the rough draft of this thesis, and to Professor R. F. Bacher for his support of the bubble chamber program.

A fellowship from the Dow Chemical Company and the partial financial support of the United States Atomic Energy Commission are duly acknowledged.

Ethan D. Alyea, Jr.

April, 1962

ABSTRACT

The feasibility of utilizing characteristic interactions of K_2^o mesons in the liquid of a CF_3Br bubble chamber for the purpose of detecting photoproduced K^o mesons has been investigated. The K_2^o mesons were produced from carbon at an average laboratory angle of 11 degrees by photons with energies ranging from threshold to 1300 Mev. Although examples of most of the possible K_2^o signatures were found, only the signature comprised of a Λ^o decay could be used to estimate the cross sections for photoproducing K^o mesons in conjunction with Λ^o and Σ^+ hyperons. If the CM cross sections for the three processes are comparable in magnitude, the average differential CM cross sections are estimated to be $(0.36 \pm 0.19) \times 10^{-30}$ $cm^2/ster$. Since an enormous amount of work is required per K_2^o detected, this technique is not recommended for more detailed examination of K^o photoproduction unless simpler methods cannot be devised.

An an auxiliary result, the thermodynamic conditions of the bubble chamber have been shown to be well stabilized over long periods of time. For this reason, measurements of the gap-length distribution of a track may be used to determine a particle's velocity without recalibration for each individual bubble chamber expansion.

TABLE OF CONTENTS

TEXT

LIST OF ILLUSTRATIONS

LIST OF TABLES

I. INTRODUCTION

Since the first indication of the existence of "strange" particles in 1947[1], many properties of these puzzling particles have been established. In particular, the "Strangeness Theory" of Gell-Mann and Nishijina[2] has been extremely successful in explaining their strong production but weak decay. Considerable progress has been made toward measuring the characteristics of individual particles. The masses, spins, and some of the branching ratios in decay have been reasonably well established. Other properties such as the hyperon-kaon relative parities and coupling constants, however, are at best only poorly indicated by the present experimental data.

A number of authors[3-9] have discussed the possibility of utilizing photoproduction experiments to investigate the kaon-hyperon relative parities and coupling constants. The advantage of photoproduction experiments as compared to production by pion-nucleon or nucleon-nucleon interactions for this purpose lies in the fact that the forces between photons and other particles are well understood in the relevant energy range, whereas those between pions or nucleons and other particles are only vaguely understood.

Six of the strange particle photoproduction processes which are permitted by known conservation laws have free nucleon thresholds within the energy limits of existing electron accelerators:

Process	Free Nucleon Threshold	
$\gamma + p \rightarrow K^+ + \Lambda^o$	911 Mev	(I-1)
$\gamma + n \rightarrow K^o + \Lambda^o$	915 Mev	(I-2)
$\gamma + p \rightarrow K^+ + \Sigma^o$	1047 Mev	(I-3)
$\gamma + p \rightarrow K^o + \Sigma^+$	1049 Mev	(I-4)
$\gamma + n \rightarrow K^+ + \Sigma^-$	1050 Mev	(I-5)
$\gamma + n \rightarrow K^o + \Sigma^o$	1050 Mev	(I-6)

Besides obtaining information on relative parities and coupling constants through the investigation of these reactions, one may also be able to study final state interactions between the kaons and hyperons in much the same way that the pion-nucleon resonances have been and continue to be investigated.

Reactions I-1, I-3, and I-5 have been and are being studied through detection of the K^+ meson[10]. Constant-field magnetic spectrometer techniques have been particularly successful in this connection, although counter-telescope and high-field pulsed magnet techniques are also being pursued.

Investigation of the other three reactions depends on the ability to detect either the hyperons or the K^o meson. Due to their short mean lives and low velocities, the hyperons decay within a few centimeters of where they are produced. Furthermore, they are accompanied by a very large background of pions, protons, and neutrons from pion production. (The relative energy thresholds and cross section magnitudes of pion versus strange particle photoproduction are responsible.) Thus, rather difficult experimental techniques involving high certainty of identification in a compact

space are required. The class of visual detection devices where a large amount of information is obtained about each event is most suitable for this type of problem. At present, an attempt is being made to observe the Σ^+ hyperon from reaction I-4 in a nuclear emulsion experiment[11] which utilizes a high-field pulsed magnet to sweep out unwanted particles. Detection of hyperons produced in the central beam tube of a bubble chamber also appears feasible.

An effort to detect the K^o meson may follow one of two approaches: (1) detection of the short-lived K_1^o component*; or (2) detection of the long-lived K_2^o component. Since the K_1^o meson travels only a few centimeters before decay, the first approach involves techniques similar to those required for detection of the hyperons. On the other hand, due to the long mean decay distances of the K_2^o meson (on the order of tens of meters), the second approach encompasses radically different techniques. For instance, one may try to observe the K_2^o meson decay far away from the target. Unfortunately, because of the long K_2^o lifetime and inability to slow down and stop neutral particles by electromagnetic interactions, only a few per cent of the traversing K_2^o mesons can, in practice, be counted this way. Detection techniques are also handicapped by the fact that the K_2^o meson undergoes three-body decay[12-15] with a resultant spectrum of energies in the decay products.

Panofsky, et al.[16] have successfully detected decays from

*The properties of the K^o meson as a particle mixture which are relevant to this thesis are summarized in Appendix I.

K_2^o mesons emanating from the Brookhaven Cosmotron. The detection scheme consisted of counter identification of the μ-e decay associated with one of the following K_2^o decays in a three-foot long, evacuated region:

$$K_2^o \rightarrow \pi^+ + e^- + \bar{\nu} \qquad \text{(I-7)}$$

$$K_2^o \rightarrow \pi^- + \mu^+ + \nu \qquad \text{(I-8)}$$

$$K_2^o \rightarrow \pi^+ + \mu^- + \bar{\nu} \qquad \text{(I-9)}$$

A serious difficulty with this method is that in order to compute the detection efficiency one must know: (a) the energy spectrum of the K_2^o mesons; (b) the branching ratios into decays I-7, I-8 and I-9 compared to other modes; and (c) the energy spectra of the decay products in decays I-7, I-8 and I-9. Although some experimental information on criterion (b)[15, 14] is becoming available, there is no data at all on criterion (c).

Under the assumption that (c) is determined by phase space considerations alone and that the rates are the same for decays I-7, I-8, I-9 and I-10 (assumed to be the only appreciable decay modes),

$$K_2^o \rightarrow \pi^- + e^+ + \nu \qquad \text{(I-10)}$$

Panofsky et al. estimate their detection efficiency to be about three per cent for a broad K_2^o energy spectrum peaked at 150 Mev. From this value, one concludes that in a typical photoproduction experiment ($d\sigma/d\Omega' \cong 10^{-31}$ cm^2/ster.) with presently available beam intensities, the counting rate would be on the order of one per hour. At this rate background identification and subtraction becomes very difficult.

R. Gomez has recently suggested[17] a variation of this technique which would provide a more definite identification of the K_2^o decay. The idea is to use spark chambers surrounding the evacuated region to positively establish that the decay occurred in the vacuum.

Another possibility is to utilize characteristic interactions of K_2^o mesons which have been allowed to travel far from the photoproduction point. When K_2^o mesons pass through matter, a variety of reactions may take place through the strong interactions of the K^o and $\overline{K^o}$ components of the K_2^o meson. Typical of these are:

1) K^o component of K_2^o:

$$K^o + p \rightarrow K^+ + n \qquad \text{(I-11)}$$

2) $\overline{K^o}$ component of K_2^o:

$$\overline{K^o} + n \rightarrow K^- + p \qquad \text{(I-12)}$$

$$\rightarrow \Lambda^o + \pi^o \qquad \text{(I-13)}$$

$$\rightarrow \Sigma^o + \pi^o$$

$$\quad \lfloor \Lambda^o + \gamma \qquad \text{(I-14)}$$

$$\rightarrow \Sigma^- + \pi^+ \qquad \text{(I-15)}$$

$$\overline{K^o} + p \rightarrow \Lambda^o + \pi^+ \qquad \text{(I-16)}$$

$$\rightarrow \Sigma^o + \pi^+$$

$$\quad \lfloor \Lambda^o + \gamma \qquad \text{(I-17)}$$

$$\rightarrow \Sigma^+ + \pi^o \qquad \text{(I-18)}$$

3) K^o and $\overline{K^o}$ components of K_2^o:

Regeneration of K_1^o mesons by

a) diffraction scattering from the matter as a whole, (I-19)

b) diffraction scattering from individual nuclei, (I-20)

c) scattering from individual nucleons. (I-21)

The reactions involving a single strangeness component alone (i.e., reactions I-11 through I-18) are directly analogous to reactions involving charged kaons. Under the assumption of charge independence the following equivalences should hold:

$$K^o + p \rightleftharpoons K^+ + n \quad \text{(I-22)}$$

$$K^o + n \rightleftharpoons K^+ + p \quad \text{(I-23)}$$

$$\overline{K^o} + p \rightleftharpoons K^- + n \quad \text{(I-24)}$$

$$\overline{K^o} + n \rightleftharpoons K^- + p \quad \text{(I-25)}$$

When reactions I-11 through I-18 and I-21 take place with a nucleon inside a nucleus, there is a high probability that either the incoming K_2^o meson or one of the two outgoing secondaries will suffer collisions with other nucleons within the nucleus.* When this occurs, a nuclear "star" is produced in conjunction with the second-generation strange particle. These collisions also distort the energy versus angle relationships that may be calculated for the two-body reactions.

All of the above interactions of K_2^o mesons have been observed experimentally. Within experimental error the data agree with the particle mixture theory of Gell-Mann and Pais and the equivalences I-22 through I-25. Some of the experiments were performed with nuclear emulsions[18-23], one was performed with a cloud chamber[13], and the rest were performed with bubble chambers[24-31].

*Such collisions between Σ hyperons and nucleons often result in "capture" reactions in which the Σ hyperon is converted to a Λ^o hyperon.

Reactions I-13 through I-21 all have the common feature that short-lived strange particles with two-body decays replace the long-lived K_2^o meson which decays into three particles. Thus the second-generation strange particles decay close to the place the reaction occurs and their charged decay modes are, at least in principle, uniquely analyzable from measurements of the energies of and angles between charged particles.

Several general statements may be made about detecting K_2^o mesons by observation of these second-generation strange particles:

1) The fraction of the K_2^o mesons which interact depends on the amount of matter traversed; i.e., roughly speaking, the number of interactions per unit path length is directly proportional to the density of the material traversed.

2) In order to separate real reactions from background (such as neutron stars), it is desirable to achieve precise identification of at least the decay of the second-generation strange particle and also, if possible, the point where the K_2^o interaction occurred.

3) The counting rate is expected to be low. Therefore, high detection efficiency is important.

4) The second-generation strange particles will display a spectrum of energies even when produced by K_2^o mesons of fixed energy. They will also display a very wide angular distribution in their direction of travel and an even wider angular distribution in their decay products. In order to be useful, a detection method

must be relatively insensitive to these variables.

Visual detection techniques alone are suitable for this type of problem. Each event may be treated with high precision despite the fact that it is different from every other event in such characteristics as: location and orientation in space, or energies of particles. The high spatial resolution of such devices may also be utilized to relate a strange particle decay to the K_2^o interaction point.

It was the purpose of this experiment to investigate the feasibility of detecting photoproduced K^o mesons through the interactions of the K_2^o component in a bubble chamber liquid. The California Institute of Technology 10" bubble chamber not only satisfies the visual device requirement but also utilizes for its sensitive liquid a moderately high density material -- CF_3Br -- in which a favorable number of K_2^o mesons should be expected to interact.

Prior to this experiment one attempt had been made to detect photoproduced K^o mesons. R. Gomez and G. Neugebauer passed a neutral beam containing K_2^o mesons through a tungsten block in front of a cloud chamber and then looked for regenerated K_1^o decays in the cloud chamber. The cloud chamber was expanded only when a system of counters indicated that a neutral particle had passed through the tungsten and into the cloud chamber and that a charged decay had occurred in the cloud chamber. The background observed was very low, but, unfortunately, no case of a regenerated K_1^o decay was seen. The experiment was abandoned

when it was realized that the published theoretical predictions of a very strong regenerated K_1^o wave from process I-19 were in error and that this type of K_1^o regeneration actually makes up only a small part of the total K_2^o interaction. The experiment should also have been sensitive to Λ^o hyperons produced by K_2^o interactions in the tungsten. The most important difference between this cloud chamber experiment and the bubble chamber experiment to be described was the location of the K_2^o interaction. The relocation of the K_2^o interaction inside the region of observation achieved two major advantages: (a) the point of the K_2^o interaction could be observed; and (b) the detection efficiency for second-generation strange-particle decays was increased appreciably. (Decay losses between the point of production and the region of observation were eliminated, and a much larger solid angle about the point of production was available for observation.) The bubble chamber experiment also had a disadvantage. It was not possible to counter control the expansion, and so the number of background events was quite large.

In principle, identification of any second-generation strange particle or K_2^o decay in the bubble chamber could have been construed as a K_2^o signature. The choice of the best K_2^o signature depended on three criteria: (1) relative probability of occurrence; (2) ease of identification in scanning; and (3) amenability to exact analysis (for separation from background). The charged Λ^o decay clearly appeared to be the most suitable despite the expected

presence of a large background of pseudo Λ^o decays from neutron stars. This hypothesis was supported by the fact that Fowler, et al.[24] successfully identified Λ^o hyperons produced by K_2^o mesons passing through a propane bubble chamber. They also observed a large number of neutron-induced pseudo Λ^o decays, but found a prominent peak at the proper place in a histogram of number of events versus Q value*. They did not use (nor do they mention in their publication) observations of the K_2^o-interaction point associated with Λ^o decays.

Charged decays of regenerated K_1^o mesons were also estimated to be useful. Although Fowler, et al. did not observe a peak in a Q-value histogram for pseudo-K_1^o decays, they did find several events associated with stars that were consistent with K_1^o regeneration from K_2^o collisions with individual nucleons. (It should be noted that diffraction regeneration in propane should be rather insignificant. The recent experiment of Good, et al.[27] indicates that diffraction regeneration in CF_3Br is only about 1/5 as important as regeneration from individual nucleons.)

In accordance with these remarks, the major emphasis in this experiment was placed on detection of Λ^o hyperon decays. A less strenuous effort was exerted on K_1^o regeneration. Other signatures were noted qualitatively. The experiment showed that photoproduced K_2^o mesons can be detected through these signatures.

---

* $Q = M_{\Lambda^o} - m_\pi - m_p$ where M_{Λ^o} is the mass of the Λ^o or pseudo Λ^o.

Examples of most of the possibilities were observed, and as expected, the Λ^o decay was found to best satisfy the practical requirements.

Several other conclusions are worthy of note here:

1) K^o mesons are definitely photoproduced.

2) If the cross sections for reactions I-2, I-4, and I-6 are equal and roughly constant in magnitude over the photon energies used (up to 1300 Mev), then at average CM* angles of 28^o for reaction I-2 and 32^o for reactions I-4 and I-6, the differential CM cross sections are $(3.6 \pm 1.9) \times 10^{-31}$ cm^2/ster.

3) This technique is a rather difficult way of investigating reactions I-2, I-4 and I-6 and is not suitable for more detailed examination of these reactions unless simpler methods cannot be devised.

---

*Throughout this thesis "center of momentum" is abbreviated "CM".

II. EXPERIMENTAL METHOD

A. GENERAL

The experimental arrangement is shown in Fig. 1. A carbon target was irradiated with a 1300 Mev*, "hardened" bremsstrahlung beam from the California Institute of Technology electron synchrotron. The long-lived K_2^o component of the K^o mesons which were produced in the carbon target by reactions I-2, I-4 and I-6 traveled in a horizontal plane over a relatively unhindered path from the carbon target to the 10" heavy freon bubble chamber. Since the γ-ray beam contained photons of all energies between the thresholds for the three reactions and 1300 Mev, the K_2^o mesons had energies ranging from 75 to 550 Mev.

Besides K_2^o mesons the neutral beam also contained neutrons and photons. The neutrons, which came from pion photoproduction and therefore had an energy spectrum extending from 0 to 1.05 Bev, formed the primary component of the beam. Although photons of various energies were present, those with energies greater than 100 Mev were rare.

The circular aperture of the collimator defined the size and shape of the γ-ray beam, which entered the fringing field of the sweeping magnet for a short distance near the carbon target and passed the bubble chamber 1 inch from the safety tank.

---

*Since the experiment was exploratory in nature, an energy was chosen which would produce the maximum flux of K_2^o mesons without also producing neutrons with energies above the threshold for strange particle production by nucleon-nucleon interactions.

Figure 1

Overall Experimental Arrangement - Plan View

Omitted from the drawing are:

a) parts of the shielding which cannot be indicated in a simple way (see Chapter III, Section B3, for discussion):

b) the γ-ray beam monitor, which was located in the beam catcher, 27 feet beyond the north wall.

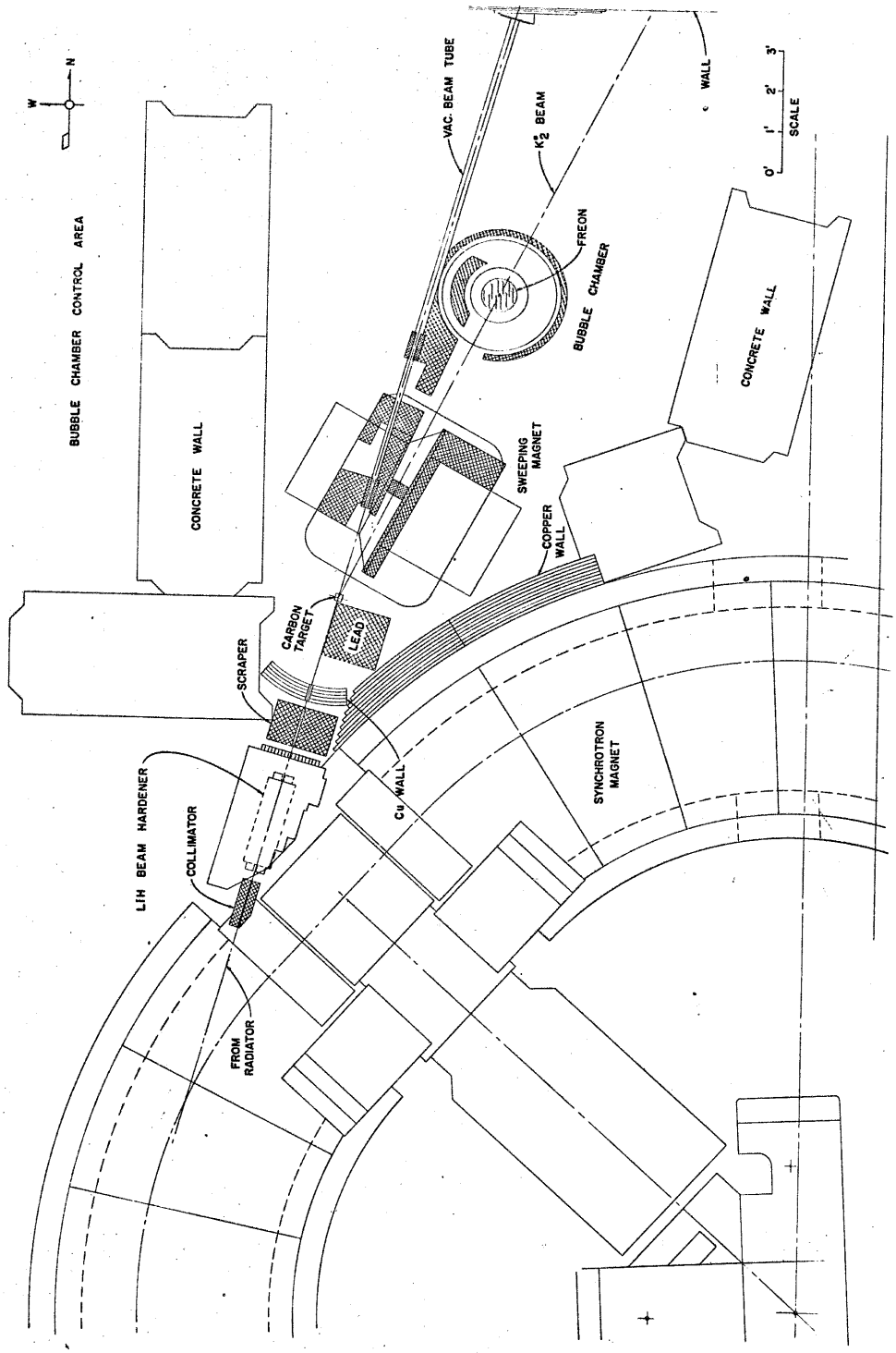
N
W
BUBBLE CHAMBER CONTROL AREA
CONCRETE WALL
VAC. BEAM TUBE
K_2^0 BEAM
℄ WALL
0' 1' 2' 3'
SCALE
FREON
BUBBLE CHAMBER
CONCRETE WALL
SWEEPING MAGNET
COPPER WALL
CARBON TARGET
LEAD
SCRAPER
Cu WALL
SYNCHROTRON MAGNET
LIH BEAM HARDENER
COLLIMATOR
FROM RADIATOR

FIGURE 1

The aperture for the K_2^o beam was formed on the sides by lead shielding; and on the top and bottom by the pole tips of the sweeping magnet and by the safety - and support - tank flanges of the bubble chamber (see Fig. 2). Midway through the sweeping magnet the K_2^o beam penetrated 4 inches of lead, and before reaching the freon chamber* it further penetrated the steel of the bubble chamber walls, the fluorocarbon support liquid, a polyethylene wall section and the rubber wall of the freon chamber (see Figs. 5 and 6). Elsewhere the K_2^o beam traveled through air.

The lithium hydride beam hardener, the series of beam scrapers, the vacuum beam tube, and the large amount of shielding were all employed to reduce the background at the bubble chamber.

About 13,000 useful pictures were taken at an average rate of 3 per minute of running time. Other important constants of the experimental setup are listed in Table 1.

B. APPARATUS

1. Sweeping Magnet. Special pole tips were designed for use with the Synchrotron Laboratory's utility magnet. The intention was to create an elongated region of high field strength so that charged particles of all possible momenta produced by the 1300

*Henceforth "freon chamber" will refer to the innermost vessel of the bubble chamber, i.e., the vessel containing the freon.

Figure 2

K_2^o Aperture and Limiting Paths of Charged Particles

The boundaries of the K_2^o aperture are shown in both plan and elevation views. For clarity, the lead shielding which defined the sides of the aperture has been omitted from the plan view. The location of this shielding is indicated in Figs. 1 (p. 13) and 10 (p. 51).

The charged particle trajectories which are drawn in the plan view are those which would have come closest to the visible volume of the bubble chamber if there had been a constant, 13.5 kilogauss magnetic field throughout the sweeping magnet, and if there had been no scattering and energy-loss effects due to the 4-inch lead absorber (not shown -- see Figs. 1 and 10) through which the K_2^o beam passed. The (+) or (-) in the figure gives the sign of the particle's charge.

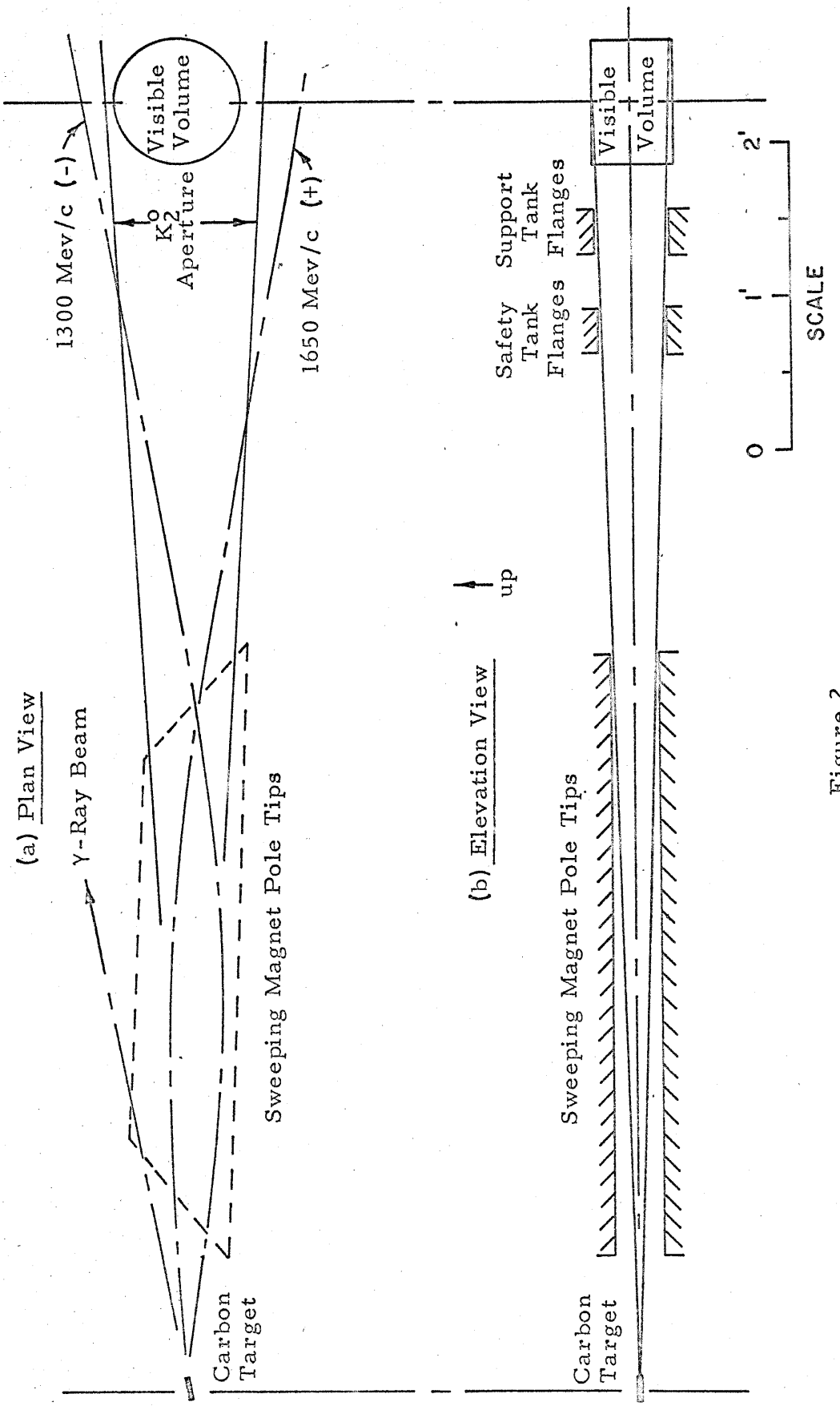
(a) Plan View
γ-Ray Beam
1300 Mev/c (-)
1650 Mev/c (+)
Visible Volume
K^0_2 Aperture
Sweeping Magnet Pole Tips
Carbon Target
(b) Elevation View
up
Safety Tank Flanges
Support Tank Flanges
Sweeping Magnet Pole Tips
Visible Volume
Carbon Target
0
1'
2'
SCALE

Figure 2

TABLE 1

Constants of Experimental Arrangement

I. Carbon Target

Length.....(5.428 ± 0.003) cm

Density.....(1.633 ± 0.002) gm/cm^3

II. Laboratory Angle between Bremsstrahlung Beam and Line from Carbon Target to Freon Chamber

Mean = 11° Maximum = 14° Minimum = 8°

III. Distance from Carbon Target to Center of Freon Chamber.....(2.54 ± 0.03) meters

IV. Total Solid Angle Subtended at Carbon Target by Visible Region of Freon Chamber.....6.2 x 10^{-3} ster.

V. Bremsstrahlung Beam Collimator and Scrapers:

A. Circular Apertures:

Label (see Fig. 10)	Aperture Diameter (inches) End a*	End b	Approx. Beam Diameter (inches)
Collimator	0.312	0.353	
BS-A	0.437	0.500	0.44
BS-C	1.000		0.70
BS-D	1.250		0.90

* End a - towards radiator; End b - towards beam catcher.

B. Lead Block, BS-B:

Distance from Beam Center (End b)..... 0.37 inches

Beam Diameter (End b)..... 0.56 inches

VI. Lead Absorber in K_2^o Path:

Thickness.....(4.00 ± 0.01) inches

Density.....$(11.3 \pm 0.1) gm/cm^3$

Mev bremsstrahlung beam striking the carbon target would be swept out of the K_2^o path. The geometry of these pole tips is shown in Fig. 3.

Stretched wire measurements were made on the magnet. The paths equivalent to those of 1650 Mev/c positive particles and 1300 Mev/c negative particles (the maximum proton and electron momenta) did indeed miss the freon chamber. These measurements did not include energy loss or scattering effects in the lead absorber later placed at the center of the magnet. No absolute field measurements were made. With other pole tips--vertical separation 4 inches--the field is known to be 13.5 kilogauss[32] at the current used for this experiment. Drawn in Fig. 2a are the particle trajectories which would have come closest to the freon chamber if the field had been constant (at 13.5 kilogauss) throughout the magnet and if there had been no scattering and energy loss effects in the 4 inch lead absorber.

2. Vacuum Beam Tube. The vacuum beam tube fulfilled several purposes. It eliminated the air close to the bubble chamber as a source of background of all kinds. Beam scrapers were incorporated into it for the sake of reducing obscuring background (see Chapter III, Section B2). Finally, since it extended through the entire bubble chamber area and therefore physically isolated the bremsstrahlung beam, it rendered the area safe to occupancy while the experiment was in progress.

Figure 3

Sweeping Magnet Pole Tips

Assembly drawings of the special pole tips and shims for the sweeping magnet are shown.

A-A View = plan view

other view = elevation view looking WNW. (See Fig. 1.)

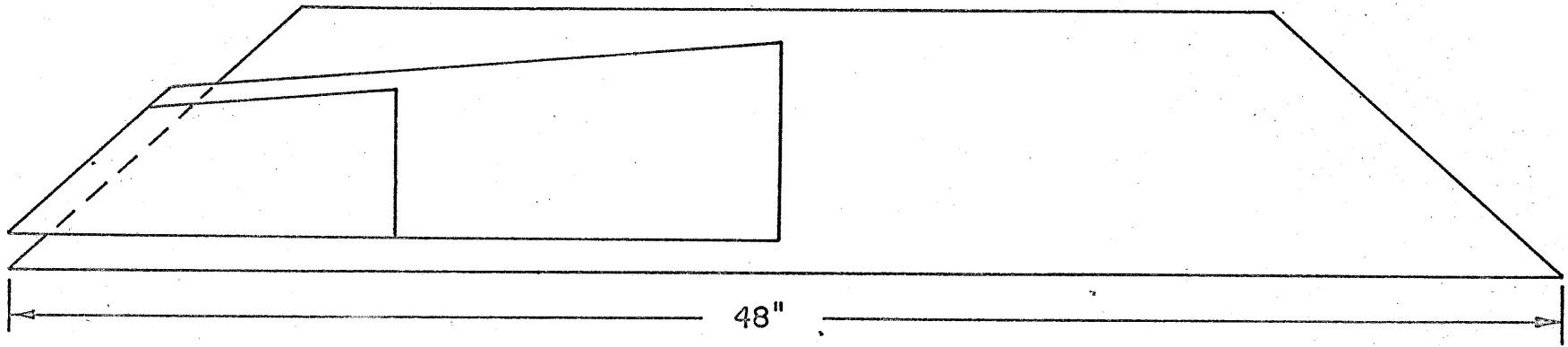

A-A VIEW

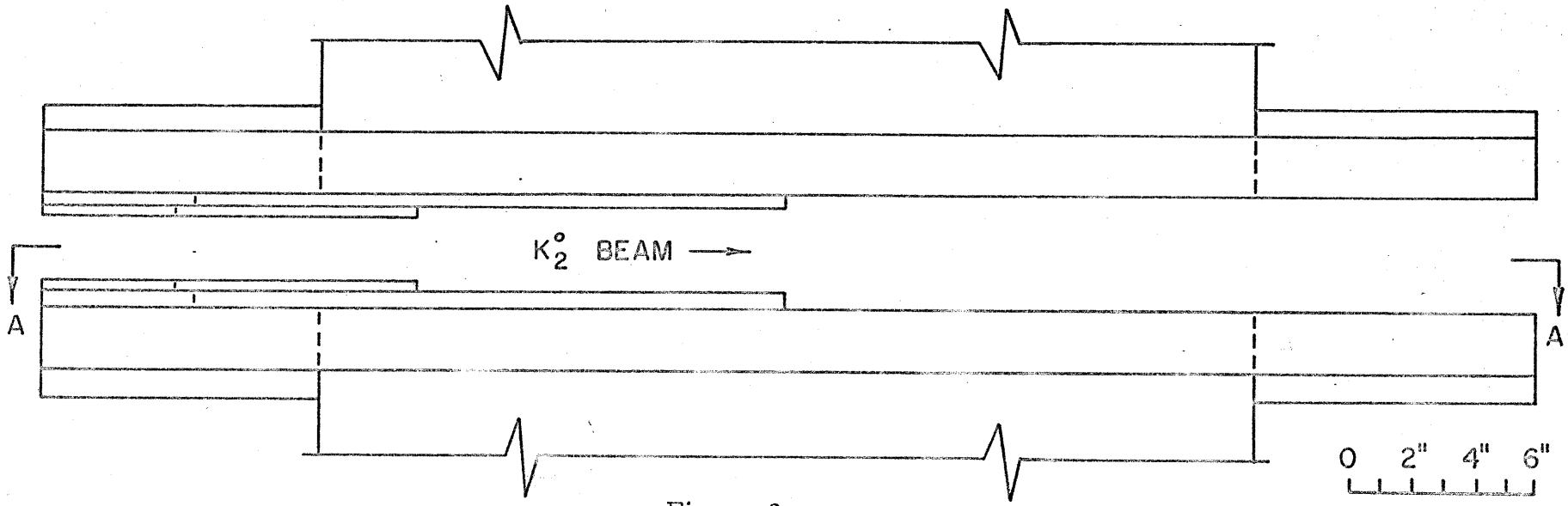

Figure 3

3. Bubble Chamber. Three views of the CIT 10^{11} heavy freon chamber are shown in Figs. 4, 5 and 6, and some important facts about the chamber are listed in Table 2. This chamber has to a large extent been described elsewhere[33,34]. A brief discussion of its usefulness as an experimental instrument is presented below.

To be useful for high energy physics experiments, a bubble chamber should provide information about: (a) geometrical positions of events; (b) directions of charged particle trajectories; (c) energies, momenta or velocities of charged particles; and (d) masses of charged particles. These quantities are measured in the CIT bubble chamber by combining high spatial resolution of bubble positions with certain properties of the CF_3Br bubble chamber liquid and one feature of the bubble formation process. Quantities (a) and (b) are derived directly from spatial location, while (c) and (d) require additional information.

The distribution of the gap lengths of a track is a function of the thermodynamic conditions of the fluid at the time the bubbles are formed and the velocity, β, of the traversing particle. Provided the thermodynamic conditions are known and a calibration has been made, a measure of the gap-length distribution yields the velocity.

The multiple scattering of the particle trajectory is a function of the material through which the particle passes and the product of momentum times velocity, $p\beta$, of the particle. Since the bromine in heavy freon has a high atomic number, multiple scattering in the bubble chamber is appreciable and can be used as a measure of $p\beta$.

Figure 4

Bubble Chamber - General Assembly

An elevation view of the general assembly of the CIT 10" heavy freon bubble chamber is shown.

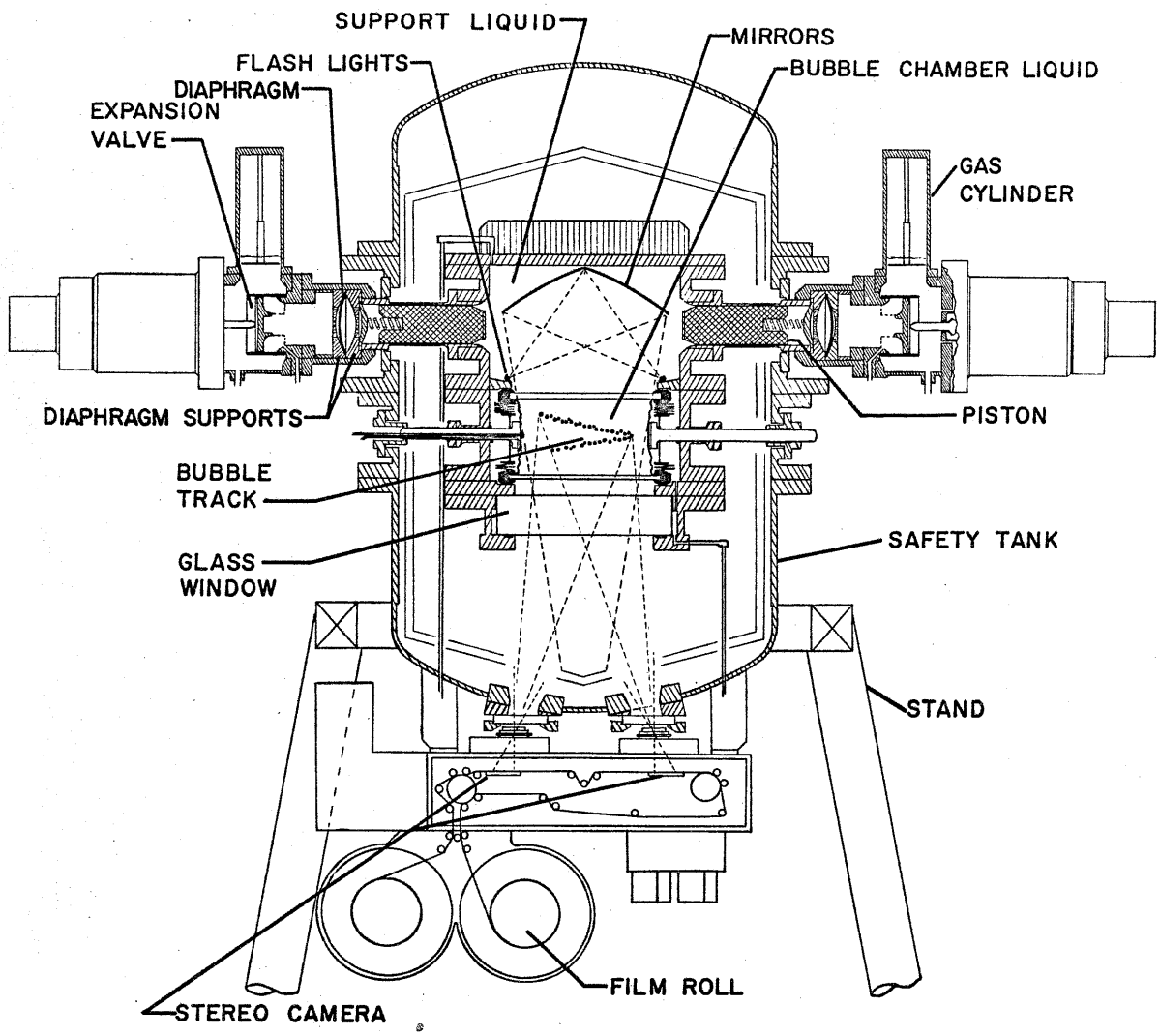
SUPPORT LIQUID
MIRRORS
FLASH LIGHTS
BUBBLE CHAMBER LIQUID
DIAPHRAGM
EXPANSION
VALVE
GAS
CYLINDER
DIAPHRAGM SUPPORTS
PISTON
BUBBLE
TRACK
SAFETY TANK
GLASS
WINDOW
STAND
FILM ROLL
STEREO CAMERA

FIGURE 4

Figure 5

Bubble Chamber - Detailed Elevation View at Freon Chamber

The drawing shows the several walls which the K_2^o beam penetrated before reaching the freon chamber. Some details of the expansion chamber are also illustrated.

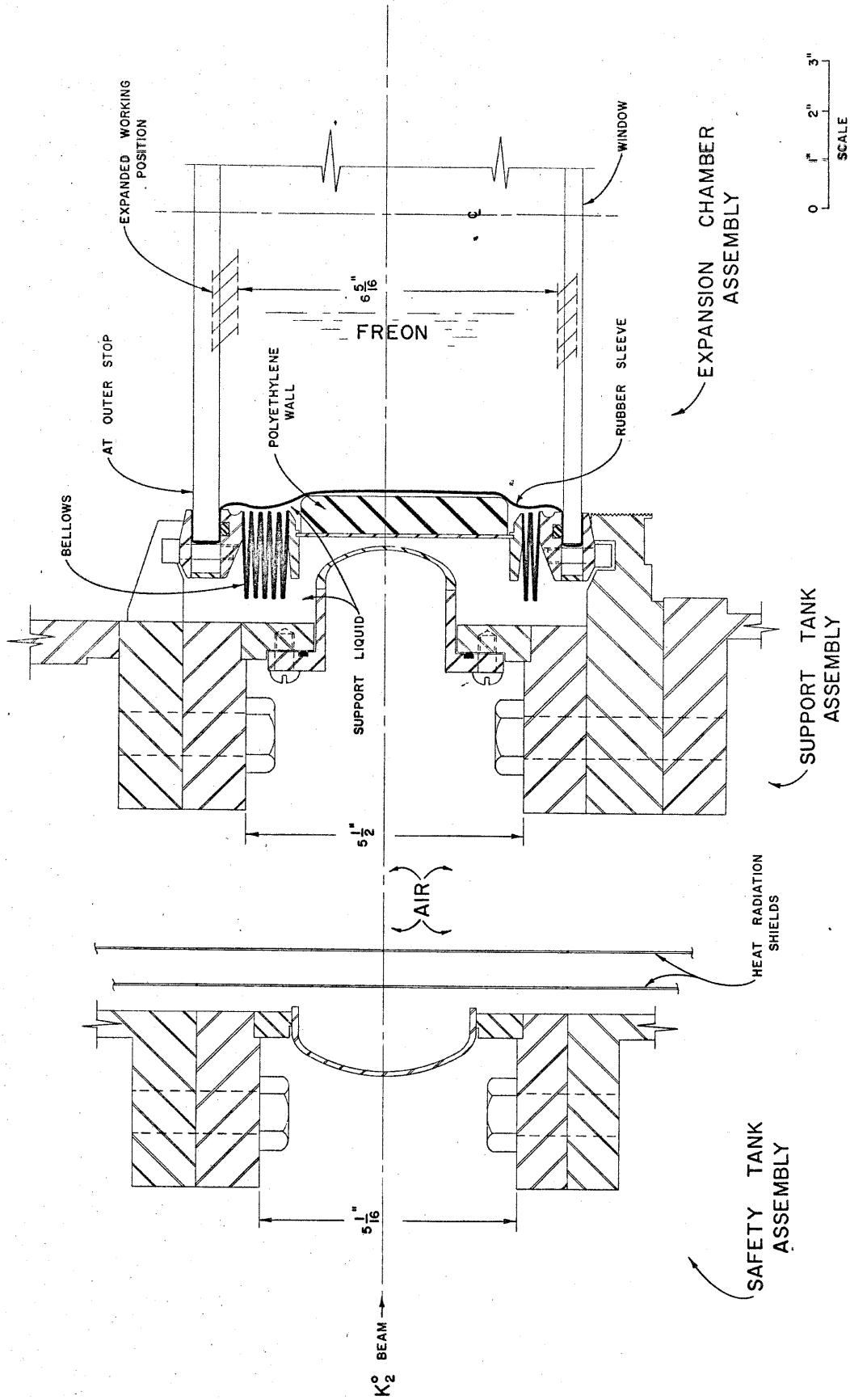
EXPANDED WORKING POSITION
WINDOW
AT OUTER STOP
POLYETHYLENE WALL
RUBBER SLEEVE
EXPANSION CHAMBER ASSEMBLY
FREON
BELLOWS
SUPPORT LIQUID
SUPPORT TANK ASSEMBLY
AIR
HEAT RADIATION SHIELDS
SAFETY TANK ASSEMBLY
BEAM
SCALE

FIGURE 5

Figure 6

Bubble Chamber - Detailed Plan View at Freon Chamber

The drawing shows the several walls which the K_2^o beam penetrated before reaching the freon chamber. Some details of the expansion chamber are illustrated. The location of the thermistor for controlling, and the thermometer for monitoring the temperature may be seen.

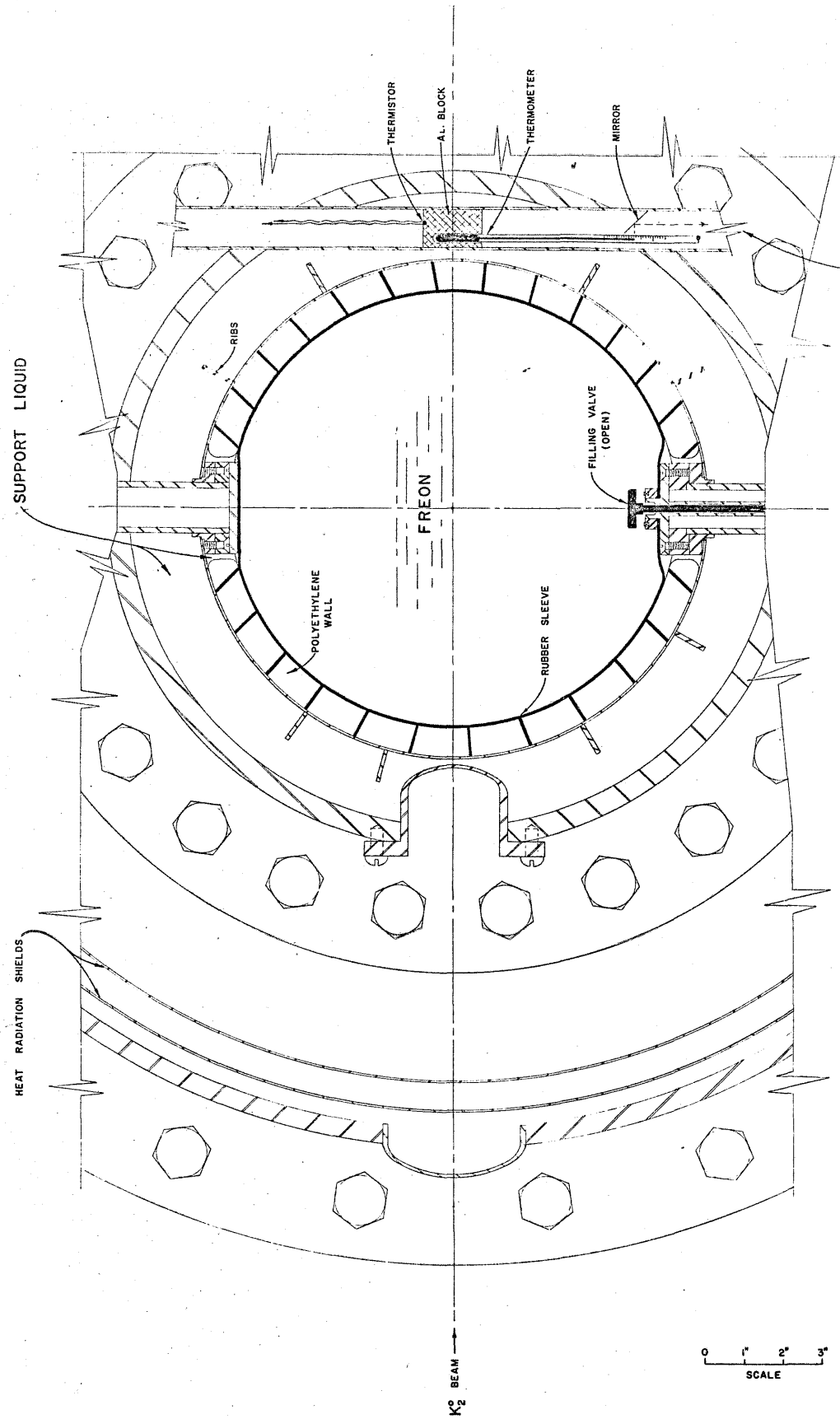
THERMISTOR
AL. BLOCK
THERMOMETER
MIRROR
TANGENT BEAM TUBE
RIBS
SUPPORT LIQUID
FILLING VALVE (OPEN)
FREON
EXPANSION CHAMBER ASSEMBLY
POLYETHYLENE WALL
RUBBER SLEEVE
SUPPORT TANK ASSEMBLY
HEAT RADIATION SHIELDS
SAFETY TANK ASSEMBLY
K_2^0 BEAM
0 1" 2" 3"
SCALE

FIGURE 6

Table 2

Bubble Chamber Component Specifications

I. Dimensions:

	Freon Chamber	Visible Volume
Diameter (cm)	28.0	approx. 25*
Depth (cm)	16.1	16.1
Volume (cm^3)	9.9×10^3	7.9×10^3

II. Freon 13B1 (CF_3Br)

Density (operating)	1.485 gm/cm^3
Index of Refraction	1.23
Radiation Length	11 cm
Nuclear Interaction Length (based on geometrical cross section)	54 cm
Range of 100 Mev Pion	25.4 cm
Range of 100 Mev Proton	7.4 cm

III. Support Liquid, FC-43 [$(C_4F_9)_3N$]

Density	1.86 gm/cm^3
Index of Refraction	1.29

IV. Operating Conditions for Run

Temperature	$(29.91 \pm 0.08)^{\circ}$ C
Expanded Pressure	(150 ± 1.5) psi
Period of Pressure Cycle	14 ms

*The shape of the visible volume is in between a right circular cylinder and a right parallelepiped.

Table 2 (Cont'd)

V. Optics

Film Type	Linagraph Ortho
Film Size	65 mm perforated
Stereo Angle	30^{o} (approx.)
Lenses	3 inch Goerz Rectagon
Illumination	dark field

Inasmuch as $p\beta = m\beta^2/\sqrt{1-\beta^2}$, these two measurements -- gap-length distribution and multiple scattering -- determine the particle's mass as well as its energy, momentum or velocity. Once the mass of a stopping particle is known, the range-energy relation for freon accurately gives the energy.

Other properties of CF_3Br, such as its radiation length, are important for certain applications, but may be classified as bonus properties to distinguish them from the basic properties discussed above.

The measurement procedures* yield reliable results only because this bubble chamber has the following three characteristics/:

---

*The specific techniques by which measurements were made for this experiment are presented in later parts of this thesis.

/Comment: The differences among most existing bubble chambers with regard to characteristics (2) and (3) tend to be subtle ones. Track distortions due to liquid motion between the time of creation and time of photographing bubbles are minimized by use of large "expansion areas" in a variety of different ways. The short time delay between creation and photography is also partially responsible for the small effects of turbulence. In the 72" liquid hydrogen bubble chamber of the Lawrence Radiation Laboratory, which employs an outmoded expansion system, the apparent radius of curvature due to distortion of this kind is estimated to be somewhat greater than 200 meters[35]. (This corresponds to a "sagitta" of 0.1 mm for a track 40 cm long!) It is clear that there is very little room for improvement over this figure.

A more serious type of distortion in its effects on multiple scattering measurements is the optical distortion caused by variations of the index of refraction associated with filaments of cooler (or hotter) liquid. The effect is "optical turbulence" in which the images of bubbles are scattered about the true track trajectory. In the 72" chamber optical turbulence was initially a serious problem, but has been reduced considerably through improved techniques of temperature control. The designs of newer chambers avoid situations where

(1) constant operating conditions -- temperature and expanded pressure; (2) distortion-free expansion; and (3) good optics. Constant

---

the bubble chamber liquid is squirted through small holes and thus eliminate the worst source of optical turbulence. Variations of index of refraction due to gradual temperature changes from top to bottom of a bubble chamber can also cause optical distortion of a track. However, present temperature control systems are precise enough that this is not a serious problem.

A third type of distortion should be mentioned -- that due to the optical system of photography, including effects of thick glass windows and lens distortions. Since optical distortions of this kind can be corrected for in the analysis procedure, they do not contribute to limitations in accuracy of measurement.

For a given geometrical arrangement, the optical resolution in a photograph depends on the properties of commercially available lenses and films. Since most bubble chambers have comparable depth-of-field and field-of-view geometries, and since film cost limits the size of film to within a factor of two (35 mm to 70 mm seems to be the practical range), bubble resolution varies by only small factors from chamber to chamber. Furthermore, depending on the particular features of a bubble chamber, one may desire larger (and easier to see) or smaller (with higher resolution) bubble images. For example, the bubble images in the 72'' chamber are perhaps twice as large as those in the CIT 10'' chamber. In the 72'' chamber, only the transverse location of the center of a bubble is desired, and this can probably be accomplished to about 0.02 mm. This certainly is greater accuracy than needed. (Compare this number to the 0.1 mm sagitta due to turbulence on a 40 cm track.) On the other hand, in the CIT 10'' chamber, where edges of bubbles can be located to 0.01 mm, higher accuracy would be desirable so that smaller longitudinal distances could be measured in gap counting.

The greatest differences among existing bubble chambers are related to their fulfillment of characteristic (1). Very few bubble chambers may be considered thermodynamically stabilized, i.e., able over long periods to time to consistently reproduce a given set of expanded thermodynamic conditions. As the importance of utilizing gap counting techniques becomes more fully recognized, it is to be expected that more chambers will be designed for thermodynamic stability. The achievement of constant expanded pressure is rather more difficult than holding the temperature constant, although the large thermal capacities of the giant chambers complicates the problem if appreciable thermal losses occur within

operating conditions are required if gap-length-distribution measurements are to be meaningful; distortion-free expansion permits the use of multiple scattering; and good optics is necessary for successful utilization of both the gap-length distribution and multiple scattering. The discussion in Appendix II is meant to supplement previous descriptions of how these characteristics are achieved. As pointed out in this Appendix, the temperature and expanded pressure of the chamber have been observed over long periods of time to be stabilized to the following accuracies:

	r.m.s. fluctuation about the mean
temperature	0.08° C
expanded pressure	1.5 psi

---

the chamber itself. Large amounts of boiling, the source of thermal losses, also prevents constancy of expanded pressure (particularly when the amount of boiling varies from one expansion to the next). B. Hahn has built the most thoroughly tested stabilized bubble chamber[36]. The CIT 10" chamber, as shown in this thesis, also seems to be well stabilized. Both of these chambers employ CF_3Br as the sensitive fluid and both are stable to better than 0.1°C and 1.5 psi over long periods of time. Temperature stability in the 20" liquid hydrogen bubble chamber of the Brookhaven National Laboratory is quoted as 0.1°C,[37] but no information is given regarding the stability of its expanded pressure. It should be noted that a comparison of absolute thermodynamic stabilities does not reflect the relative stabilities in bubble density for chambers employing different sensitive liquids. Relative stabilities of reduced thermodynamic quantities should, however, be reasonably representative[38]. For instance, from a comparison of critical temperatures, one would predict that thermal stability in liquid hydrogen must be ten times more precise than in CF_3Br in order to insure equal stability of bubble density. (Experimental information indicates that the factor may be closer to five times[39,34], although not conclusively. The factor 5 was obtained from a comparison of the percentage changes in bubble density with temperature, i.e., $(1/n)(dn/dT)$, where n is the bubble density. This function is quite non-linear with the thermodynamic conditions, and it is not known whether or not the measurements were made at the corresponding thermodynamic conditions for the two liquids.)

C. TIMING OF EXPANSION SEQUENCE

Since the bubble chamber pressure cycle is roughly sinusoidal with a period of 14 ms, the electrons in the synchrotron must be dumped quickly at the time the pressure reaches its minimum. If the relative timing fluctuates too much, the pressure at beam dump fluctuates more than is permissible for thermodynamic stability. Electronic controls[40] developed by J. H. Mullins, A. Barna and J. O. Maloy determine the bubble chamber timing and allow the north beam experiments to operate independently of and concurrently with south beam experiments. A description of the sequence of events for one complete bubble chamber cycle is illustrative. Typical specific numbers are used for simplicity.

After completion of the previous cycle, ten synchrotron master pulses are counted. This period constitutes a dead time for the bubble chamber, during which the chamber pressure is restored to its initial value, the expansion engine and flash tube condenser banks are recharged, and the film is advanced in the camera. Throughout this phase the north beam radiator is held out of the electron beam, the south beam radiator remains in the radiating position, and the south beam set of plateau and RF dump controls are operative. (Call this condition "south beam control".)

After the ten pulses, the bubble chamber is "ready" and the amplitude of the 40 mc probe, which monitors the number of electrons in the beam, is examined during the initial 10 ms of each succeeding synchrotron pulse. The synchrotron remains under

south beam control until a 40 mc probe pulse with an amplitude between 3 and 4 volts occurs. (The amplitude must be in this "window" at the end of the inspection period for the pulse to be accepted.) The bubble chamber electronics immediately issues the command to transfer control of the synchrotron to the north beam. This transfer, which requires 100 ms, entails flipping the south beam radiator out of, and the north beam radiator into, the radiating position; and disconnecting the south beam, and connecting the north beam, set of plateau and RF dump controls. The two sets of controls allow the north and south beams to operate at different energies.

In order to reduce timing jitter the bubble chamber expansion cycle is initiated by one of the standard synchrotron timing circuits set to give a pulse, called the pre-plateau pulse, 44 ms before the magnet plateau. 30 ms after the pre-plateau pulse, the expansion valves start to open, and 15 ms later, the minimum in the pressure cycle occurs. By this time the synchrotron magnet has reached its plateau. Concurrently with the pressure minimum the RF is turned off as quickly as possible, and the beam dumps in 0.25 ms. 2 ms after the beam dump the flash tubes are fired, and 5 ms later the expansion valves close. Finally, control of the synchrotron is automatically transferred back to the south beam before the start of the next synchrotron pulse.

The beam dump command is timed from the initiation of the expansion valve opening so that the beam dump and minimum

pressure will occur at very nearly the same instant. As long as the expansion valves operate frequently (i.e., once a minute), the timing jitter is less than 0.1 ms. Since this is smaller than the 0.25 ms duration of the fast beam dump, the pressure fluctuations are mainly determined by the latter. Assuming a sinusoidal pressure cycle of 14 ms period and 108 psi amplitude, one finds that the variation in pressure during beam dump is ± 0.3 psi about the mean if the beam dump commences at the minimum pressure and ± 0.1 psi if the beam dump is symmetric about the minimum pressure.

Unfortunately, when there is a delay of a few minutes between expansions, the O-ring seals in the valves lose their lubrication. This causes the valves to stick slightly for several succeeding operations. The resulting timing lag is at most 1 ms. Using the pressure cycle described above, one calculates for this case that the pressure at beam dump is 10.7 psi above the minimum. This lag can be (and in this experiment generally was) eliminated by adjusting the beam dump control for a few cycles after a delay.

D. BEAM MONITORING

1. General. For a bremsstrahlung spectrum, the number of photons, $N(k)dk$, in the energy interval between k and $k+dk$ is given by:

$$N(k)dk = QB(k, E_o)dk/k \qquad \text{(II-1)}$$

where the constant Q gives the total energy contained in the spectrum and the function $B(k, E_o)$ defines the shape of the spectrum (see Appendix III):

Q = total energy/E_o

E_o = electron energy = spectrum end point energy

$$\int_0^1 B(k, E_o)\, d\,(k/E_o) = 1$$

The purpose of a beam monitoring system is to measure Q. The output of the monitor is related to Q through some calibration constant. In the case of an ion chamber monitor, the constant U relates the charge collected, q, to Q ($U = E_o\, Q/q$). The less-elaborately designed ion chambers have values of U that vary slightly with E_o and must therefore be calibrated. During this experiment, q was integrated on one of the Synchrotron Laboratory's ion current integrators (Model 4).

2. Monitor for Fast Beam Dump. The 1'' cu-air ion chambers used for counter experiments are designed for a slow beam dump (about 20 milliseconds long) such as that employed in the south beam of the synchrotron. The beam produces within the chamber a certain ion density determined by the beam intensity, the geometrical beam size, and the collection time of the ions. The charge collected is a linear function of the beam size if the ion density is low enough that saturation* effects are negligible.

*The first saturation effect expected as the ion density increases is recombination. For a low degree of recombination, the chance that a particular ion will recombine rises linearly with the number

If one of these standard ion chambers had been used, unmodified, to monitor the fast beam dump employed for this experiment, the ion density would have been about 20 times the maximum attained in the south beam* and saturation effects would have been large. Mullins and Gomez devised a simple solution to this problem. Five inches of copper were placed in front of one of the standard ion chambers. This reduced the radiation reaching the ion chamber and therefore the saturation effect to a tolerable level.

The ion chamber plus 5 inches of copper combination was calibrated for the median beam intensity by comparing the response with and without copper to a known amount of slow beam dump from beam pulses falling into a narrow range of intensity about the median value. Since the absolute calibration of the ion chamber alone for slow beam dump is known, this comparison plus several corrections give the absolute calibration of the beam monitoring system. The corrections are for: saturation effect; attenuation in the carbon target; distortion of bremsstrahlung spectrum by lithium hydride beam hardener; and integration of early beam dump. The experimental investigation of the monitor changes and these corrections are discussed in Appendix III.

---

of oppositely-charged particles through which it must pass. This means that the percentage of recombination is initially a linear function of the ion density.

*For this experiment the north beam magnitude per pulse was about 1/10 the maximum south beam magnitude per pulse.

3. Total Beam Used. Figure 7 shows, for the entire experiment, the number of photons per Mev in the energy range 900 to 1300 Mev. The following quantities are of particular interest:

Quantity	Average per Picture	Total for Run
$E_o Q$ (Mev)	7×10^{10}	$(8.7 \pm 0.3) \times 10^{14}$
$\int_{910}^{1300} N(k)dk$	1.6×10^{7}	$(2.01 \pm 0.13) \times 10^{11}$
$\int_{1050}^{1300} N(k)dk$	0.9×10^{7}	$(1.15 \pm 0.11) \times 10^{11}$

The errors are the orthogonal combinations of the effects of errors in U', $B(k, E_o)$, and E_o (see Appendix III).

Figure 7

Bremsstrahlung Spectrum N(k)

Shown in this figure is the total number of photons per Mev which struck the carbon target during the experiment if: (a) E_o = 1300 Mev (curve a); or (b) E_o = 1328 Mev (curve b). Curve b illustrates the effect of the uncertainty in the end point energy (see Appendix III). The curves are drawn for the energy range of interest for this experiment.

N(k) = total number of photons per Mev

k = photon energy

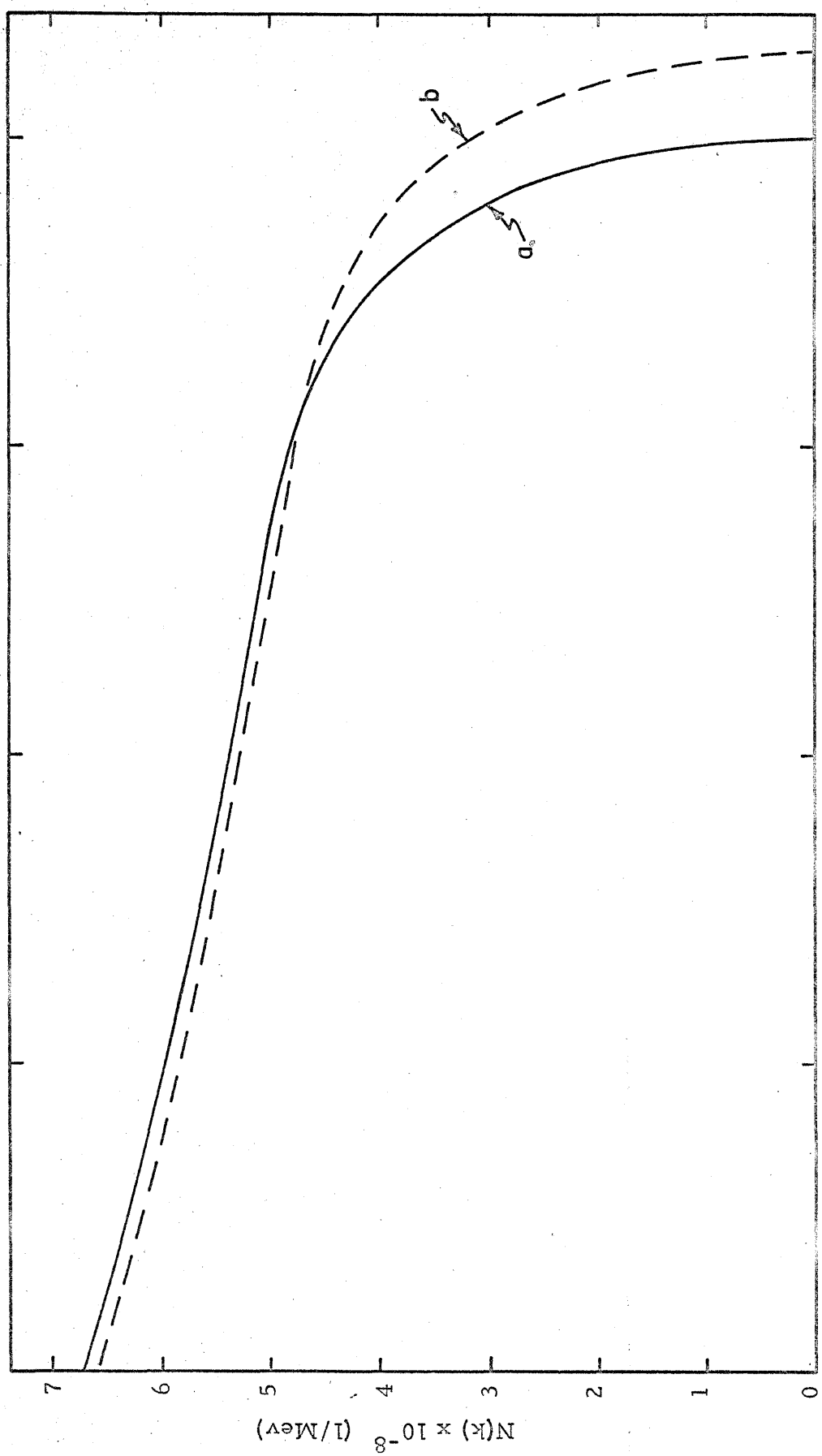

Figure 7

III. BACKGROUNDS

A. INTRODUCTION

The background in this experiment may be divided into four classes: obscuring background; extraneous events and crossing tracks; pseudo events; and real events from other than photoproduced K^o mesons.

B. OBSCURING BACKGROUND

1. General. As the title implies, the unpleasant feature of obscuring background was its ability to hide interesting events from detection and interfere with their measurement. Figure 8 dramatically illustrates the urgency of holding this type of background to a tolerable level. Most of the obscuring background was introduced by low energy gamma rays and neutrons. Due to the sweeping magnet and vacuum beam tube, charged particle sources were essentially eliminated. Low energies were of primary importance because of the predominance of low energy photons in the bremsstrahlung spectrum and the difficulty of shielding out certain low energy bands of photon and neutron energies. The conversion of the gamma rays and neutrons into charged particle tracks took place through Compton scattering, pair production, and nuclear interactions in the freon. A study of the distribution in track lengths showed a marked peaking toward short lengths. (The ratio of number of tracks with one, two and three bubbles was 10:4:1.) Although it was certain that both photons and neutrons contributed to this background, no quantitative information on their relative importances was obtained.

Figure 8

Obscuring Background

This photograph was taken before the improvements in the shielding against obscuring background were completed. The bremsstrahlung beam intensity was one half the intensity used during the run.

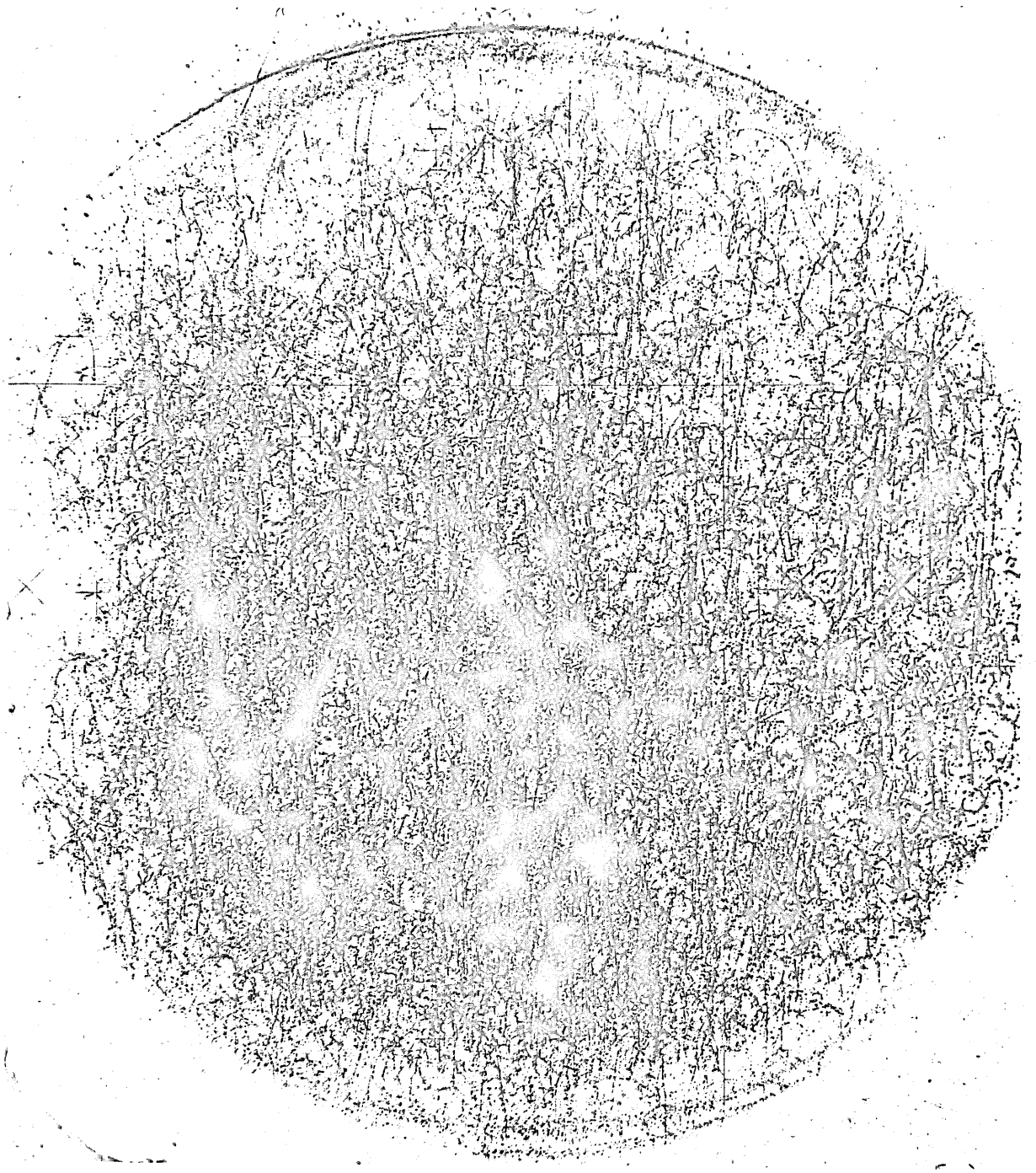

FIGURE 8

Figure 9

Typical Bubble Chamber Photograph

Besides illustrating the typical level of obscuring background during the run, this photograph shows a stopping pion and a stopping proton both of which occur at about the same depth in the chamber and with about the same dip. One should be able to identify the pion by inspection.

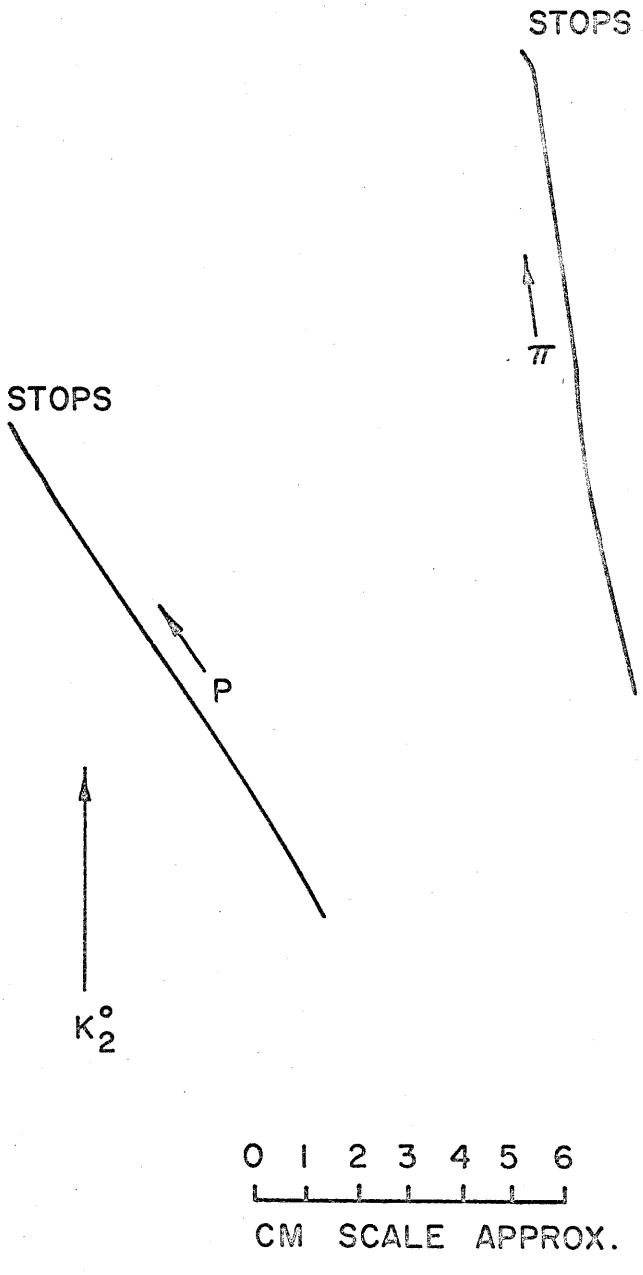

Figure 9

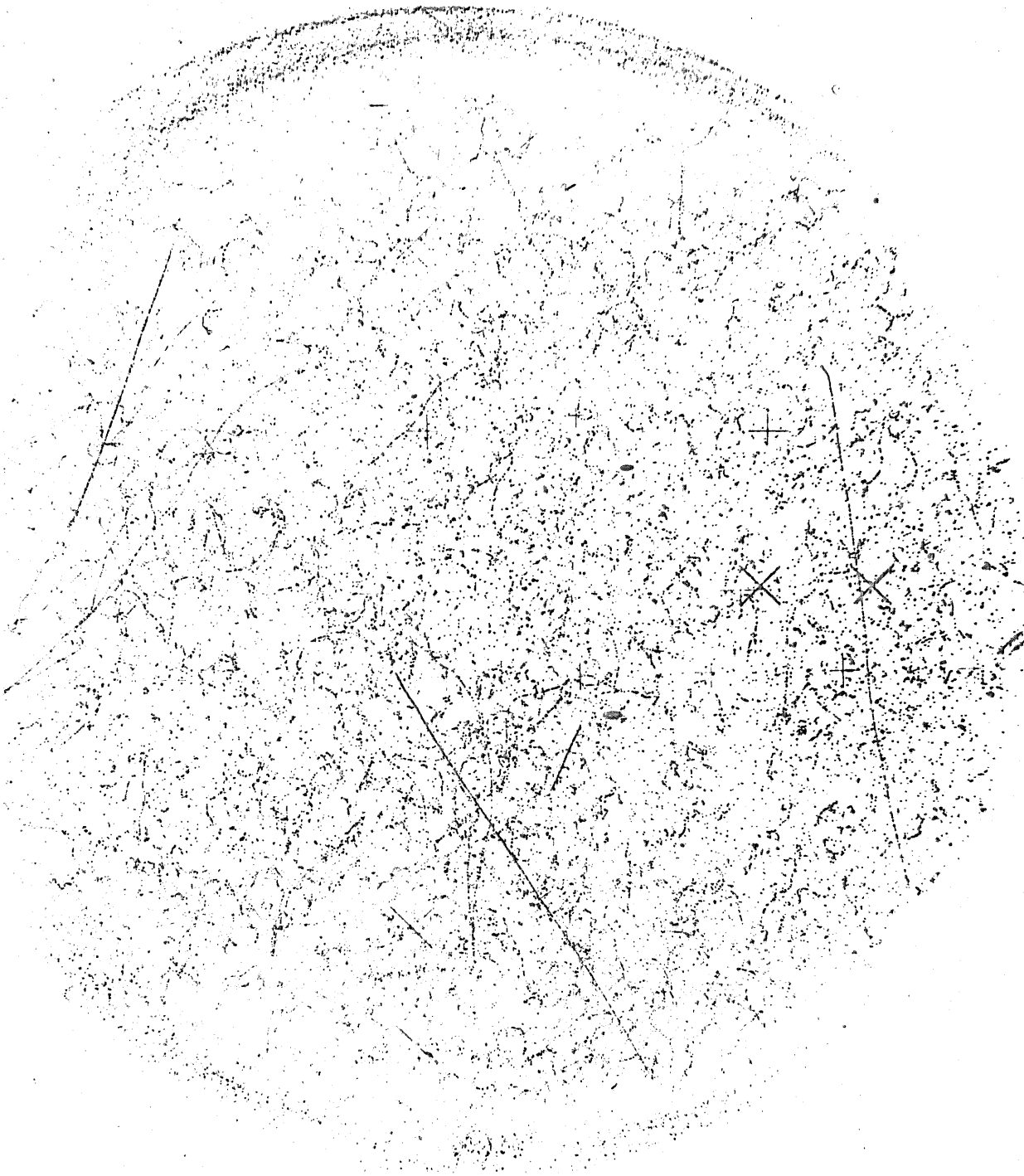

FIGURE 9

The bubble chamber itself was employed to test the effect of each of the many improvements in the experimental setup required to reduce the initial background level to an acceptable value. The procedure was simply to count the number of bubbles within a fixed area on the scanner and divide by the beam intensity. The bubble chamber sensitivity, of course, was held constant so that instrumental effects would not have to be corrected for. A neutron counter was also used to carry out a survey of the neutron sources.

It was convenient to classify the background sources as local or remote. Local sources were those located somewhere between the first beam scraper (BS-A in Fig. 10) and the exit end of the beam tube while remote sources included all others. Although the initial setup contained a considerable amount of shielding for remote sources and some shielding for local sources, the background was roughly one hundred times as great as that which was finally accepted as satisfactory. Since the measurements made applied only to relative improvements from the initial conditions and since there was also an interrelation between many of the changes, no information was obtained on the absolute importance of each type of shielding. Nevertheless, a few remarks can be made.

2. Local Sources. All but one of the local sources were produced by a small-angle spray in the beam which originated mostly in the photon beam collimator and partially in the lithium hydride of the beam hardener. It is believed that this spray was

composed primarily of photons with a minor component of neutrons. (The sweeping magnet of the beam hardener should have eliminated most electrons.) Local sources were produced when this spray struck each of the beam scrapers. The other local source was generated when the bremsstrahlung beam passed through the carbon target.

Each source gave rise to obscuring background through direct and indirect means. Photons and neutrons traveling in the proper direction from the sources passed directly into the freon chamber, while others only reached the freon chamber indirectly after scattering in the surrounding material (e.g., the steel of the safety and support tanks). Since the angular distribution of the intensity from each source was sharply peaked forward (in the direction of the bremsstrahlung beam), comparable amounts of obscuring background were attributable to the direct and indirect processes. The obscuring background due to these local sources was strikingly asymmetric, varying by perhaps a factor of two across the freon chamber (in the direction perpendicular to the bremsstrahlung beam). This decrease in background with increasing distance from the bremsstrahlung beam was a direct result of the angular distributions of the source intensities.

About 95 per cent of the improvement between the initial and final background was attained by better shielding of local sources. The final arrangement of local shielding (and sources) is shown in Fig. 10. It was imperative to place as much lead as

Figure 10

Experimental Arrangement - Local Details

This plan view of the experimental arrangement shows details of the layout and shielding between the first beam scraper and the bubble chamber. The following abbreviations are used:

BS.....Beam Scraper

LS.....Shielding against Local sources

RS.....Shielding against Remote sources

Capital letters are suffixed to these abbreviations in order to designate specific components.

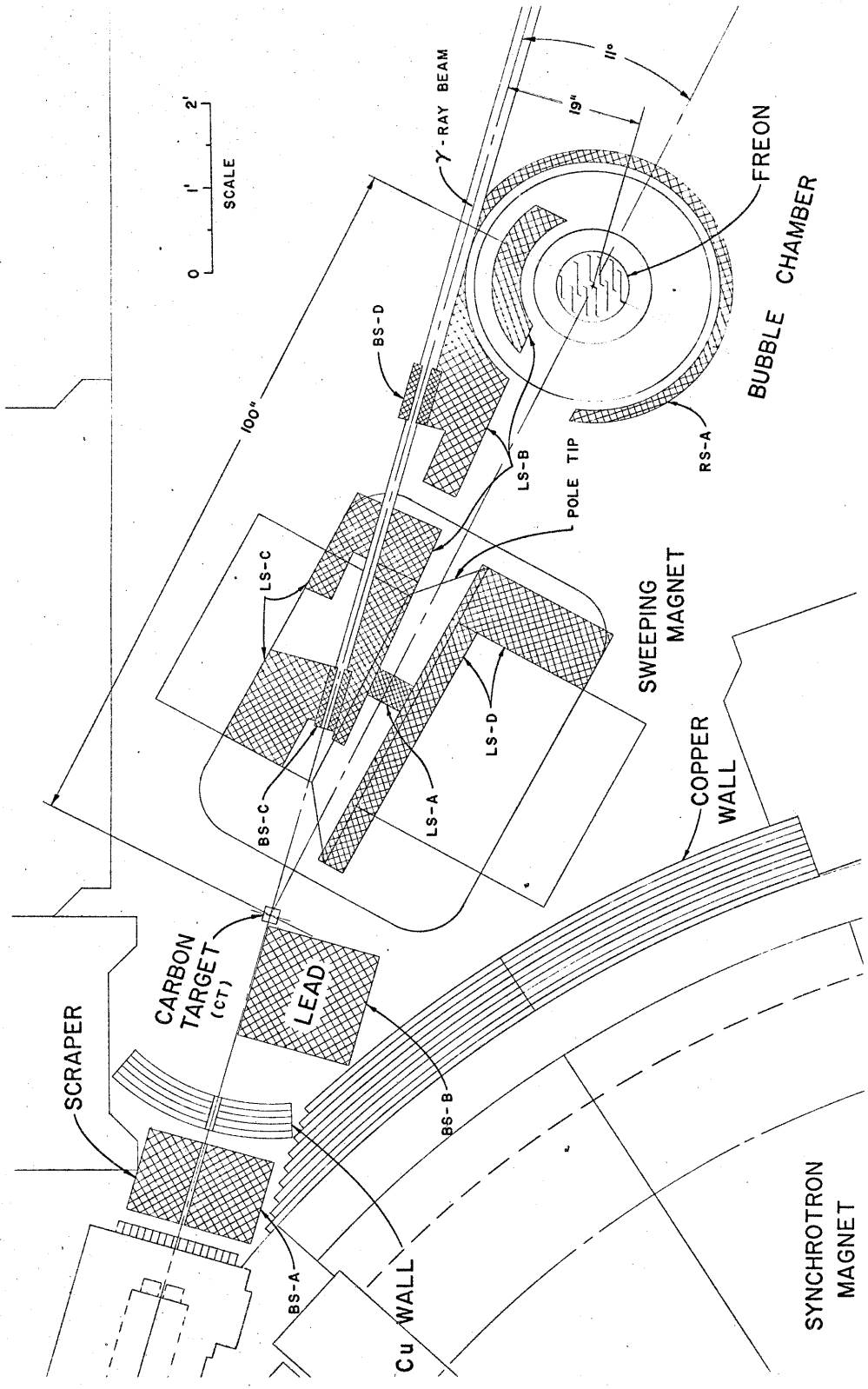
SCRAPER
CARBON TARGET (CT)
LEAD
BS-A
BS-B
BS-C
BS-D
LS-A
LS-B
LS-C
LS-D
POLE TIP
RS-A
100"
19"
11°
γ-RAY BEAM
FREON
BUBBLE CHAMBER
SWEEPING MAGNET
COPPER WALL
Cu WALL
SYNCHROTRON MAGNET
SCALE
0
1'
2'

FIGURE 10

possible between the freon chamber and the beam line. In fact, lead was even put on a shelf erected inside the bubble chamber safety tank. An absorber also had to be inserted into the K_2^o path. The 4 inches of lead located at the center of the sweeping magnet roughly maximized the ratio of K_2^o meson intensity to background. Table 3 has been assembled to give a rough idea of the relative importance of each source, how it was shielded, and the effectiveness of the shielding. It is to be emphasized that the numbers in this table are estimations. The complex interrelationships* between the several sources and effects of shielding made the experimental investigation of each source individually a major project. Since such investigations were not carried out, only the approximate statements of the table can be made.

The effect of the lithium hydride beam hardener should be mentioned in connection with local sources. Through its reduction of the low end of the bremsstrahlung spectrum, it decreased slightly the intensity of the carbon target source. Its net effect on the obscuring background was a small reduction. (The background ratio -- with/without the beam hardener -- was about 3/4.)

---

*As an example of the complex nature of the shielding, consider the effect of BS-B on the background from the source at BS-A. Although BS-B shielded the freon chamber from the direct radiation emanating from this source, it also presented material in which scattering might take place and thereby added to the indirect background from this source. LS-A provided the primary shielding of this scattered radiation and for this reason was of more importance in the overall shielding of the source at BS-A than might at first have been expected.

TABLE 3. Local Sources and Shielding Therefrom

Source[a]	Strength[b]	Shielding[a]	Relative Importance[c]	Shielding Purpose[d]	Background Ratio[e]
Small angle spray from collimator and LiH beam hardener	VERY LARGE	BS-A	0.99	d and i	
		Other scrapers		i	?
		All local shielding		i	
BS-A	10	BS-B	0.4	d and i	1/100
		(BS-C)+(BS-D)+(LS-B)	0.4	i	
		LS-A	0.1	i	
		(LS-C)+(LS-D)	0.1	i	
CT	10	LS-A	0.5	d	1/50
		(BS-C)+(BS-D)+(LS-B)	0.4	i	
		(LS-C)+(LS-D)	0.1	i	
BS-C	2	LS-B	0.7	d and i	1/50
		(LS-A)+(LS-D)	0.2	i	
		(LS-C)+(BS-D)	0.1	i	
BS-B	1	LS-A	0.5	d	1/50
		(BS-C)+(BS-D)+(LS-B)	0.4	i	
		(LS-C)+(LS-D)	0.1	i	
BS-D	1	LS-B	1.0	d and i	1/20

(a) See Figure 10 for explanation of abbreviations.

(b) Relative magnitude of background produced in freon chamber when little local shielding was present. (BS-A present except in first case.)

(c) Fraction of decrease attributable to each section of shielding.

(d) d = shielded freon chamber from direct radiation; i = shielded freon chamber from indirect radiation.

(e) Ratio of background in freon chamber; (after final shielding in place) to (little local shielding in place).

3. Remote Sources. Intrinsically, the most important remote source (by a factor estimated to have been between 4 and 10) was the collimator - lithium hydride beam hardener combination. (90 to 98 per cent of this source may be attributed to the beam that was dumped into the collimator.) The other remote sources were the synchrotron itself, particularly the tangent tanks close to the bubble chamber, and the beam catcher. The relatively direct paths from these sources to the freon chamber were well shielded before the background investigation was undertaken. Therefore, since the remaining radiation which reached the freon chamber had to scatter at least several times through large angles, one may safely say that it was composed to a large extent of thermalized neutrons.

The approach taken to counteract these sources was to shield both the bubble chamber and the sources as well as possible. The location of a large part of this shielding may be seen in Fig. 1. The concrete walls were about 12 feet tall; the copper walls extended a few feet above and below the beam line; and the lead shown as RS-A in Fig. 10 covered about 2/3 of the surface of the bubble chamber safety tank. The following shielding has been omitted from the figures:

1) 6 inches of copper and 12 inches of paraffin piled on three sides of the collimator (the few inches of space between the synchrotron magnet and the collimator were filled with copper).

2) 6 inches of copper (shown in outline in Fig. 1) and 12 inches of paraffin piled on three sides of beam hardener (the side towards the synchrotron tangent tank was partially shielded by copper as shown in outline).

3) The beam catcher and 10 to 24 inches of paraffin surrounding it.

4) A 2-inch thick lead wall extending from the bottom of beam scraper, BS-A, to the floor.

5) The steel yoke and copper windings of the sweeping magnet (shown in outline in Figs. 1 and 10).

6) A concrete block placed on top of the sweeping magnet.

7) A 12-inch thick paraffin wall piled below and around the sides of the sweeping magnet.

8) 10 inches of paraffin covering the top of the bubble chamber safety tank.

9) A 2-inch thick lead wall filling the window through which the γ-ray beam passed into the power room.

The local shielding also helped insofar as it provided a continuous lead wall across the sweeping magnet aperture.

With the final shielding in place, neutron measurements indicated that the collimator had been successfully shielded to the point where its importance as a background source was comparable to the synchrotron tangent tanks and magnet. (Clearly, shielding installed was least effective against the synchrotron itself.) At this final stage, the beam catcher source was unimportant.

4. Final Background Composition. Under the final shielding arrangement the relative importances of local and remote sources were investigated by blocking the bremsstrahlung beam with an 8-inch thick lead wall close to the first beam scraper (BS-A). The conclusion was drawn that 2/3 of the final obscuring background was due to local sources, while 1/3 was due to remote sources. Figure 9 shows the typical background level during the run.

C. EXTRANEOUS EVENTS AND CROSSING TRACKS

Extraneous events were those which originated from sources unrelated to true K_2^o signatures and could not be confused with K_2^o signatures. One of the beneficial consequences of using the sweeping magnet was that the most numerous extraneous events were neutron stars. Tracks of charged particles entering the chamber also occurred frequently. Most of these particles probably came from neutron stars in the material surrounding the freon chamber. A sample of 500 pictures was examined for extraneous events and crossing tracks. Table 4 presents the findings of this study. The data has been normalized to the average beam intensity per picture.

This type of background did not cause serious difficulty in scanning or analysis. The major problem associated with it was that occasionally an extraneous event was taken for the star from which a possible K_2^o signature originated. In nearly all such cases the false relationship could be proved by analysis.

TABLE 4

Extraneous Events and Crossing Tracks

Classification	Average Number per Picture
1) One prong events originating in the freon chamber	
a) Length on scanner less than 3 cm	1.36
b) Length on scanner greater than 3 cm	1.97
2) Two prong events originating in the freon chamber	
a) Both lengths on scanner less than 3 cm	0.30
b) One or both lengths on scanner greater than 3 cm (not including pseudo Λ^o decays)	0.36
3) More than two prong events originating in the freon chamber	
a) All lengths on scanner less than 3 cm	0.20
b) At least one length on scanner greater than 3 cm	0.34
4) Tracks entering freon chamber	
a) Length on scanner greater than 3 cm, but stopping in freon chamber	1.00
b) Not stopping in freon chamber	0.34
Totals	
Extraneous events	4.53
Crossing tracks	1.34

D. PSEUDO EVENTS*

Pseudo events also originated from sources unrelated to true K_2^o signatures, but, unlike extraneous events, they displayed the same particles as true K_2^o signatures. The most prevalent pseudo event was a visible pion and proton pair produced by a high energy neutron interaction in the freon. Such a star had the same superficial appearance as a Λ^o-hyperon decay. Two proton tracks from neutron interactions also formed V's and occasionally one of the tracks was mistakenly identified as a π-meson track. Other examples were π-meson scatter appearing as K^o decay, proton scatter appearing as Σ^+ decay, and very high energy pair production appearing as K_2^o decay. The main object of the analysis program was to separate true from pseudo events, and further discussion of this type of background is reserved for a later chapter.

E. REAL EVENTS FROM OTHER THAN PHOTOPRODUCED K^o MESONS

This type of event might have arisen from strange particle production and K^+ meson charge exchange scattering in or near the freon chamber. These reactions occurring at more than a few centimeters from the bubble chamber were unimportant since the short-lived components could not reach the chamber and the K_2^o intensity thereby introduced was at least several orders of magnitude below the photoproduced K_2^o intensity. The thresholds for

---

* Also called pseudo K_2^o signatures, pseudo Λ^o decays, etc.

strange particle production by nucleons and pions on complex nuclei are 1.1 Bev and 0.6 Bev, respectively, while the maximum energy nucleon from pion production by 1300 Mev γ-rays on carbon is 1.05 Bev. Therefore, only charged pions and K^+ mesons could have generated spurious strange particle decays.

Since the sweeping magnet prohibited any primary charged particles from passing through the bubble chamber, any pions and kaons reaching the chamber must have first been scattered. The kaon intensity from a second order process of this kind must have been very low for several reasons. First, the primary kaon intensity was low. Second, the maximum primary kaon momentum was about one half the maximum primary proton momentum for which the sweeping magnet was designed, and so the kaons would have to have been scattered through a large laboratory angle in order to have traversed the bubble chamber. An estimate of the total number of very high energy pions which passed through the bubble chamber during the entire exposure was made by scanning 1000 pictures for appropriate tracks. The upper limit estimate was 100 pions and 0.7 resulting strange particles.* Furthermore, no case of strange particle production associated with a high energy incoming pion was observed. Thus it is very unlikely that any real events not associated with a K_2^o meson occurred during the run.

---

*1 mb was used for the total pion-nucleon strange particle production cross section.

IV. SELECTION OF BEST K_2^o SIGNATURE

A. INTRODUCTION

Since the experimental conditions were designed so that the primary K_2^o mesons were essentially the only source of strange particles in the bubble chamber, a K_2^o decay or a strange particle decay or interaction following one of the possible K_2^o interactions (e.g., reactions I-11 through I-21) could have been construed as a K_2^o signature. The visible decays are listed below:

$$K_2^o \rightarrow \mu^{\pm} + \{\overset{\nu}{\bar{\nu}}\} + \pi^{\mp} \qquad \text{(IV-1a)}$$

$$\rightarrow \pi^+ + \pi^- + \pi^o \qquad \text{(IV-1b)}$$

$$\rightarrow e^{\pm} + \{\overset{\nu}{\bar{\nu}}\} + \pi^{\mp} \qquad \text{(IV-2)}$$

$$K_1^o \rightarrow \pi^+ + \pi^- \qquad \text{(IV-3)}$$

$$K^+ \rightarrow \pi^+ + \pi^o \qquad \text{(IV-4)}$$

$$\rightarrow \mu^+ + \nu \qquad \text{(IV-5)}$$

$$\Lambda^o \rightarrow p + \pi^- \qquad \text{(IV-6)}$$

$$\Sigma^+ \rightarrow p + \pi^o \qquad \text{(IV-7)}$$

$$\Sigma^{\pm} \rightarrow n + \pi^{\pm} \qquad \text{(IV-8)}$$

The usefulness of each signature was determined by the three criteria mentioned in Chapter I, i.e., (1) probability of occurrence per traversing K_2^o meson; (2) ease of identification in scanning;

and (3) amenability to exact analysis. The second criterion was directly related to the ability to identify particles by inspection. The reader is referred to Chapter V for a discussion of this identification process. A fourth criterion, the availability of experimental information needed to calculate the first criterion, was not intrinsically as important as the other three, but had a direct effect on the accuracy with which the observations could be related to the K^o photoproduction cross sections.

The signatures are discussed below and their relative merits are summarized in Table 5.

B. K_2^o DECAYS

From the measured mean life of the K_2^o meson (see Appendix I), one easily calculates the percentage which decayed while traversing the 17 useful centimeters of the freon chamber:

Kinetic Energy of K_2^o (Mev)	100	200	300	400	500	600
Percent which Decayed	1.4	0.9	0.8	0.7	0.6	0.5

The three pion and lepton decay schemes are the only appreciable modes of decay[14,15] of the K_2^o meson. Furthermore, since the branching ratio into 3π is less than, or of the order of 25%[15], and since the ratio of $3\pi^o$ to $\pi^+ + \pi^- + \pi^o$ is expected to be 3/2[41], the charged decays listed as IV-1 and IV-2 constitute 85% or more of the K_2^o decays. Neagu et al.[15] have measured the branching ratio of the electron mode IV-2:

$$\frac{K^o_{e3}}{K^o_2 \rightarrow \text{charged products}} = (42 \pm 12)\% .$$

All of the charged K^o_2 decays should be easy to scan for, although decay schemes IV-1a and IV-1b cannot be distinguished from each other nor from K^o_1 decay IV-3 by particle identification during scanning. The K_{e3} decay IV-2, however, can often be uniquely identified.

Unfortunately, the three-body K^o_2 decays are not subject to exact analysis. Even if the energies of both visible decay products are known as well as the direction of the incoming K^o_2, there is still one free parameter in the decay. The situation is worse for K_{e3} decays since electron energies cannot be measured with any reasonable precision. Therefore, separation from background events such as pion scattering and wide angle electron pairs is difficult if not impossible.

C. K^o_1 DECAYS

Rough estimates of the cross sections for reactions I-19, I-20 and I-21 are carried out in Appendix IV. The results obtained are:

Reaction	Regeneration from	Total Cross Section per Molecule of CF_3Br (mb)	Angular Distribution
I-19	whole liquid	$<< 50$	"exactly" forward
I-20	whole nuclei	50 ± 30	sharply peaked forward
I-21	individual nucleons	240 ± 200	very broad

These estimates when combined with the observed branching ratio:

$$\frac{K_1^o \rightarrow \pi^+ + \pi^-}{(K_1^o \rightarrow \pi^+ + \pi^-) + (K_1^o \rightarrow \pi^o + \pi^o)} = 0.75^{(42,43)} \qquad \text{(IV-9)}$$

indicate that for a 17 cm path in freon, about 2.3% of the traversing K_2^o mesons should have given rise to charged K_1^o decays.

K_1^o decays are identifiable in scanning and can be analyzed for a unique Q value. However, the high energy of at least one of the pions leads to some difficulty in identification and rather large errors in the measured Q values.

D. K^+ DECAYS AND K^- INTERACTIONS

From the data of Chinowsky et al.[44] on K^+ charge-exchange scattering in deuterium one may estimate* that 1 or 2% of the K_2^o mesons which crossed the freon chamber were transformed into K^+ mesons. About the same percentage should have been converted to K^- mesons.

Since the energy spectrum of the K_2^o mesons extended from 75 to 550 Mev, the energies of the $K^{\pm}$ mesons probably tended to be high, and so, most likely, only a small fraction of those produced stopped in the freon chamber. (A 100 Mev $K^{\pm}$ meson has an 11.5 cm range in freon.) Furthermore, inasmuch as (a) the mean life of a $K^{\pm}$ meson is long compared to a typical transit time across the chamber, and (b) the geometrical interaction length in freon is about

* The calculation is similar to that presented in Appendix IV for K_1^o regeneration from individual nucleons.

four times a typical path length in the chamber, few of the $K^{\pm}$ mesons decayed or interacted in flight.

Most K^+ decays satisfy the scanning and analysis requirements of a good K_2^o signature. K^- interactions vary considerably in the degree to which they fulfill these requirements. (E.g., K^- capture stars at the ends of stopping K^- mesons are more readily identified than K^- interactions in flight.)

Although a non-stopping $K^{\pm}$ meson can very likely be identified through quantitative measurements of both the gap-length distribution and the multiple scattering of its track, the lack of automated apparatus precluded any attempt to make this identification.

E. Λ^o DECAYS

Arguments are set forth in Appendix IV which establish that, over the range of K_2^o energies possible in this experiment, the total cross section per CF_3Br molecule for Λ^o production from K_2^o mesons is (450 ± 100) mb.

This cross section plus the branching ratio for the charged mode of decay,

$$\frac{\Lambda^o \rightarrow \pi^- + p}{(\Lambda^o \rightarrow \pi^- + p) + (\Lambda^o \rightarrow \pi^o + n)} \approx 0.65 \quad (43) \qquad \text{(IV-10)}$$

implies that about 3.1% of the K_2^o mesons which passed through the freon chamber gave rise to observable Λ^o decays.

Λ^o decays fulfill the scanning and analysis criteria better than any of the other K_2^o signatures. The primary reason is that the pions from Λ^o decays tend to have energies which are moderate

and therefore most suitable for the scanning and analysis techniques.

The one serious inconvenience associated with the Λ^o-decay signature was the sizeable background of neutron-induced pseudo Λ^o decays.

F. $\Sigma^{\pm}$ DECAYS

Although Σ hyperon production occurs with a probability commensurate with that of Λ^o production, their decays are not practicable as K_2^o signatures for several reasons:

1) The decay scheme IV-7 often appears the same as an inelastic proton scatter.
2) Since the energy of the Σ is unknown, a measurement of the charged decay product does not determine the Q value of the decay.
3) Stopping Σ^- hyperons are captured by freon nuclei and therefore do not decay. These captured stars are difficult to identify.
4) Inasmuch as the Σ^- energy spectrum is not known, the ratio of the number of decays in flight to the number of captures cannot be estimated. Therefore, the related correction factor cannot be applied to the number of observed decays.
5) The charged pion decay modes cannot be uniquely identified without analysis because neutron stars producing a pion and proton can have the same track geometry.

Under certain circumstances, however, the $\Sigma^{\pm}$ hyperons can be identified:

1) If the direction of the neutral particle from a $\Sigma^{\pm}$ decay is known, the decay can be analyzed uniquely. Conversion of the two γ rays from the π^{o} decay or identification of an associated neutron recoil would establish this direction.
2) If the direction of travel of the Σ is established, the observation of a capture star or a charged pion decay is sufficient. Bubble density measurements on the Σ track or identification of a suitable star out of which the Σ emerged might be used.
3) If the energy of the Σ can be established by bubble density measurements, the decay can be analyzed uniquely.

G. CONCLUSIONS

The characteristics of the K_2^o signatures are summarized in Table 5. It is clear from an examination of this table that the Λ^o decay is the most suitable signature. The K_1^o decay, which appears to be second best, might also be useable. Although observation of the other strange particle decays or interactions would provide proof of the existence of photoproduced K^o mesons, the quantitative use of these signatures is severely limited. Thus the major effort in this experiment was directed towards investigating Λ^o decays and a minor effort was directed towards investigating

K_1^o decays. The other modes were noted qualitatively.

Most of the K_2^o signatures are illustrated in Figs. 11 through 19. These examples are "prize" events in that the directions in which the strange particles were traveling before decay are established. This knowledge provides over-determination in the analysis and can be used to more definitely prove the validity of the assigned signature.

TABLE 5

Characteristics of the K_2^o Signatures

Observable Signature	Frequency of Occurrence (% of K_2^o crossing 17 cm of CF_3Br)	Scanning Ease	Analysis Quality	Experimental Information Available
K_2^o decay	0.4 to 1.2	Good	Poor	Good
K_1^o decay	2.3	Good	Fair	Poor
K^+ decay	< 1	Good	Good	Poor
K^- interaction	< 1	Poor to Good	Fair to Good	Poor
Λ^o decay	3.1	Very Good	Very Good	Fair
$\Sigma^{\pm}$ decay	1.5	Poor	Poor	Fair

Figures 11 through 19

Figure Number	Frame Number	Reaction Involved[a,b]	Decay Illustrated
11.	17667		IV-2
12.	17932	I-20	IV-3
13.	12489	I-21	IV-3
14.	18869	I-21	IV-3
15.	8373	I-11	IV-4 or IV-5
16.	11082	I-13 or I-14	IV-6
17.	15091	I-16 or I 17	IV-6
18.	15763	I-16 or I-17	IV-6
19.	16996	I-15 or I-18	IV-8

(a) Most likely reaction.

(b) The direction of the incident K_2^o meson is indicated in each event sketch.

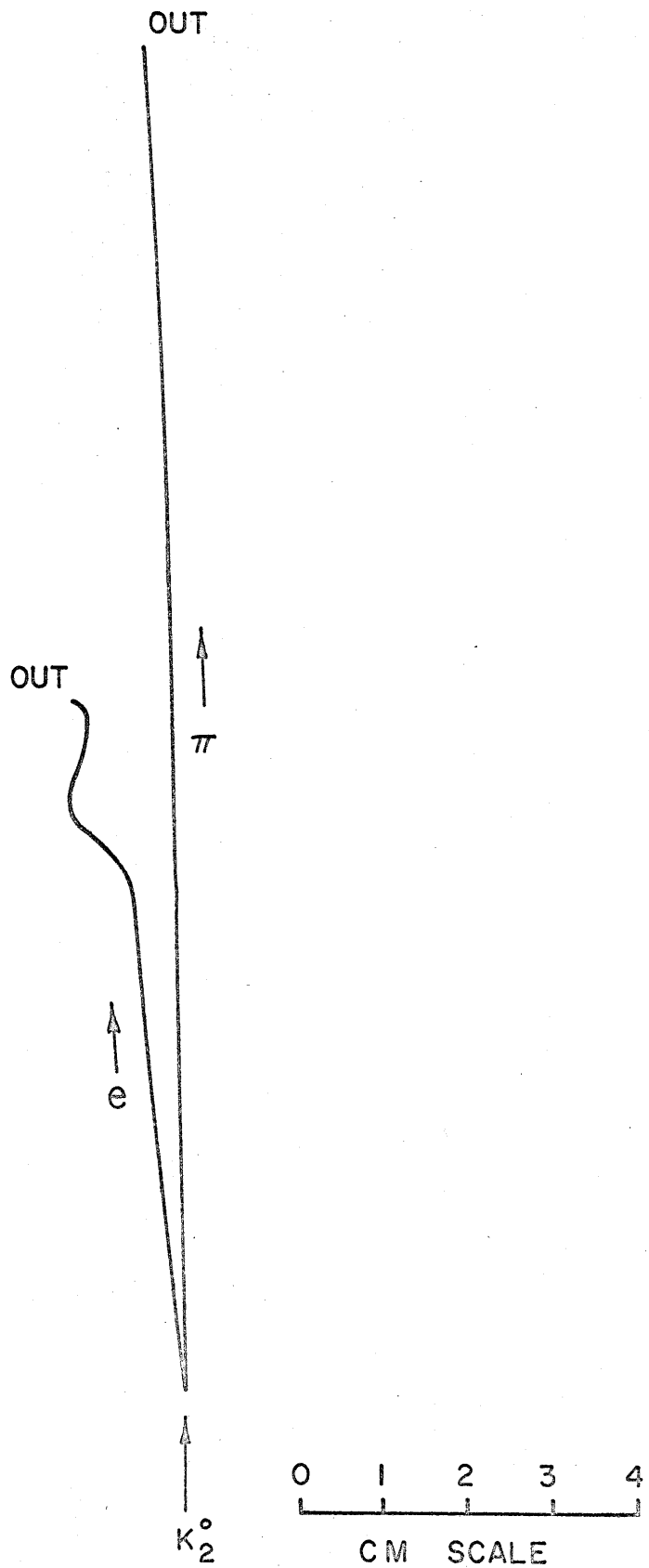

Fig. 11. Example of K_2^o decay.

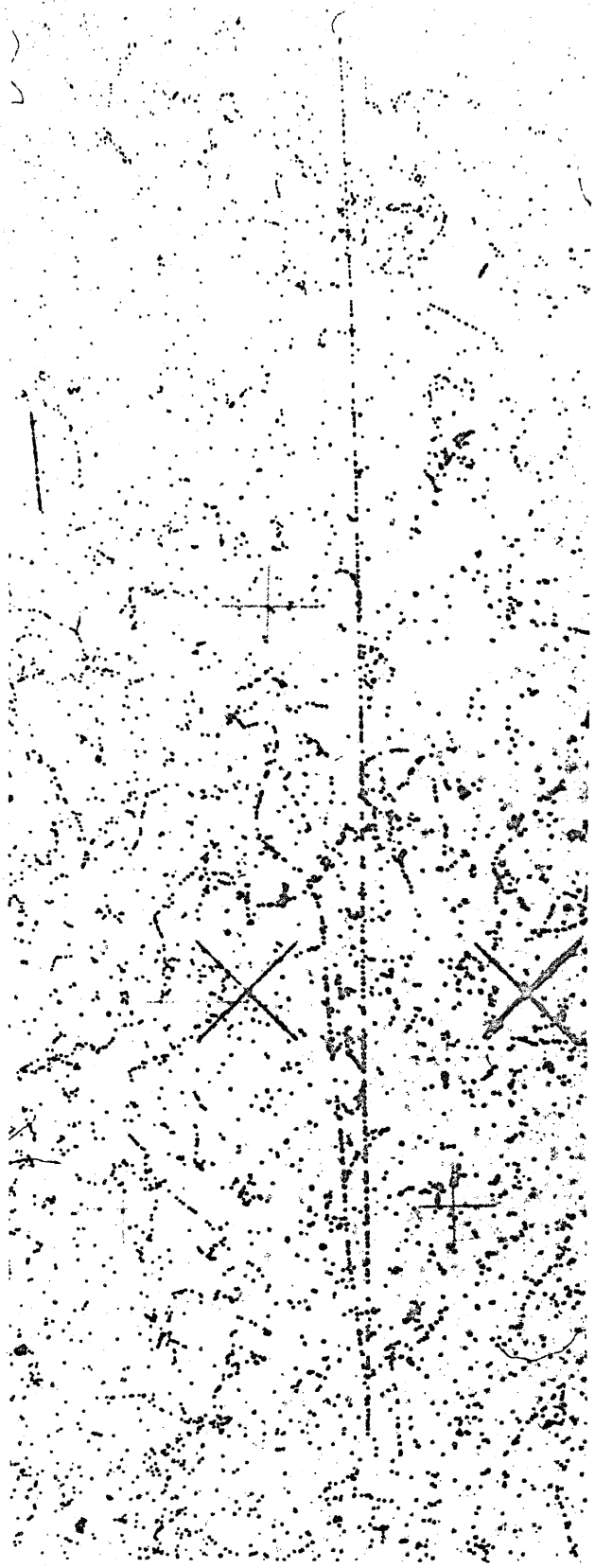

FIGURE II

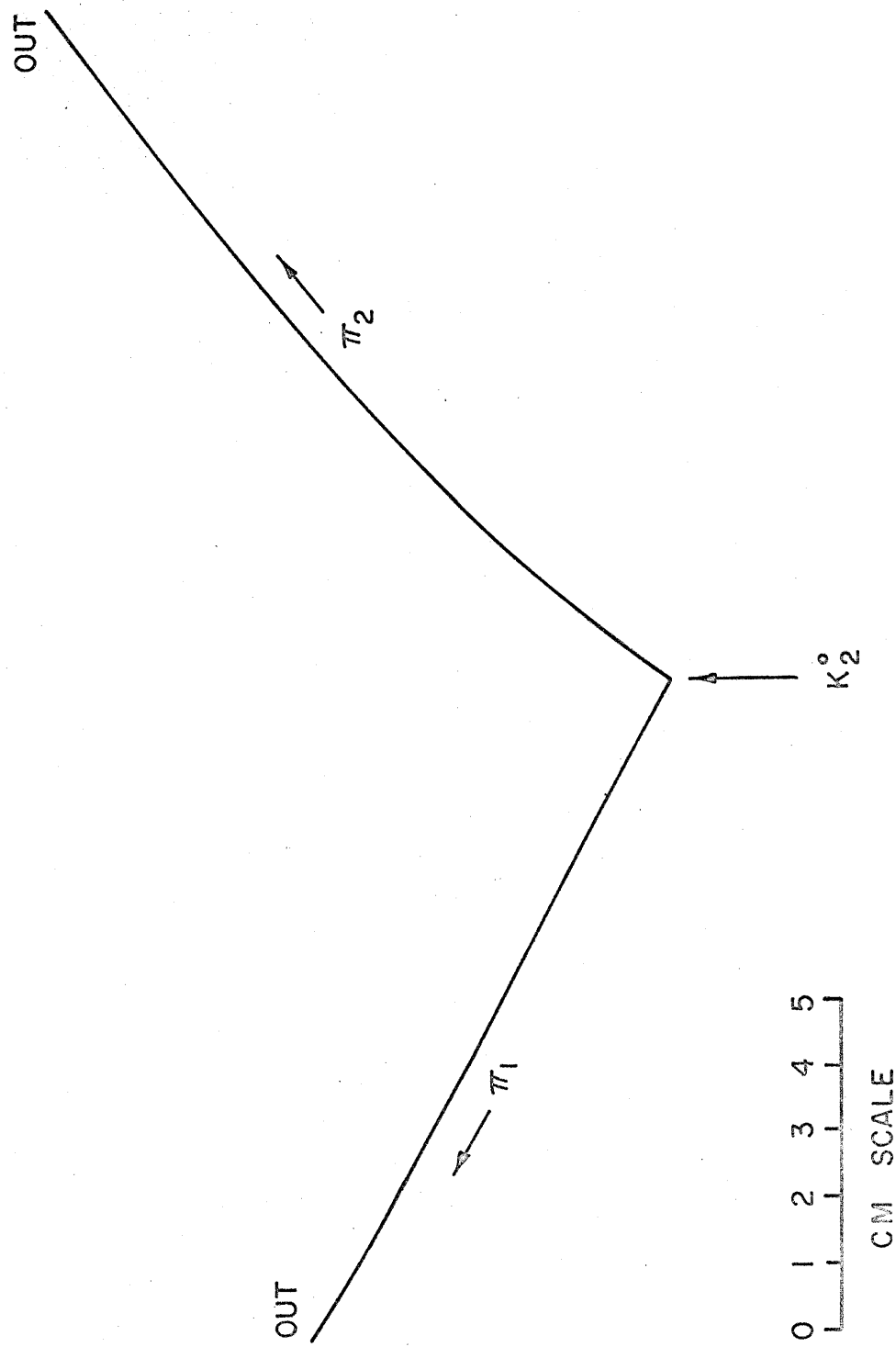

Fig. 12. Example of diffraction regeneration of K_1^o meson and subsequent K_1^o decay.

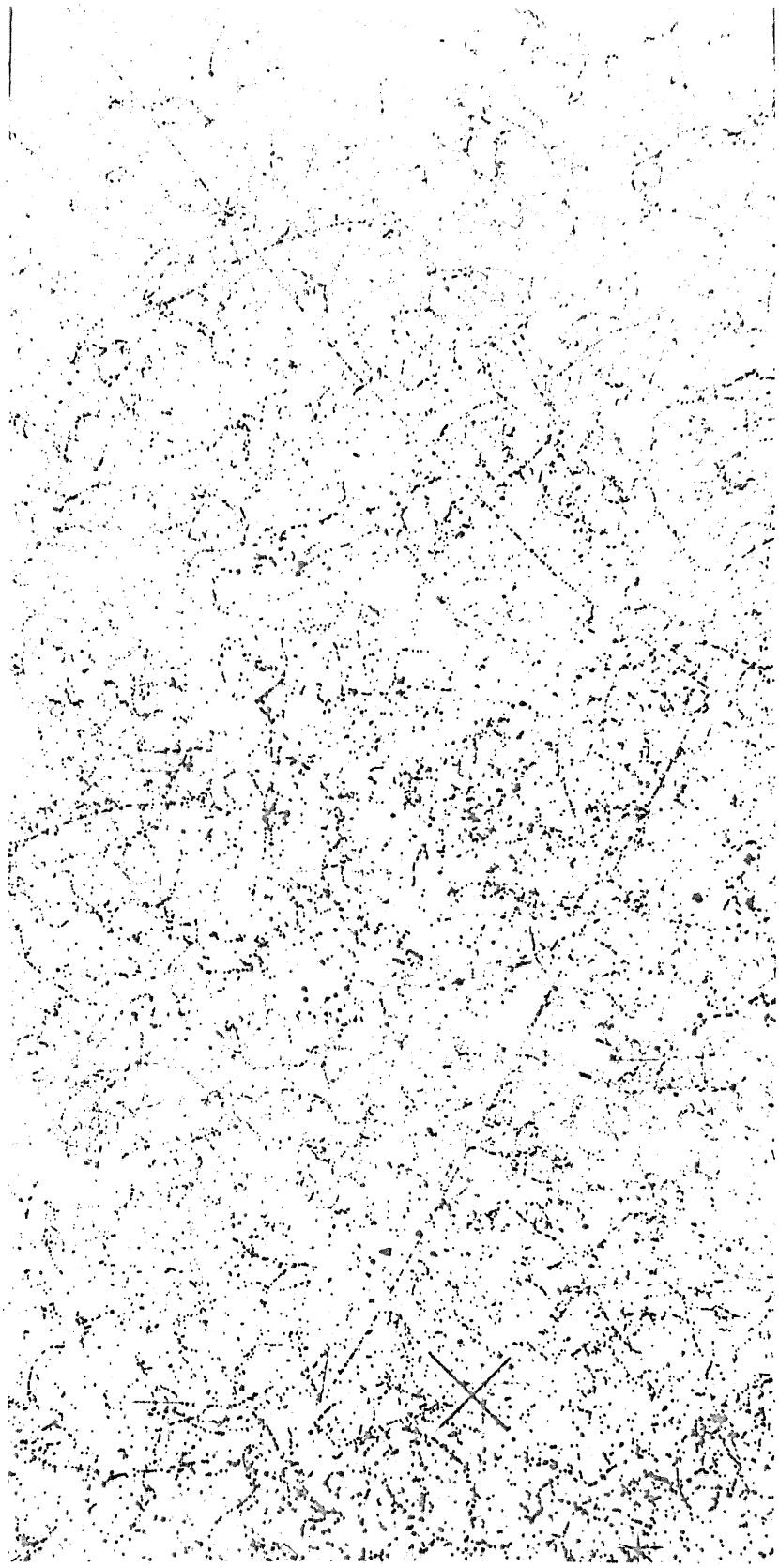

FIGURE 12

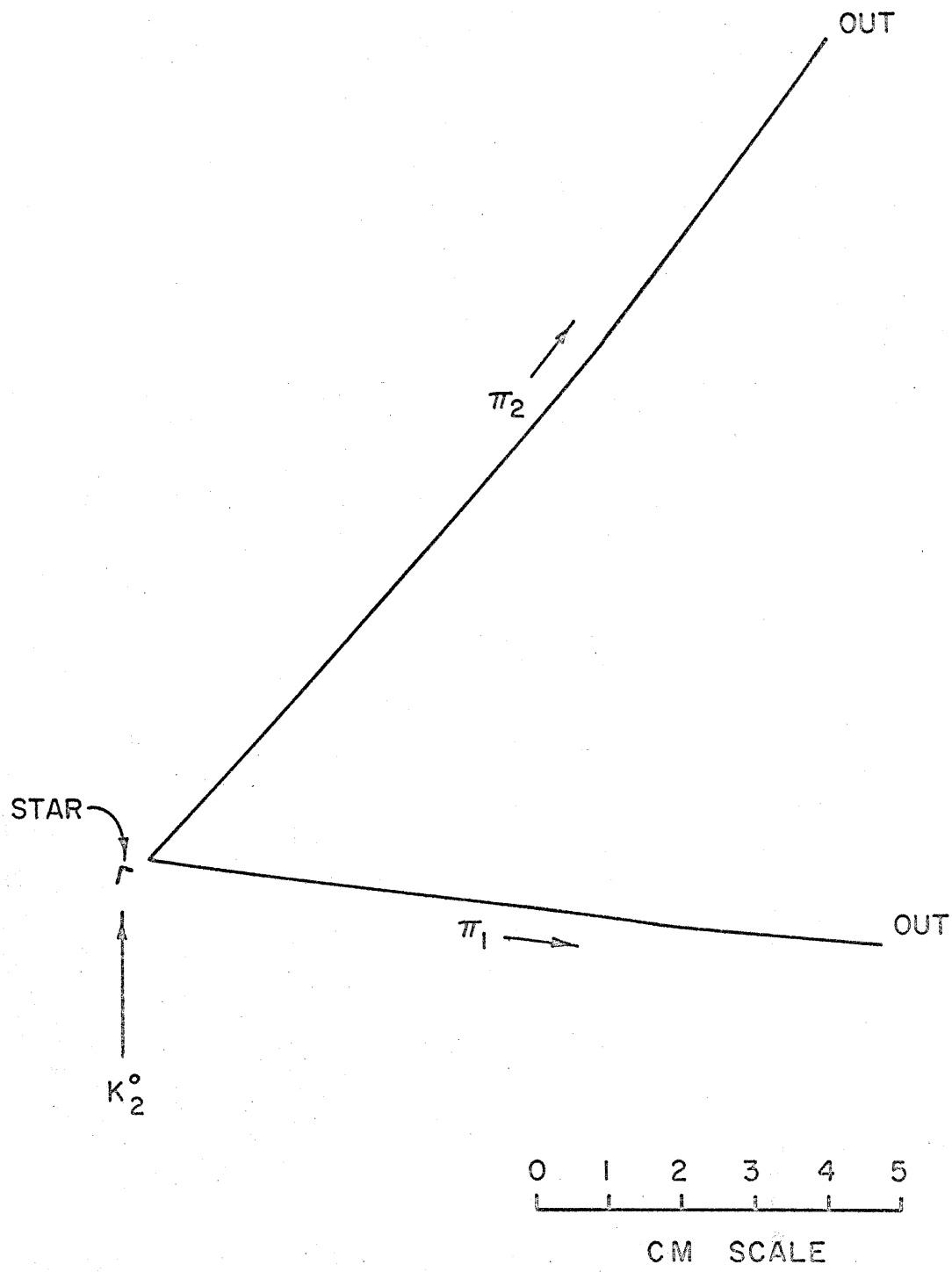

Fig. 13. Example of K_1^o regeneration from K_2^o-nucleon scattering within nucleus, and subsequent K_1^o decay.

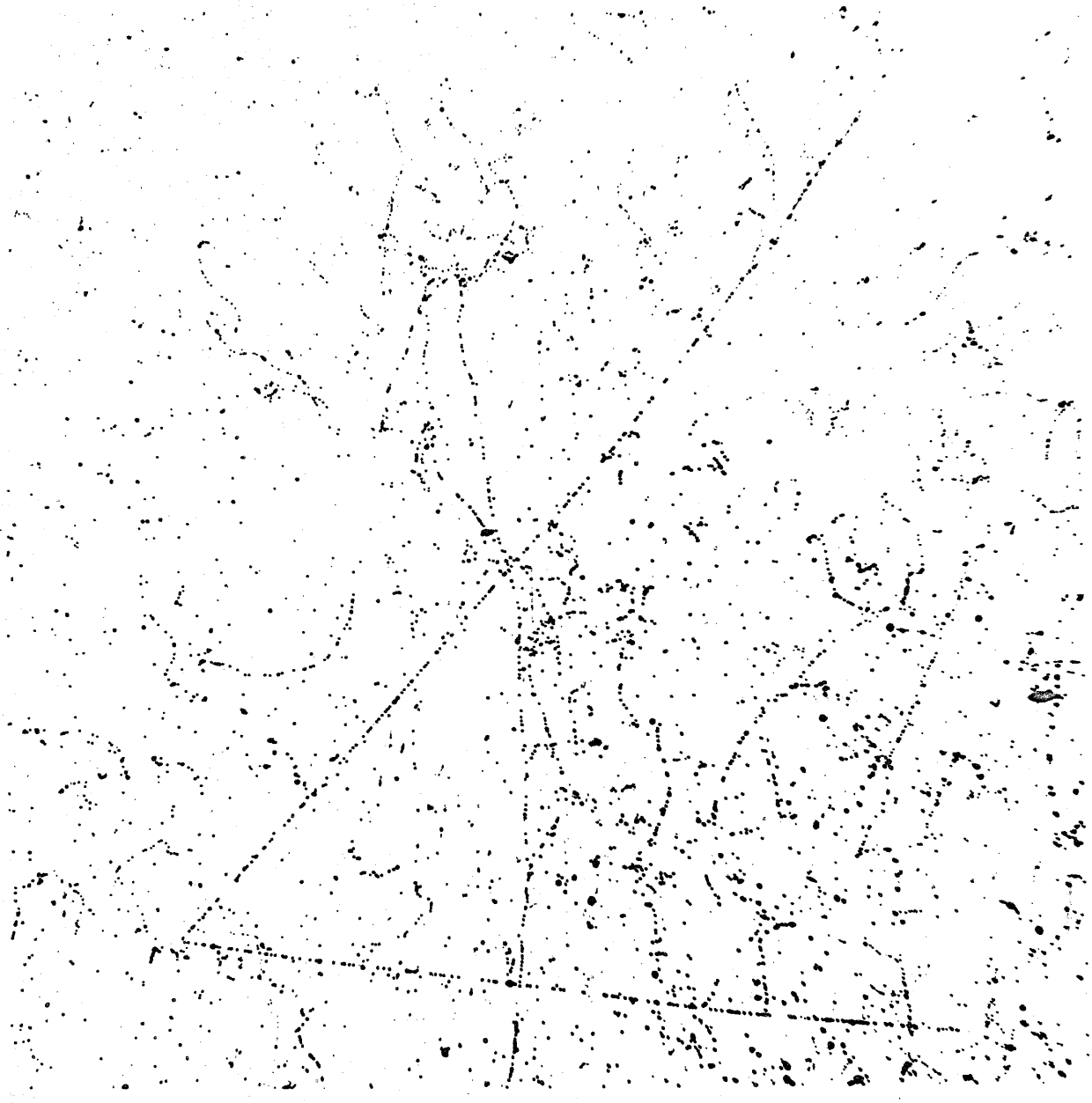

FIGURE 13

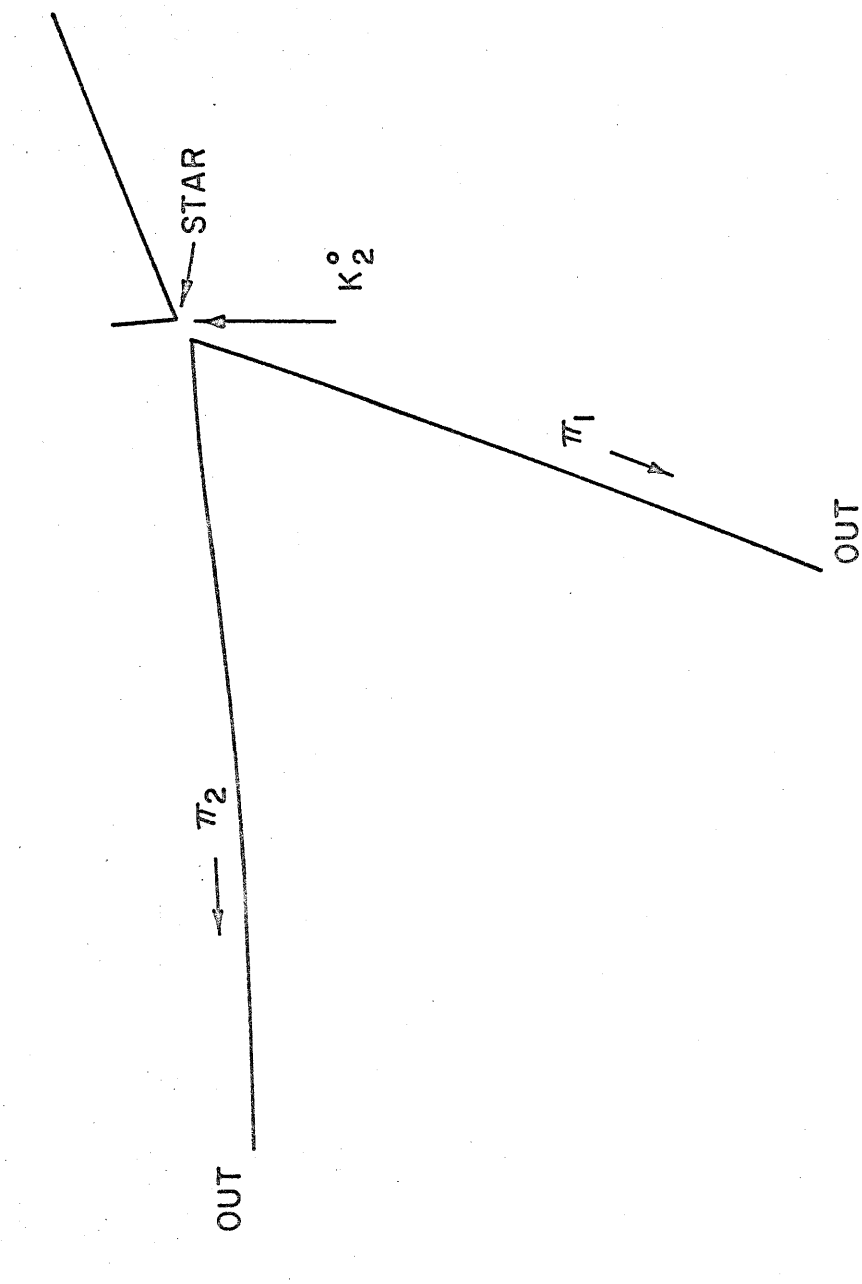

Fig. 14. Example of K_1^o regeneration from K_2^o-nucleon scattering within nucleus, and subsequent K_1^o decay.

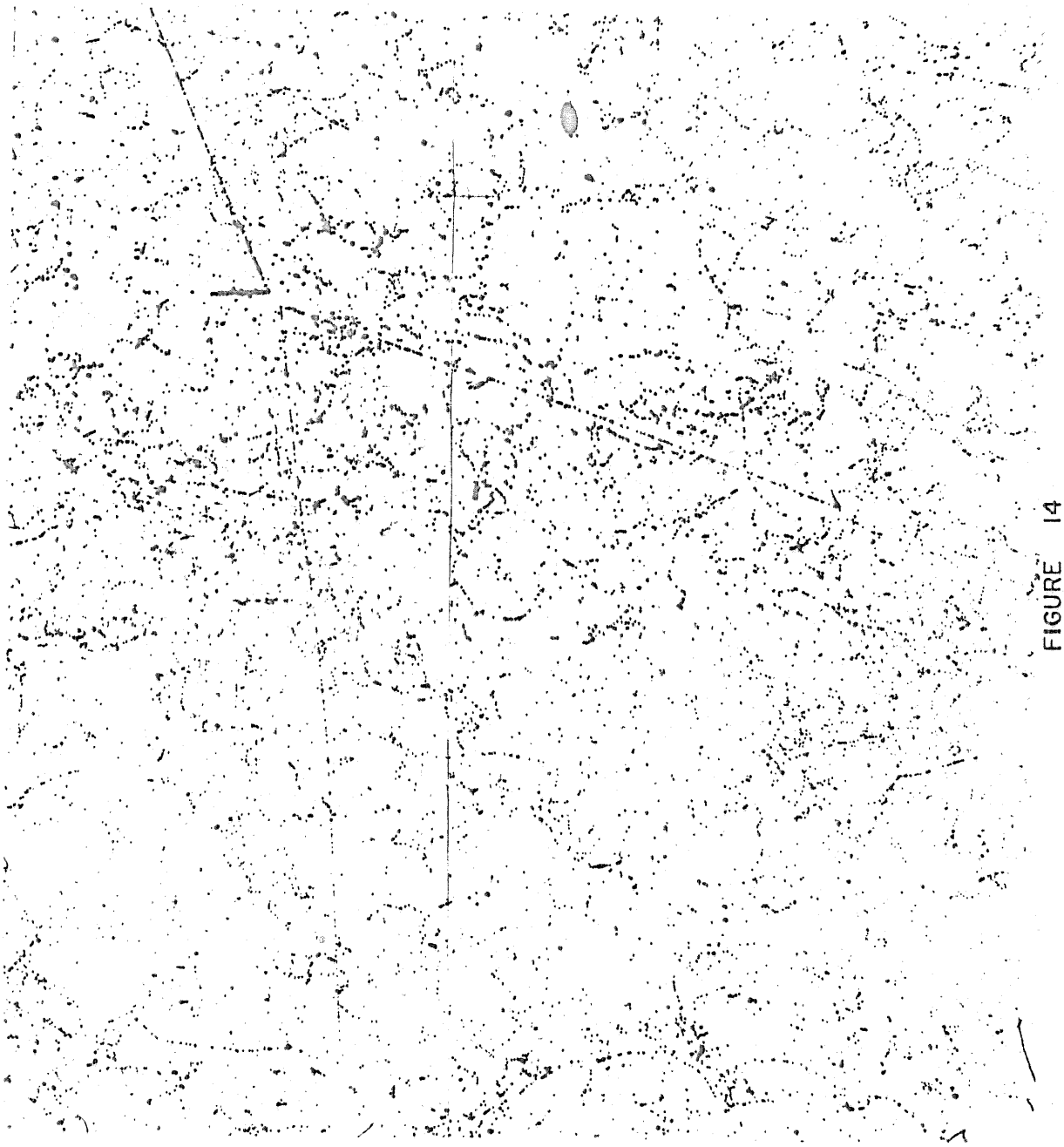

FIGURE 14

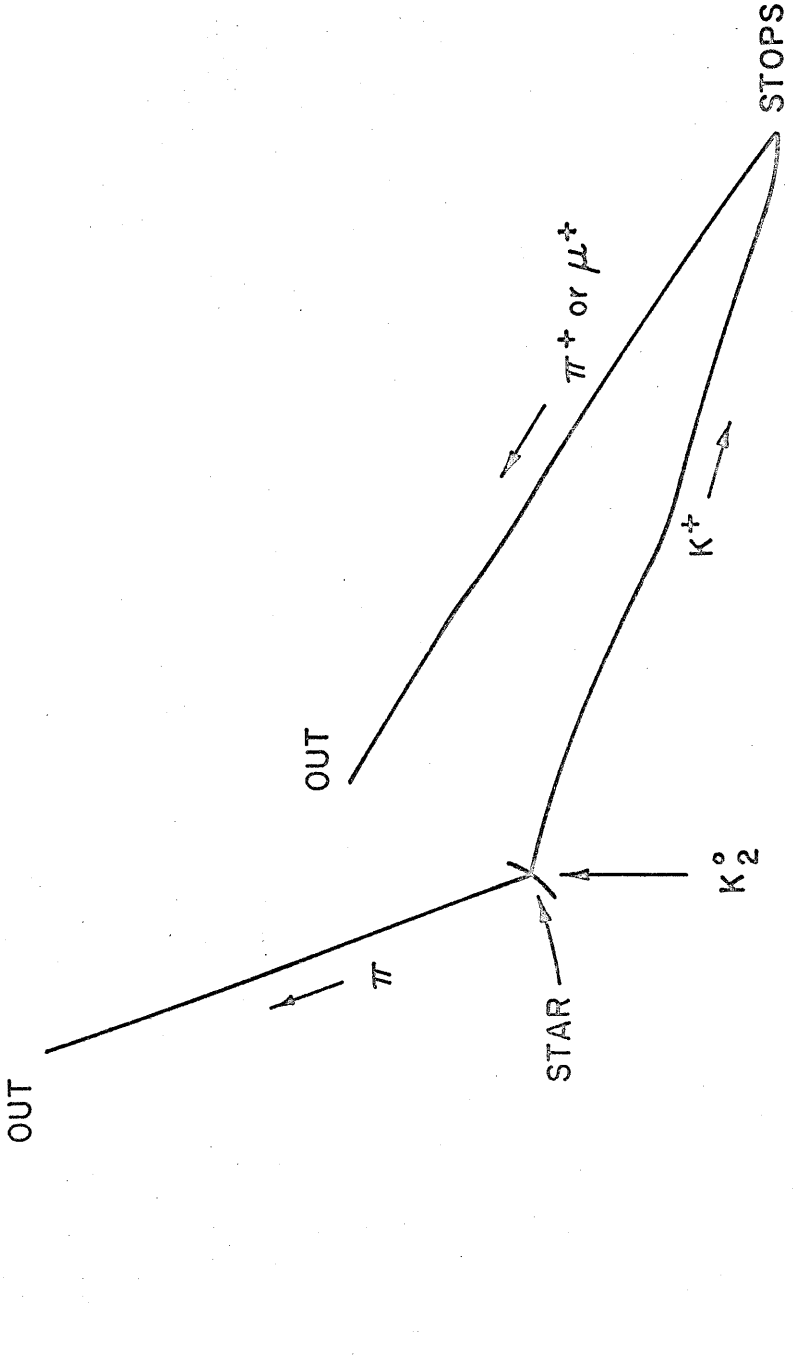

Fig. 15. Example of inelastic charge-exchange scatter and subsequent K^+ decay.

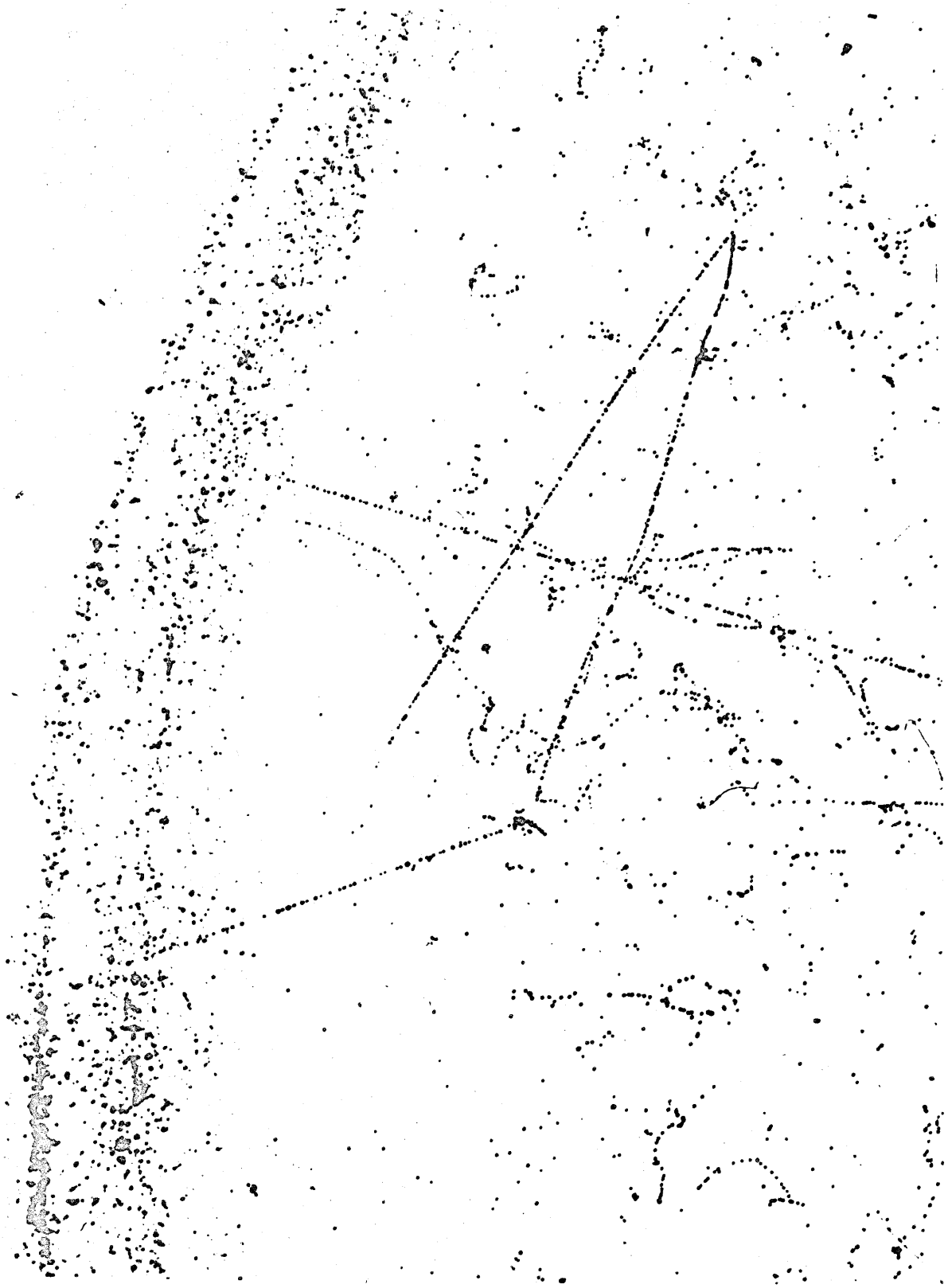

FIGURE 15

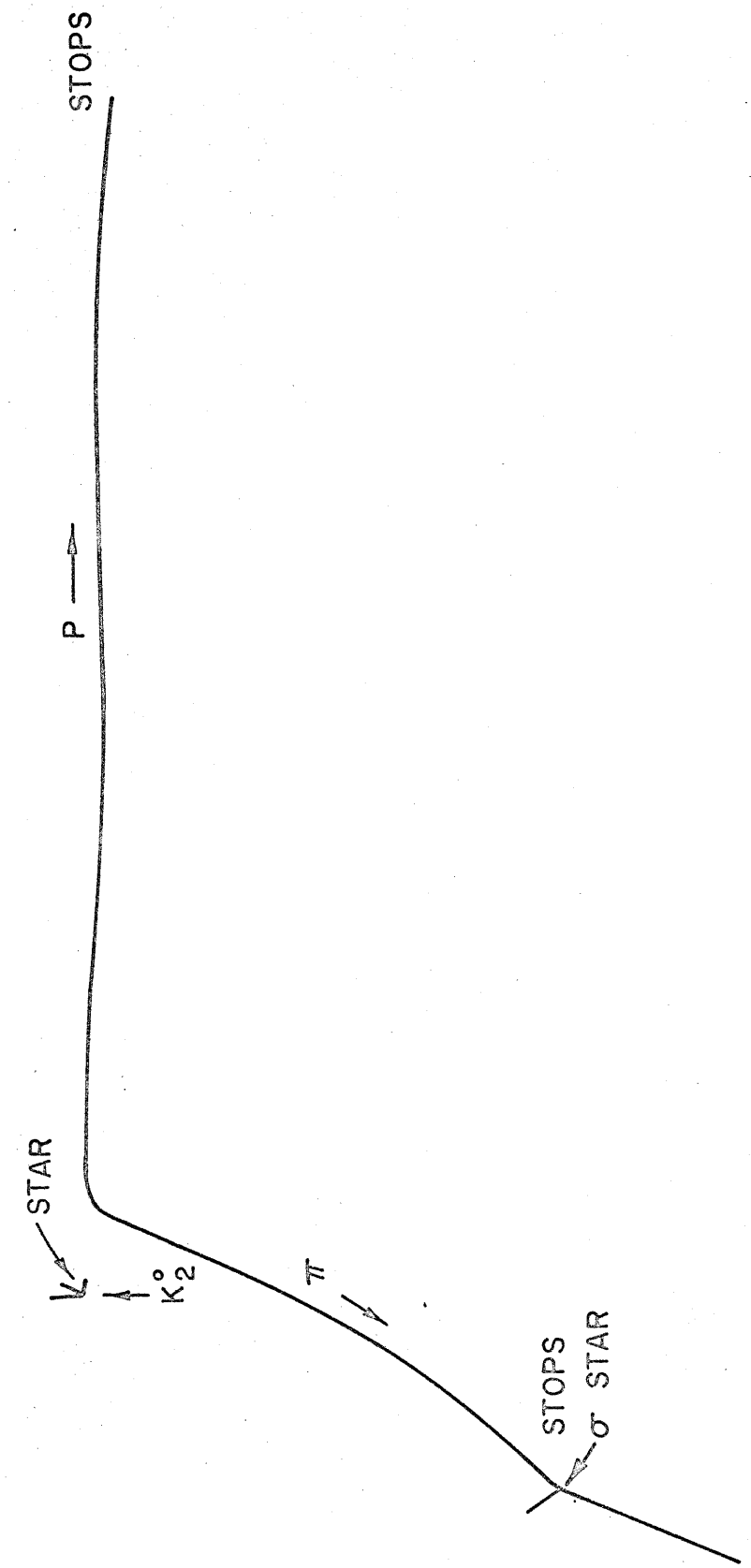

Fig. 16. Example of Λ° production in conjunction with star and subsequent Λ° decay.

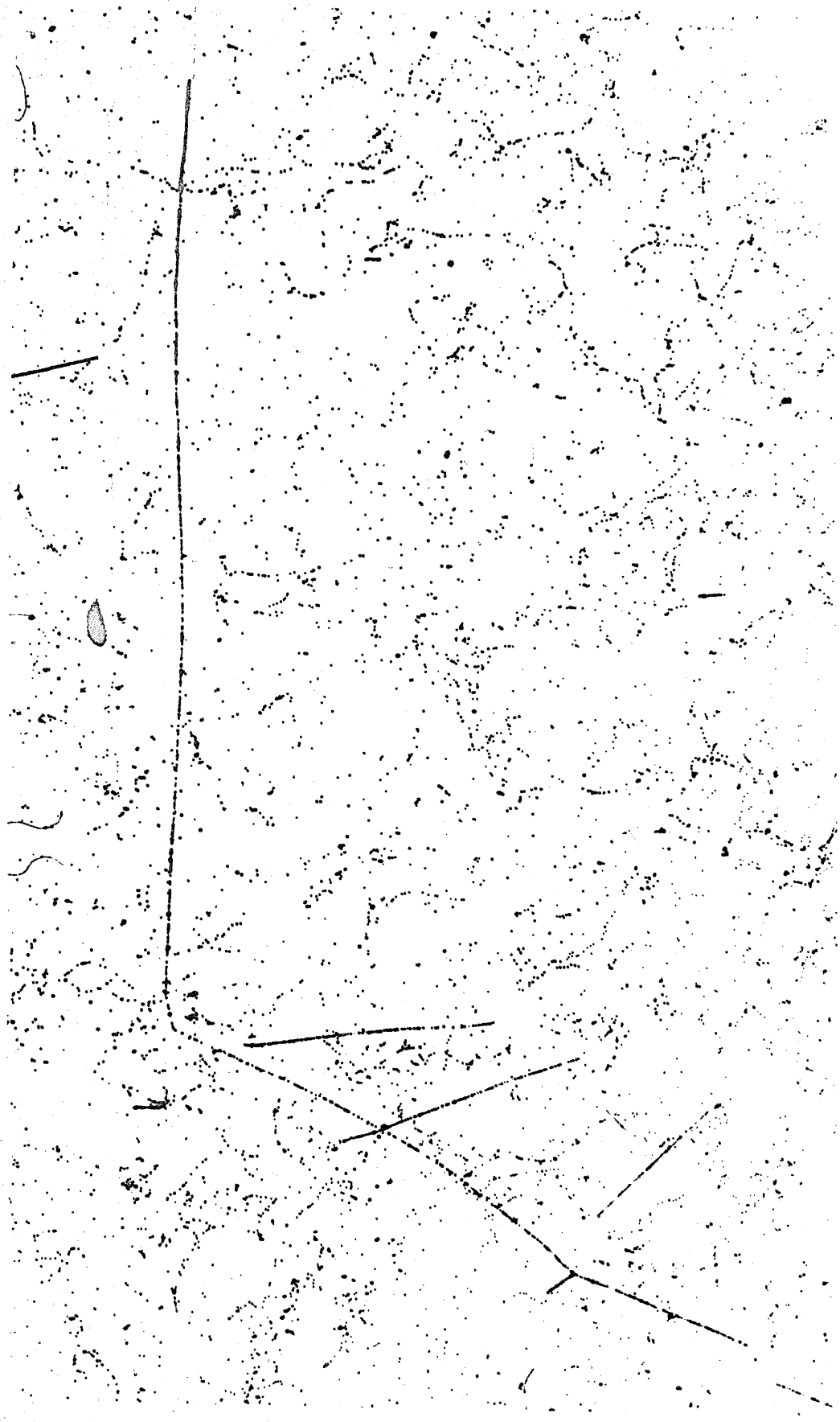

FIGURE 16

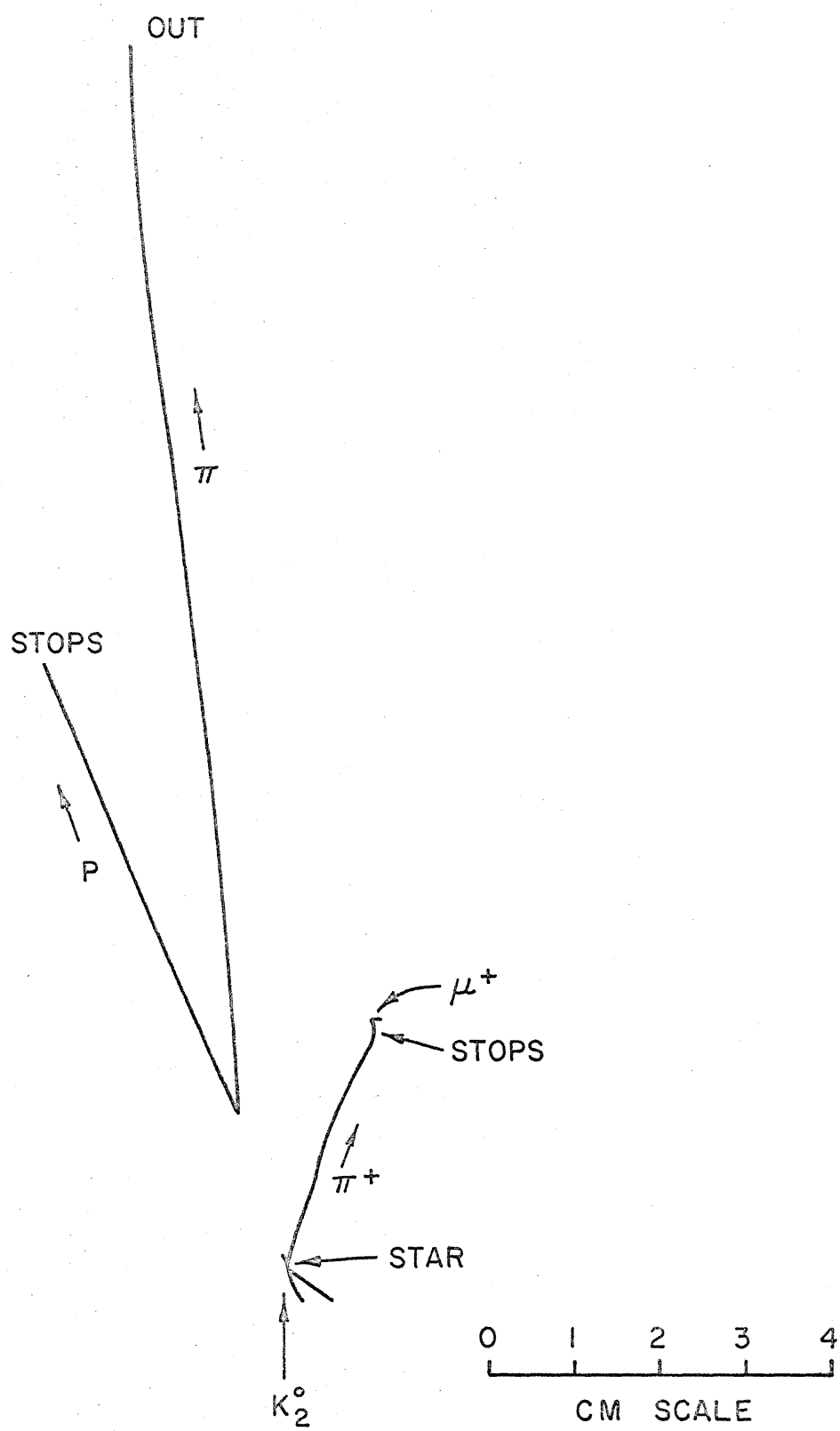

Fig. 17. Example of Λ° production in conjunction with star and subsequent Λ° decay.

FIGURE 17

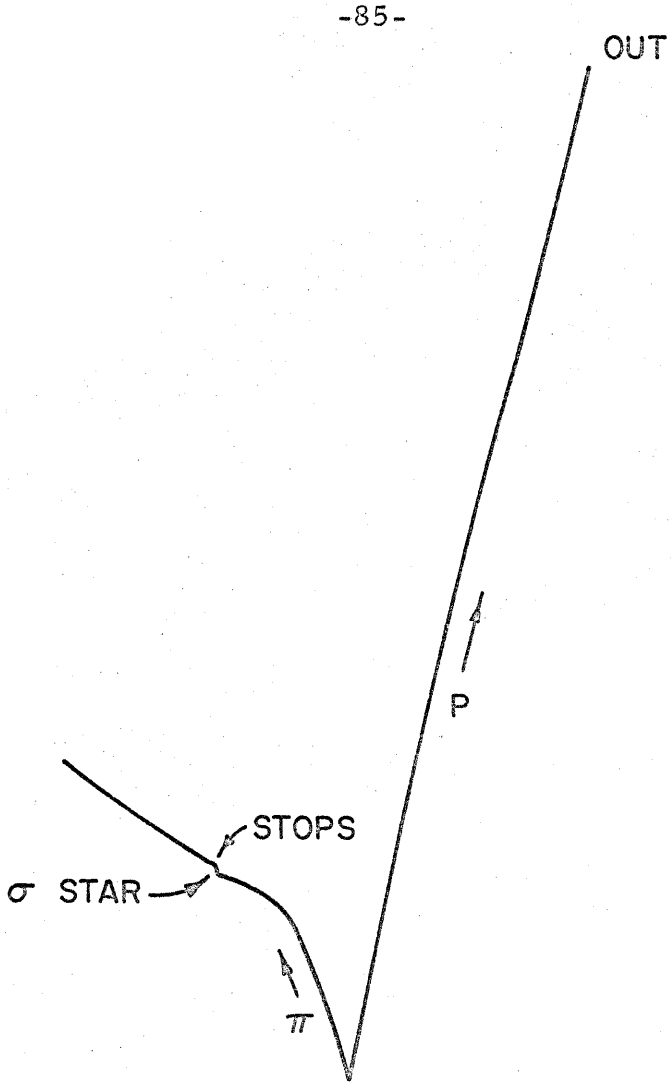

Fig. 18. Example of Λ^{o} production in conjunction with star, and subsequent Λ^{o} decay.

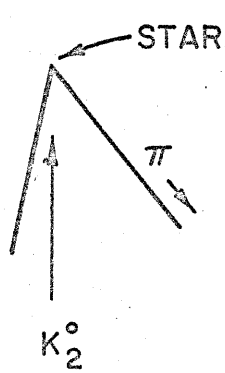

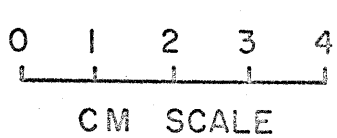

FIGURE 18

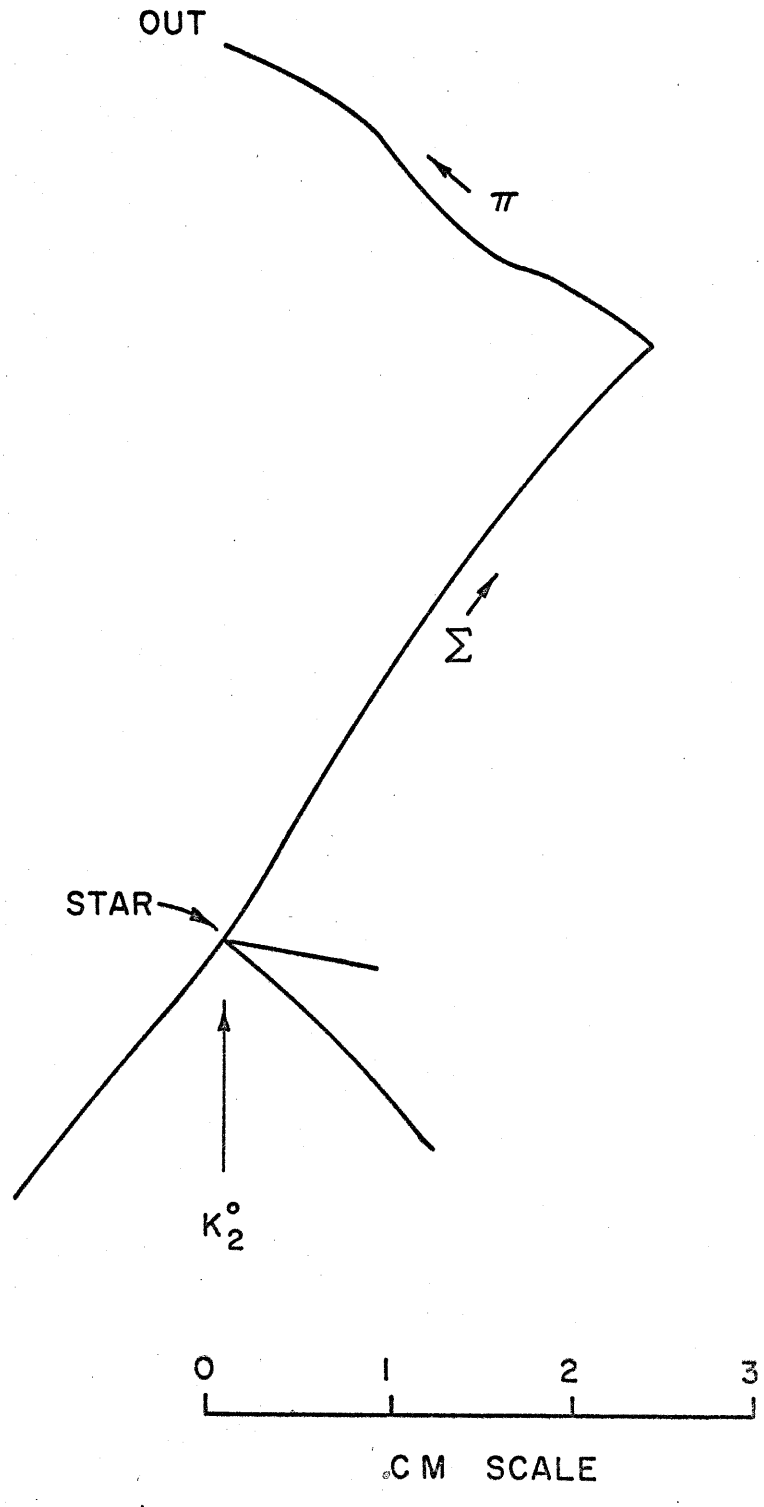

Fig. 19. Example of $\Sigma^{\pm}$ production in conjunction with star and subsequent $\Sigma^{\pm}$ decay.

FIGURE 19

V. SCANNING

A. PARTICLE IDENTIFICATION BY INSPECTION

The constancy of the bubble chamber operating conditions throughout the run allowed one to combine qualitative estimates of the gap-length distribution and multiple scattering of a particle in order to approximately establish its mass (see page 32). With practice, this process became intuitive for identification of various particles over a wide range of energies. The three mass groups: electrons; muons and pions; and, protons and hyperons; could in most cases be easily identified by inspection. The scarcity of observed tracks attributable to "definite" kaons makes any statement about kaons purely speculative. Nevertheless, it is believed that kaons could have been distinguished to a low degree of confidence. Separation of muons from pions, and protons from hyperons might have been possible with quantitative gap-length-distribution and multiple-scattering measurements, but no attempt was made to do this. The differences between various particles are displayed graphically in Fig. 20 where $1/p\beta$ for each particle is plotted as a function of a normalized mean gap length. The actual difference in appearance between a stopping pion and a stopping proton is illustrated in Fig. 9.

Difficulty in differentiating between pions and protons occurred for very high energy and low energy particles. In the former case the mean gap length was large and rather insensitive to energy, and the multiple scattering was small and difficult to estimate. In

Figure 20

Relationship between Multiple Scattering and Mean Gap Length

Curves of $1/p\beta$ vs $\langle x \rangle / \langle x \rangle_{max}$ are plotted for various particles. For a given track-segment length the quantity $1/p\beta$ is proportional to the r.m.s. angle of deflection due to multiple scattering. The ratio $\langle x \rangle / \langle x \rangle_{max}$ is the mean gap length normalized so that its maximum value is one. Due to the relativistic rise in bubble density (see Appendix VII), the functions are double valued in $1/p\beta$. The low energy branch is plotted for μ, π, K, p and Σ. The high energy branch is plotted for e and π up to energies of 1 Bev.

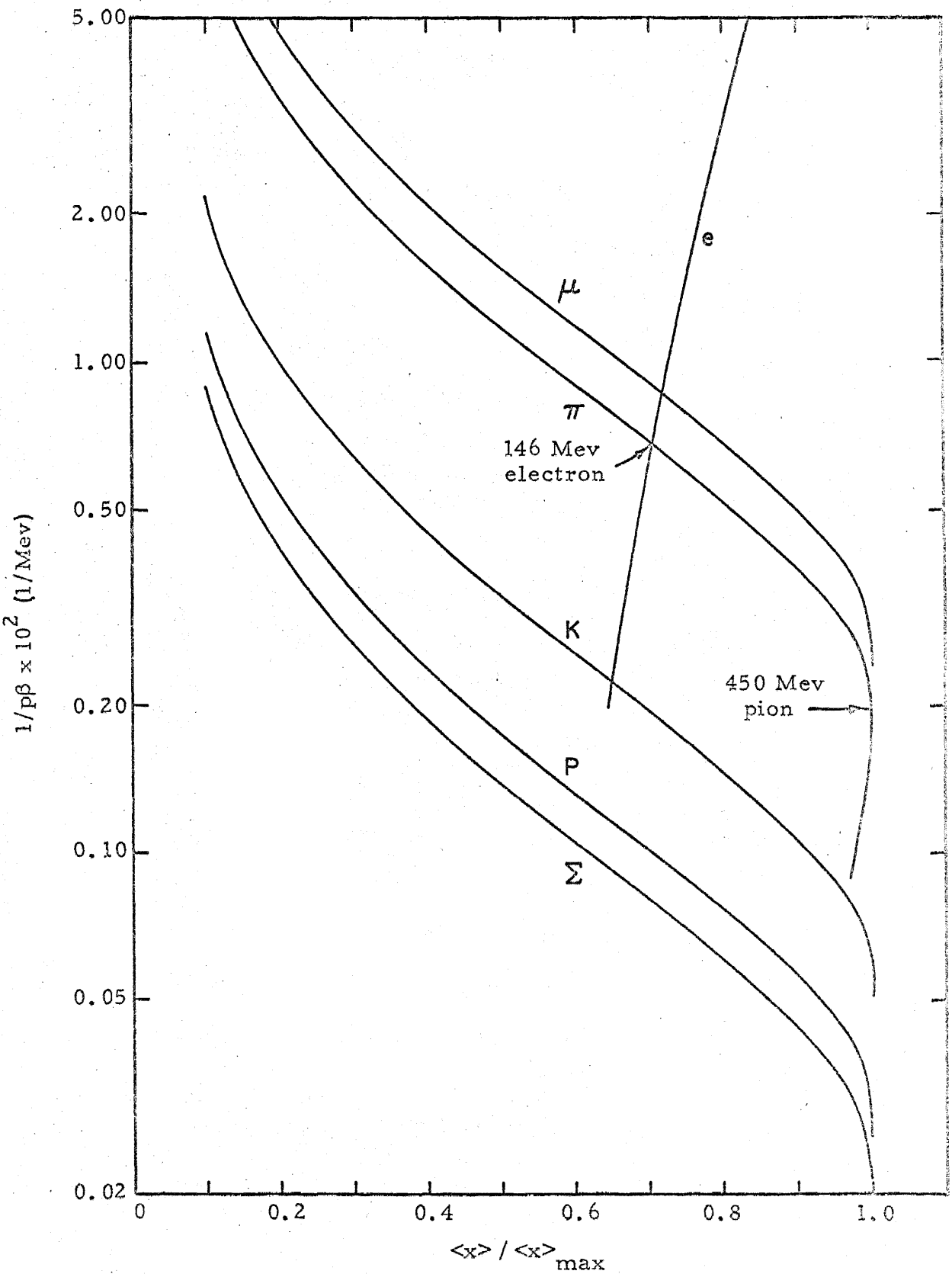
5.00
2.00
1.00
0.50
0.20
0.10
0.05
0.02
0
0.2
0.4
0.6
0.8
1.0
1/pβ x 10^2 (1/Mev)
<x> / <x>max
μ
e
π
146 Mev
electron
K
450 Mev
pion
P
Σ

Figure 20

the latter case, the mean gap length was too small to use (very few visible gaps) and the track was too short for a good multiple scattering estimate. Further difficulty was associated with steeply dipping tracks and short tracks from particles leaving the chamber. The large stereo angle of the camera reduced the problem of dipping tracks since the estimates could be made from the better view. The track lengths required for each of several confidence levels of intuitive pion identification are listed in Table 6. The table has been compiled from the events chosen for analysis without recourse to quantitative measurements.

Two further aids existed for the identification of pions. A small star, called a σ star, from the nuclear capture of a stopping negative pion was often visible, and occasionally a pion decayed. (Stopping positive pions could nearly always be identified by their decay.) A study of 166 "definite" stopping pions* from two prong events indicated that 36% of them exhibited σ stars and 7% decayed.

Unless a sizeable radiative collision occurred, identification of a very high energy electron was difficult since the relativistic rise in bubble density** promoted confusion with lower velocity pions.

---

*These pions were mostly negative, but positive pions were possible, e.g. $n + 2p \rightarrow \pi^+ + p + 2n$. In this study the identifications were made independently of stopping signatures.
**See Appendix VII.

TABLE 6

Confidence Levels of Intuitive Pion Identification

I. Definitions:

Label	Abbreviation (used later in text)	Rough Estimate of Identification Confidence (per cent which are pions)
definite	def	95 - 100
probable	prob	70 - 95
possible	pos	30 - 70

II. Average track lengths and r.m.s. variation from average length for each confidence level:

	Definite		Probable		Possible	
Kinetic Energy (Mev)	average length (cm)	r.m.s. variation (cm)	average length (cm)	r.m.s. variation (cm)	average length (cm)	r.m.s. variation (cm)
N.S.[a]						
30 - 50	5.5	1.7	3.6	0.6	4.2	1.1
50 - 75	8.9	2.7	5.7	2.1	5.2	1.7
75 - 100	11.7	4.3	6.5	2.5	6.0	3.1
> 100	12.7	5.2	7.4	3.6	3.7	1.0
S.[b]						
all	7.9	3.8	5.1	1.5	4.6	1.6

(a) Non-stopping pions.

(b) Stopping pions.

B. SCANNING PROCEDURE AND DATA

All of the picture scanning and event analysis for this experiment was performed on a self-contained projector and table called the scanner. A brief description of the scanner is given in Appendix V.

Not counting electron pairs, a two-prong event occurred on the average every 1.37 pictures. These two-prong events fell into three categories in the proportions listed below*:

Category	Number of Tracks with Mass ≅ proton	Number of Tracks with Mass ≅ pion	Percentage of Total	Source
A	2	0	88	neutron stars
B	1	1	9	neutron stars, $\Lambda^o, \Sigma^{\pm}$ decays
C	0	2	3	neutron stars, pion scatters, K_1^o, K_2^o decays

In scanning, the primary objectives were to select from the large number of two-prong events all candidates for category B which satisfied the criterion that a questionable pion track be longer than 3 cm and all candidates for category C which satisfied the criterion that at least one of the pions be energetic enough to leave the bubble chamber. (Since exact length measurements could not be made on the scanner, all questionable pion tracks close to 3 cm long

* Rare events such as $K^o + n \rightarrow K^- + p$ are not included in this table.

were accepted.) This cutoff criterion on the pion track length was necessary for the reason discussed above--that low energy pions are easily confused with protons and vice versa--and because there were a very large number of short proton tracks which were candidates for confusion. Events with short pion tracks which could be definitely identified by σ stars were recorded. A high energy cutoff was not necessary because there were few very high energy protons and thus it was feasible to consider all such tracks as possible pions. A low energy cutoff was not applied to the proton tracks during scanning since the observation of one pion was sufficient to place an event in category B or C and if there was any question concerning the identity of a particle associated with a pion, the event was analyzed for both possibilities. In actual practice a low energy cutoff occurred for tracks too short to see.

The only restriction placed on the location of the origin of an event was that it be within the visible region of the bubble chamber. A track with a very short visible path-length was difficult to identify and impossible to analyze accurately. Therefore, a natural boundary determined by the limit of identifiability and analyzability existed. This boundary was not equidistant from the various chamber walls since tracks tended to run in the general direction of the K_2^o beam. The several correction factors to the Λ^o detection efficiency arising from the finite extent of this "useful" volume and the cutoffs on stopping track lengths are discussed later.

The scanning procedure was divided into four stages: (a) first scan -- done by non-physicist scanners, henceforth called scanners, and by the author; (b) classification of first scan events -- done by the author; (c) second scan -- done by scanner; and (d) classification of new events found in second scan -- done by the author. In the first scan 65% of the pictures were double scanned by the scanners and 30% of the pictures were scanned by the author, while in the second scan all of the pictures were rescanned by one of the scanners. An interesting sidelight on the increase in scanning ability with practice is provided by the fact that about 1500 spurious events of type A were recorded by the scanners during the first scan but only about 300 such events were recorded during the second. (Approximately the same number of acceptable events were found in the two scans.)

In the classification of events each track was labeled according to one of the confidence levels described in Table 6. The number of events which fell into each of the several categories is given in Table 7. Concurrently with the classification procedure the end of each track was carefully examined to tell whether the particle stopped in the bubble chamber or not. Two criteria were required for a track to be specified as stopping: (1) the bubble density had to be appropriate; and (2) the location of the end of the track as estimated from approximate measurements at the scanner had to be well within the boundaries of the

TABLE 7

Classification of Events Found in Scanning

Total Number: 839

	Pion Identification		
	def	prob	pos
Proton Identification			
def-prob	373	89	120
pos	81	24	110
Pion Identification			
def	13	-	-
prob	0	3	-
pos	10	4	12

An entry in this table is the number of events which fell into the specified category.

visible volume. Tracks which satisfied the first, but were questionable on the second criterion, were so labeled and were later checked against a set of curves called the Chamber Boundary Graphs*.

Scanning for "unusual" events which might also have indicated the presence of strange particles in the bubble chamber was carried out at the same time as the search for two-prong events of types B and C. A few candidates for most of the signatures discussed in Chapter IV were found.

This experiment was not without its quota of mysterious events. The most numerous was a two-pronged, proton-electron event. Six of these were found with a variety of proton energies, electron energies, and angles between proton and electron. An event of this kind is reproduced in Fig. 21. Unfortunately, the obscuring background precluded any direct proof that these events were not protons plus "Dalitz" pairs in which one of the electrons was emitted at low enough energy to be lost in the background.

C. SCANNING EFFICIENCIES

1. Λ^o Decays. Since the pion energies for true Λ^o decays were comparable to those for the pseudo Λ^o-decay background, the scanning efficiency for true Λ^o decays is well approximated by the scanning efficiency for pseudo Λ^o decays. As shown in

---

*These graphs were assembled from the measurements on tracks which definitely left the visible region. By this means the side boundaries were established to $\pm$ 2 mm and the positions of the windows to $\pm$ 1 mm.

Figure 21

Example of Proton-Electron Event

(Frame 13862)

Reproduced in this figure is one of the "mysterious" two-pronged events composed of a proton and an electron. A one-pronged star which was consistent with being coplanar with the event is also shown. Note the high multiple scattering and low bubble density of the electron.

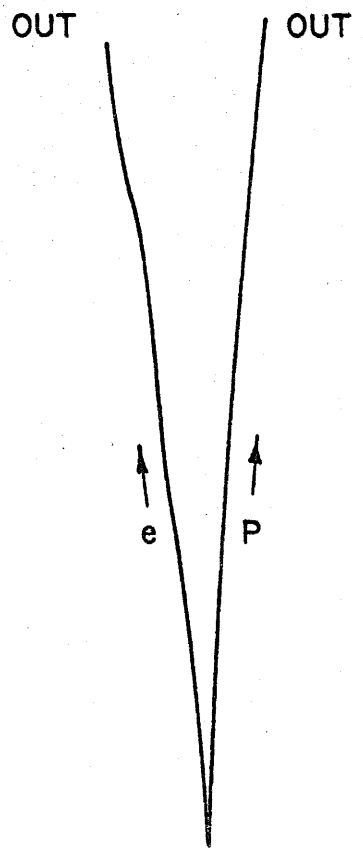

Figure 21

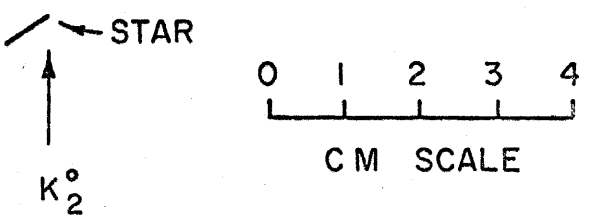

FIGURE 21

Appendix VI, the latter may be computed from the data obtained in the two scans. If E_c is the scanning efficiency for the combined data of the two scans, one finds that $E_c = 0.95 \pm 0.03$, independent of the event classification.

2. K_1^o Decays. In marked contrast to the Λ^o case, the energies of the pions from two-pion events tended to be considerably smaller than those expected from true K_1^o decays. For this reason the scanning efficiency for K_1^o decays is not well approximated by the efficiency for finding any two-pion event. Furthermore, there were so few events with pion energies comparable to those from K_1^o decays that an estimate using only events with high energy pions is statistically poor. Nevertheless, from the data on the 26 events which had estimated Q values above 100 Mev, one computes that $E_c = 0.65 \pm 0.13$, where the error represents the statistical error associated with 26 measurements.

VI. ANALYSIS

A. METHODS OF ANALYSIS

1. Q Values. For simplicity, the following discussion will deal specifically with the Λ^o case though most of the principles are general in character.

The number of true Λ^o decays was determined by means of a Q-value analysis. A background of neutron-induced pseudo Λ^o decays and mistakenly identified events is characterized by a slowly-varying Q-value distribution. In contrast to this, the Q-value distribution for true Λ^o decays is peaked at 37.6 Mev and has a known shape determined by measurement errors. By finding a "best" fit to the observed distribution using the sum of background and true-Λ^o distributions, one can obtain the number of true Λ^o decays.

The kinematics of a two-body decay may be displayed on a nomogram. For the proton-pion case nomograms relating the Q value to the proton kinetic energy, the pion kinetic energy, and the cosine of the angle, θ, between the proton and pion directions have been calculated by G. W. Stupian. The nomograms for three Q-value ranges are presented in Fig. 22. The absolute accuracy of these nomograms has been experimentally determined by calculating out the Q values for a variety of input parameters. For most input data, the r.m.s. error is about 0.5 Mev, while for a few cases in which the nomogram is difficult to read the r.m.s. error ranges up to 3 Mev. Of much better accuracy are measurements of changes in Q values due to small changes in the input parameters.

Figure 22

Q-Value Nomograms for Proton-Pion Events

Solution of the two-body decay kinematics for proton-pion events is provided by these nomograms. The Q value, proton kinetic energy, pion kinetic energy and cosine of the angle, θ, between the proton and pion directions all fall on a straight line drawn across the nomogram. Three ranges of Q value are shown:

Fig. 22 a. ..... 2 to $17\frac{1}{2}$ Mev

b. ..... $17\frac{1}{2}$ to 62 Mev

c. ..... 62 to 105 Mev

For this figure the nomograms have been reduced to one half the original size.

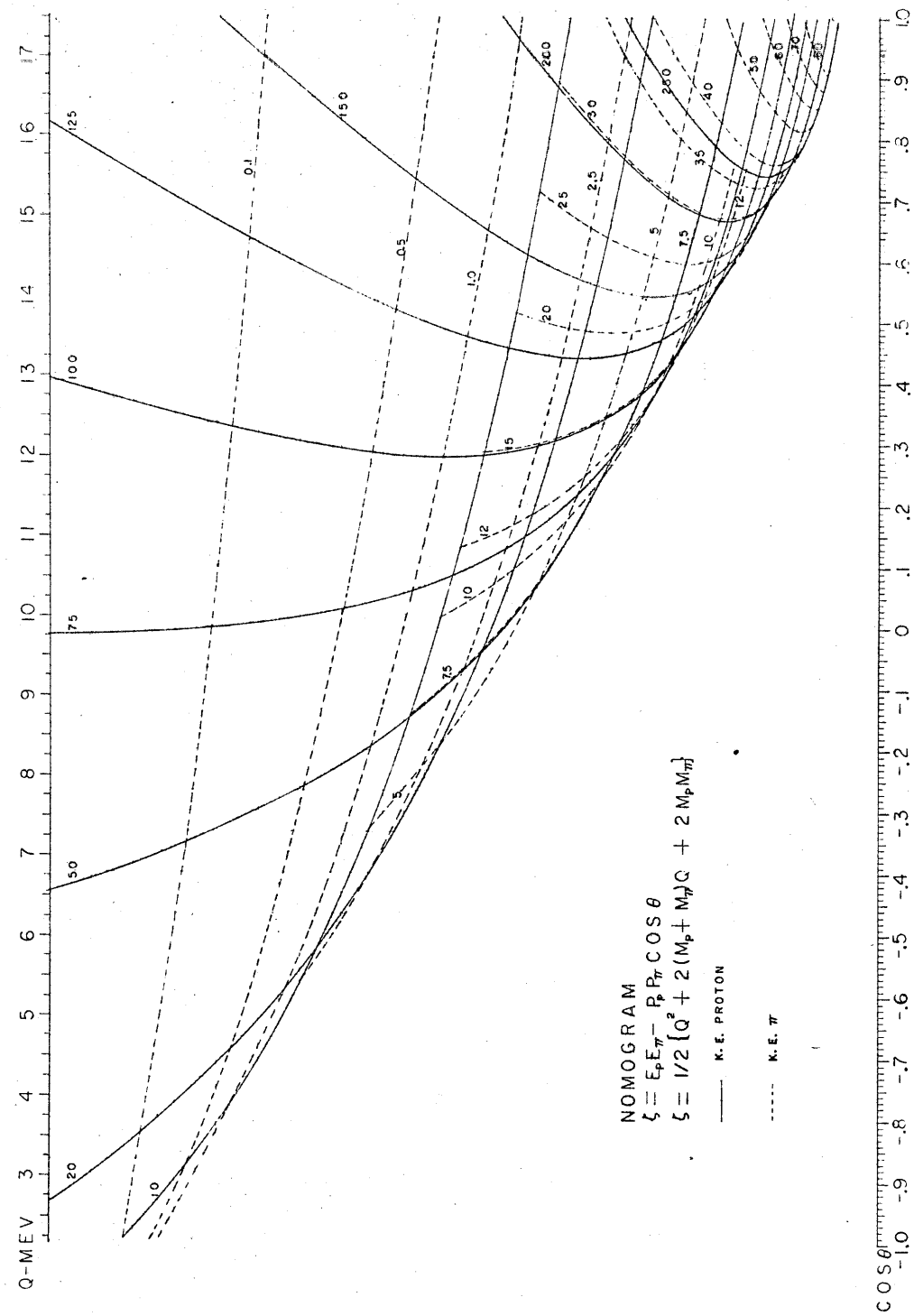
Q-MEV
COS θ
NOMOGRAM
ζ = E_p E_π − P_p P_π COS θ
ζ = 1/2 [Q² + 2(M_p + M_π)Q + 2M_p M_π]
K.E. PROTON
K.E. π

FIGURE 22 a

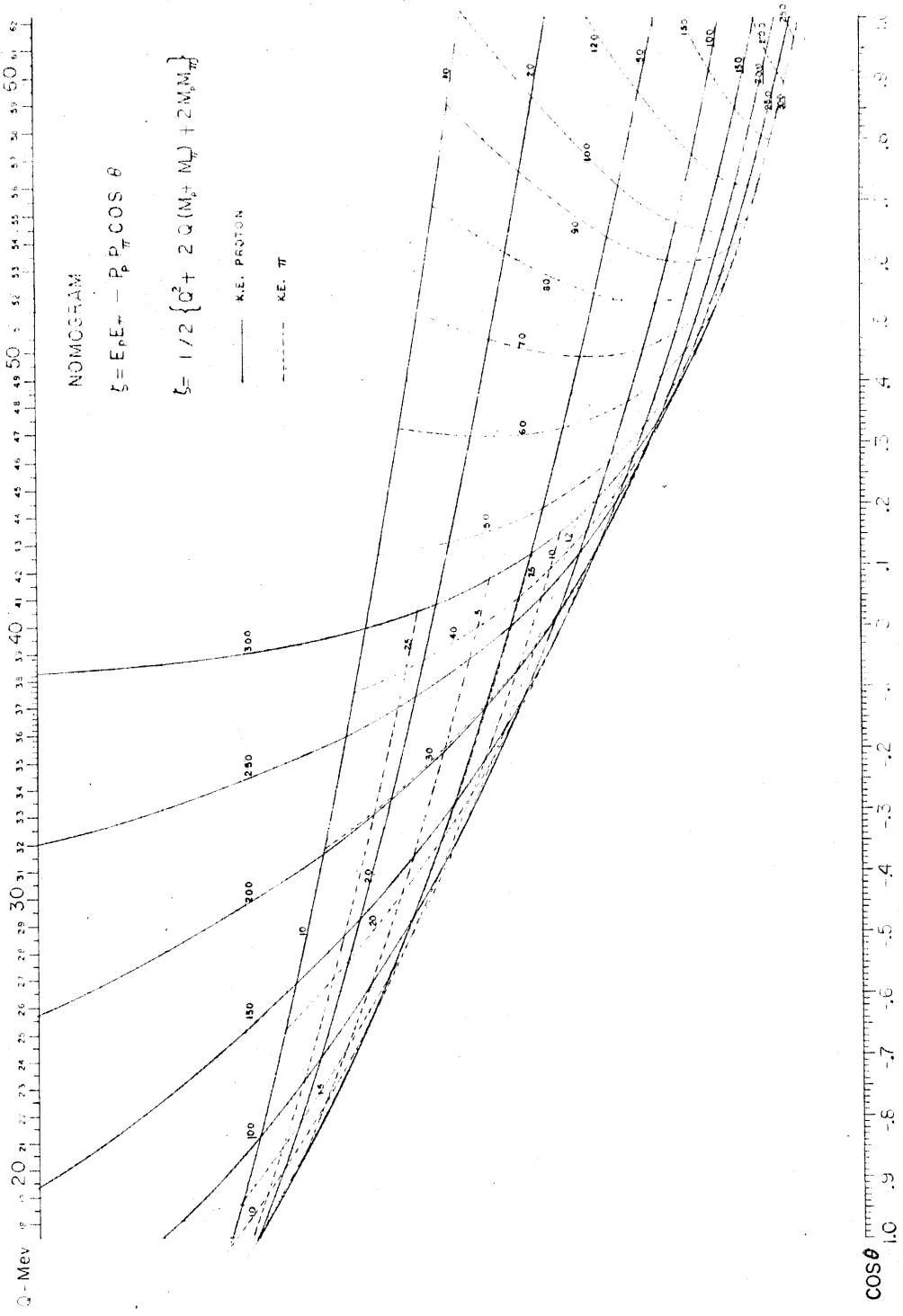
NOMOGRAM
$\zeta = E_p E_\pi - P_p P_\pi \cos\theta$
$\zeta = 1/2\{Q^2 + 2Q(M_p + M_\pi) + 2M_p M_\pi\}$
K.E. PROTON
K.E. π
Q - Mev
$\cos\theta$

FIGURE 22b

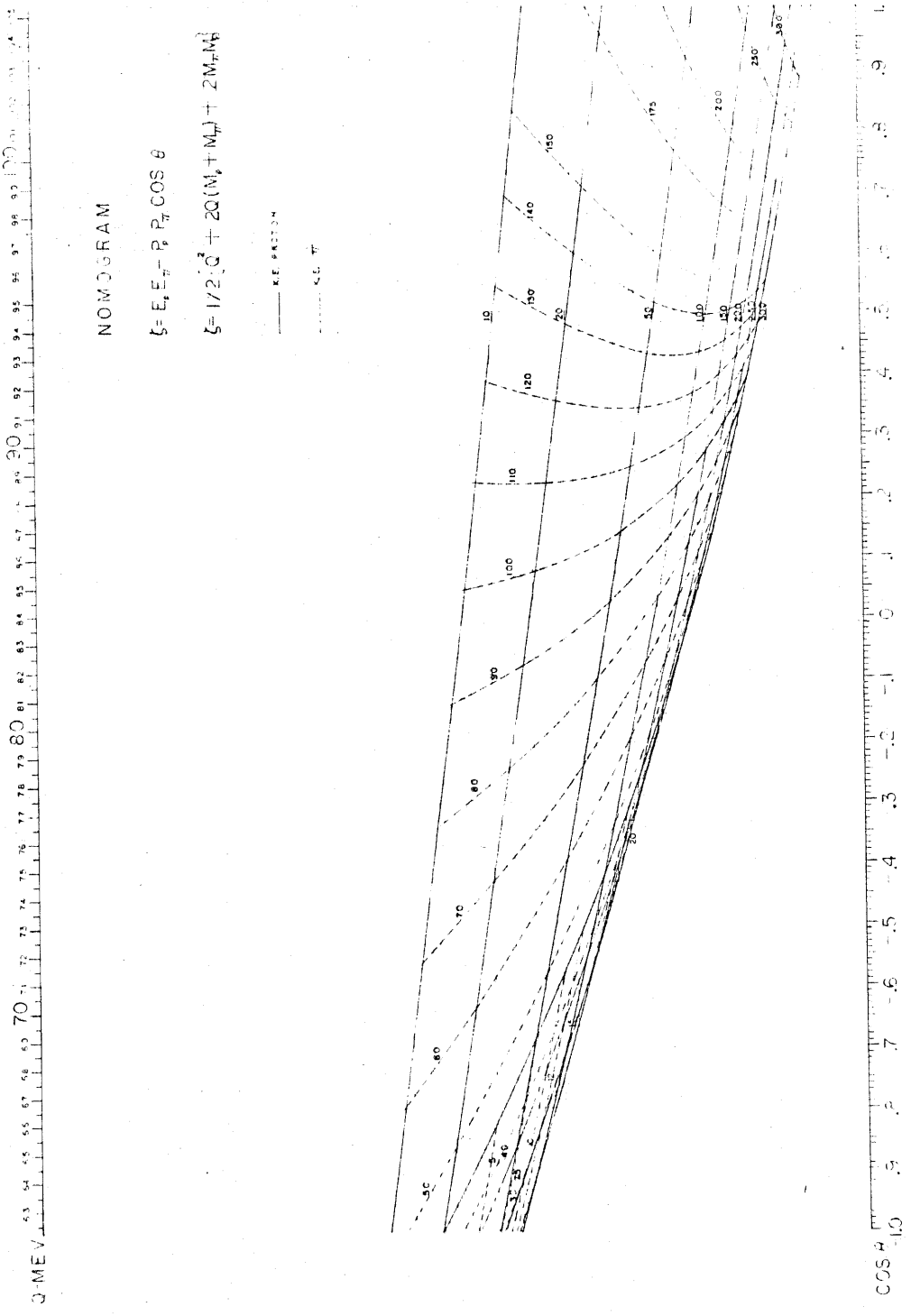
NOMOGRAM
$\zeta = E_\mu E_\pi - P_\mu P_\pi \cos\theta$
$\zeta = 1/2\,[Q^2 + 2Q(M_\mu + M_\pi) + 2M_\pi M_\mu]$
K.E. PROTON
K.E. π
Q-MEV
COS θ

FIGURE 22c

Errors in such measurements are of the order of 0.1 Mev.

The nomograms may be used to relate the estimated measurement errors in cos θ, pion kinetic energy, T_π, and proton kinetic energy, T_p, to an overall measurement error in the Q value. Since the three measurement errors and the absolute error in reading the nomogram are independent, the overall error in the Q value, ΔQ, is given by

$$[\Delta Q]^2 = [\Delta Q(\cos\theta)]^2 + [\Delta Q(T_\pi)]^2 + [\Delta Q(T_p)]^2 + [\Delta Q(\text{nomogram})]^2 \quad \text{(VI-1)}$$

where $\Delta Q(x)$ is the change in the Q value when the parameter x is changed by an amount equal to its error and the other parameters are held constant.

2. Associated Stars

a. General. When a star which is the apparent source of a true or pseudo Λ^o hyperon is located, and therefore the apparent direction of travel of the Λ^o is established, the decay process is overdetermined by two parameters. Since it is rather unlikely for a pseudo Λ^o decay to satisfy these two parameters, the background in the Q-value plot for such events is enormously reduced. Furthermore, the distribution in distance from star to decay point differs strikingly for true and pseudo decays and is helpful in determining the absolute number of true Λ^o decays.

b. Coplanarity. The first test which the possible Λ^o path must satisfy is that of coplanarity with the pion and proton

direction vectors. If $\vec{e}_\Lambda$, $\vec{e}_\pi$ and $\vec{e}_p$ are unit vectors in the directions of the subscripts, then the angle, α, between $\vec{e}_\Lambda$ and the normal to the plane of $\vec{e}_\pi$ and $\vec{e}_p$ is given by

$$\cos \alpha = \vec{e}_\Lambda \cdot \vec{e}_\pi \cdot \vec{e}_p / \sin \theta \qquad \text{(VI-2)}$$

where, as before, θ is the angle between $\vec{e}_\pi$ and $\vec{e}_p$. For coplanarity $\cos \alpha = 0$.

The measurement error in α depends on both the errors in and the relative directions of the three unit vectors. The error in $\vec{e}_\Lambda$ is easily computed since it depends only on the errors in two point-measurements and the distance from the star to the point of decay. If S is this distance in cm, the angle of the error cone is estimated to be 0.03/S radians.

The errors in $\vec{e}_\pi$ and $\vec{e}_p$ may be estimated from the data in Table 13. Listed in this table are the expected errors in the angle θ for four measurement-difficulty classifications. An error in this angle is the sum of the two independent errors in the projections of the measured directions, $\vec{e}_\pi$ and $\vec{e}_p$, onto the plane determined by the true pion and proton directions. A general feature of an event that was used in the compilation of the table was that one of the two direction measurements was "good"*, while the other was "good", "fair", "poor", or "impossible". If one makes the reasonable assumption that the error surfaces about the true directions are right circular cones, the expected errors in the projection

*See the text associated with the table for an explanation of the four terms.

of $\vec{e}_\pi$ ($\vec{e}_p$) onto any plane containing the true pion (proton) direction are found to be:

Classification:	Good	Fair	Poor	Impossible
R.m.s. Error:	0.9°	2.0°	3.3°	12.3°

The influence of the relative directions of the three unit vectors on the error in cos α is simplified by the fact that for events of interest the three vectors are nearly coplanar. Thus it is reasonable to investigate variations about the coplanar case and apply the results to all possible associated stars. It is clear that for such variations the only component which affects cosα is the one normal to the common plane. For this reason the significant measurement errors are those projected onto a plane (such as those listed above for $\vec{e}_\pi$ and $\vec{e}_p$) rather than those giving the angle of the error cone (such as that given for $\vec{e}_\Lambda$).*

The normal variation of $\vec{e}_\Lambda$ (in terms of an angular change) produces an equal (in magnitude) variation in α.

Straightforward vector analysis may be used to show that the change in cosα, Δcosα, due to a small normal variation in $\vec{e}_\pi$ is given by:

$$\Delta \cos \alpha \approx \epsilon \ (\sin \pi \ \mathrm{ctn}\ \theta - \cos \pi) \qquad \text{(VI-3)}$$

where ϵ is the normal variation in $\vec{e}_\pi$, and π is the angle between

*The two types of error are simply related: (projection error) $\approx \frac{2}{\pi}$ (angle of error cone).

$\vec{e}_\pi$ and $\vec{e}_\Lambda$. A similar equation holds for $\vec{e}_p$. Since $\vec{e}_\Lambda$ is limited to the angular region between $\vec{e}_\pi$ and $\vec{e}_p$, equation VI-3 is only of interest for $\pi \leq \theta$. In Fig. 23 the ratio $\Delta\cos\alpha/\epsilon$ is plotted as a function of θ for several values of π. For all but very large values of θ, the error in $\cos\alpha$ is comparable to the error in $\vec{e}_\pi$.

The overall error in $\cos\alpha$ is the orthogonal sum of these three independent errors.

c. Transverse Momentum Balance. The other test which must be satisfied by a decay associated with a star is the balance of transverse momentum:

$$p_\pi \sin\pi = p_p \sin\rho \qquad \text{(VI-4)}$$

where ρ is the angle between $\vec{e}_\Lambda$ and $\vec{e}_p$ and p_x is the momentum of particle x.

The degree to which equation VI-4 is violated may be expressed in terms of the quantity, δ, which is given by:

$$\delta = 1 - \frac{p_\pi \sin\pi}{p_p \sin\rho} \qquad \text{(VI-5)}$$

For events with true associated stars, the measured value of δ is expected to differ from zero by an amount that is easily computed from the expected measurement errors in the momenta and angles. (See Section b above and Appendix VII.)

d. Distribution of Decay Distances. Pseudo decays associated with stars occur through one of two processes:* (1) the

*It is not known which of these processes is more important.

Figure 23

Effect of Directions on Coplanarity Test

The ratio $-\cos\alpha/\varepsilon$ from equation VI-3 is plotted as a function of the angle θ for several constant values of the angle π. (See text for explanation of symbols.) The curves are plotted for $\theta \geq \pi$ since only such values of θ are of practical interest. All curves (except $\pi = 0$) go to infinity at $\theta = 180^{\circ}$. Note that ε is expressed in radians.

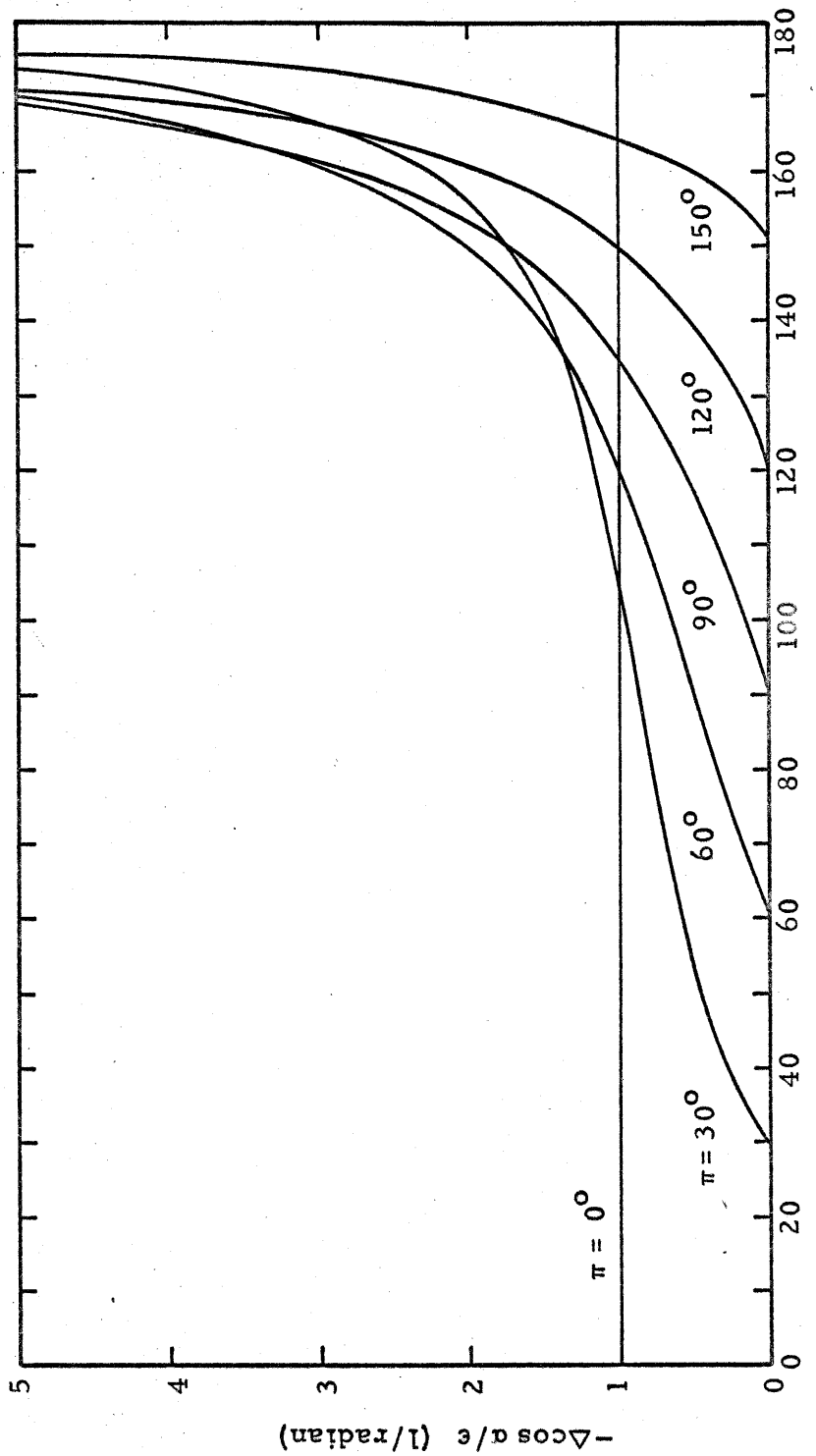
-Δcos α/ε (1/radian)
0
1
2
3
4
5
θ (degrees)
0
20
40
60
80
100
120
140
160
180
π = 0°
π = 30°
60°
90°
120°
150°

Figure 23

pseudo decay and the star are produced by two independent neutrons; or (2) the pseudo decay is produced by a neutron coming from the star or vice versa. In the former case, except for the effect of the finite boundaries of the bubble chamber, the number of events should increase as the square of the distance, S, from star to decay point*. In the latter case, except for boundary effects, the number of events should decrease exponentially with the exponent S/S_o. The value of S_o is about 54 cm (the geometrical interaction length in CF_3Br).

Except for boundary effects** true Λ^o hyperons associated with stars should exhibit exponential decay distributions with mean decay distances determined by the Λ^o kinetic energies. (For this experiment, the range of mean decay distances was 0 to 8.4 cm.) The measured Λ^o kinetic energies can be used to reduce this continuum of distributions to a single exponential distribution:

$$N = N_o e^{-\zeta} \qquad \text{(VI-6)}$$

---

*Proof: for each pseudo decay, there is a pseudo direction of travel, $\vec{e}_\Lambda$, of the pseudo Λ^o. Because of the errors in determining coplanarity and transverse momentum balance, there is an error cone about $\vec{e}_\Lambda$ into which neutron stars fall by chance. Since the cross-sectional area of this cone increases as S^2, and since the density of neutron stars is a constant throughout the bubble chamber, the probability that a neutron star falls between S and S+dS is proportional to S^2.

**The importance of boundary effects increases with the Λ^o kinetic energy. For the maximum energy Λ^o hyperons of this experiment, about 50 per cent of the decays are estimated to have been lost.

where ζ is the reduced decay distance, N is the number of events between ζ and $\zeta + d\zeta$, and N_o is the total number of events. In terms of the Λ^o momentum, p_Λ (in Mev/c) and the spatial decay distance, S (in cm),

$$\zeta = (m/\tau c)_\Lambda \cdot S/p_\Lambda = 148\ S/p_\Lambda \qquad \text{(VI-7)}$$

When plotted as a function of ζ, pseudo Λ^o decays should display a distribution which is either peaked at large values of ζ or slowly decreasing with ζ. In either case, the distribution should be quite different from the true Λ^o distribution. Thus qualitative examination of the distribution for all events with Q values consistent with true Λ^o decay may be used: (a) to more definitely establish that true Λ^o decays are being observed; and (b) to determine the absolute number of true Λ^o decays.

3. Measurement Techniques. As mentioned in Chapter II, energies of stopping particles are accurately determined by the range-energy relation in CF_3Br, while energies of particles which do not stop may be established through measurements of the gap-length distributions of their tracks. In this experiment the thermodynamic stability of the bubble chamber was sufficiently precise that gap-length-distribution measurements could be made throughout the run without recalibration in each picture.

The simple method which was used for obtaining a particle's direction of travel consisted of drawing tangents to the two stereoscopic views of the track and finding the direction vector which

corresponded to these two tangents. Most problems associated with multiple scattering of the particle could be qualitatively compensated for by skillful use of this method.

Appendix VII contains a more detailed account of these techniques and the ways in which point measurements were made.

B. ANALYSIS PROCEDURE - Λ^o DECAYS

The analysis of possible Λ^o decays was carried out in several steps. The effects of the selection criteria on the number of events retained may be found in Table 8.

Step 1. Pion Decays. Events with $\pi\mu e$ decays were discarded. Fields, et al.[45] have measured the probability for decay of a π^- stopping in liquid hydrogen to be on the order of 0.1 per cent. Since π^- mesons are slowed down and captured in freon much more quickly than in hydrogen, it is very unlikely that any of the pions which stopped and decayed in this experiment were π^-'s. (In all, 263 pions stopped and 14 decayed.)

Step 2. Geometrical Measurements. Geometrical quantities, e.g., track lengths and angles, were measured. Once these measurements had been made, the selection criteria on track lengths could be applied to questionable cases:

a) range of stopping pion > 3 cm unless ending in a σ-star;

b) range of stopping proton > 0.1 cm.

Step 3. Qualitative Estimate and Q-Value Cutoff. The bubble densities of all non-stopping tracks were estimated qualitatively. The author made the estimates by carefully inspecting the last few

TABLE 8

Λ^{o} Event Selection

Total number of events initially = 797

Selection Criterion	Percentage* Eliminated			Percentage* Retained			
	Both Particles Stop	One Particles Stop	Neither Particles Stop	Both Particles Stop	One Particles Stop	Neither Particles Stop	Total
None				28.6	50.8	20.6	100
Step 1							
$\pi\mu e$	1.0	0.8	—	27.6	50.0	20.6	98.2
Step 2							
a) R_{π}>3 cm	6.2	3.1	—	21.4	46.9	20.6	88.9
b) R_{p}>0.1 cm	1.3	0.0	0.0	20.1	46.9	20.6	87.6
Step 3							
Q<70 Mev	—	12.4	5.8	20.1	34.5	14.8	69.4
Step 4							
a) particle assignment wrong	0.1	3.4	1.9	20.0	31.1	12.9	64.0
b) poor meas.	0.0	3.3	2.9	20.0	27.8	10.0	57.8
Step 5							
a) error ≤14 Mev (0≤Q≤70)	0.0	4.6	3.5	20.0	23.2	6.5	49.7
b) Q<70 Mev	—	7.3	2.1	20.0	15.9	4.4	40.3

* Percentage of initial number.

centimeters of each track. Qualitative-estimate Q values were then found using this data and a selection* was made of events satisfying

$$Q < 70 \text{ Mev} \qquad \text{(VI-8)}$$

Forty events with Q values outside this limit had large uncertainties in the qualitative estimate and were therefore also selected.

A comparison of the qualitative-estimate and the final-analysis Q values revealed that in the qualitative estimates there was a systematic tendency to overestimate the bubble density of steeply dipping tracks. For events retained through the entire analysis procedure, the r.m.s. difference between the qualitative-estimate and final-analysis Q values was found to be about 8 Mev independent of the bubble density. An examination of the events which were discarded on the basis of the qualitative estimate indicated that no events with mean Q values below 65 Mev were eliminated by this selection criterion (inequality VI-8).

Step 4. Gap-Length-Distribution Measurements. Gap-length-distribution measurements were performed on the non-stopping tracks of the events retained. A number of events were eliminated at this stage for one of two reasons:

a) measurement inconsistent with particle assignment (mostly "possible pions" shown to be protons);

b) measurement too poor to use (e.g., only a few

*This selection only applied to events with non-stopping tracks.

visible gaps because of track dip or length).

Step 5. Final Q Values and Errors. The final Q values and the related errors were found. For each significant error in pion energy, proton energy, and angle between pion and proton, the effect on the Q value was independently and explicitly traced. In the case of the statistical error* in gap-length-distribution measurements, positive and negative errors were treated separately. The positive and negative net errors in the Q values were then computed according to equation VI-1. Typical distributions of net errors are shown in Fig. 24. Since there was no hope of detecting a very broad peak in the Q-value histogram, events with either positive or negative errors greater than 14 Mev were discarded.

A number of the final Q values fell above the 70 Mev selection limit. Events of this class with non-stopping tracks were discarded from the group used to plot standard histograms but were retained in the group used to generate the distributed-event histogram (see Section C).

The composition of the final group of events used in the standard histograms is given in Table 9.

*This was by far the most important error.

Figure 24

Q-Value Error Histograms

Shown in this figure are two typical histograms in which the number of events per 5 Mev interval in the net Q-value error, ΔQ, is plotted against ΔQ. Each event contributes twice to a histogram; once to each of the positive and negative halves. The events used in the histograms are:

a. Events with Q values between 10 and 70 Mev in which both particles stopped;

b. Events with Q values between 32.5 and 42.5 Mev in which at least one particle did not stop. This histogram is cut off at $\Delta Q = \pm 14$ Mev.

None of the events associated with stars are included.

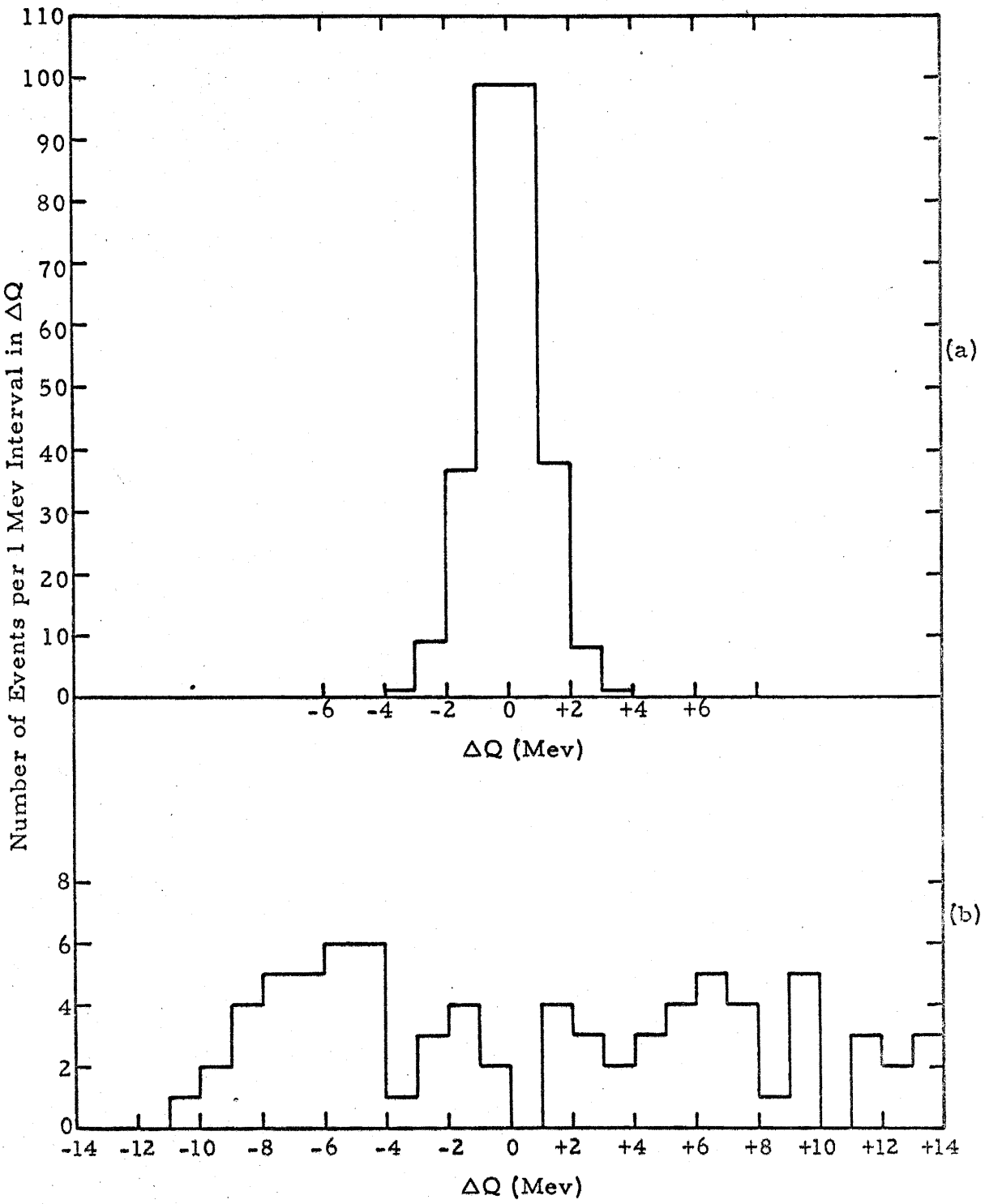
Number of Events per 1 Mev Interval in ΔQ
110
100
90
80
70
60
50
40
30
20
10
0
-6
-4
-2
0
+2
+4
+6
ΔQ (Mev)
(a)
8
6
4
2
0
-14
-12
-10
-8
-6
-4
-2
0
+2
+4
+6
+8
+10
+12
+14
ΔQ (Mev)
(b)

Figure 24

TABLE 9

Composition of Finally Selected Events*

Category	Particles Which Stop	Number of Events with Pion Identification:			Total Number
		Definite	Probable	Possible	
A	neither	24	6	4	34
B	pion	34	5	10	49
C	proton	49	7	12	68
A+B+C		107	18	26	151
D	both	91	14	55	160
Total A+B+C+D		198	32	81	311

*Not including events associated with stars

C. DISPLAY OF DATA AND RESOLUTION FUNCTIONS - Λ^o DECAYS

The experimental information is displayed in two different ways. Standard histogram plots of the mean Q values for events not associated with stars* are presented in Figs. 25 and 26. The events with two stopping particles** are plotted separately from those with non-stopping particles** because of the large difference between the resolution functions for the two cases (see below and Fig. 28). The great variation of errors among non-stopping events (see Fig. 24) is taken account of in the other type of histogram employed. In this second kind of histogram, called a distributed-event histogram, an event is distributed among the intervals according to the probabilities, computed from the estimated error for the event, that the true Q value falls within the individual limits of the intervals. The distributed event histogram for the no-star, non-stopping events is shown in Fig. 27.

In order to compute the probabilities mentioned above, the assumption was made that the errors in the Q values are adequately represented by "positive" and "negative" Gaussian distributions whose standard deviations are the positive and negative errors found in Step 5 of the analysis procedure. Thus, if Q_o is the measured Q value, and ΔQ_+ and ΔQ_- are the positive and negative errors, then the probability that the true Q value fell between $Q_i - q/2$ and $Q_i + q/2$ (i.e., in the interval of width $|q|$ centered at Q_i) is given by:

---

* Hereinafter called no-star events.

** Hereinafter events of these two types will be called two-stopping events and non-stopping events.

Figure 25

Two-Stopping, No-Star Events

Fig. 25 a. Standard, Q-Value Histogram

i) The constant-background fit for $10 < Q < 55$ Mev , which is discussed on pp. 134-135, is indicated by a dashed line.

ii) The Q value for Λ^o decay is marked by an arrow.

Fig. 25 b. Resolution Function Containing Ten Events

i) The mathematical expression for the histogram is $10 \times R_1$ (ed, Q_i - 37. 5, 5), where the energies on which R_1 depends are expressed in Mev. (Henceforth, all such energies will be implicitly expressed in Mev.) R_1 is defined by equation VI-10.

ii) The error distribution of the two-stopping, no-star events with $10 < Q < 70$ Mev (Fig. 24a) was used to generate R_1 .

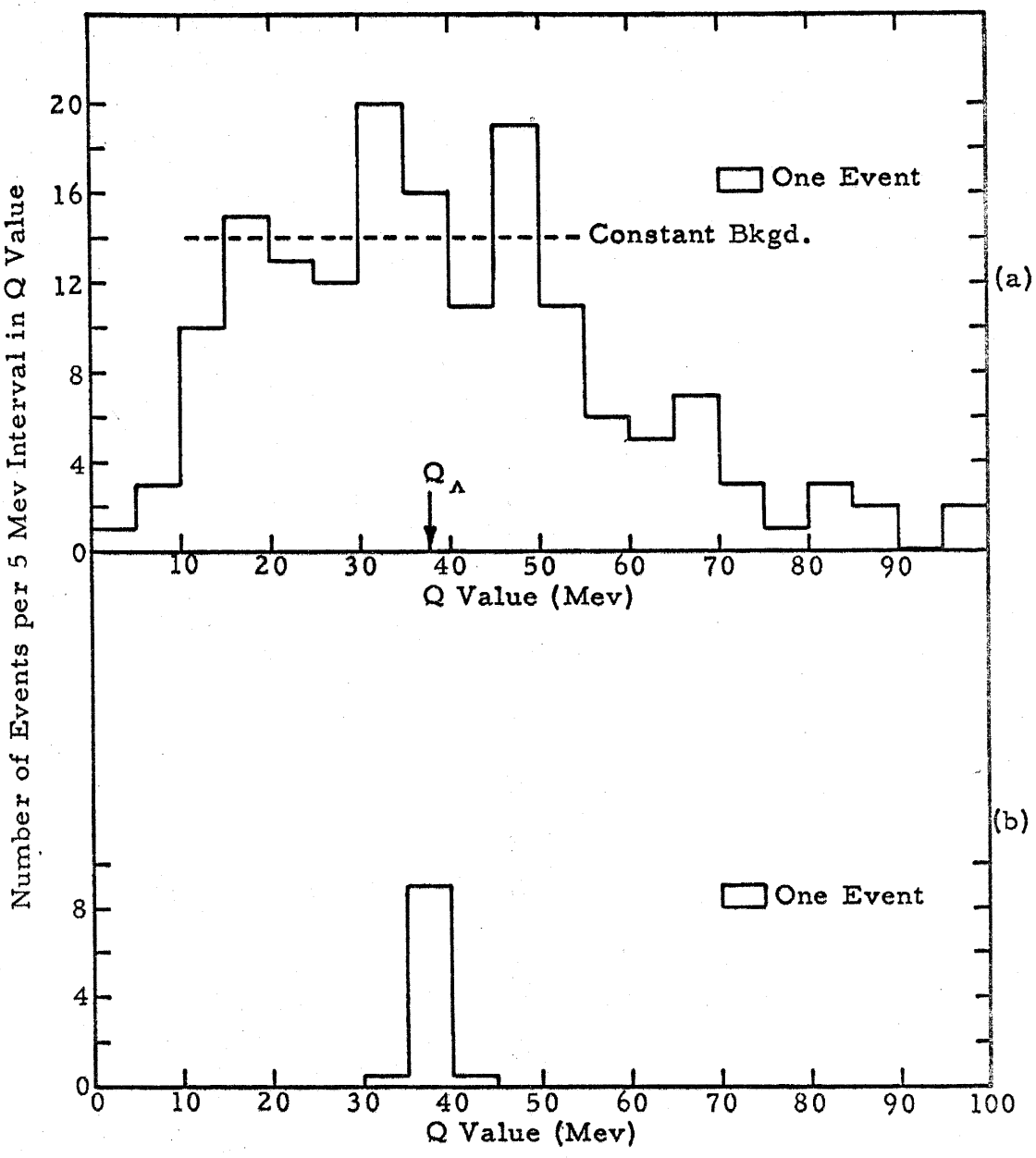
Number of Events per 5 Mev Interval in Q Value
20
16
12
8
4
0
One Event
Constant Bkgd.
(a)
Q_Λ
10 20 30 40 50 60 70 80 90
Q Value (Mev)
(b)
8
4
0
One Event
0 10 20 30 40 50 60 70 80 90 100
Q Value (Mev)

Figure 25

Figure 26

Non-Stopping, No-Star Events -- Standard Histograms

Fig. 26 a. Q-Value Histogram of Events with $Q < 70$ Mev and $|\Delta Q| \leq 14$ Mev

i) The constant-background and linear-background fits for $10 < Q < 65$ Mev, which are discussed on pp. 136-141, are indicated by dashed lines.

ii) The Q value for Λ^o decay is marked by an arrow.

Fig. 26 b. Resolution Function Containing 29 Events

i) The mathematical expression for the histogram is $29 \times R_1$ (ed, Q_i - 37. 5, 5) (see equation VI-10).

ii) The error distribution of the non-stopping, no-star events with $32.5 < Q < 42.5$ Mev (Fig. 24b) was used to generate R_1.

Fig. 26 c. "Pure Background"

i) This histogram was obtained by subtracting Fig. 26 b from Fig. 26 a.

ii) The two background fits (see above) are shown.

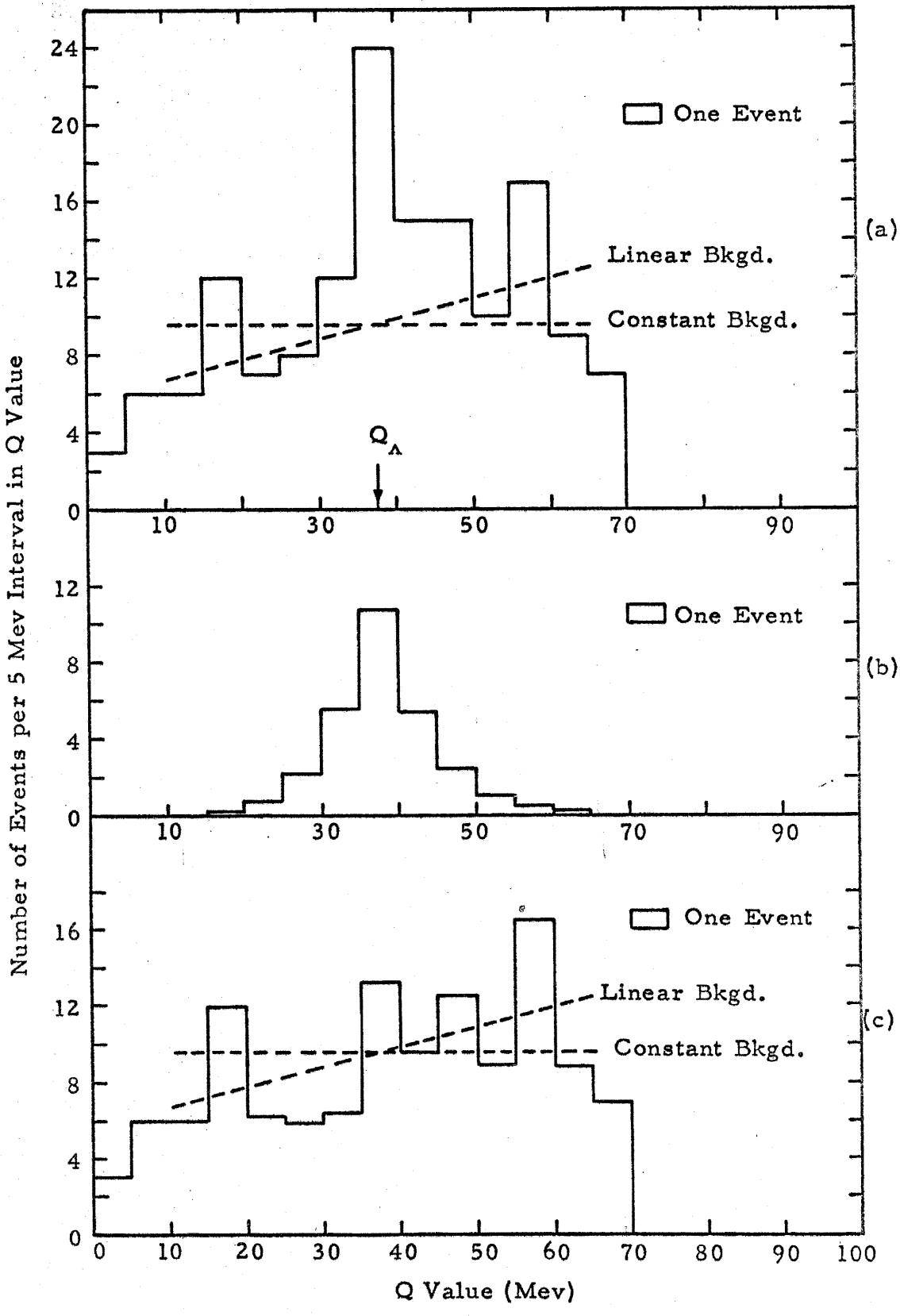
Number of Events per 5 Mev Interval in Q Value
One Event
Linear Bkgd.
Constant Bkgd.
Q_A
(a)
One Event
(b)
One Event
Linear Bkgd.
Constant Bkgd.
(c)
Q Value (Mev)

Figure 26

Figure 27

Non-Stopping, No-Star Events -- Distributed-Event Histograms

Fig. 27 a. Q-Value Histogram of Events with $Q < 70$ Mev and $|\Delta Q| \leq 14$ Mev

i) The estimated level of the histogram above 70 Mev is indicated by a zone about a dashed line. (See pp. 135-136 for discussion.)

ii) The Q value for Λ^o decay is marked by an arrow.

Fig. 27 b. Resolution Function Containing 29 Events

i) The mathematical expression for the histogram is $29 \times R_2$ (ed, Q_i - 37.5, 5) (see equation VI-11).

ii) The error distribution of the non-stopping, no-star events with $32.5 < Q < 42.5$ Mev (Fig. 24b) was used to generate an R_1, which was then used to generate R_2.

Fig. 27 c. "Pure Background"

i) This histogram was obtained by subtracting Fig. 27 b from Fig. 27 a.

ii) The estimated level above 70 Mev (see above) is shown.

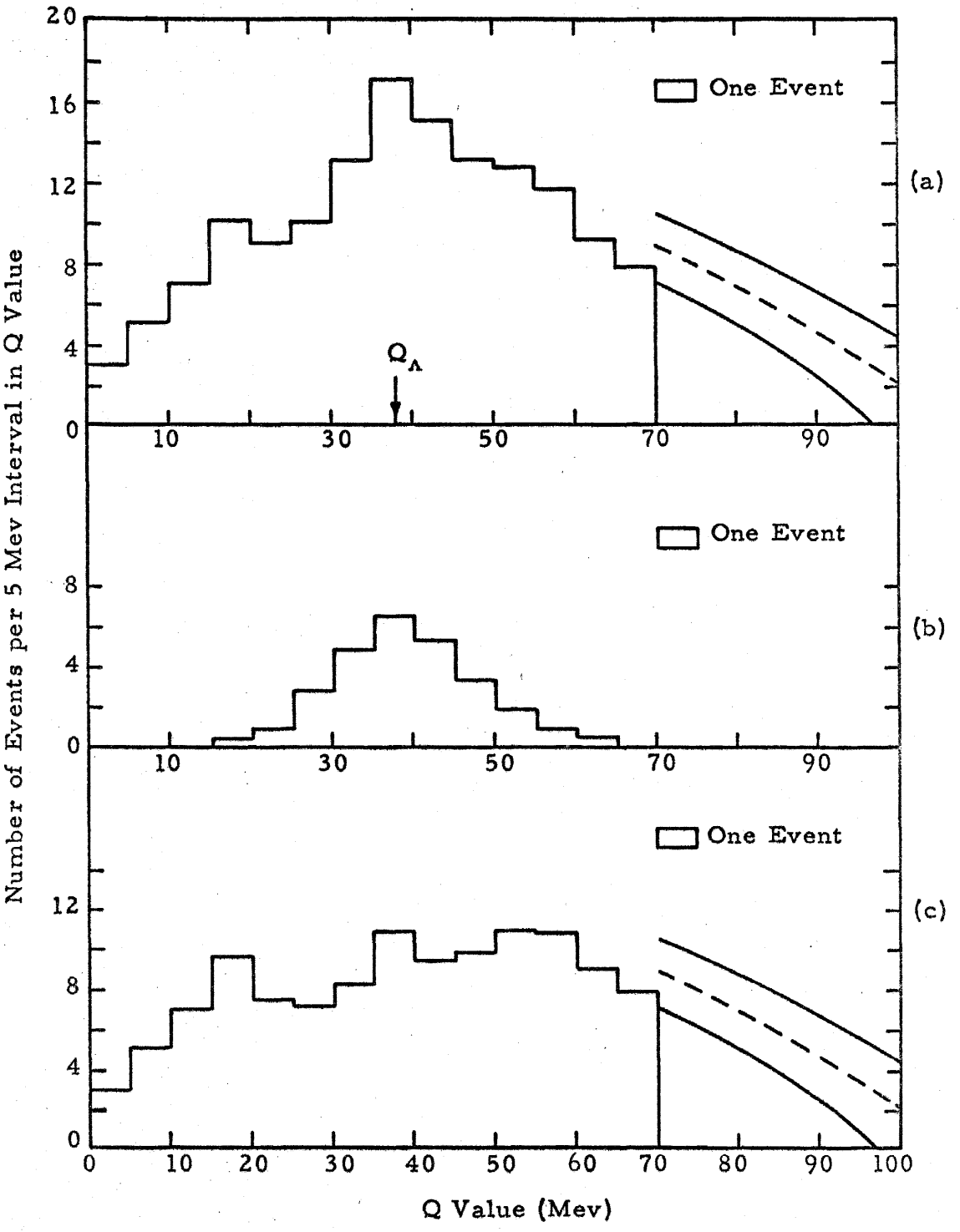
Number of Events per 5 Mev Interval in Q Value
One Event
(a)
Q_Λ
One Event
(b)
One Event
(c)
Q Value (Mev)

Figure 27

$$P(\Delta Q_{\pm}, Q_i - Q_o, q) = \frac{1}{\Delta Q_{\pm} \sqrt{2\pi}} \int_{Q_i - q/2}^{Q_i + q/2} \exp\left[-(Q' - Q_o)^2 / 2\Delta Q_{\pm}^2 \right] dQ' \quad \text{(VI-9)}$$

where the abbreviation ($\pm$) has the obvious meaning, and q is positive or negative according to whether $(Q_i - Q_o)$ is positive or negative.

This probability function may also be used to generate the resolution functions for the two types of histogram. For practical purposes the true distribution of Λ^o Q values is represented by a δ function. Therefore, the resolution function for the standard histogram (called the first resolution function) may be obtained by: (a) selecting a sample of events with the same error distribution as the actual events; (b) setting $Q_o = 0$ (or any constant) for all events of the sample; and (c) distributing each event of the sample among the intervals of a "resolution" histogram according to the probability function $P(\Delta Q, Q_i, q)$. In mathematical terms, if for a specific error distribution $N_j(\Delta Q_j, ed)$ is the number of events with error ΔQ_j,* the first resolution function $R_1(ed, Q_i, q)$ is computed from:

$$R_1(ed, Q_i, q) = \frac{1}{N} \sum_j N_j(\Delta Q_j, ed)\, P_j(\Delta Q_j, Q_i, q) \quad \text{(VI-10)}$$

where the sum is to be taken over all values of ΔQ_j and the function is normalized by the factor 1/N, in which

$$N = \sum_j N_j(\Delta Q_j, ed) \ .$$

---

* ΔQ_j has two values for each event: ΔQ_{j+} and ΔQ_{j-} .

The resolution function for the distributed-event histogram (called the second resolution function) may be derived from the first resolution function. Since the first resolution function represents both the expected distribution of measured Q values (for true Λ^o decays) about the true Λ^o Q value and the average error distribution for each event, the second resolution function may be found by: (a) selecting a sample of events with Q values distributed about zero (or any constant) according to the first resolution function; and (b) distributing each event of the sample among the intervals of a second "resolution" histogram according to the first resolution function. This folding of the first resolution function into itself is expressed mathematically as:

$$R_2\,(ed, Q_i, q) = \sum_{j=-\infty}^{+\infty} R_1(ed, Q_i - Q_j, q)\; R_1\,(ed, Q_j, q) \qquad \text{(VI-11)}$$

The resolution functions are shown in Fig. 28. The error distributions used were those derived from all events satisfying:

Class of events	Q range (Mev)	ΔQ range (Mev)
two-stopping	$10 < Q < 70$	$-14 \leq \Delta Q \leq 14$
non-stopping	$32.5 < Q < 42.5$	$-14 \leq \Delta Q \leq 14$

The first resolution function for non-stopping events in the Q range $10 < Q < 70$ Mev was also calculated and found to be nearly identical to the one used. If the error distribution for true Λ^o decays had been appreciably different from that for pseudo Λ^o decays, these two resolution functions should have differed by an appreciable amount. (One half of the events of the restricted range case were probably true

Figure 28

Resolution Functions

The resolution functions defined by equations VI-10 and VI-11 are illustrated for $q = 1$ Mev and the error distributions associated with the following classes of events:

a. Two-stopping, no star events with $10 < Q < 70$ Mev (abbreviated "2s");

b. and c. Non-stopping, no-star events with $32.5 < Q < 42.5$ Mev and $|\Delta Q| \leq 14$ Mev (abbreviated "ns").

Note that the scale for (a) differs from that for (b) and (c).

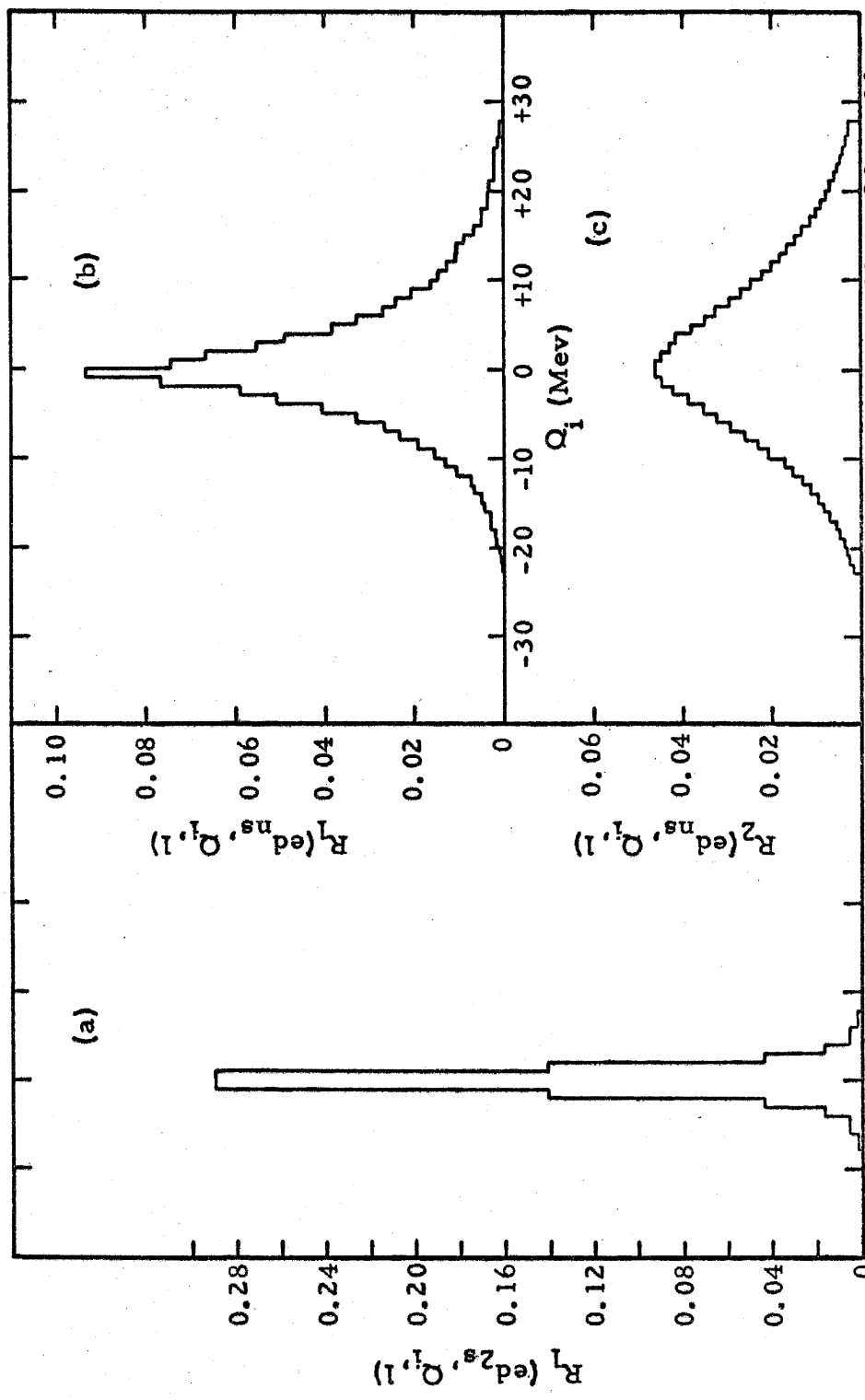
(a)
(b)
(c)
$R_1(ed_{2s}, Q_i, 1)$
$R_1(ed_{ns}, Q_i, 1)$
$R_2(ed_{ns}, Q_i, 1)$
Q_i (Mev)
0.28
0.24
0.20
0.16
0.12
0.08
0.04
0
0.10
0.06
0.02
-30
-20
-10
+10
+20
+30

Figure 28

Λ^o decays while only one fifth of the events of the extended range case were probably true Λ^o decays.) Thus one can believe with some confidence the inherent assumption that the resolution functions for true Λ^o decays are adequately represented by the resolution functions which were derived from the errors of all the events (pseudo plus true Λ^o decays).

D. DISCUSSION OF HISTOGRAMS—NUMBER OF TRUE Λ^o DECAYS

1. Two-Stopping, No-Star Events. The two-stopping event histogram (Fig. 25a) has pronounced cutoffs at low and high Q values. As may be seen from the Q value nomograms (Fig. 22), the lower limit of 27 Mev on pion energies (from range of $\pi > 3$ cm) is responsible for the low energy cutoff. The high energy cutoff is attributable to the finite size of the visible region. In particular, pions from events with large Q values tended to be energetic enough to escape from the visible region.

The first resolution function for two-stopping events implies that 90 per cent of the true-Λ^o Q values should have fallen between 35 and 40 Mev. The lack of a peak in this interval may be interpreted to mean that there were very few true Λ^o decays among the two-stopping, no-star events. In fact, the distribution of events between 10 and 55 Mev appears to be consistent with a constant background and no true Λ^o decays. The results of a chi-square test support this hypothesis:

a) (mean number of events per 5 Mev interval) = 14

b) (number of degrees of freedom) = 8

c) (χ^2 for observed distribution) = 7.3

d) (Probability that a larger value of χ^2 would occur) = 0.50

Consideration of the 16 events observed in the 35 - 40 Mev interval compared to the mean number per interval leads to the conclusion that there is a 36 per cent chance that as many as 4 true Λ^o decays, and a 33 per cent chance that no true Λ^o decays occurred among the two-stopping no-star events. For the purposes of estimating the K_2^o photoproduction cross sections, the number of true Λ^o decays among these events will be taken to be 2 ± 2.

2. Non-Stopping, No-Star Events. The non-stopping event histograms (Figs. 26a and 27a) also fall off at low Q values, though not as drastically as does the two-stopping event histogram. While the reason for the decrease is the same in the two cases (see Section 1 above), the decrease in the non-stopping case is less drastic because the pseudo-Λ^o kinetic energies for non-stopping events tended to be considerably greater than those for two-stopping events (see Section 3 below); and therefore the pion kinetic energies for non-stopping events also tended to be greater.

The upper ends of the non-stopping event histograms show a slight decrease because of the qualitative estimate technique used to discard events with Q values above 70 Mev. As mentioned earlier, the standard histogram should be unaffected below 65 Mev. The effect on the distributed-event histogram should be negligible below 55 Mev*. A rough idea of the shape the histograms would

*This estimate was made using the observed r.m.s. difference of 8 Mev between the qualitative estimate and final-analysis Q values.

assume above 70 Mev if the large Q-value events were included may be obtained from the qualitative estimates of these events. A correction must be made for the fraction of events that would be discarded because of Q value errors > 14 Mev. In the range $15 < Q < 70$ Mev this fraction is approximately given by:

$$(\text{fraction discarded}) \approx (0.011 \pm 0.001)(Q - 15) \quad . \qquad \text{(VI-12)}$$

When applied to the qualitative estimate data, the extrapolation of this function predicts that the histograms would taper off at high Q values as shown in Fig. 27. The zone about the central line is derived from the error indicated in equation VI-12.

Both types of histogram show a peak at the proper Q value for true Λ^{o} decays. The smoothing of statistical fluctuations and the resultant increased statistical significance of the small peak in the distributed-event histogram should be noted. This histogram is particularly useful in its visual indication that the pseudo-Λ^{o} decay background was, at most, slowly varying in the range 10 to 65 Mev. Figure 27c presents the "pure" background distributed-event histogram if 29 times the second resolution function is subtracted from the measured histogram. Note that the prediction for the histogram above 70 Mev agrees satisfactorily with this "pure" background.

Because of this visual indication is seemed reasonable to try to fit the standard histogram between 10 and 65 Mev with both a constant background, and one varying linearly with Q. The constant background fit was carried out in the following steps:

a) A number, N_Λ, of true Λ^o decays was assumed.

b) A constant background, N_B, per 5 Mev interval was assumed. The quantity ($11 \times N_B + N_\Lambda$) was normalized to the total number of events (135) between 10 and 65 Mev.

c) The value of $\chi^2(N_\Lambda)$ with 10 degrees of freedom was calculated for the observed spectrum:

$$\chi^2(N_\Lambda) = \sum_{i=-5}^{+5} \frac{[N_B + N_\Lambda R_1(ed, Q_i - Q_\Lambda, 5) - N_i(obs)]^2}{[N_B + N_\Lambda R_1(ed, Q_i - Q_\Lambda, 5)]} \qquad \text{(VI-13)}$$

where $N_i(obs)$ is the number of events observed in the i^{th} 5-Mev interval between 10 and 65 Mev, and Q_Λ is the Λ^o decay Q value ($Q_\Lambda = Q_{i=0}$).

d) The minimum value of $\chi^2(N_\Lambda)$ was found, thus yielding the best value for N_Λ.

The linear background fit proceeded as follows:

a) and b) The same as for constant background case.

c) The normalized linear background, $N_i(LB)$, was written as

$$N_i(LB) = N_B + k_{N_\Lambda} (Q_i - Q_\Lambda)$$

and the slope, k_{N_Λ}, found by minimizing the sum of the squares of the differences between the hypothetical and measured distributions*. Thus,

*Note that χ^2 was not minimized in this fitting procedure.

$$k_{N_\Lambda} = \frac{\sum_{i=-5}^{+5} [N_i(obs) - N_B - N_\Lambda R_1(ed, Q_i - Q_\Lambda, 5)][Q_i - Q_\Lambda]}{\sum_{i=-5}^{+5} (Q_i - Q_\Lambda)^2}$$

d) $\chi^2(N_\Lambda)$ with 9 degrees of freedom was calculated from equation VI-13, in which N_B was replaced by $N_i(LB)$.

e) The same as step (d) for constant background case.

The functions $\chi^2(N_\Lambda)$ for the two types of fit are shown in Fig. 29. The linear background fit is seen to be the better of the two, though both fits give $N_\Lambda = 29$ as the most probable value.

According to statistical theory(46)*, if the measurement error in N_Λ is Gaussian, $\chi^2(N_\Lambda)$ should be parabolic and the r.m.s. error in the measurement of N_Λ is found from

$$\Delta N_\Lambda (r.m.s.) = |N_\Lambda (\chi^2_{min}) - N_\Lambda (\chi^2_{min} + 1)| \quad . \qquad (VI\text{-}14)$$

The triangles and crosses in Fig. 29 are points on parabolas fitted to the curves for the constant- and linear-background cases respectively. The agreement is seen to be reasonable in both instances, and the following conclusions may be drawn:

*The author is indebted to C. W. Peck and D. E. Groom for elucidating these points.

Figure 29

χ^2 vs N_Λ for Non-Stopping, No-Star Events

The functions $\chi^2(N_\Lambda)$ are plotted for the constant- and linear-background approximations. The triangles (crosses) are points on a parabola which is fitted to the constant (linear) background curve in the following way:

a) minimum of parabola placed at $N_\Lambda = 29$ and adjusted to the experimental value, χ^2_{min}; and

b) $|N_\Lambda - 29|$ at $(\chi^2_{min} + 1)$ set equal to the average of the two experimental values.

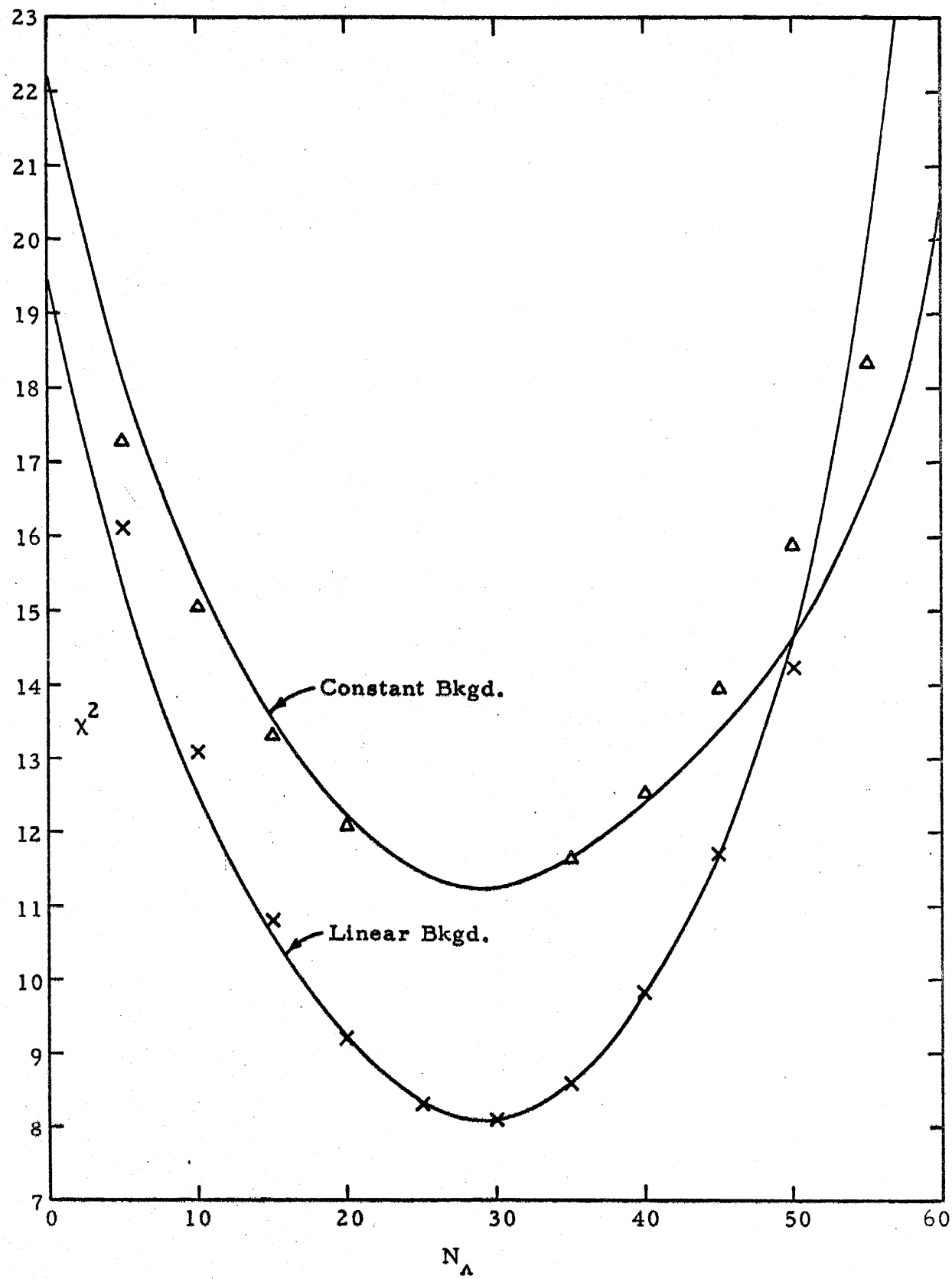
23
22
21
20
19
18
17
16
15
14
13
12
11
10
9
8
7
χ^2
Constant Bkgd.
Linear Bkgd.
0
10
20
30
40
50
60
N_Λ

Figure 29

Type of Fit	N_Λ (best value)	ΔN_Λ (r.m.s.)
constant background	29	$\pm$ 10
linear background	29	$\pm$ 8.5

The interesting features of the best fits are shown in Figs. 26 and 27.

Finally, one may list for several values of N_Λ the probability that $\chi^2(N_\Lambda)$ should have exceeded its observed value:

	Probability: $\chi^2(N_\Lambda) >$ Observed Value	
N_Λ	constant background (10 degrees of freedom)	linear background (9 degrees of freedom)
0	0.01	0.02
29	0.32	0.50

3. Comparison of Two-Stopping and Non-Stopping, No-Star Events. The fact that true Λ^o decays were observed among the non-stopping events but not among the two-stopping events is a direct result of the pseudo (plus true) Λ^o kinetic energy spectra. The integral spectra for events with Q values in the range $25 < Q < 50$ Mev are shown in Fig. 30. (The spectra for the range 0 - 70 Mev are almost identical to these.) In 71 per cent of the non-stopping, but only 12 per cent of the two-stopping events the energy exceeded 100 Mev. Thus, if no-star true Λ^o hyperons tended to be energetic, one should not be surprised by the observations. The following arguments support this contention:

Figure 30

Pseudo- Plus True-Λ^{o} Kinetic-Energy Spectra

The integral kinetic-energy spectra for (a) two-stopping, no-star events, and (b) non-stopping, no-star events are presented. All events satisfying the following criteria were used:

$$25 < Q < 50 \text{ Mev}$$

$$-14 \leq \Delta Q \leq 14 \text{ Mev}$$

The kinetic energies were calculated from:

$$T_{\Lambda} = T_{p} + T_{\pi} - Q_{\Lambda}$$

where Q_{Λ} is the measured Q value.

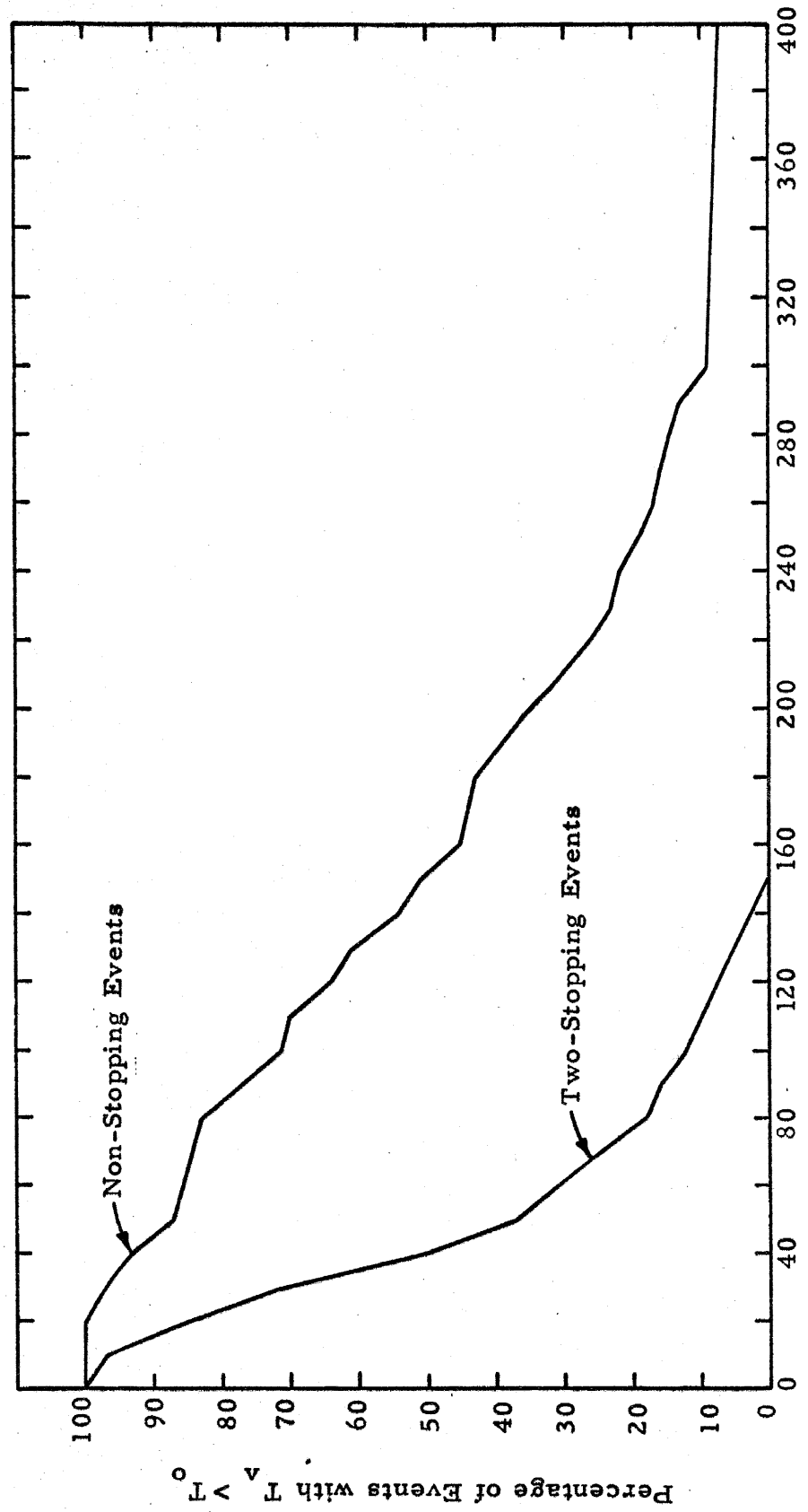
Percentage of Events with $T_A > T_o$
100
90
80
70
60
50
40
30
20
10
0
0
40
80
120
160
200
240
280
320
360
400
T_o (Mev)
Non-Stopping Events
Two-Stopping Events

Figure 30

Case 1. K_2^o Interaction Within Visible Region. The kinematics of the Λ^o production process I-13 for the K_2^o energies of this experiment favors Λ^o kinetic energies between 100 and 300 Mev. There was less chance of a visible associated star being produced if the Λ^o escaped from the nucleus without suffering an inelastic collision than if it suffered one or more such collisions before escaping.

Case 2. K_2^o Interaction Outside Visible Region. Since the mean decay distance increases with kinetic energy, the probability that a Λ^o reached the visible region before it decayed was greater for high energy Λ^o hyperons than for low energy ones.

For these reasons one would expect no-star Λ^o hyperons to have been more energetic than those associated with stars. The energy distribution of the 9 events consistent with the latter type (see Table 10) was very board. The mean kinetic energy for these 9 events was 123 Mev and the r.m.s. difference from this mean was 63 Mev. One may conclude that few of the no-star Λ^o hyperons should have fallen into the low energy range covered by the two-stopping events.

Further evidence for this hypothesis is presented in Fig. 31. The distributed-event histograms and second resolution functions are shown for all events (non-stopping plus two-stopping) in which the pion identification was probable or definite and the pseudo (or true) Λ^o kinetic energy was (a) greater than 100 Mev, or (b) greater than 200 Mev. The true Λ^o peak is seen to persist at these energies.

Figure 31

"Good", High-Energy Events -- Distributed Event Histograms

Fig. 31 a. Q-Value Histogram of "Good" Events with $T_\Lambda > 100$ Mev

i) All no-star events (both two-stopping and non-stopping) for which the pion identification was "probable" or "definite" fell into this "good" category.

ii) The histogram is cut off at 70 Mev.

iii) The Q value for Λ^o decay is marked by an arrow.

Fig. 31 b. Resolution Function (for Fig. 31 a) Containing 20 Events

i) The mathematical expression for the histogram is $20 \times R'_2$ (ed, Q_i - 37.5, 5).

ii) Since 15 two-stopping and 89 non-stopping events contributed to Fig. 31 a, R'_2 was calculated from:

$$R'_2 = 0.14 \times R_2 (ed_{2s}, \ldots) + 0.86 \times R_2 (ed_{ns}, \ldots).$$

The subscripts are explained, and the error distributions are given, on p. 132.

Fig. 31 c. Q-Value Histogram of "Good" Events with $T_\Lambda > 200$ Mev

Comments (i) and (ii) on Fig. 31 a also apply to Fig. 31 c.

Fig. 31 d. Resolution Function (for Fig. 31 c) Containing 10 Events

Since all events with $T_\Lambda > 200$ Mev were non-stopping, $10 \times R_2$ (ed_{ns}, Q_i - 37.5, 5) is plotted. The error distribution is defined on p. 132.

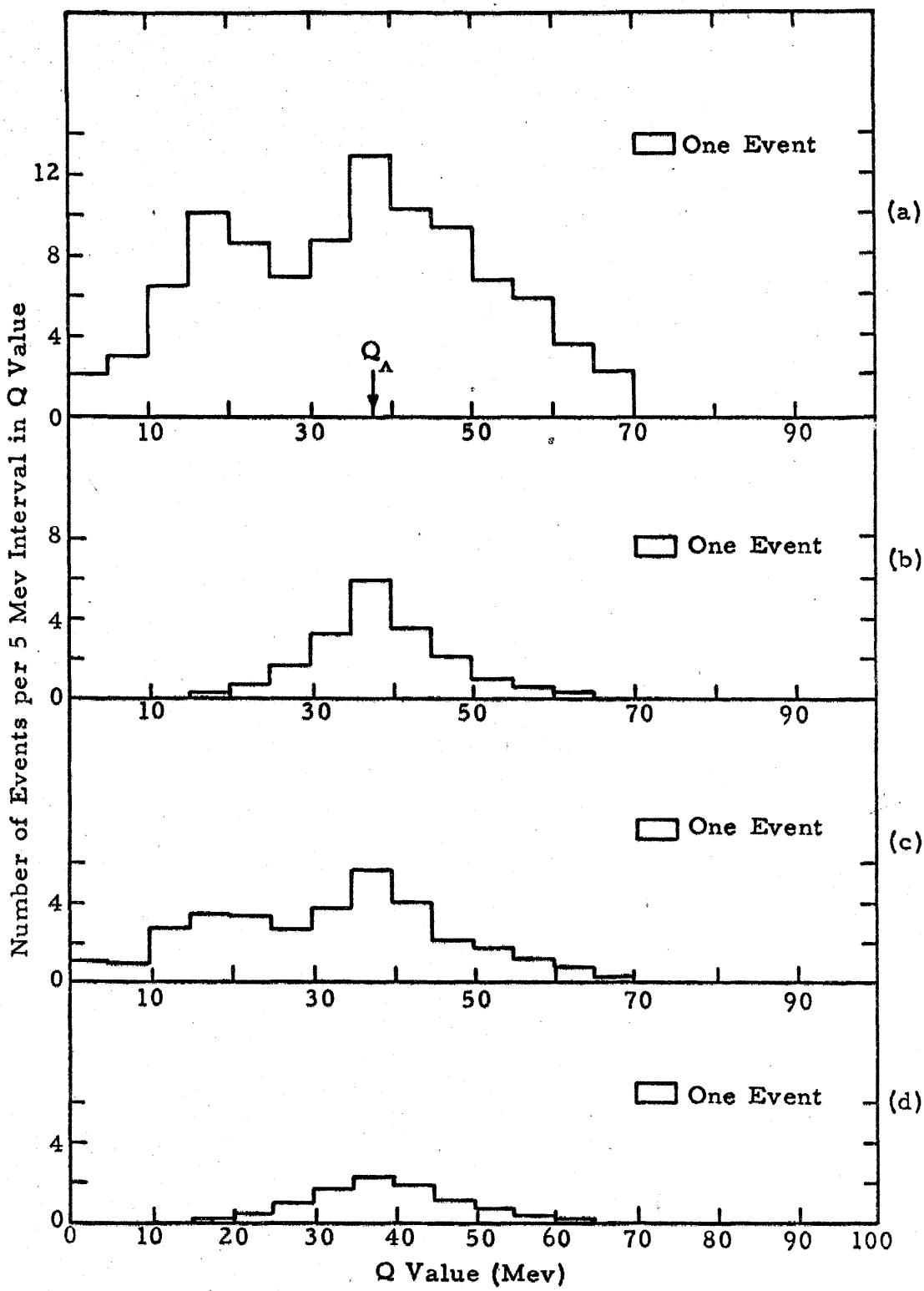
One Event
(a)
12
8
4
0
Q_A
10
30
50
70
90
One Event
(b)
8
4
0
10
30
50
70
90
One Event
(c)
4
0
10
30
50
70
90
One Event
(d)
4
0
0
10
20
30
40
50
60
70
80
90
100
Number of Events per 5 Mev Interval in Q Value
Q Value (Mev)

Figure 31

E. Λ^o DECAYS ASSOCIATED WITH STARS

After Step 3 in the Q-value analysis procedure, a thorough search was made by the author for stars that might be associated with the retained events. The only restrictions placed on a candidate star were that it appear roughly coplanar with the possible Λ^o decay and that in both scanner views the vector joining it to the origin of the possible Λ^o decay fall between the direction vectors of the pion and proton. In all 105 such candidate stars were found and measured. The Q-value analysis for the events was completed according to the steps described above (Section B).

The tests for associated stars discussed in Section A2 were applied to these events. An associated star was discarded if it failed either of the tests by more than two standard deviations. Fifty two stars failed the coplanarity test and forty others failed the momentum balance test. Three of the remaining stars were discarded because the error in the Q-value measurement exceeded the 14 Mev limit. The important features of the ten events which were left are presented in Table 10. The standard Q-value histogram of these events and the reduced decay distance histogram of the events with Q values consistent with 37.6 Mev are presented in Fig. 32. Also shown on the latter histogram are:

1) the values of ζ (the reduced decay distance) into which 10 cm in true space is transformed by 100, 200, and 300 Mev Λ^o hyperons;

2) the ζ intervals defined by:

TABLE 10

Λ^o Events Associated with Stars

Legend

α = angle between $\vec{e}_\Lambda$ and $\vec{e}_p \times \vec{e}_\pi$

$\Delta\cos\alpha$ = estimated error in the measurement of $\cos\alpha$

δ = deviation from momentum balance (see equation VI-5)

δ_m = measured value of δ

δ_e = value of δ computed from the estimated errors in the measurement

T_Λ = Λ^o kinetic energy = $T_\pi + T_p - Q$

ζ = reduced decay distance (see equation VI-7)

Notes

1. Errors are estimated standard deviations.
2. The associated star kinetic energies are estimations. All tracks other than pions were assumed to be protons.
3. For the nine events consistent with Λ^o decay, the r.m.s. values of $(\cos\alpha/\Delta\cos\alpha)$ and (δ_m/δ_e) are 0.96 and 0.68, respectively, in reasonable agreement with the expected value of 1.00.
4. Pion identification was "definite" for all events except: frame 13,424 in which a short pion had a possible σ-star and therefore, the identification was "possible"; and frame 17,376 in which the identification was "probable".

TABLE 10

Frame Number	Stopping Particles	Coplanarity Test		Momentum Balance Test		Q value (Mev)	T_Λ (Mev)	ζ	Associated Star			
									Number		Kinetic Energy (Mev)	
		$\cos\alpha$	$\frac{\cos\alpha}{\Delta\cos\alpha}$	δ_m	δ_m/δ_e				all prongs	pions	total visible	pion
11082	π,p	0.020	0.38	0.20	0.61	39 ± 2	137	0.54	3	0	60	—
12816	π,p	0.080	1.70	0.11	0.92	37 ± 1	30	3.61	3	0	180	—
13227	p	0.007	0.12	0.15	0.44	30^{+7}_{-6}	94	0.21	1	1	80	80
13362*	p	~0.16	~1.0	~0.4	~0.8	43^{+5}_{-6}	114	~0.02	1	0	30	—
13424	π	0.017	0.29	0.31	0.36	41^{+7}_{-8}	193	0.81	2	1	40	20
15091	p	0.031	1.04	0.19	1.19	42^{+10}_{-10}	155	0.46	5	1	100	30
15763	π	0.002	0.10	0.05	0.33	37^{+3}_{-2}	242	1.31	4	1	200	100
16809	p	0.033	1.18	0.05	0.31	36^{+9}_{-7}	54	2.95	1	0	180	—
19682	p	0.039	1.30	0.10	0.53	46^{+12}_{-10}	89	3.32	1	0	40	—
17376		0.043	2.00	0.87	1.78	13^{+5}_{-3}	215	2.88	1	0	70	—

*relations to star approximate since star very close to decay point (~0.7 mm).

Figure 32

Λ^o Decays Associated With Stars

Fig. 32 a. Standard Q-Value Histogram

The number of events per 5-Mev interval in Q value is plotted against the Q value.

Fig. 32 b. Resolution Function Containing 8 Events

i) The mathematical expression for the histogram is $8 \times R_1$ (ed, Q_i - 37.5, 5).

ii) The error distribution of the events associated with stars was used to generate R_1.

iii) The number of events per 5-Mev interval in Q value is plotted against the Q value.

Fig. 32 c. Reduced Decay Distance Histogram of Events Consistent with Λ^o Decay

i) ζ is defined by equation VI-7.

ii) The number of events per 0.1 interval in ζ is plotted against ζ.

iii) The vertical arrows below the ζ scale mark the values of ζ into which 10 cm in true space is transformed by Λ^o hyperons with the kinetic energies indicated.

iv) The ζ intervals designated by ζ_1, ζ_2 and ζ_3 are 1/3 probability intervals for true Λ^o decays (see equation VI-15).

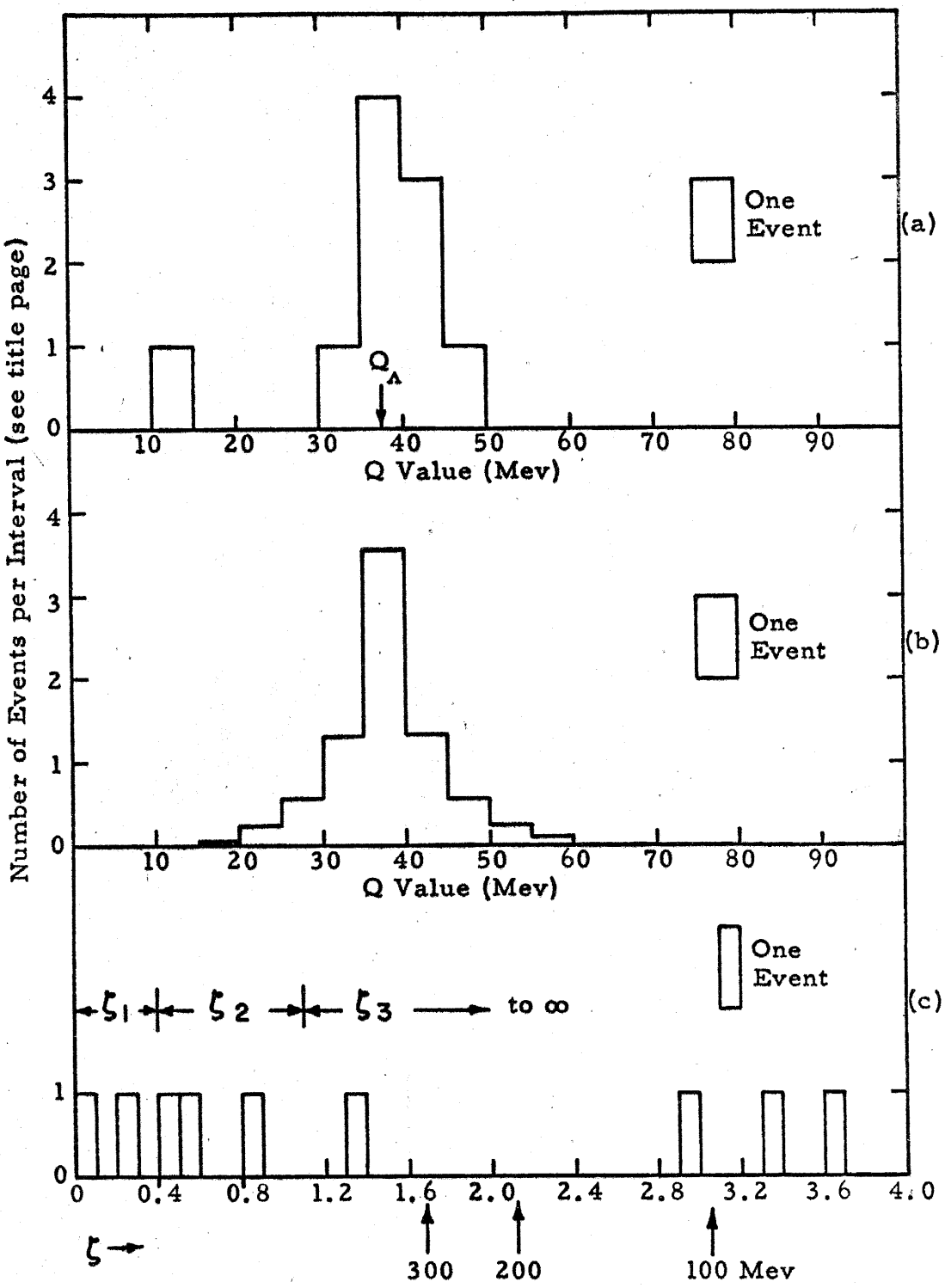
Number of Events per Interval (see title page)
One Event
(a)
Q_Λ
Q Value (Mev)
One Event
(b)
Q Value (Mev)
One Event
(c)
ζ_1
ζ_2
ζ_3
to ∞
ζ
300
200
100 Mev

Figure 32

$$1 > \exp(-\zeta_1) > 2/3 > \exp(-\zeta_2) > 1/3 > \exp(-\zeta_3) > 0. \quad \text{(VI-15)}$$

That 10 cm in true space transforms into rather large values of ζ means that the effects of the bubble chamber boundaries were minor and may be ignored. Therefore, if the 9 observed events are true Λ^o decays, 3 of them should fall into each of the ζ intervals defined above. With the possible exception of one or two of the events at large ζ, this condition is satisfied. In fact, it is not unreasonable that all 9 events are true Λ^o decays. The average value of ζ as calculated from the 9 independent measurements is 1.5 ± 0.5, where the error is the standard deviation due to the low statistics. The agreement is satisfactory between this and the actual value of 1.0 for true Λ^o hyperons.

The conclusion may be drawn that 8 ± 1 true Λ^o decays associated with stars occurred in the bubble chamber. Several of these events are reproduced in Figs. 16, 17 and 18.

In summary of this and the previous section, one may say that the most probable total number of Λ^o decays of the observable type was

$$N_\Lambda = 39 \pm 14 \quad \text{(VI-16)}$$

where the error is the standard deviation which includes both measurements and statistical uncertainties.

F. DISCUSSION OF K_1^o DECAYS

1. Analysis Procedure. The analysis of the 257 possible two-pion events found in scanning proceeded in a fashion similar to that for Λ^o decays, though different selection criteria were used. Events with one long pion and one short track which was not identified as a probable or definite proton were treated both as possible Λ^o decays and possible K_1^o decays. Because of the great difference between the kinematics for these two decays, such events were easily eliminated from one or the other class. A qualitative estimate of the possible K_1^o decays was employed to eliminate events with low Q values* (< 100 Mev), and the analysis was completed on the remaining 26 events. Unfortunately, the measurement errors were so large (about +60, -40 Mev for events with Q values consistent with K_1^o decay) that a Q-value histogram could not be used to separate true K_1^o decays from the background which is believed to have consisted mostly of pion scatters. Twelve events other than the five special ones discussed below were consistent with K_1^o decay.

2. Associated Stars. Out of 13 events in which the two pions appeared to be coplanar with a star, four were found to satisfy a coplanarity test similar to that applied in the Λ^o analysis. Unfortunately, the large errors in the pion energy measurements precluded the use of a momentum balance test. The only recourse was to qualitatively compare the observations with the properties which a true K_1^o decay associated with the star would have had.

---

*Note that the K_1^o Q value is 217 Mev.

Perhaps the most convincing evidence was the reduced decay distance, ζ. Because of the very short lifetime of the K_1^o meson, it was very unlikely for an accidental star to occur close enough to a pseudo decay to give a reasonable value for ζ. One of the four events which passed the coplanarity test was discarded for this reason ($\zeta \approx 8.8$, $e^{-\zeta} \approx 1.5 \times 10^{-4}$). The other three had satisfactory values of ζ and were quite likely true K_1^o decays. Their interesting features are listed in Table 11a. All the pions of these events fell into the "definite" classification. The geometrical features (namely angles) of each event were used to determine the properties (K_1^o and $\pi^{\pm}$ kinetic energies) which a true K_1^o decay would have had. These properties are also listed in the table.

3. Diffraction Regeneration. Two events were very nearly coplanar with the K_2^o beam direction and therefore may have been decays of diffraction-regenerated K_1^o mesons. Their relevant features are listed in Table 11b.

For the first event (Frame 15355) it was possible to choose a K_1^o meson which, within the error introduced by Δ (see legend for Table 11), was consistent with: (a) the energy of the stopping pion, which was only 0.7 cm long and could not be definitely identified; and (b) the directions of both pions. Thus at least one independent criterion was satisfied by this choice.

The K_1^o meson consistent with the second event (Frame 17932) was determined by the angles between the pion directions

TABLE 11

Special K_1^o Decays

a. Events Associated with Stars

b. Events from Diffraction Regeneration

Legend

α = angle between $\vec{e}_{K_1^o}$ and $\vec{e}_{\pi_1} \times \vec{e}_{\pi_2}$

$\Delta \cos\alpha$ = estimated measurement error in $\cos \alpha$.

Measured Values:

Best = the value obtained in the measurement

Min = (best value) - (r.m.s. measurement error)

Max = (best value) + (r.m.s. measurement error)

TB = too big (mean gap length) > (max value possible)

ζ = reduced decay distance for K_1^o = 165 $S/p_{K_1^o}$; where

$p_{K_1^o}$ = momentum of K_1^o consistent with event (in Mev/c)

S = decay distance in true space (in cm)

Δ = average angle in CF_3Br which nuclear diffraction-scattered K^o meson of energy $T_{K_1^o}$ makes with incident direction. The estimated r.m.s. fluctuation about Δ is also listed.

α' = angle between incident beam direction and normal to plane of event. Errors include uncertainty in K_2^o beam direction and measurement errors. Since plane of true events can take on any orientation containing K_1^o direction, $(90 - \alpha')$ should on the average be less than Δ.

TABLE 11a

Frame No.	Coplanarity Test		Properties of K_1^o Decay Consistent with Event		Measured Values					Associated Star /	
					T_π (Mev)			ζ	S (cm)	No. Prongs	Visible Energy (Mev)
	cosα	$\frac{\cos\alpha}{\Delta\cos\alpha}$	$T_{K_1^o}$ (Mev)	T_π (Mev)	Best	Min	Max				
10946	0.026	0.9	210	1) 294 2) 135	1) 192 2) TB*	129 137	TB TB	2.0	6.0	2	50
12489	0.018	0.3	115	1) 170 2) 164	1) 125 2) 150	94 120	179 190	0.12	0.3	2	20
18869	0.005	0.1	80	1) 123 2) 176	1) 178 2) TB*	TB TB	116 430	0.12	0.2	2	150

* Poor statistics on track.

/ Visible energy of associated star estimated. All prongs assumed to be protons.

TABLE 11b

Frame No.	Pion Identification	Properties of K_1^o Decay Consistent with Event			Measured Values			
					T_π (Mev)			(90 - α') (degrees)
		$T_{K_1^o}$ (Mev)	T_π (Mev)	Δ (degrees)	Best	Min	Max	
15355	1) pos 2) def	450	1) 12 2) 657	5 ± 3	1) 12 2) 313	11 198	13 TB	6 ± 2
17932	1) def 2) def	100	1) 122 2) 195	13 ± 9	1) 101 2) 203	84 146	126 TB	9 ± 2

and the K_2^o beam direction. The properties of the decay are fairly insensitive to small changes in these angles.

One may conclude that at least 4 ± 1 K_1^o decays occurred during the run. Several of these decays are illustrated in Figs. 12, 13 and 14.

VII. RESULTS FOR K^O PHOTOPRODUCTION CROSS SECTIONS

A. FROM Λ^O DETECTION

The three photoproduction processes which contributed to the K_2^O beam are listed as reactions I-2, I-4 and I-6. Letting superscripts denote the reaction, one may relate the number of observed Λ^O decays, N_Λ^i, to the K^O photoproduction cross section:

$$N_\Lambda^i = \tfrac{1}{2} N_{CT} \int\int N(k)\, (d\sigma/d\Omega')^i (d\Omega'/d\Omega)^i \eta_1^i \eta_2^i \, d\Omega \, dk \qquad \text{(VII-1)}$$

where primes refer to the CM system; the integrals are to be carried out over the solid angle subtended by the freon chamber and over photon energies; and

$\frac{1}{2}$ = fraction of K^O mesons contributing to K_2^O beam

N_{CT} = number of neutrons (or protons)/cm^2 in carbon target

$N(k)dk$ = number of photons in dk

$d\sigma/d\Omega'$ = differential cross section in CM system

$d\Omega'/d\Omega$ = solid angle transformation from CM system to laboratory system

η_1 = correction for K_2^O losses

η_2 = K_2^O conversion and Λ^O detection factor.

In equation VII-1 N_{CT} has been placed outside the integral because: (1) the transverse variation of the photon beam intensity was unimportant; and (2) the longitudinal attenuation of the photon beam in the target was small and the beam was calibrated for the mean intensity within the target. The assumption has been made that the nucleons

in the carbon nucleus may be treated as if free. Thus the photons are assumed to have interacted independently with each nucleon and the Fermi momenta of the nucleons is ignored.

Inasmuch as (1) the solid angle subtended at the carbon target by the freon chamber was small; (2) the K_2^o losses were rather insensitive to the direction and energy of the K_2^o meson within the K_2^o beam; and (3) the K_2^o conversion and Λ^o detection were not strongly dependent on the K_2^o energy, equation VII-1 may be simplified through the use of average quantities:

$$N_\Lambda^i = \tfrac{1}{2} N_{CT} \langle \overline{\eta_1} \rangle \int \overline{\eta_2}\, d\Omega \int N(k) \langle d\sigma/d\Omega' \rangle^i \langle d\Omega'/d\Omega \rangle^i dk \quad \text{(VII-2)}$$

where a bar above a quantity signifies an average over K_2^o energy and brackets signify an average over solid angle.

Since there was no way of differentiating among Λ^o decays from the three sources, one must assume specific forms for the photoproduction cross sections in order to obtain their magnitudes. Three possible sets of assumptions will be considered. Assumptions (a) and (b) are common to all three.

a) The CM cross sections are step functions of the photon energy, the steps occurring at 30 Mev (16 Mev) above the laboratory (CM) threshold energy.

b) The cross sections are constant over all CM angles involved in the experiment.

c) The relative magnitudes, a_j^i, of the three cross sections are:

Assumption Set Number	Reaction Products		
	$\Lambda^o + K^o$ (i = 1)	$\Sigma^o + K^o$ (i = 2)	$\Sigma^+ + K^o$ (i = 3)
(j = 1)	1	1	1
(j = 2)	1	0	0
(j = 3)	0	1	0
	or 0	0	1

The displacement from threshold of each cross section step is imposed to avoid an unreasonable weight being placed on the cross section near threshold. ($d\Omega'/d\Omega$ becomes very large in this region, while the true cross section is probably small.)

The total number, N_Λ, of observed Λ^o decays may be written:

$$N_\Lambda = \tfrac{1}{2} N_{CT} \langle \overline{\eta_1} \rangle \, (d\sigma/d\Omega')_{sj} \int \overline{\eta_2} \, d\Omega \sum_{i=1}^{3} a_j^i \int_{k^i+30}^{1300} N(k) \langle d\Omega'/d\Omega \rangle^i \, dk \quad \text{(VII-3)}$$

where $(d\sigma/d\Omega')_{sj}$ is the height of the step functions for assumption set j and k^i is the laboratory threshold energy of the i^{th} reaction. Solution of this equation for $(d\sigma/d\Omega')_{sj}$ completes the data reduction.

The K_2^o loss factor and the K_2^o conversion and Λ^o detection factor are discussed in Appendices VIII and IX. The following values are found:

$$\langle \overline{\eta_1} \rangle = 0.33 \pm 0.07$$

$$\int \overline{\eta_2} \, d\Omega = (0.83 \pm 0.25) \times 10^{-4} \text{ ster.}$$

N_{CT} is easily calculated from the properties of the carbon

target (see Table 1) and is found to be:

$$N_{CT} = 2.66 \times 10^{24}/cm^2$$

The error in N_{CT}, which is less than one per cent, may be ignored.

N(k) is given in Fig. 7. Figure 33 shows the dependence of the CM angle and $d\Omega'/d\Omega$ on the laboratory photon energy for the central K_2^o ray (at 11^o to the photon beam). With the aid of these two figures one obtains:

Assumption Set Number	$\sum_{i=1}^{3} a_j^i \int_{k^i+30}^{1300} N(k) \langle d\Omega'/d\Omega \rangle^i \, dk$
1	$(2.97 \pm 0.24) \times 10^{12}$
2	$(1.23 \pm 0.08) \times 10^{12}$
3	$(0.87 \pm 0.08) \times 10^{12}$

Insertion of these numbers and $N_\Lambda = 39 \pm 14$ into equation VII-3 yields the following values for the cross sections:

Assumption Set Number	$(d\sigma/d\Omega')_s$ * $(cm^2/ster.)$
1	$(0.36 \pm 0.19) \times 10^{-30}$
2	$(0.87 \pm 0.45) \times 10^{-30}$
3	$(1.23 \pm 0.64) \times 10^{-30}$

*Small error approximations were used to obtain the overall error. This procedure was justified because 22% was the largest single error in quantities whose reciprocal was taken.

Figure 33

Energy Dependence of CM Angles and Solid Angle Transformations

a. The CM angles, and

b. the solid angle transformations

which correspond to 11 degrees in the laboratory for photoproduction processes I-2 (labeled Λ^{o}), I-4 and I-6 (labeled Σ) are plotted as functions of the photon energy.

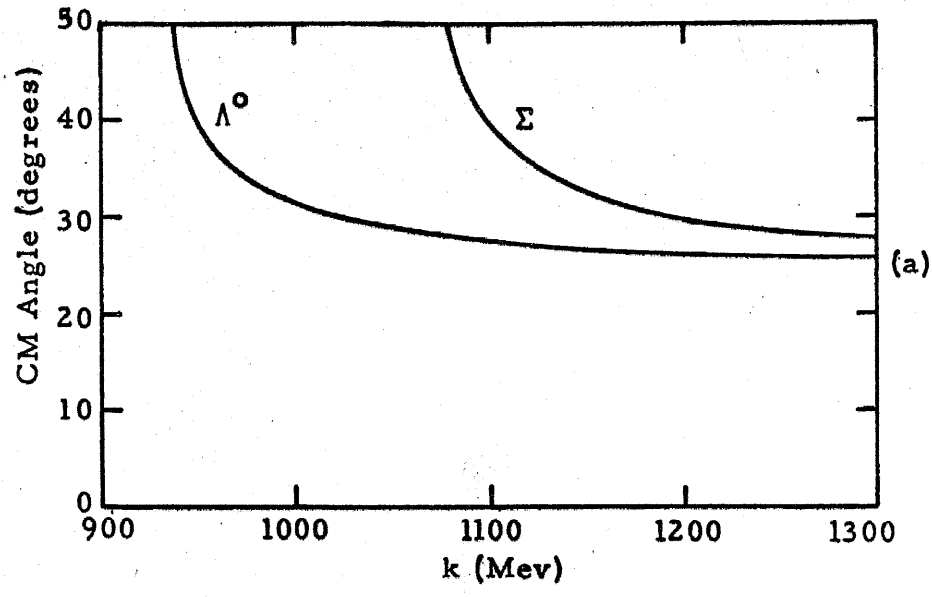
CM Angle (degrees)
50
40
30
20
10
0
900
1000
1100
1200
1300
k (Mev)
Λ°
Σ
(a)

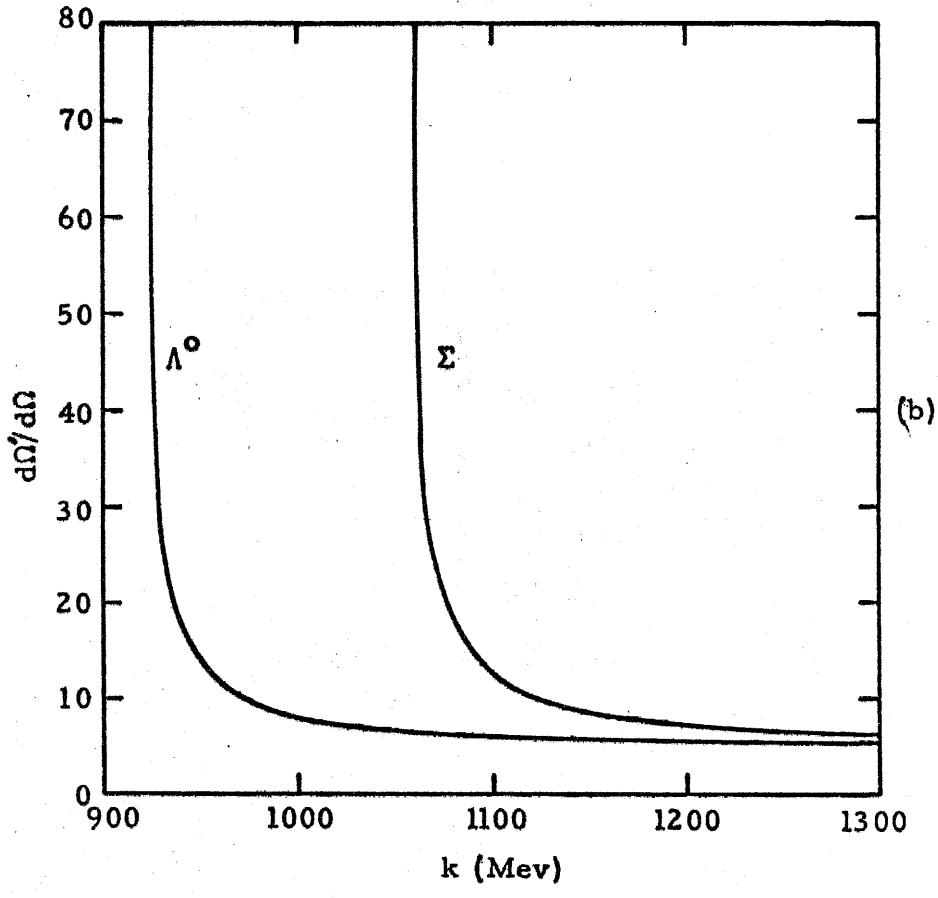
dΩ'/dΩ
80
70
60
50
40
30
20
10
0
900
1000
1100
1200
1300
k (Mev)
Λ°
Σ
(b)

Figure 33

A final note may be made on a lower limit for the cross sections using the $8 \pm 1 \Lambda^o$ decays which were associated with stars and were therefore more clearly separated from the background than the other Λ^o decays. Since these eight events constitute about one fifth of the total N_Λ, it is quite certain that the cross sections are larger than one fifth of those listed above.

B. FROM K_1^o DECAYS DETECTED

Equation VII-3 may be used to relate the cross sections to the number of K_1^o decays detected if $\int \overline{\eta}\, d\Omega$ is computed for K_1^o rather than Λ^o decays. The result of a rough estimate made in Appendix IX is

$$\left[\int \overline{\eta}\, d\Omega\right]^{-1}_{K_1^o} = (2^{+8}_{-1}) \times 10^4/\text{ster.}$$

Using this number, the data which is the same for the Λ^o and the K_1^o cases, and the lower and upper limits on the number of K_1^o decays (4 ± 2 and 17 ± 4), one obtains for assumption set No. 1:

$$(d\sigma/d\Omega')_s = (0.06^{+0.24}_{-0.04}) \times 10^{-30} \text{ cm}^2/\text{ster. for } N_{K_1^o} = 4$$

$$= (0.26^{+1.04}_{-0.16}) \times 10^{-30} \text{ cm}^2/\text{ster. for } N_{K_1^o} = 17$$

Only two statements may safely be made concerning the K_1^o decays: (a) they add evidence to the proof that K^o mesons are photoproduced, and (b) the number observed does not disagree with the cross section calculated from the Λ^o decays.

VIII. CONCLUSIONS AND SUGGESTIONS

A. K^o EXPERIMENT

This experiment has demonstrated conclusively that K^o mesons are photoproduced, and a rough estimate of the differential cross section has been obtained through use of the Λ^o decay signature. Although the observations on K_1^o-regeneration were not in disagreement with this estimate, large measurement errors prohibited effective use of this signature.

The detection technique employed has several serious drawbacks which limit its projected usefulness for further experiments:

1) An enormous amount of work is required per K_2^o detected. This is partly due to the fact that the measurement errors for true Λ^o decays tend to be large, and therefore a large number of pseudo events must be measured in order to establish the background level beneath the broad Λ^o peak. Thus, cross section measurements with good statistics are impractical.

2) Large errors are associated with the estimations of K_2^o losses,* the efficiency for conversion of K_2^o mesons into Λ^o hyperons,* and the efficiency for Λ^o detection. For the experiment performed these three errors and the statistical error all fell within a factor of two of each other. There is little point in

---

* Errors in these two factors tend to partially cancel. E.g., if the fraction of K_2^o mesons which are absorbed is underestimated, the fraction that are converted to Λ^o hyperons is quite likely also underestimated. Therefore, although fewer K_2^o mesons pass through the freon chamber, a larger fraction of those that do are converted to Λ^o hyperons.

exerting much effort towards reducing one error without also reducing the other three. Reducing all four errors is, indeed, a formidable task.

3) The energy of the K_2^o mesons cannot be determined to any reasonable accuracy. For this reason, subtraction experiments would have to be performed in order to measure the excitation function for a cross section.

Nevertheless, if no better method for studying the reactions involving K^o mesons is devised, it might be worthwhile pursuing this technique further. Under these circumstances one or more of the following suggested alterations in the analysis procedure probably would be advisable:

1) Use only the events which fall within a fixed fiducial volume located at the center of the "useful" volume. By this means the accuracy of the K_2^o conversion and Λ^o detection factors could be improved. Also, fewer events would be analyzed and then discarded. The disadvantage would be that the number of pictures per event would be increased.

2) Place a low energy cutoff on the events accepted. Since true Λ^o hyperons tend to be energetic, a sizeable fraction of the background could be eliminated in this way. Of course, the efficiencies would have to be corrected for the true events lost.

3) Analyze only the events associated with stars. Although a large fraction of the true Λ^o decays would be discarded, a much larger fraction of the background events would be rejected in

scanning, and nearly all the remaining background events would be eliminated in the analysis. Unfortunately, many more pictures would have to be taken and a correction would have to be made for the number of true events lost.

B. BUBBLE CHAMBER OPERATION

It has been shown that the thermodynamic conditions of the bubble chamber are well stabilized over long periods of time. For this reason gap length measurements can be used, without calibration in each picture, to measure particle velocities. Because of limited statistics, measurements of velocities above 0.85 c (125 Mev pion) are of little use. (A rule of thumb for pions is that gap counting doubles the effective size of the bubble chamber.) Finally, it is of great practical importance that a particle can be identified by the inspection of (1) its gap-length distribution, and (2) its multiple scattering in CF_3Br.

APPENDIX I

PROPERTIES OF NEUTRAL K MESONS

Though probably not rigorously true,[47,48] the description given by Gell-Mann and Pais[49] of the relationships between the four neutral K mesons is sufficiently correct[47,48,50] for the purposes of this experiment. These relationships and some of the properties[51] of the neutral K mesons are summarized below:

Mass = (497.8 ± 0.6) Mev

Modes for Strong Interactions		Modes for Weak Decay	
Particle	Strangeness	Particle	Mean Life (sec.)
K^o	+1	K_1^o	$(1.00 \pm 0.038) \times 10^{-10}$
$\overline{K^o}$	-1	K_2^o	$6.1(+1.6/-1.1) \times 10^{-8}$

Relationships:

$$|K^o\rangle = (|K_1^o\rangle + |K_2^o\rangle)/\sqrt{2} \qquad |K_1^o\rangle = (|K^o\rangle + |\overline{K^o}\rangle)/\sqrt{2}$$

$$|\overline{K^o}\rangle = (|K_1^o\rangle - |K_2^o\rangle)/\sqrt{2} \qquad |K_2^o\rangle = (|K^o\rangle - |\overline{K^o}\rangle)/\sqrt{2}$$

Consequences:

a) K^o mesons produced in a strong interactions decay: 50% as K_1^o mesons and 50% as K_2^o mesons.

b) A K_2^o meson interacting strongly in matter behaves as if its wave function were 50% $|K^o\rangle$ and 50% $|\overline{K^o}\rangle$ (with a certain phase relationship).

APPENDIX II

BUBBLE CHAMBER INSTRUMENTATION

A. TEMPERATURE CONTROL

Since the operating temperature of a bubble chamber containing CF_3Br is about $30^{\circ}C$, a refrigerator as well as heaters must be incorporated into the thermal control system. Accurate regulation for this chamber has been achieved by continuously circulating the support liquid through external cooling and heating heat-exchangers. The fluid is drawn out of the bottom of the support tank, passes in succession through a circulating pump, cooling heat-exchanger, filter, and heating heat-exchanger, and finally is returned to the top of the support tank. The pump, a Chempump Model E-1-S, has a special case to withstand high pressure, develops approximately 14 psi at the pumping speed employed, and consumes about 400 watts of power. This pump and the illuminating flash tubes (200 joules per flash) are the two most important heat sources in the system.

The cooling heat-exchanger consists of 25 feet of 1/2 inch copper tubing coiled into a five-gallon stirred thermal bath of Dowgard fluid. An American Instrument Company thermal switch in the bath operates a solenoid valve controlling the flow of refrigerant to a cooling coil also immersed in the bath. The temperature of the bath is monitored by a standard mercury thermometer. Under running conditions, the bath temperature is maintained at $(12 \pm 1)^{\circ}C$.

Most of the pressure drop (approximately 12 out of 14 psi) in the circulating system occurs across the filter which thus limits

the flow rate to about a quart a minute. It was necessary to continuously filter the support liquid in order to insure that it remain clear. As previously reported, a Millipore filter of 0.45-μ pore size was used.

The heating heat-exchanger* is composed of a 40-foot, 1/2-inch-copper-tubing coil suspended in air inside a thermally insulated bucket which is lined with aluminum foil. The coil is coated with carbon black and is heated by a radiant heater located on its axis. The power to the heater is supplied by a thermistor-controlled thyratron power supply. The control thermistor is in thermal contact with the point in the tangent beam tube closest to the inner chamber (see Fig. 6). A change of 0.03°C at this point produces a completely-off to full-on change in the power delivered to the heater.

The temperature of the chamber can be monitored with a mercury thermometer which makes thermal contact in the tangent beam tube at the same location as the thermistor (see Fig. 6). This thermometer, which has 0.1°C divisions, is easily read in place by means of a special mirror arrangement. Furthermore, the temperatures at various places are continuously monitored by thermocouples whose outputs are registered on a Wheelco recording potentiometer. (See reference 33 for a more complete description of this thermocouple system.)

---

*The final model of the heating heat-exchanger is described herein. This model was installed about 2/5 of the way through the K° run. The earlier model required constant attention, but nevertheless held the chamber temperature to a reasonable accuracy.

The low heat capacity of the heating heat-exchanger, and the fact that cool liquid inserted at the top of the support tank falls rapidly to the region of the inner chamber, combine to reduce the thermal oscillations of the system. The oscillations are so tiny that they are difficult to observe. The peak-to-peak temperature change is less than $0.1^{\circ}C$. The oscillations are definitely asymmetric with the cooling phase lasting 5 to 10 minutes and the heating phase lasting anywhere from 20 to 60 minutes depending on the exact adjustment of the controls. Good evidence for the stability of the temperature over long periods of time is found in the r.m.s. fluctuation from the mean of some 110 temperature readings of the thermometer described above. These readings were taken at more or less regular intervals throughout 75 hours of running time spread over a period of 36 days. The measurements are summarized below:

	Early Model Heat Exchanger	Final Model Heat Exchanger	Whole Run
Number of readings	52	58	110
Mean temperature	$29.87^{\circ}C$	$29.94^{\circ}C$	$29.91^{\circ}C$
RMS from mean	$0.089^{\circ}C$	$0.057^{\circ}C$	$0.081^{\circ}C$

If the thermodynamic losses per cycle in the freon chamber are small--all available data indicate that they are small--then the temperature in the freon should fluctuate even less than this outside temperature.

B. PRESSURE CONTROL

1. General Considerations. At a fixed temperature the expanded pressure of this bubble chamber is determined by two initial pressures: (a) the pressure to which the liquid system inside the expansion valves is pumped between expansions (the pressure in this region is called the support pressure), (b) the gas pressure in the bias cylinders prior to expansion. Let P_E, P_{SI} and P_{BI} be the expanded, initial support and initial bias pressures respectively, and let Δ signify a change in these pressures. For constant P_{SI} the ratio $\Delta P_E/\Delta P_{BI}$ has been measured over a range extending 20 psi above and below the operating expanded pressure of 150 psi. It was found to be constant throughout this range:

$$(\Delta P_E/\Delta P_{BI})_{P_{SI}} = 1.3 \qquad \text{(AII-1)}$$

where the subscript outside the parenthesis indicates the pressure which was held constant. Under the reasonable assumption that only relative pressures are important in determining the local dependence of P_E on P_{BI} and P_{SI}, it can be shown that

$$(\Delta P_E/\Delta P_{SI})_{P_{BI}} = 1 - (\Delta P_E/\Delta P_{BI})_{P_{SI}} = -0.3 \qquad \text{(AII-2)}$$

The problem of holding P_E as constant as possible thus reduces to holding P_{BI} and P_{SI} constant to the extents indicated by equations AII-1 and AII-2. Since the overall expansion system is a closed loop and since the bias cylinders have a finite volume, the task of maintaining both P_{BI} and P_{SI} constant during a short

period is accomplished by the accurate loss pump system described below.

Over a long period, other effects become significant. The most important of these is the change in P_{BI} due to variations of the room temperature. The bias cylinders are exposed to this temperature and since their volume is fixed, the effect of temperature changes is:

$$\Delta P_{BI}/P_{BI} = \Delta T/T \qquad \text{(AII-3)}$$

Noting that P_{BI} is about 225 psi, one sees that a $1^{o}C$ change in the temperature gives a 3/4 psi change in P_{BI}. This effect is easily counteracted by occasionally readjusting P_{BI}. (During the K^{o} run, P_{BI} was checked every 5 or 10 minutes and required resetting about every 30 minutes in order to hold the fluctuations in P_{BI} to less than $\pm$ 0.5 psi.)

2. Loss Pump. The present system which returns the bubble chamber pressure to its initial value after expansion by transferring oil from the bias cylinders to the high-pressure side of the expansion values is illustrated schematically in Fig. 34. The pressure in the one-quart accumulator is maintained at 500 psi* by the self-stalling pneumatic pump. A pressure transducer which monitors the support pressure automatically controls normally-closed solenoid valve 1. This valve is opened when the support pressure falls below 380 psi and closes when this pressure

*The pressures indicated in this discussion were those used during the K^{o} run.

Figure 34

Loss Pump Plumbing (Schematic)

Explanation of Symbols:

H. P. = High Pressure

L. P. = Low Pressure

H. V. = Hand Valve

Notes:

1) The direction of flow through the loss pump is indicated by an arrow.
2) "Oil pressure" is the pressure between the expansion engine diaphragms and the expansion valves. Except for the effect of the diaphragms and other minor factors, this pressure is the same as that in the freon chamber and the support tank.
3) Pneumatic pump: Model S-216C-10; Sprague Engineering Corporation.

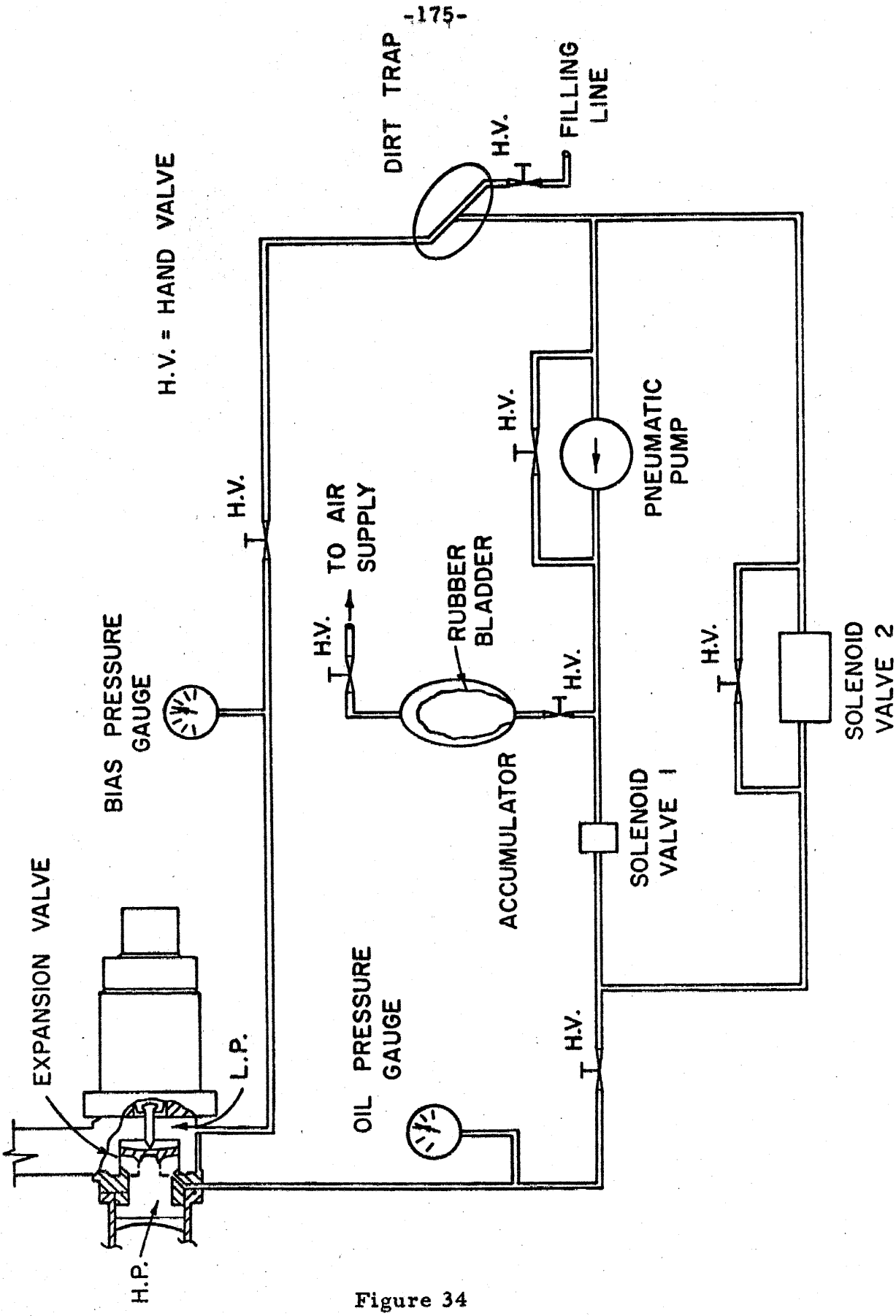
DIRT TRAP
H.V.
FILLING LINE
H.V. = HAND VALVE
H.V.
PNEUMATIC PUMP
H.V.
TO AIR SUPPLY
H.V.
RUBBER BLADDER
BIAS PRESSURE GAUGE
H.V.
H.V.
SOLENOID VALVE 2
ACCUMULATOR
SOLENOID VALVE 1
EXPANSION VALVE
L.P.
OIL PRESSURE GAUGE
H.V.
H.P.

Figure 34

reaches 400 psi. Since this solenoid valve has a small orifice, about one second is needed to deliver the required oil from the accumulator (4.7 cubic inches for a typical expansion). The final support pressure is reliably set to $\pm$ 0.5 psi. During the following 6 or 7 seconds the pump replaces the oil in the accumulator, thus returning the bias pressure to the proper value. The chamber is then ready for the next expansion.

Solenoid valve 2 serves as both a safety device and a manual control. If there is an expansion engine failure, or if the pressure between the expansion valves and the diaphragms (as indicated on a mechanical gauge equipped with an electrical contact) surpasses a predetermined value, this valve automatically opens and remains open until manually reset.

This pumping system has two admirable features: (a) P_{SI} is accurately set; and (b) there is no heating of the expansion engine oil which would indirectly heat the gas in the bias cylinders. It also has two disadvantages: (a) the total cycle requires 8 seconds; and (b) the volume of oil contained in the pump and accumulator varies from one expansion to the next. Difficulty (b) can affect the initial bias pressure through the resulting variation of oil volume in the bias cylinders. In order to minimize the variation in oil volumes the gas volume in the accumulator is kept small. This makes the ratio

$$\Delta \text{ pressure in accumulator} \; / \; \Delta \text{ volume of oil}$$

large, and therefore the uncertainty in the oil volume small. Nothing

can be done about the volume of oil contained in the pump, which depends on the final position of the piston. Any appreciable effect on the initial bias pressure, however, has been eliminated by the addition of a 5-gallon tank to the gas reservoir of the bias cylinders. The tank is connected to the bias cylinders through a 10-foot length of 3/16 inch-diameter copper tubing so that the tank is statically connected but dynamically isolated. Therefore, little change in the dynamic expansion cycle has resulted from the installation of this tank. Without the tank the initial bias pressure drifted through a range of several psi; with the tank the initial bias pressure is stable to better than 1 psi.

3. Observations. The expanded pressure, then, is expected to vary no more than 1 to 2 psi. Data from the K^{o} run supports this estimate. Sixty-three independent measurements over an extended period of time were made of the expanded pressure. The output of the control pressure transducer was photographed with a Polaroid Land oscilloscope camera, and the expanded pressure was calculated from the displayed amplitude and the known calibration of the pressure transducer. The relative accuracy of the measurements was approximately 0.5 psi. The r.m.s. fluctuation about the mean value was 1.5 psi.

Finally, there is the possibility that a systematic pressure variation of 3 to 4 psi from bottom to top of the freon chamber is created by the dynamics of the expansion cycle. The only experimental information to date on this effect comes from the study of the gap

length distribution for stopping pions, which was made during this experiment and is discussed in Appendix VII. To the statistical accuracy of the observations no effect was observed.

C. OPTICAL SYSTEM

Several features of the optical system which are directly related to the accuracy with which the measurements discussed in Chapter II can be made deserve emphasis. The procedures by which the information on the film is related to the actual tracks are described in Appendix VII.

1. Size of Bubbles. The actual bubbles are very tiny -- probably an order of magnitude smaller than their apparent size in the photographs. The image size is determined solely by the optical system. Considerable effort was expended to achieve a small, uniform-sized image for bubbles in all parts of the chamber. Tests[52] of six lens candidates showed that the Goerz Rectagon had the best resolving power for point sources under the conditions in which the lens was to be used. Calculations of expected resolution as a function of the film size indicated that for the geometry of this bubble chamber, 65 mm film would give 30 to 40% better resolution than 35 mm film.

The image size is fundamentally determined by the film's response to a fuzzy spot produced by the lens. The fuzzy spot size is the best combination of a blur from the depth of focus requirement and the diffraction pattern from the small lens aperture. The accompanying sketch schematically illustrates the light

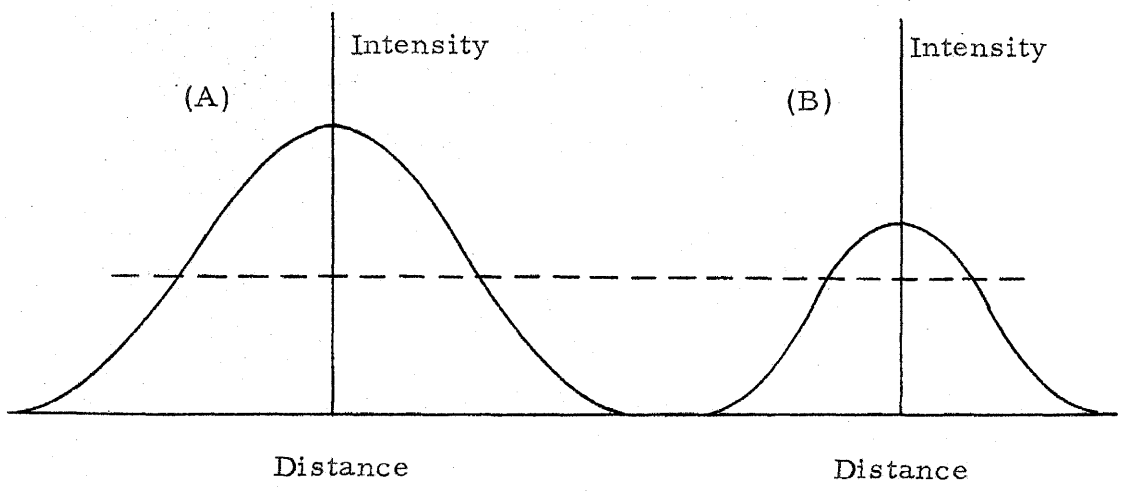

intensity as a function of the distance from the center of the spot for two bubbles of different brightness. Since the film is developed for very high contrast, there is a threshold of light intensity above which the film turns quite black and below which the film remains essentially clear. This threshold level is represented on the sketch by the dashed line. The "size" of the image is determined by the intersection of this line with the intensity contour. The brighter bubble, A, obviously produces a larger image than the dimmer bubble, B. In the design of the illumination system, a moderately successful attempt is made to create equally bright bubbles throughout the chamber. The problem is complicated because the intensity of light scattered from a bubble at small angles is a rapidly decreasing function of the scattering angle. Furthermore, nearly all bubbles are viewed at different angles by the two cameras.

Another problem is attributable to the fact that the light from a bubble traverses a considerable amount of material with high refractive index. Dispersion in this material leads to severe chromatic aberration of the bubble image. In order to reduce to a negligible level the resultant smearing of the image on the film, the light used to photograph the bubbles is limited to a band 1400 Å wide centered about 5300 Å. The orthochromatic film itself provides the cutoff on the long wavelength side and a Kodak Wratten filter (K2) provides the cutoff on the short wavelength side.

2. Geometrical Layout. The general layout of the optical system may be seen in Fig. 4. Special care was taken to align the lens axes perpendicular to the thick support-tank window. All of the geometrical distances are accurately known and fixed. In particular, the relation of the lenses to the film plane is very well defined by the precision machining of the camera and the vacuum backs which hold the film. (The lens axes are perpendicular to the film plane.) The importance of the wide stereo angle (about 30°) with regard to the accurate determination of bubble positions should be noted.

APPENDIX III

BEAM MONITORING

A. EXPERIMENTAL MEASUREMENTS ON MONITOR

A 40 MC probe integrator (see Fig. 35) was set up by Mullins. A condenser which was charged to the DC voltage of the 40 MC probe output was discharged into a current integrator each time a beam pulse was accepted. The output of this integrator indicated the total internal electron beam used. By also selecting a particular beam intensity with the 40 MC probe gate (see pp. 35-36), one could investigate the properties of the ion chamber beam monitor.

Figure 36a shows the observed saturation effect for fast beam dump when no copper was placed in front of the ion chamber. The value of the fast-to-slow ratio at zero intensity beam was greater than one, indicating that (a) a slightly larger percentage of the internal electron beam was utilized in producing the external photon beam for fast dump than for slow dump; or (b) the electrons striking the radiator were of slightly higher energy for fast dump than for slow dump (see Section C); or (c) a combination of effects (a) and (b) occurred.

When 5 inches of copper (see Chapter II, Section D2) was placed in front of the ion chamber and the same 40 MC probe window setting used as that for the 0.472 IS_{ave} point* (see Fig. 36a), the fast-to-slow ratio jumped to 0.99 ± 0.02 while IS_{ave} decreased to 0.083. Since the addition of one more inch of copper only improved

---

* This was also the range in which the K^o run was made.

Figure 35

40 MC Probe Integrator Circuit

The relays are shown in their normally closed positions. The timing sequence of the relays is indicated below the circuit drawing. A base line represents a de-energized relay, while a raised line represents an energized relay.

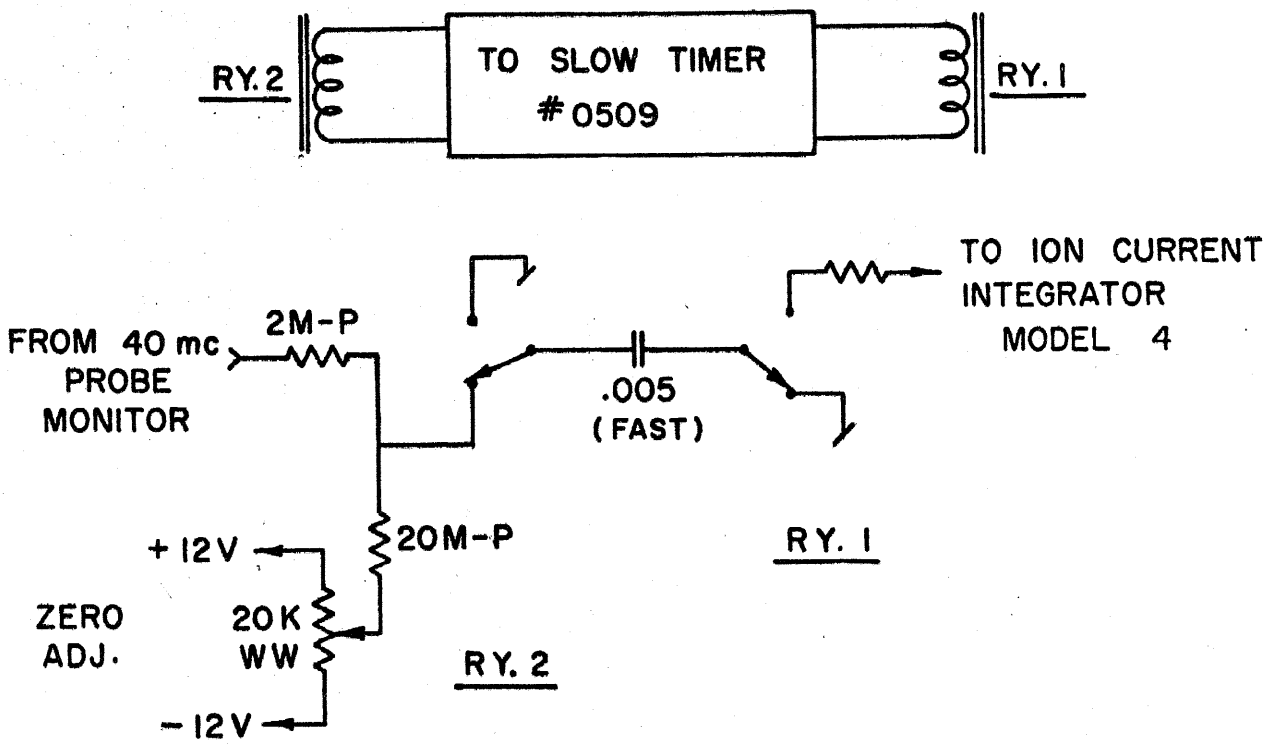

TIMING SEQUENCE

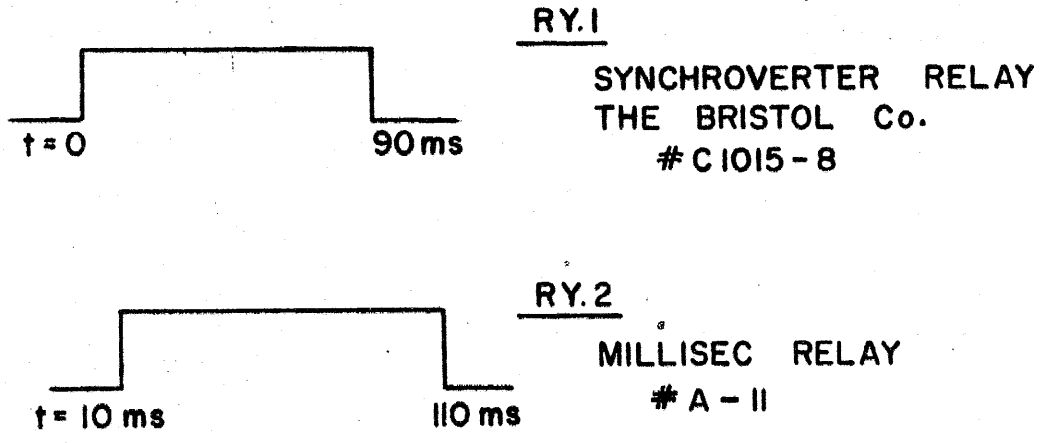

Figure 35

Figure 36

Effects of Fast Beam Dump and Beam Position
on Ion Chamber Sensitivity

a. The ratio of the ion chamber (without added copper) sensitivity for fast and slow beam dumps is plotted as a function of the average beam magnitude per pulse for slow dump. The following symbols are used:

IF (IS) = Integrated fast- (slow-) dump ion current from ion chamber

40F (40S) = Integrated 40 MC probe signal for fast- (slow-) dump run

The errors in the fast- to-slow ratio derive from the estimated error in reading the integrators, while the errors in IS_{ave} represent the width of the window setting on the 40 MC probe gate (see pp. 35-36). One "Scale 2 Bip" equals 2.15×10^{-8} coulombs.

b. The sensitivity of the ion chamber plus 5 inches of copper combination is plotted as a function of the beam position. The following symbol, not defined above, is used:

d = horizontal distance between center of beam and center of ion chamber

The circles show the measured points. The errors, which are not shown, were small.

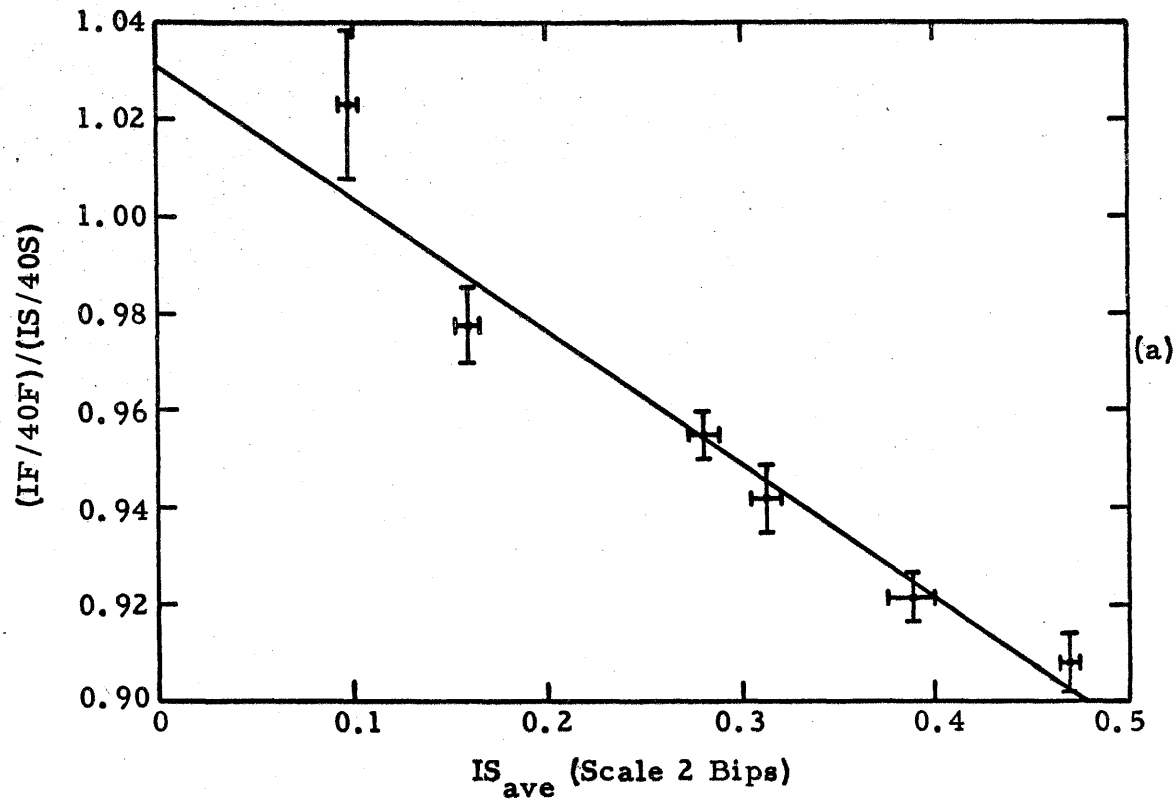
1.04
1.02
1.00
0.98
0.96
0.94
0.92
0.90
(IF/40F)/(IS/40S)
0
0.1
0.2
0.3
0.4
0.5
IS ave (Scale 2 Bips)
(a)

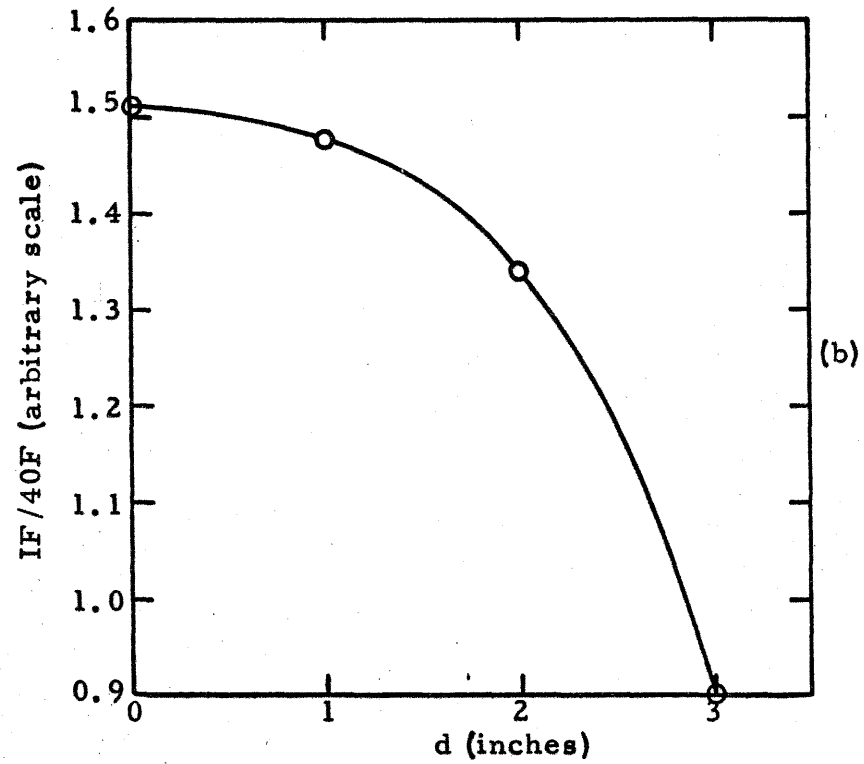
1.6
1.5
1.4
1.3
1.2
1.1
1.0
0.9
IF/40F (arbitrary scale)
0
1
2
3
d (inches)
(b)

Figure 36

the fast-to-slow ratio slightly but decreased IS_{ave} to 0.042, 5 inches of copper was selected as a good compromise between reducing the saturation effect and producing enough ions to integrate easily. In terms of the beam intensities accepted during the K^o run, the saturation ranged from $2\frac{1}{2}\%$ to $5\frac{1}{2}\%$. The median value (4%) is, then, a good approximation to the average saturation.

The sensitivity of the ion chamber (with 5 inches of copper) as a function of the position of the beam is shown in Fig. 36b. The chamber was carefully centered on the beam line during the K^o run.

The ratio of the ion chamber sensitivity with and without 5 inches of copper at 1300 Mev beam energy for slow beam dump was 0.175 ± 0.002 at the start of the K^o run and 0.167 ± 0.001 at the end. The reason for the discrepancy is not understood. The value 0.171 ± 0.005 will be used for further calculations.

A rough check of the dependence of the with-to-without-copper ratio on the beam energy was made. A + 10 Mev change in the beam energy at 1300 Mev produced a + 0.5% change in the ratio.

B. ATTENUATION IN C TARGET

The attenuation of the 1300 mev bremsstrahlung beam by the carbon target was measured experimentally with the ion chamber plus 5 inches of copper monitor and the 40 MC probe integrator. The ratio with-to-without carbon target was found to be 0.885 ± 0.005. The exponentially-weighted average beam passing through the target was then 1.063 ± 0.003 times the beam detected by the beam monitor.

C. BREMSSTRAHLUNG SPECTRUM – EFFECT OF BEAM HARDENER

Lithium hydride has a higher interaction cross section for low-energy photons than for high-energy ones and can therefore be used to "harden" a bremsstrahlung beam[53,54]. The purpose of hardening the beam was to reduce the obscuring background originating from the carbon target (see Chapter III, Section B2). One section* of the lithium hydride beam hardener built by T.-H. Chang was used.

The effect the beam hardener had on the bremsstrahlung spectrum may be calculated under the assumption that all photon interactions in the lithium hydride were catastropic (i.e., that the probability of a photon being removed from the beam was given by the total cross section). The calculations of Mullins have been applied to the unhardened bremsstrahlung spectrum as measured by Boyden[55]. Figure 37 presents both the unhardened spectrum (normalized) and the computed hardened one. The integral attenuation (i.e., the ratio of the integrals of the two spectra) is 0.73. Except at very low energies the shape of spectrum is essentially unaltered. (If the hardened and unhardened spectra are "fitted" at high energies, the difference between the integrals of the spectra is only one per cent.) Therefore, the sensitivity of the beam monitor need not be corrected for the change in shape of the spectrum. Furthermore, since both the carbon target and the beam monitor

*One section contains 37.7 gm/cm^2 of LiH.

Figure 37

Bremsstrahlung Spectrum $B(k, E_o)$

The function $B(k, E_o)$ of equation II-1 with E_o = 1300 Mev is plotted for the unhardened and hardened beams. The unhardened spectrum is shown normalized, while the hardened spectrum is shown unnormalized in order to illustrate the attenuation which one section of the lithium-hydride beam hardener imposes on the normalized, unhardened spectrum. Further discussion may be found in the text.

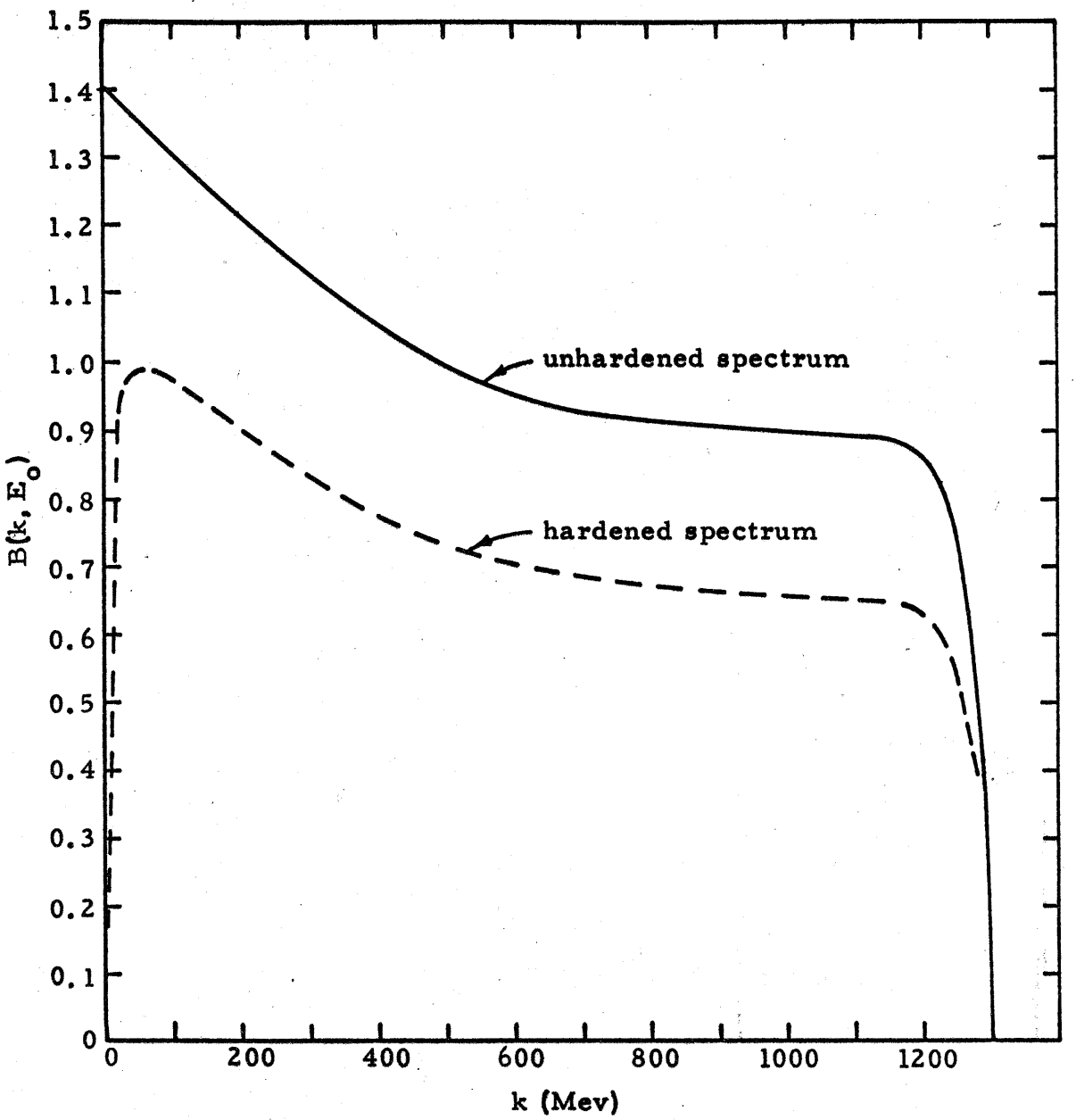
1.5
1.4
1.3
1.2
1.1
1.0
0.9
0.8
0.7
0.6
0.5
0.4
0.3
0.2
0.1
0
B(k, E_o)
unhardened spectrum
hardened spectrum
0
200
400
600
800
1000
1200
k (Mev)

Figure 37

were exposed to the hardened beam, no correction need be made for the overall attenuation of the beam.

An important error in the bremsstrahlung spectrum is that due to uncertainty in the end point of the spectrum. In the south beam this uncertainty is believed to be about $1\frac{1}{2}$ per cent[56]. One must assume that the uncertainty in the north beam may be slightly larger than this. The important points related to this are: (1) No absolute beam calibrations have been carried out in the north beam. (2) The end point energy depends on the relative position between the radiator and the equilibrium orbit*. The relative positions undoubtedly differ in the north and south beams. (3) Slow and fast beam dumping may proceed through different mechanisms so that even if the south and north radiators were in the same relative positions with respect to the equilibrium orbit, the energies of the electrons striking the radiators might differ. For instance, slow beam dump may entail large oscillations in the beam while fast dump may not. The uncertainty in the north beam end point energy, then, is believed to be on the order of 2 per cent (26 Mev for this experiment).

Boyden estimates the error in the gross shape (i.e., the relative heights of the low and high energy ends) of the unhardened spectrum to be about 4 per cent. The error in computing the relative shapes of the hardened and unhardened spectra is small for

---

* A 1" change in relative position is roughly equivalent to a 1/4 per cent change in the end point energy.

two reasons: (a) the total γ-ray cross section in LiH is nearly constant over most of the energy range involved; and (b) the attenuation of the beam is small.

The validity of the assumption that all γ-ray interactions in the LiH were catastrophic may be questioned. Two possible difficulties should be considered: (1) cascade and scattering effects in the LiH could have distorted the spectrum of the beam reaching the beam monitor; and (2) cascade photons of sufficient energy to produce strange particles ($k > 900$ Mev) may have passed through the carbon target without reaching the beam monitor. The magnitudes of these processes were determined by the solid angles subtended at the lithium hydride by the beam scrapers. The solid angle available for process (1) was 6×10^{-5} steradian and for process (2) was 2×10^{-4} steradian. To illustrate how tiny the effect of process (1) was, consider an absurd case. Suppose all the absorbed photon energy had been re-radiated uniformly over the forward half sphere in the interval 50 to 100 Mev. The spectrum of the beam reaching the ion chamber would have been distorted by only 0.01 per cent. The effect of process (2) was also well below 1 per cent. (Process (2) involved the product of two unlikely events: first, that a pair was produced with one particle having energy greater than 900 Mev; and second, that this high energy particle re-radiated a photon having energy greater than 900 Mev.)

D. EARLY BEAM DUMP

At the time the K^{o} run was made, there was some difficulty supplying enough RF power to the electron beam with the consequence that there was a certain amount of early beam dump. The resulting premature photon beam was integrated by the beam monitor, but was not used experimentally since the bubble chamber was not sensitive at the time it passed through the target.

A scintillation counter* placed a foot or so from the carbon target** was used to observe quantitatively the fraction of early beam dump. The current from the photomultiplier was integrated on one of the ion current integrators during the beam dump period. The rest of the time, in order to avoid integrating the dark current, the anode was disconnected from the integrator and connected to ground through a limiting resistor. Since the 1 ms time constant of the integrator was short compared to the early beam dump duration (10 to 20 ms), the integrator output voltage at the time of fast beam dump was a measure of the total amount of early beam dump. The measurements were made on oscilloscope photographs as illustrated in Fig. 38. The fraction of early beam dump was found to vary from 0 to 0.13 depending on the RF tuning, but was quite constant over a period of hours. The total early beam dump for the whole run was estimated to be 3.6% of the total beam

---

* The author is indebted to R. Gomez for supplying this counter.

** The angle between the vector from target to counter and the photon beam direction was about 135^{o}.

Figure 38

Early Beam Dump Monitor Oscilloscope Traces

Both traces display the output voltage of the ion current integrator as a function of time. (Trace 2 is inverted.)

Sweep speed = 20 ms/cm*

Vertical gains:

Trace 1 = 200 mv/cm*

Trace 2 = 50 mv/cm*

The dark current is responsible for the initial slopes in the traces, and the early beam dump causes the steeper slopes within 30 ms of the fast beam dump, which occurs at the step in Trace 1 and the place Trace 2 goes off scale. The fraction of early beam dump, EBD, is:

$$EBD = \frac{b}{a} \times \frac{50}{200}$$

$$= 0.093 \text{ for example shown.}$$

* Grid on oscilloscope has 1 cm x 1 cm squares.

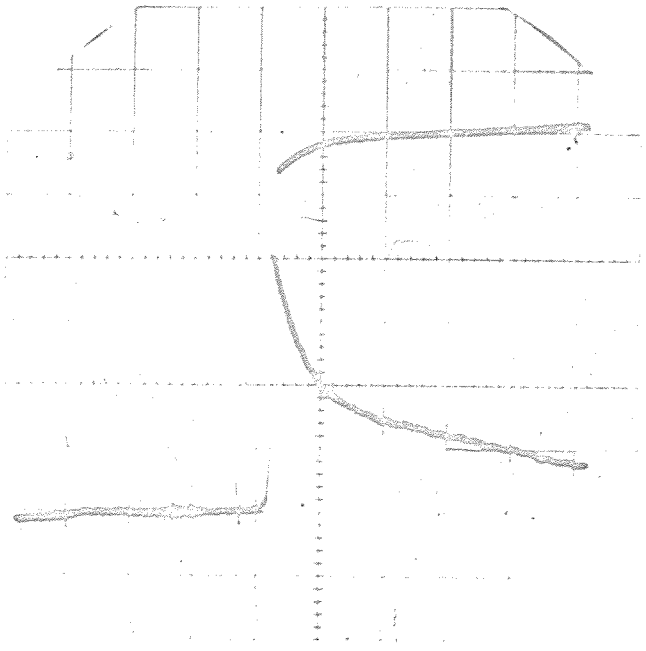

TIME

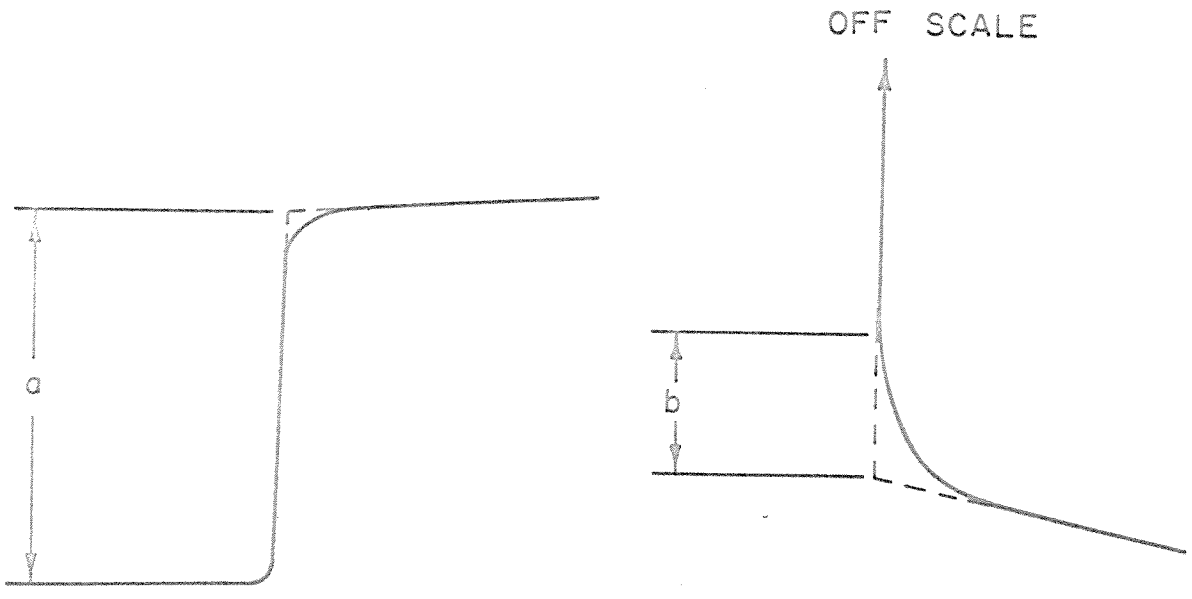

TRACE 1

TRACE 2

FIGURE 38

recorded.

E. SUMMARY – NET CALIBRATION OF BEAM MONITOR

The ion chamber* calibration for slow beam dump and "undistorted" bremsstrahlung spectrum has been carried out by R. Gomez. At STP and for $E_o = 1300$ Mev,

$$U = (5.50 \pm 0.16) \times 10^{18} \text{ Mev/coulomb.}$$

The effects discussed in this appendix may be summarized in terms of a series of factors whose product time U gives the calibration of the beam monitoring system for this experiment. The factors are:

1) Attenuation from 5 inches of copper:

$$f_1 = 5.72 \pm 0.06$$

2) Ion chamber saturation:

$$f_2 = 1.04 \pm 0.01$$

3) Loss in carbon target:

$$f_3 = 1.06 \pm 0.003$$

4) Effect of lithium hydride:

$$f_4 = 1.00 \pm 0.01$$

5) Extra beam integrated because of early beam dump:

$$f_5 = 0.96 \pm 0.004$$

6) Temperature and pressure corrected to STP:

$$f_6 = 1.17 \pm 0.006$$

If U' is the calibration for this experiment, then

---

* The 1" Cu-Air Chamber with Hole was used.

$$U' = f_1 f_2 f_3 f_4 f_5 f_6 U = (3.90 \pm 0.14) \times 10^{19} \text{ Mev/coulomb.}$$

U', $B(k, E_o)$, E_o, and the amount of integrated charge from the ion chamber, which was measured with relatively high accuracy, determined the features of the beam used. The number of photons per Mev in the energy range of interest is shown in Fig. 7. Also shown in this figure is the number of photons per Mev for $E_o' = E_o + 28$ Mev. (28 Mev was the uncertainty in the end point of the spectrum if the uncertainty of the beam calibration was 26 Mev and the error in setting up the beam controls was 10 Mev.) The difference between the two curves, expressed in terms of the number of photons above threshold for Λ^o (Σ) production, is 4 per cent (8 per cent).

APPENDIX IV

K_2^o CROSS SECTIONS IN FREON

A. OPTICAL MODEL FORMULAE

Since the optical model of Fernback, Serber and Taylor[57] is used several places in this and a later appendix, the formulae derived from the model are assembled here in one section. This model treats the particle wave function outside and inside the nucleus as a plane wave, assumes the nuclear surface effects are small, and ignores refraction at the nuclear surface.

The total nuclear absorption cross section, σ_a, is related to the average total nucleon cross section, σ, through a nuclear absorption coefficient, K:

$$\sigma_a = \pi R^2 \left\{ 1 - \frac{[1-(1+2KR)e^{-2KR}]}{2K^2R^2} \right\} \qquad \text{(AIV-1)}$$

where R is the nuclear radius, and

$$K = 3A\sigma/4\pi R^3 \qquad \text{(AIV-2)}$$

where A is the atomic number of the nucleus.

The nuclear-diffraction-scattered wave amplitude, $f(\theta)$, at angle θ to the incident direction is calculated from K, the propagation vector outside the nucleus, k, and the propagation vector inside the nucleus, $k + k_1$:

$$f(\theta) = k \int_o^R [1-\exp(-K+2ik_1)s]\ J_o(q\rho)\rho d\rho \qquad \text{(AIV-3)}$$

where $s \equiv (R^2-\rho^2)^{\frac{1}{2}}$ and $q \equiv k \sin\theta$. J_o is the 0^{th} Bessel function of the first kind. For K mesons k and k_1 may be obtained from the plane wave solution of the Klein-Gordon equation:

$$\nabla^2\psi + \frac{(E-V)^2}{\hbar^2c^2}\psi - \frac{m^2c^4}{\hbar^2c^2}\psi \equiv 0$$

where the K meson-nuclear potential, V, is included as the fourth component of a 4-vector. The solutions are:

$$k \equiv \frac{1}{\hbar c}(E^2 - m^2c^4)^{\frac{1}{2}} \qquad \text{(AIV-4)}$$

and to a good approximation if $V << (E - mc^2)$,

$$k_1 \cong -\frac{EV}{\hbar c\,(E^2 - m^2c^4)^{\frac{1}{2}}} \qquad \text{(AIV-5)}$$

The assumptions made in the derivations of equations AIV-1 and AIV-3 are: $kR >> 1$; $|k_1/k| << 1$; and $K/k << 1$. For the K_2^o meson energies possible in this experiment and for the nuclei to which the model is applied below, these inequalities are reasonably satisfied. (In the worst case, four must be considered much greater than one.)

In all of the calculations R has been taken to be:

$$R \equiv 1.3 \times 10^{-13}\, A^{1/3}\ \text{cm}. \qquad \text{(AIV-6)}$$

B. K_1^o REGENERATION

1. General. The possibility of observing K_1^o mesons regenerated from a K_2^o meson beam passing through matter was first proposed by Pais and Piccioni[58]. Although regeneration through each

of the reactions I-19, I-20 and I-21 has been observed[25-29], the experimental data is very limited. Therefore, the estimations made below are only crude approximations to the regeneration cross sections in CF_3Br.

2. Regeneration from Individual Nucleons. The only experimental information on this channel comes from an exposure of the Adair hydrogen bubble chamber to a K_2^o beam. The energy distribution of the incident K_2^o mesons is adequately described as a Gaussian distribution centered at 600 Mev with a half-width of 90 Mev[28]. The preliminary result for the total regeneration cross section is 3.9 mb[29]. This cross section can be used in conjunction with the optical model relationships to estimate the corresponding cross section in freon. Three assumptions are made:

a) The total regeneration cross section from neutrons is also 3.9 mb.

b) The K_2^o wave passing through the nucleus remains a K_2^o wave at every point.

c) No second order process need be considered.

Under assumptions (b) and (c) one would expect that:

$$\left[\frac{\sigma(K_2^o \rightarrow K_1^o)}{\sigma\,(\text{total})}\right]_{\text{nucleus}} = \left[\frac{\sigma(K_2^o \rightarrow K_1^o)}{\sigma\,(\text{total})}\right]_{\text{nucleon}} \qquad \text{(AIV-7)}$$

where the nucleon cross sections are averages over protons and neutrons in the nucleus. (To the accuracy of the estimate one may

assume equal numbers of protons and neutrons.) The average total nucleon cross section may be calculated from the charged K-meson cross sections (see equivalences I-22 through I-25). Experimental measurements of the latter[44,59] indicate that 27 mb is a reasonable value for the total K_2^o-nucleon cross section in the energy interval 200 to 600 Mev. Using this value, the measured cross section for K_1^o regeneration from protons, assumption (a), and equations AIV-1, AIV-2 and AIV-7, one obtains for the total cross section from a molecule of CF_3Br:

$$\sigma \approx (K_2^o \rightarrow K_1^o)_{\text{molecule}} \approx (240 \pm 200) \text{ mb}$$

where the error represents a guess by the author.

3. Regeneration from Whole Nuclei. The experimental data on this channel is from the work of Muller, et al.[25-27] in which the cross section for regeneration from iron nuclei was found to be 15 mb. (The energy of the incident K_2^o meson beam was 340 Mev.) Under the assumption that the dependence of this cross section on nuclear size is adequately described by an $A^{2/3}$ rule, one computes that the total cross section for the regeneration of K_1^o mesons by diffraction scattering from all the nuclei in a molecule of CF_3Br is (50 ± 30) mb. Again the error represents a guess by the author.

4. Regeneration from Whole Liquid. The observations of Muller, et al. imply that in CF_3Br the total cross section for this channel is considerably less than the total cross sections for the

other two channels.

C. Λ^o PRODUCTION

1. General. Λ^o hyperons may be produced directly, e.g., reactions I-13 and I-16; indirectly through Σ^o hyperon production, e.g., reactions I-14 and I-17; or indirectly through capture reactions within the nucleus, e.g., reactions I-15 and I-18 followed by the capture processes:

$$\Sigma^- + p \rightarrow \Lambda^o + n$$

$$\Sigma^+ + n \rightarrow \Lambda^o + p$$

The Λ^o production rate of interest is the sum of all direct and indirect processes.

Although several experiments to study the interactions of K_2^o mesons with complex nuclei in xenon and propane bubble chambers are in progress, the present data[24, 31, 30] on Λ^o hyperon production is extremely fragmentary and of no practical use. Therefore, the cross section for Λ^o production by K_2^o interactions in freon must be estimated from available data on K^- interactions in emulsion and kaon-nucleon cross sections. The approximation will be made of treating the negative strangeness, $\overline{K^o}$, component of the K_2^o wave function independently from the positive strangeness, K^o, component. This is permissible since the transit time of a K_2^o meson passing through a nucleus is very much shorter than the lifetime of the K_1^o meson. Furthermore, since the regeneration of K_1^o mesons in the

bubble chamber is small, the K_2^o beam remains nearly pure across the whole chamber. The cross section for Λ^o production by K_2^o mesons is, then, one half of the cross section for Λ^o production by the hypothetical $\overline{K^o}$ mesons. The latter cross section is estimated below in several separate ways, all of which use equivalences I-24 and I-25 to relate K^- cross sections to $\overline{K^o}$ cross sections.

2. Emulsion Experiment. The first estimate utilizes the results of a nuclear emulsion experiment by Freden et al.[60]. The interaction mean free path for K^- mesons in emulsion was measured as a function of the K^- meson kinetic energy in the range 20 to 300 Mev. All interactions with emulsion nuclei, except hydrogen, were included in which there was an observable energy loss. The data described below fell between 150 and 300 Mev. The average mean free path in this range is 35 cm, while the geometric mean free path (with R given by equation AIV-6) is 28 cm. Thus the total interaction cross section is 80% of geometrical. After correction for the interactions due to inelastic K^- scattering (about 15% of the interactions) and elastic K^- scattering from light nuclei (about 2%), the total cross section for absorption of K^- mesons is found to be 66% of geometrical.

Charged Σ hyperons and hyperfragments were observed in $(21 \pm 5)\%$ and $(6 \pm 2)\%$ of the K^- absorptions. The remaining 73% of the K^- absorptions must have been cases where Λ^o hyperons were produced and escaped, hyperons were permanently trapped

in the nucleus by the nuclear and coulomb potentials, or a $\overline{K^O}$ meson was produced by charge exchange scattering.

The percentage of events which were charge exchange scatterings can be estimated. Elastic K^--nucleon charge exchange scattering occurs only on protons. The cross section in this energy range is about 5 mb[61, 62]. On the other hand, the K^--nucleon elastic scattering cross section, which is responsible for the K^--nucleus inelastic scattering, is about 20 mb* in this energy range. Therefore, charge exchange scattering from the nucleus should be about1/8 as frequent as inelastic scattering which accounted for 15% of all the interactions. Charge exchange scatterings, then, should take place in about 2% of the K^- absorptions.

The chance of a hyperon being trapped permanently in the nucleus is somewhat harder to estimate. Freden et al. state that probably 15% of the Σ hyperons produced in this energy range are trapped. A large fraction of the Λ^O hyperons produced when these trapped Σ hyperons are captured should escape from the nucleus. Since the Λ^O hyperons produced directly by K^- interactions have more energy than the corresponding Σ hyperons, a smaller percentage of these Λ^O hyperons should be trapped than of the Σ hyperons. The guess will be made that 10% of all the hyperons produced in the emulsion experiment of Freden et al. were trapped in the nucleus. (Note that this is over and above the percentage which form

* Experimental data on the K^- proton elastic scattering cross section is given in the paper of Freden et al., ref. 60. The K^--neutron elastic scattering cross section is assumed to be roughly the same.

hyperfragments.)

These two estimates lead to the conclusion that in 61% of the K^- absorptions Λ^o hyperons were produced and, therefore, that in this energy range the total cross section for Λ^o production by K^- mesons on emulsion nuclei is 40% of geometrical.

If emulsion nuclei contained equal numbers of neutrons and protons, the same cross section would hold for K^- and $\overline{K^o}$ mesons. The excess neutrons which cannot be paired with protons in emulsion nuclei (about 13% of the nucleons) have a larger total cross section, and a smaller Λ^o plus Σ^o production cross section, for $\overline{K^o}$ mesons than for K^- mesons. The effect of these excess neutrons is to reduce the $\overline{K^o}$ cross section for Λ^o production relative to the K^- cross section. However, the reduction (to 38% of geometrical*) is slight and does not warrant further discussion.

Finally, the emulsion cross section must be scaled to freon. The simplest approximation is that the cross section scales geometrically, i.e. as $A^{2/3}$. A somewhat better approximation takes into account the different transparencies of carbon, fluorine and bromine nuclei to $\overline{K^o}$ mesons. Several ways of doing this are discussed in the next section from which the following cross section ratios are taken:

Optical Model Using for $\overline{K^o}$-Nucleon Cross Section:	$\left[\frac{\sigma_C/R_C^2}{\sigma_{Br}/R_{Br}^2}\right]$	$\left[\frac{\sigma_F/R_F^2}{\sigma_{Br}/R_{Br}^2}\right]$
total	0.82	0.88
hyperon production**	0.64	0.74

*Estimated from K^--nucleon data of Kerth, ref.59, and Dahl et al., ref. 63.

** The high energy data has been used.

The resultant Λ^o production cross sections are listed below:

Scaling Approximation	σ_C (mb)	σ_F (mb)	σ_{Br} (mb)	σ_{CF_3Br} (mb)
Geometrical	108	146	375	921
Optical model using for $\overline{K}^o$-nucleon cross section:				
total	89	128	375	848
hyperon prod. ...	69	108	375	768

3. Optical Model Calculation.

a. Preliminary Remarks. The experimental information on $\overline{K}$-nucleon cross sections may be used to make an optical model calculation of the total cross section for Λ^o plus Σ^o production from complex nuclei. The best procedure would be to make a Monte Carlo type calculation in which the path of a $\overline{K}^o$ meson is traced through the nucleus. Whenever a hyperon producing reaction occurs, the $\overline{K}^o$ is absorbed, but when a scattering – elastic, inelastic or charge exchange – occurs, the negative strangeness K meson is preserved and is followed on through the nucleus. The ratio of the nucleon cross section for neutral hyperon production to that for all hyperon production could then be used to predict the direct neutral-hyperon production cross section from the nucleus. In principle the conversion

of charged to neutral hyperons could also be computed from observed nuclear-capture cross sections. The effect of nuclear trapping and hyperfragment formation could also be included. Unfortunately, this computation requires details of the K-nucleon interaction which have not yet been measured. Therefore, two simplified calculations have been made. In both, the hyperon capture, nuclear trapping and hyperfragment production processes were ignored. At the energies of interest they are minor effects and tend to cancel in the net number of Λ^o produced. The differences in the numbers of protons and neutrons in the nuclei were also ignored since the resultant effects are relatively unimportant.

b. Using Total $\overline{K^o}$-Nucleon Cross Sections. A lower limit on the nuclear Λ^o plus Σ^o production cross section was obtained by assuming that all $\overline{K^o}$-nucleon collisions within the nucleus are catastrophic. The total nuclear absorption cross section was calculated from equation AIV-1 using the absorption coefficient, K, as computed from the mean total $\overline{K^o}$-nucleon cross section. The nuclear Λ^o plus Σ^o production cross section was then found from the relation:

$$\left[\frac{\sigma(\Lambda^o + \Sigma^o)}{\sigma(\text{total})}\right]_{\text{nucleus}} = \left[\frac{\overline{\sigma}\,(\Lambda^o + \Sigma^o)}{\overline{\sigma}\,(\text{total})}\right]_{\text{nucleon}}$$

where the nucleon cross sections were averaged over proton and neutron. The following cross sections were used as reasonable approximations for $\overline{K^o}$ energies between 200 and 600 Mev.[59,63,62,29]

$\bar{\sigma}_{\text{nucleon}}$ (total) = 34 mb

$\bar{\sigma}_{\text{nucleon}}$ ($\Lambda^o + \Sigma^o$) = 10 mb

The resultant nuclear cross sections are:

Products	σ_C(mb)	σ_F(mb)	σ_{Br}(mb)	σ_{CF_3Br}(mb)
$\Lambda^o+\Sigma^o$	60	87	243	564

c. Using Hyperon Production Cross Sections Alone. In this approximation only the hyperon-producing $\overline{K^o}$-nucleon interactions were considered. The average $\overline{K^o}$ meson path length through the nucleus was assumed to be unaltered by $\overline{K^o}$-nucleon scattering. The absorption coefficient was computed from the mean hyperon-production, $\overline{K^o}$-nucleon cross section and the nuclear Λ^o plus Σ^o production cross section found from the relation:

$$\left[\frac{\sigma(\Lambda^o + \Sigma^o)}{\sigma(\text{all hyperons})}\right]_{\text{nucleus}} = \left[\frac{\bar{\sigma}(\Lambda^o + \Sigma^o)}{\bar{\sigma}(\text{all hyperons})}\right]_{\text{nucleon}}$$

where again the nucleon cross sections were averaged over proton and neutron. Separate low energy[62,63] (75-150 Mev) and high energy[62,29] (500-750 Mev) calculations were made, the relevant cross sections being:

	$\bar{\sigma}_{\text{nucleon}}$(all hyperons)	$\bar{\sigma}_{\text{nucleon}}(\Lambda^o+\Sigma^o)$
Low Energy	25 mb	14 mb
High Energy	12 mb	9 mb

This estimate gives for the nuclear, Λ^o plus Σ^o production cross sections:

	σ_C(mb)	σ_F(mb)	σ_{Br}(mb)	σ_{CF_3Br}(mb)
Low Energy	104	153	451	1013
High Energy	83	129	449	920

4. Conclusions. The conclusion may be drawn from these estimates that 450 $\pm$ 100 mb is a reasonable total cross section per molecule for Λ^o production in CF_3Br by K_2^o mesons and that the cross section is relatively independent of the K_2^o meson energy from 100 to 600 Mev.

APPENDIX V

THE SCANNER

The scanner which is described in this appendix was designed by D. E. Groom and constructed in the central engineering shop. The film transport mechanism handles 1000-foot rolls of 65 mm perforated film intact and can drive the film forward or backward either in slow drive (one frame at a time) or in fast drive (1000 feet in 3 minutes). Since both stereo views are on the same film strip a fixed distance apart, there is no registering problem between the two views, and in fact, the views are automatically centered on the scanner after each advance by means of counting sprocket holes with a mechanical cam arrangement. A pressure front system holds each projected section of film flat by blowing air between the film and a piece of optical glass mounted in a nylon frame which is pressed down on the film, which in turn rests on the horizontal flat glass top of the illuminating condenser boxes. The air pressure between the film and the glass is just high enough to lift the frame slightly and allow the air to continuously leak out, thus helping to cool the film. When the film is advanced, the nylon frames are lifted free from the film which then springs free from the backing glass. The 500-watt projection lamps are contained in air-cooled condenser boxes which utilize infrared reflecting and transmitting interference filters.

The projection lenses are Schneider Xenar, f:4.5, 210 mm focal length. The projection is done vertically, and two mirrors, whose normals are coplanar, perpendicular and each at 45^{o} to the

vertical, throw the image onto a horizontal table. The projected image ranges from 1.2 to 1.5 times the actual size in the bubble chamber. The two stereoscopic views are projected on the same region of the table and may be looked at separately or together. The relative location of the two views may be adjusted linearly in either direction, but neither view may be rotated with respect to the other. The frame number, which is recorded in one corner of each view, and write-on information, which is recorded in another corner of one view, are visible on the table. A reversible electric counter also displays the frame number.

Considerable effort was exerted to align the projection system so that the magnification over the whole of each view would be as constant and isotropic as possible. Measurements show that this was achieved to within $\pm 0.3\%$. The overall magnification from bubble chamber to scanner was adjusted to be the same for the two views to within $\pm 0.05\%$.*

*This accuracy refers to the separation in each view of two symmetrically located fiducials. The magnification of non-symmetric distances differs in the two views because of index of refraction effects.

APPENDIX VI

DERIVATION OF EXPRESSION FOR SCANNING EFFICIENCY

Though neither is rigorously true, two reasonable assumptions are made which greatly simplify the derivation:

1) Every event occurring in the bubble chamber had the same likelihood of being found.

2) The two scans were statistically independent.

It is not necessary to assume that the scanning efficiencies were the same for both scans.

Let:

N_a (N_b) = the number of events found only in the first (second) scan

N_c = the number of events found in both scans

N = the true number of events of the type corresponding to N_a, N_b and N_c

E_a (E_b) = the scanning efficiency for the first (second) scan

E_c = the scanning efficiency for the combined data of the first and second scans

The object of the derivation is to derive an expression for E_c involving only N_a, N_b and N_c.

By definition of scanning efficiency,

$$E_a = \frac{N_a + N_c}{N}$$

$$E_b = \frac{N_b + N_c}{N} \qquad \text{(AVI-1)}$$

$$E_c = \frac{N_a + N_b + N_c}{N}$$

Utilizing the first assumption, we may write:

$E_a(E_b)$ = the probability of having found any one of the N existing events during the first (second) scan

Under the second assumption,

$E_a \times E_b$ = the probability of having found any one of the N existing events during both scans,

and since $E_a \times E_b$ is a constant (first assumption)

$$N_c = N \times E_a \times E_b. \qquad \text{(AVI-2)}$$

Solving equations AVI-1 and AVI-2 for E_c, we find

$$E_c = \frac{N_c(N_a + N_b + N_c)}{(N_a + N_c)(N_b + N_c)} \qquad \text{(AVI-3)}$$

which is the desired expression.

APPENDIX VII

MEASUREMENT TECHNIQUES

A. DETERMINATION OF POINTS IN TRUE SPACE

1. Introductory Remarks. All quantities to be measured fall into one of two classes: (a) those which are calculated from the true* space coordinates of a few points; (b) those which are derived from many measurements in scanner space plus the true space coordinates of a few points. In this experiment three methods for determining the true locations of points were employed for various purposes. In order of increasing accuracy, they were:

1) uniform index of refraction approximation;
2) ray tracing by mechanical analog computer, called the Transordinator;
3) ray tracing by digital computer program.

The latter two techniques take into account the several high indices of refraction through which the photographs are taken. All three techniques assume that corresponding points are measured in the two stereoscopic views. (Corresponding points are the unique pair of points in scanner space associated with a particular point in true space.)

The uniform index approximation was used to make rough estimates of positions, ranges, etc. It gives results quickly and can be used at the scanner. The Transordinator was used to make

---

* Throughout this appendix "true" refers to quantities in the bubble chamber coordinate system and "scanner" to quantities in the projected image on the scanning table.

some preliminary measurements and to double check that the computer program was working properly. Though not quite as convenient as the uniform index approximation, the Transordinator resides in the vicinity of the scanner and yields accurate results. It is best suited to the situation in which a small number of accurate measurements need to be made on short order. The computer program was used for all the final data analysis. Because of the elaborate arrangements required, this method is most practical for large quantities of data.

Before a brief description of the theory of each method is given, it is useful to define two standard coordinate systems. The first is for true space:

$\vec{i}$ = unit vector in the direction of the line joining the two camera lenses and therefore parallel to the interfaces of different indices of refraction

$\vec{j}$ = unit vector perpendicular to $\vec{i}$ and parallel to the interfaces of different indices of refraction

$\vec{k}$ = unit vector perpendicular to interfaces of different indices of refraction.

$\vec{i}$, $\vec{j}$ and $\vec{k}$ are unit vectors in the x, y and z directions respectively.

The second is for scanner space (see Fig. 39b):

Left (right)* pivot point = point in left (right) projected view corresponding to true space axis of left

* The designations "left" and "right" have historical significance only but have been retained for lack of a better choice. The two views on the scanner are also color-coded red and blue; right and red are matched because of the common "r". The author is greatly indebted to L. R. Gallagher for suggesting the color coding technique.

(right) lens

= origin of left (right) view polar coordinates

R_L (R_R) = left (right) view radius

a_L (a_R) = left (right) view polar angle

The axis of the right lens in true space transforms into a radial line in the left view of scanner space, and vice versa. The positive directions of these radial lines are taken as the 90^o polar angles. The definitions of the sense of the angles either side of 90^o are not required for the following discussion.

Note that among the four coordinates in scanner space related to the three coordinates in true space, there must be a single redundancy. As will be seen, this redundancy is useful.

2. Uniform Index Approximation. In this simplified approximation all the light rays* from bubbles to film are considered to travel in straight lines, and explicit expressions giving x, y and z in terms of R_L, a_L, R_R, and a_R are easily derived. If the true space origin is located at the left camera lens, then:

$$x = \frac{R_L \sin a_L}{L(R_L \sin a_L + R_R \sin a_R)} = L - \frac{R_R \sin a_R}{L(R_L \sin a_L + R_R \sin a_R)} \qquad \text{(AVII-1)}$$

$$y = \frac{R_L \cos a_L}{L(R_L \sin a_L + R_R \sin a_R)} = \frac{R_R \cos a_R}{L(R_L \sin a_L + R_R \sin a_R)} \qquad \text{(AVII-2)}$$

* "Light ray" here and later refers to a ray which is undeviated by the camera lens, the so-called "undeviated ray" in geometrical optics.

$$z = \frac{S'}{L(R_L \sin a_L + R_R \sin a_R)} \qquad \text{(AVII-3)}$$

where L is the true space separation of the camera lenses and S' is the effective distance from camera lens to scanner table (see Fig. 39a).

On the scanner the two views are superimposed in the manner shown in Fig. 39b. In terms of the geometrical quantities shown in this figure:

$$D - \epsilon = R_L \sin a_L + R_R \sin a_R \qquad \text{(AVII-4)}$$

and therefore:

$$z = \frac{S'}{L\,(D-\epsilon)} \quad . \qquad \text{(AVII-5)}$$

This expression for z is exceedingly useful since D may be held constant. Equation AVII-5 implies that the z coordinate of a bubble is completely determined by the distance, ϵ, between the two projected images on the scanner.

It is clear from equation AVII-2 that in this approximation the redundancy in the scanner space coordinates is that:

$$R_L \cos a_L = R_R \cos a_R \quad . \qquad \text{(AVII-6)}$$

As may be seen from Fig. 39b, this condition means that corresponding points lie at the same distance from the 90^o line. Even in the actual case of several indices of refraction, this condition holds

Figure 39

Bubble Location – Geometry of Uniform Index Approximation

a. This sketch illustrates the three-dimensional relationship between bubble location and coordinates on the scanner. The plane of the scanning table is "perpendicular" to the paper.

b. This sketch shows the two-dimensional relationship on the scanner between corresponding bubble images. The plane of the scanning table "coincides" with the paper.

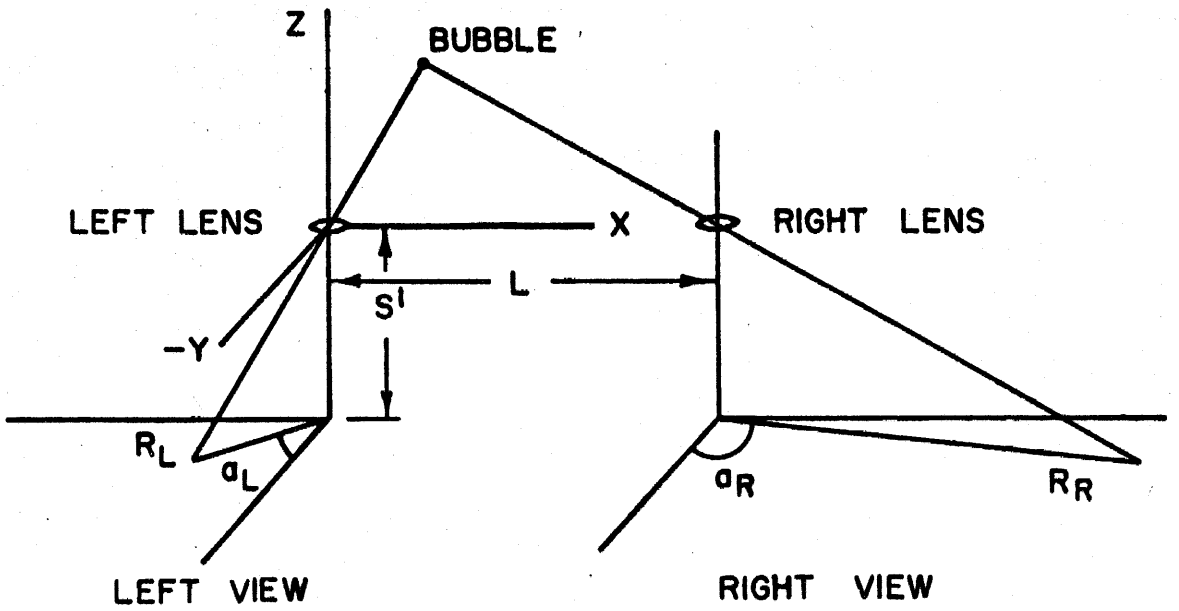

Figure 39a

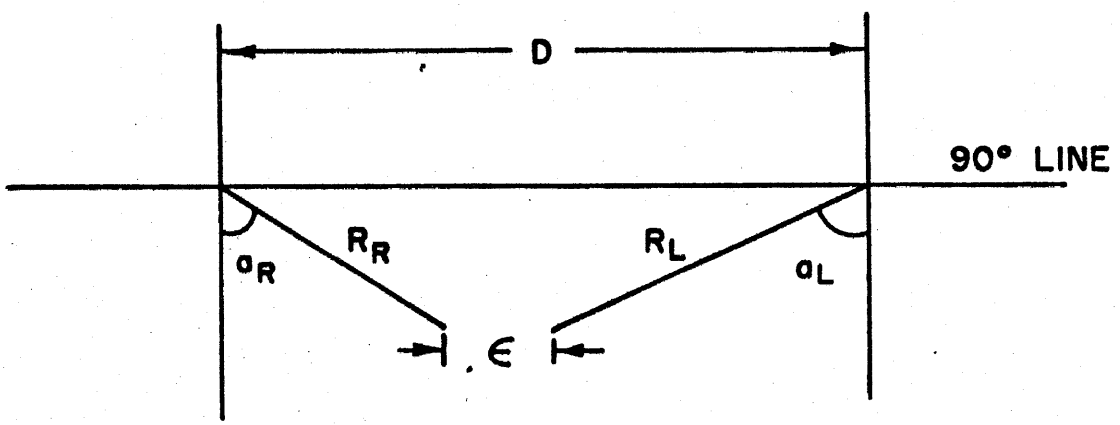

Figure 39b

approximately throughout the bubble chamber volume.* Since the small variations from AVII-6 depend systematically on the true space coordinates, a skilled person knows the relative distances from the 90^{o} line of any set of corresponding points. This knowledge greatly simplifies the task of locating corresponding points.

3. Light Ray Tracing for Real Case – General Remarks. There are eight interfaces separating media of different indices of refraction between the camera lenses and the bubbles being photographed. All interfaces are parallel to each other and perpendicular to both lens axes. Furthermore, the light rays originate in freon with an index of refraction different from that of air from which the rays enter the lenses. The rays are refracted at each interface and their final directions before entering the lenses are different from their initial directions in the bubble chamber. At each interface the incident ray, refracted ray and normal to the interface lie in a common plane and the direction of the refracted ray is given by Snell's law. Since all interfaces are parallel, an individual ray traces a zigzag path in a single plane. In general, the left-lens and right-lens rays from a particular bubble are not coplanar at the lenses.

Although expressions can be derived relating the true space coordinates to the scanner coordinates, they are complicated and will not be written out here. The reader is referred to pp. 109 ff.

* On the scanning table the largest discrepancy is about 1-1/2 mm.

of reference (64) where a set of equations is given for the two interface situation. One way of deriving such equations is to trace each of a stereoscopic pair of light rays back into the bubble chamber and find out where they intersect. Since the path of a light ray is uniquely determined by the scanner coordinates, the geometrical positions of lens and interfaces, and Snell's law, this ray tracing procedure is clearly possible if the stereoscopic pair of points is used. Unfortunately, however, errors in the measurement of corresponding points generally lead to a pair of rays which do not intersect at all. The Transordinator and the digital computer program employ different techniques for surmounting this problem.

4. The Transordinator. This mechanical device, which was invented by J. H. Mullins, perfected by D. D. Sell and aligned by D. G. Coyne and the author, consists of two independent parts which are mechanically coupled so that the scanner coordinates need to be set up only once in order to read out all three space coordinates. The x,y coordinates are located on one part and the x,z coordinates on the other. The two readings of x are independent -- this is possible because of the redundancy in the scanner coordinates. The difference between the two x values is an indicator of the accuracy of the overall measurement. Absolute true space positions of points can be found to about 2 mm and local relative positions to 0.5 mm.

x-y Section. It has already been pointed out that each light ray zigzags from bubble to film in a single plane, the plane of re-

fraction. Since this plane contains the lens axis, it intersects the film in a single radial line from the point the lens axis passes through the film. On the scanner this is the pivot point. The plane of refraction is thus determined by the angle on the scanner. The stereo pair of such planes intersect in a line in the z-direction which passes through the bubble. In a (z = constant) plane, the planes of refraction are represented by two lines which intersect at the x,y coordinates of the bubble. The Transordinator constructs these two lines on a grid, and the x,y coordinates are read off of this grid at the place the lines cross. The grid is full scale. This measurement of x is degenerate when the planes of refraction coincide, and then x must be taken from the x,z measurement.

x-z Section. Call the x,z plane containing the lens axes, plane A. The x,z coordinates of a bubble are the same as those of the intersection of the normal projections onto plane A of the stereoscopic pair of light rays emanating from the bubble. The Transordinator constructs these two projections on a second full-scale grid and the location of the intersection is read from the grid, thus giving x and z. The geometrical construction of the two projections is accomplished as follows. Again it is important that a light ray remain in a single plane of refraction throughout its path. Because it does, a straight line extension of the original ray segment (freon segment) intersects the lens axis somewhere, say at point P and at an angle ϕ. P_{left} and ϕ_{left} depend only on R_L; P_{right} and ϕ_{right} only on

R_R*. Calculations of ray paths provide data for relating P and ϕ to R. A very nonlinear scale, which in true space units turns out to be $2\frac{1}{2}$ cm long, can then be constructed in order to locate P for R values associated with bubble chamber points. The projection of the freon segment onto plane A is easily found after observing that the intersection of plane A with the plane of refraction is the lens axis, and remembering that ϕ is the angle between the lens axis and the freon segment. The projection onto plane A, then, also passes through P and makes with the lens axis an angle, ψ, which is the projection of ϕ onto A. Since $(a - 90^\circ)$ is the angle between A and the plane of refraction,

$$\tan \psi = \tan \phi \cos (a - 90^\circ) \quad .$$

On the Transordinator, ψ_{left} and ψ_{right} are constructed with vertices at P_{left} and P_{right}. Figure 40 illustrates the mechanics. The scale giving L(R) is very nearly linear in R.

Note that the problem of non-intersecting light rays is eliminated on the Transordinator by projecting both light rays onto a single plane. In the x,y section this plane is a z = constant plane, and in the x,z section, this plane is a y = constant plane.

---

* a_L and a_R determine the orientations of the left and right planes of refraction respectively, while R_L and R_R determine the paths of the rays in these planes. The orientation of the planes and the paths of the rays in the planes are independently determined by this choice of coordinates.

Figure 40

Transordinator — Mechanics of the x-z Section

This figure schematically illustrates the method by which the projection of a light ray onto plane A is mechanically constructed by the Transordinator. Only half of the overall x-z section is shown since the two halves are independent of each other. The x-z position of a bubble is located by the intersection of the two projected rays. See text for a more detailed discussion.

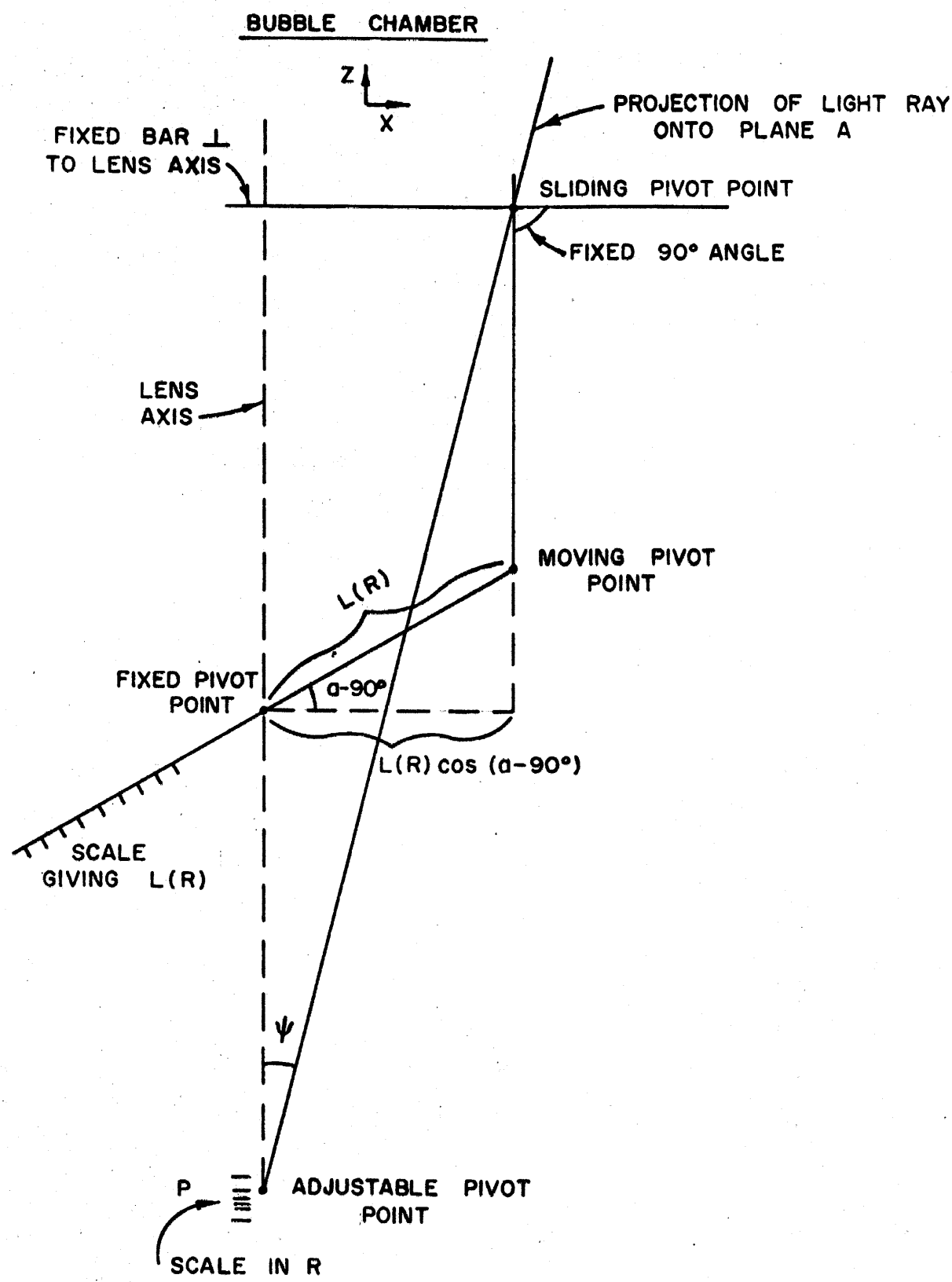
BUBBLE CHAMBER
Z
X
PROJECTION OF LIGHT RAY ONTO PLANE A
FIXED BAR ⊥ TO LENS AXIS
SLIDING PIVOT POINT
FIXED 90° ANGLE
LENS AXIS
MOVING PIVOT POINT
L(R)
FIXED PIVOT POINT
α-90°
L(R) cos (α-90°)
SCALE GIVING L(R)
ψ
P
ADJUSTABLE PIVOT POINT
SCALE IN R

Figure 40

5. Digital Computer Program. The Datatron 220 computer program, which L. J. Fretwell, Jr. has written, also traces light rays back into the bubble chamber, but locates the true space point in a different manner from that used by the Transordinator. Having once traced the rays corresponding to the scanner measurements, the computer proceeds to locate the shortest segment joining the two rays, hereinafter called the error segment. The point on this segment midway between the two rays is defined as the true space location of the point. The length of the error segment, δ, is also calculated, and is an indicator of the measurement error. There is no redundancy in the scanner measurements when used this way since four quantities are calculated from the four knowns.

The interpretation of δ as the measurement error can be misleading because its magnitude depends on the vectorial direction of the actual error. For instance, if the two reconstructed rays lie in plane A as defined in the Transordinator description, the rays always intersect and $\delta = 0$ despite the fact that R_L and R_R can take on any values. (This is the degenerate case for the Transordinator x-y measurement.)

The accuracy of this point location procedure is limited by the precision of the data read into the computer. Inaccuracies from lens distortions, scanner alignment, and measurement of images are all important. For careful measurements, absolute positions are probably good to 1 mm and local relative positions to 0.3 mm.

6. Method of Point Measurement. During this experiment the coordinates of points were measured by hand utilizing an instrument called the measuring board which was placed on the scanning table. The pictures were projected onto the central region of the board and the fiducials in both stereo views were simultaneously aligned by an iteration process which combined the x-y projection lens motions with rotation of the measuring board. With the board in the aligned position a pivot point for each view was located at the point in the image corresponding to the lens axis. The location of this point relative to the fiducial marks was established experimentally. Use was made of the fact that true space lines in a plane containing the lens axis appear on the scanner as radial lines emanating from the pivot point. Such a line was generated by photographing the reflections of a small lighted cross from the thick support-tank window surfaces which were perpendicular to the lens axis. The two images defined the desired line* on the scanner. The pivot point was determined by the intersection of two such radial lines.

An independent check on the accuracy with which the pivot points were determined was made by computing the distance between the two lens axes using the positions of the pivot points relative to fiducials of known separation on the lower surface of the support tank window. This calculation gave agreement with the actual lens

*The effect of the 8 inches of glass through which the upper reflection was viewed, was simply to displace the scanner image along this radial line.

separation to within ± 0.2 mm.

With the aid of verniers the scanner coordinates could be measured to the following estimated accuracies:

Coordinate	Local Error	Large Scale Relative Error	Absolute Error (including Measuring Board alignment)
R (mm)	±0.05	±0.1	±0.3
a (degrees)....	±0.005	±0.02	±0.06

B. OVERALL COMPUTER PROGRAM

For the purposes of this experiment an overall computer program was written by Fretwell. Besides the true space positions of points and their error segments, this program computed and printed out the following quantities:

1) In true space: direction cosines of vectors, lengths of individual vectors, ranges which could be sums of several individual vector segments, and cosines of angles between vectors (i.e. dot product of two specified direction cosines).

2) In scanner space: lengths in each view

3) Combined true and scanner space: ratio of true length to scanner length (i.e. magnification of track segment)

C. RANGE RELATIONS AND MEASUREMENT

The energies of particles which stopped in the bubble chamber were found from range-energy tables. The calculations of the range-energy functions were carried out by Fretwell. He integrated Bethe's expression[65] for the energy loss, $-\frac{dE}{dx}$, of a

heavy charged particle with unit charge passing through matter. For an absorber, such as freon, composed of a complex molecule, the expression for -dE/dx is:

$$-\frac{dE}{dx} = \left(\frac{4\pi e^4}{mc^2\beta^2}\right)\frac{\rho N_o}{A}\sum_i Z_i\left[\ell n\frac{2mc^2\beta^2}{(1-\beta^2)I_i} - \beta^2\right] \qquad \text{(AVII-7)}$$

where: e = charge of incident particle

m = mass of electron

c = velocity of light

β = velocity of incident particle/c

ρ = density of absorber in gm/cm^3

N_o = Avogadro's Number

A = molecular weight of absorber in gm

Z_i = atomic number of $i^{\underline{th}}$ atom of molecule

I_i = average ionization potential of $i^{\underline{th}}$ atom.

The summation is to be taken over every atom of the molecule. Fretwell used the following values for the average ionization potentials[66,67]:

Carbon: I/Z = 13.0 ev

Fluorine: I/Z = 13.0 ev

Bromine: I/Z = 12.1 ev

The density of liquid freon at vapor pressure has been accurately measured as a function of temperature by the manufacturer[68]. A 1% correction to the density was made for the reduced pressure at beam dump. The correction was found from the measured ratio:

(volume of bubble chamber when expanded) to (volume at slightly above vapor pressure).

Equation AVII-7 is not valid for very low energies. Fretwell estimated the place where the integral should be cut off for freon and by interpolating some experimental data[66], he found that the residual range in freon for protons with this cutoff energy was about 0.1 mm. Though relatively unimportant, this residual range was added to the result obtained from integrating equation AVII-7.

Since the calculations did not extend to very relativistic energies (the bubble chamber is small), the shielding by neighboring atoms, known as the density effect, was not included.

Errors in energies of stopping particles are primarily attributable to multiple scattering, straggling and measurement errors. The importance of each of these is discussed below.

1) Multiple Scattering

The rectified range for which Fretwell's calculation was carried out differs from the measured range because of multiple scattering effects. The magnitude of the error introduced may be calculated using the r.m.s. angle of scatter[69], $\theta(x)$, and integrating the arc length given by:

$$d\ell = \frac{dx}{\cos\theta(x)} \approx dx\,(1 - \frac{1}{2}\theta(x)^2) \qquad \text{(AVII-8)}$$

where $d\ell$ is the increment of rectified range, dx that of measured range, and $x = 0$ at one end of the track. Unfortunately, $\theta(x)$ may

be written in simple form only for values of x such that $p\beta$ may be considered constant. Since a rough estimate of the effect is sufficient, a constant value of $p\beta$ may be used (that for the middle point on the track). After integration and rearrangement, one finds for the fractional error in range,

$$\frac{\ell - x}{x} = \frac{1}{4} \overline{\left(\frac{E_s}{p\beta}\right)^2} \frac{x}{X_o} \qquad \text{(AVII-9)}$$

where the constant $E_s = 21$ Mev and X_o is the radiation length (11 cm for freon). From AVII-9, the error for pions is computed to be about 2.5%, independent of range, between 3 cm and 30 cm; and for protons about 0.3% for ranges between 1 cm and 30 cm. Ranges, of course, are always underestimated because of this error. (I.e., the error as defined by equation AVII-9 is always positive.)

2) Fluctuations in Range

The accuracy of range-energy measurements is also limited by straggling effects. The problem has been treated theoretically[70] and the agreement with experiment is reasonable[71]. For ranges used in the bubble chamber, the r.m.s. fluctuation in range varies between 2.4% and 3% for pions and between 1% and 2% for protons.

3) Measurement of Range

Most ranges were approximated by the length of the chord from origin to end of track. Occasionally a track suffered one or more apparently elastic*, large-angle scatters or had a large curvature due to multiple scattering. In these cases two or more chords

*The classification of a scatter as elastic or inelastic depended on the apparent bubble density on either side of the scatter. Tracks with inelastic scatters were treated as not stopping.

were used. The accuracy of this procedure may be estimated by approximating the trajectory by the arc of a circle.

Let ℓ = arc length

c = chord length

δ = sagitta length

$\Delta\ell = \ell - c$

It is easy to show that for small δ,

$$\frac{\Delta\ell}{\ell} \approx \frac{8}{3}\left(\frac{\delta}{c}\right)^2 \qquad \text{(AVII-10)}$$

An upper limit of about 1/10 was placed on (δ/c) for each track segment. From equation AVII-10 the corresponding maximum error in track length was 3%.

For the case of curvature due to multiple scattering, the segmentation procedure eliminated anomalously large errors. The statistical error in range from this process has already been considered above, and should not also be considered a measurement error. Single scatterings which resulted in $(\delta/c) \sim 1/10$ were rather rare and therefore related errors were treated individually.

Chord length errors arose from errors made in locating points. As pointed out in Section A5, the characteristic error for careful, local relative-position measurements was 0.3 mm.

D. GAP-LENGTH DISTRIBUTION.

1. General Relationships. A number of authors[33,36,39,72,81] have studied the process by which bubbles are formed and the resultant properties of the gap-length distribution. It is well established

that for a charged particle of constant velocity passing through a bubble chamber with constant thermodynamic conditions throughout, the bubble spacings are given by a Poisson distribution. Thus if $P(x)dx$ is the probability of a gap length falling between x and x+dx, then:

$$P(x) = n\ e^{-nx} \qquad \text{(AVII-11)}$$

where n* is a constant depending on the thermodynamic conditions, and on the particle velocity and charge, but not depending on the particle mass.

The relationship between n and the particle velocity, β, has been investigated by several experimenters[36, 39, 73-80]. The evidence from experiments performed in several liquids indicates that in all liquids for $0.2 < \beta < 0.8$, n is reasonably well given by:

$$n = n_o/\beta^2 \qquad \text{(AVII-12)}$$

where n_o depends only on the thermodynamic conditions and particle charge. At highly relativistic velocities the general features of the velocity dependence seem to vary from liquid to liquid[76, 39]. The work of Hahn, et al.[76] in CF_3Br agrees well with a relativistic increase in n given by

$$n = \frac{n_1}{\beta^2}\left[\log\left(\gamma^2 - 1\right) + 15 - \beta^2\right] \qquad \text{(AVII-13)}$$

---

* It is easily shown that n is the number of bubbles formed per unit length of track. It is called the "bubble density".

where $\gamma = (1-\beta^2)^{-\frac{1}{2}}$ and n_1 is a constant dependent on the thermodynamic conditions and particle charge. Hahn, et al. varied the operating conditions (both temperature and pressure) of their chamber to show that only n_1 varies appreciably with the thermodynamic conditions. Recently a semiquantitative theoretical explanation of this rise has been put forward[81].

Given the relation between n and β, a measurement of the gap distribution (equation AVII-11) may be used to obtain β. In order to obtain the exact relationship between n and β for the particular thermodynamic operating conditions employed, both the constant, n_o, of equation AVII-12 and the ratio n_m/n_o, in which n_m is the minimum value of n from equation AVII-13, must be found. Given these two pieces of experimental information, one can construct a smooth curve of n vs β which fits both equations AVII-12 and AVII-13 in the proper regions.

2. Chamber Calibration.

a. Determination of n_o.

i. Introductory Remark. Fretwell, et al.[82] have developed a technique by which n_o may be obtained from integral gap-length measurements on stopping particles. (Pions are particularly suitable for ease of measurement.)

ii. Ideal Track. First consider an ideal track free from background bubbles. All quantities defined below refer to true space. Let d be the apparent bubble diameter resulting from the combined effects of actual bubble size, track geometry, optics of

photography, optics of reprojection and resolution of measuring device. d is assumed constant over the entire length of a particular track, but may vary from one track to another. Let L be the length of track measured and R be the residual range from the end of the measurement (R + L is, then, the total length of the track.) x is the length coordinate along the trajectory.

Because of the finite size of d, the distance between centers of bubbles as given by the coordinate x and equation AVII-11 must be distinguished from the visual gap length, ℓ. If $P_1(\ell)d\ell$ is the probability that the distance between bubble centers will display a visual gap falling between ℓ and $\ell + d\ell$, then from equation AVII-11:

$$P_1(\ell) = n\, e^{-n(d+\ell)} \qquad \text{(AVII-14)}$$

One can show that the total expected visual gap length, G, and the total expected number of visual gaps, N, are given by:

$$G = \int_R^{R+L} e^{-n(x)d}\, dx \qquad \text{(AVII-15)}$$

$$N = \int_R^{R+L} n(x)\, e^{-n(x)d}\, dx \qquad \text{(AVII-16)}$$

where the fact that n may vary along the track has been indicated explicitly.

Define the independent functions F_1 and F_2 as follows:

$$F_1 \equiv \frac{N}{n_o G} \approx \frac{\int_R^{R+L} \frac{n(x)}{n_o} e^{-n(x)d} dx}{\int_R^{R+L} e^{-n(x)d} dx} \qquad \text{(AVII-17)}$$

$$F_2 \equiv \frac{G}{L} \approx \frac{1}{L} \int_R^{R+L} e^{-n(x)d} dx \qquad \text{(AVII-18)}$$

For a certain particle and a particular velocity dependence of n (assumed to be given by equation AVII-12), F_1 and F_2 depend solely on R, L and $n_o d$. Once the values of N, G, L and R have been established for a track, equations AVII-17 and AVII-18 can be solved simultaneously for F_1, and $n_o F_1$ can be found directly from the definition of F_1. Division then yields n_o.

To facilitate the solution of equations AVII-17 and AVII-18, Fretwell et al. carried out computer calculations of F_1 and F_2 as functions of R, L and $n_o d$. The range-energy relation in CF_3Br and equation AVII-12 were used in the calculations. The resultant tables apply specifically to pions, but may be easily converted for use with other particles. For the special case $R \approx 0$ two families of superimposed graphs were drawn of F_1 vs F_2 for constant L and for constant $n_o d$.

iii. Real Track. Due to measurement difficulties only gaps longer than a minimum length may be feasibly used. Thus a predetermined cutoff is applied to the distribution of true gaps and

an effective bubble diameter, which is the sum of the real bubble diameter and the cutoff length, must be employed in the calculations. Henceforth, the word "gap" will refer only to gaps longer than the cutoff, "gap length" will refer to the excess length over and beyond the cutoff that a gap may have, and "bubble diameter" will refer to the effective bubble diameter.

Measurements on a track yield the following quantities:

$N_m \equiv$ total number of gaps (the same number in scanner or true space)

$G_{ms} \equiv$ integral gap length on the scanner

$S \equiv$ total track length on the scanner (AVII-19)

$T \equiv$ total track length in true space

$n_{bs} \equiv$ mean number of background bubbles expected to be overlapping the track per unit length on the scanner

Conversion of the length measurements to true space lengths is accomplished to first order by using the ratio T/S. Thus the true-space quantities corresponding to AVII-19 are:

$$G_m = (T/S)\, G_{ms}$$

$$n_b = (S/T)\, n_{bs} \qquad \text{(AVII-20)}$$

A small second order correction related to the change in magnification along a steeply dipping track has been investigated by Fretwell et al. Since the statistical error associated with steeply dipping

tracks is large, this correction has little practical importance. Furthermore, the calibration tracks were chosen to have low dip.

The measured quantities N_m and G_m represent an apparent track containing both real track bubbles and background bubbles. The effect of the background bubbles must be subtracted in order to obtain F_1 and F_2 for the real track. The distribution of background bubbles is assumed to be independent of position along the track. The probability function (equation AVII-14) for the apparent track is separable by the substitution:

$$n(x)_{apparent} = n(x)_{real} + n_b \qquad \text{(AVII-21)}$$

Since both n_b and d are assumed constant, the factors containing n_b in equations AVII-17 and AVII-18 may be taken outside the integrals and the following formulas derived for the real track:

$$n_o F_1 = (N_m/G_m) - n_b \qquad \text{(AVII-22)}$$

$$F_2 = (G_m/T)\, e^{n_b d} \qquad \text{(AVII-23)}$$

where d is the bubble diameter in true space. Although d is constant along a particular track, the quantity which is very nearly constant* for all tracks is the bubble diameter on the scanner, d_s. For this reason, equation AVII-23 is more conveniently written:

$$F_2(G_m/T)\, e^{n_{bs} d_s} = (G_{ms}/S)\, e^{n_{bs} d_s} \qquad \text{(AVII-23a)}$$

* Since the background correction tends to be small--10% or less,--the effect of the slight variation of d_s from track to track may be neglected and a constant value may be used for d_s in the calculations.

iv. Method of Measurement. Each gap length on the scanner was hand measured by comparison under magnification* with a folded wedge. The folded wedge, which is illustrated in Fig. 41a, was calibrated with a microscope. The deviation from linearity was less than 1%. Each unit was very close to 0.1 mm and the gap lengths were read to 0.01 mm. It is estimated that the measurement errors were of the order of ± 0.02 mm.

The background measurements were made by counting the number of bubbles falling on each of two lines straddling the track. A bubble was counted if it satisfied the same relation to the line as a bubble which was counted as part of a track satisfied with respect to the center of the track. Since few background bubbles overlapped, n_{bs} was simply the number counter per unit length.

v. Calibration Data and Observations. Twenty-two stopping pions were chosen for the determination of n_o. These tracks were picked in such a way that there was at least one track from each of the 13 individual runs of the experiment and two or more from the extended runs. Tracks were required to have: (1) a low (true length/scanner length) ratio; (2) medium to low background, n_{bs}; (3) track length greater than 12 cm; and (4) good optical quality. Other than these requirements, there were no biases imposed on the selection of the tracks. The distribution in track lengths was roughly

* A pair of jeweler's binocular 3x magnifying glasses were used for this purpose.

Figure 41

Photographic Wedges for Gap-Length Measurements

This figure illustrates the photographically reduced "wedges" which were compared to the gap lengths in the projected image of a track in order to perform gap-length measurements by hand. A measurement was made by adjusting the position of the wedge until the edges of the two bubble images defining a gap were tangent to the two lines of the wedge. For this figure, the wedges have been photographically enlarged about three times. The folded wedge, (a), was used for integral gap-length measurements, while the single wedges, (b), were used for gap-length-distribution measurements. (See text for further discussion.)

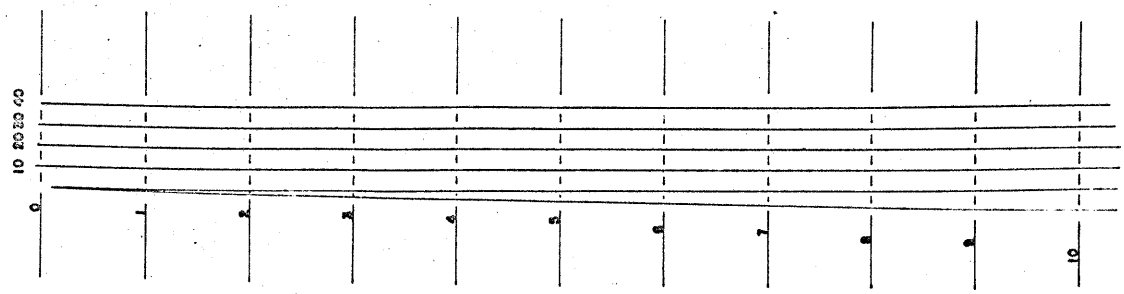

(a)

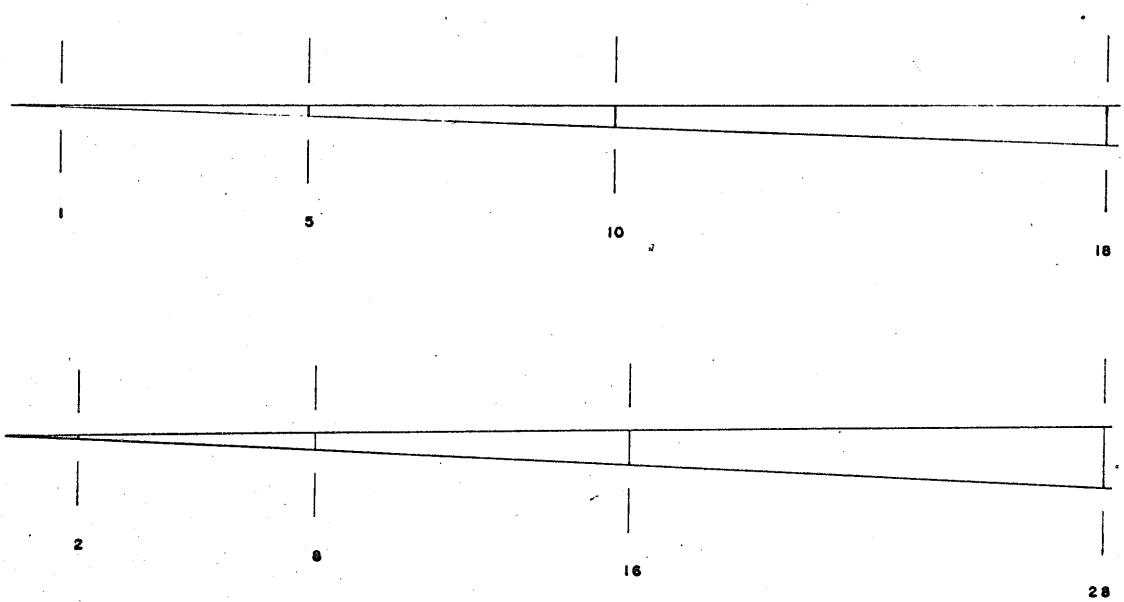

(b)

FIGURE 41

constant between 12 and 23 cm, the mean length being 16.6 cm.

For the i^{th} track, n_{oi} was found for each of five different minimum gap-length cutoffs. A weighted average was then computed for each cutoff from the formula:

$$\overline{n_o} = \frac{1}{N} \sum_{i=1}^{22} N_i \, n_{oi} \qquad \text{(AVII-24)}$$

where N_i is the number of gaps in the i^{th} track, and

$$N = \sum_{i=1}^{22} N_i \ .$$

The r.m.s. deviation from the mean, σ, in units of the statistical error, $\overline{n_o} / \sqrt{N_i}$, was calculated from:

$$\sigma^2 = \frac{1}{21} \sum_{i=1}^{22} \left(\frac{n_{oi} - \overline{n_o}}{\overline{n_o}} \right)^2 N_i \ . \qquad \text{(AVII-25)}$$

The values of these quantities are presented in Table 12. It is clear from an examination of this table that there was a systematic measurement error for the cutoff at 0.2 mm. Discarding the $\overline{n_o}$ associated with this cutoff and computing an average weighted by N in a way similar to equation AVII-24, one obtains for the best estimate of $\overline{n_o}$:

$$\langle \overline{n_o} \rangle = (11.91 \pm 0.3) \text{ bubbles/cm} \ . \qquad \text{(AVII-26)}$$

The fractional deviation of $\overline{n_o}$ from this best value is also presented in Table 12. The fact that these deviations* are appreciably less

* Note that the measurements at various cutoffs are not statistically independent.

than the statistical error indicates that systematic measurement errors associated with the choice of cutoff and the effect of the relativistic rise in bubble density are small and may be ignored.

TABLE 12. Calibration Data for n_o

Cutoff ..... (mm on scanner)	0.2	0.3	0.4	0.5	0.6
$\bar{n}_o$ (1/cm in true space	12.65	11.96	11.85	11.74	12.12
σ	0.87	0.79	0.93	0.94	1.17
N	2766	2087	1662	1324	1097
$N^{-\frac{1}{2}}$	0.019	0.022	0.024	0.027	0.030
Fractional deviation from weighted mean (see text)	—	+0.004	-0.005	-0.014	+0.018

In order to test the importance of the background subtraction, $\bar{n}_o$ was also calculated without the background subtraction. Independent of the cutoff, the background correction reduced $\bar{n}_o$ by about 7 per cent.

That the values of σ in Table 12 are close to 1 implies three things:

1) The effect of random measurement errors is less than the statistical errors and is therefore unimportant.

2) The thermodynamic stability of the bubble chamber was sufficiently precise throughout the run to allow the use of a single value of n_o for the whole run, i.e., percentagewise the temporal

fluctuation of n_o was appreciably less than the statistical error in measurable quantities.

3) The thermodynamic conditions were sufficiently constant from the bottom to the top of the freon chamber to allow the use of a single value of n_o throughout the whole chamber, i.e., percentage-wise the spatial variation of n_o was appreciably less than the statistical error in measurable quantities.

In order to further substantiate statement (3), the calibration tracks were divided into three classes -- those having average "z" coordinates in the lower, middle, or upper third of the freon chamber. For the 0.3 mm cutoff case, the weighted (equation AVII-24) average value of n_o was calculated for each class. The results are presented below:

Cutoff 0.3 mm

Third of Chamber.....	Lower	Middle	Upper
Number of tracks.....	$4\frac{1}{2}$	$8\frac{1}{2}$	9
[Total number of gaps] $^{-\frac{1}{2}}$.....	0.047	0.035	0.035
$\overline{n_o}$ (1/cm).....	12.17	11.99	11.81
Fractional deviation of $\overline{n_o}$ from best value (11.91).....	+0.022	+0.007	-0.008

No significant variation is evident in this data.

b. Determination of n_m. The best procedure for obtaining n_m would have been to inject momentum-selected pions of 450

Mev* kinetic energy into the bubble chamber and measure the mean bubble density. Unfortunately, this was not done, and therefore a less direct method was employed.

The bubble density measurements performed on possible K_2^o signatures plus 17 additional long light tracks were utilized in plotting a histogram of frequency-of-occurrence versus mean-gap-length** for mean gap-lengths greater than 0.6 mm in true space. The gap-length-distribution method, which is discussed in Section D3 below, was employed in the measurements. The frequency-of-occurrence parameter was defined as the sum of all gaps from tracks falling within the particular mean-gap-length interval. The histogram is presented in Fig. 42. Since the true energy spectrum of the particles which created the tracks is not known, a guess must be made of the true mean-gap-length spectrum† which is smeared out by the statistics to give the observed histogram. The end point of the guess is the desired quantity $(1/n_m)$. Two possible guesses as well as the end point computed from $n = n_o/\beta^2$ with $\beta = 0.971$†† are indicated in the figure. It is believed that curve (a) is the better guess.

---

* This is the pion energy for which the bubble density is a minimum.

** Mean-gap-length = 1/bubble density.

† Note that the energy spectrum differs vastly from the mean-gap-length spectrum.

†† This is the value of β yielding the minimum for Hahn's expression (equation AVII-12).

Figure 42

Determination of n_m

l/n = mean gap length.

N_g = total number of gaps per 0.004 cm interval in l/n.

N_t = number of tracks in interval.

ϵ = typical statistical standard deviation in the measurement of l/n for a single track (due to the limited number of gaps).

$(l/n)_o$ = value of l/n computed from $n=n_o/\beta^2$ with $n_o = 11.91/cm$ and $\beta = 0.971$. This value of β corresponds to the minimum in Hahn's expression for n (equation AVII-13).

a = "better" guess for true spectrum which is smeared out by statistics to give the observed spectrum. Curves (a) and (b) are unnormalized.

b = "possible" guess for true spectrum.

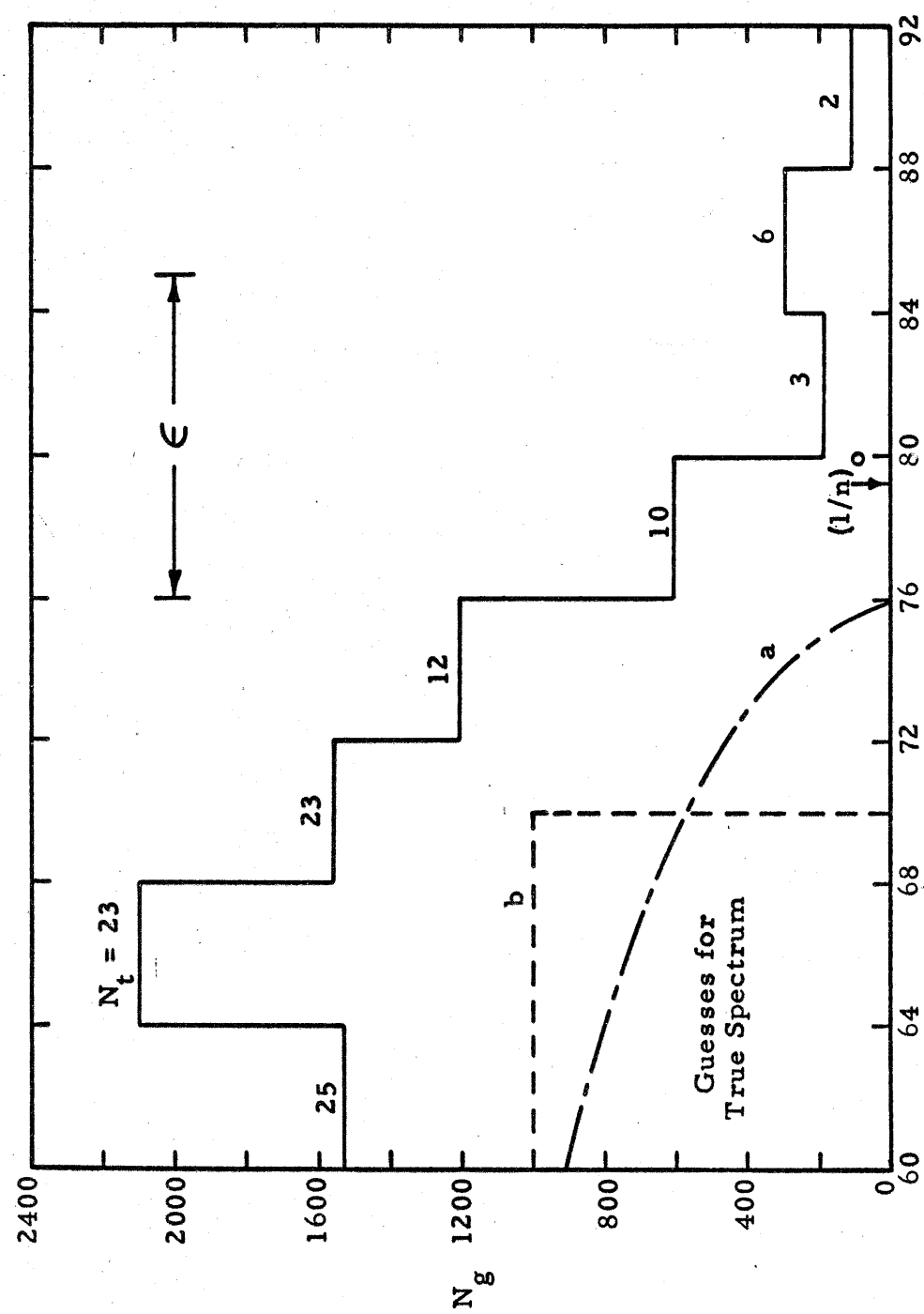
2400
2000
1600
1200
800
400
0
N_g
60
64
68
72
76
80
84
88
92
$\frac{1}{n} \times 10^3$ (cm)
$(1/n)_o$
$N_t = 23$
25
23
12
10
6
3
2
ϵ
a
b
Guesses for
True Spectrum

Figure 42

c. Resultant Calibration. Figure 43 shows the relation between the mean gap length, l/n, and β^2 for guesses (a) and (b) in Fig. 42. The percentage difference in the two curves for a few pion kinetic energies are:

Pion kinetic energy (Mev)	50	100	150	200	250	300	450
Percentage difference in l/n	0	0.9	3.8	5.5	7.1	8.3	8.2

The statistical standard deviation in the measurement of longer tracks tends to be about 8 per cent. Thus, for pion energies less than 150 Mev, the systematic difference between these two calibration curves is relatively unimportant. For pion energies above 150 Mev, the effect of the statistical error is so large that the measurements have little significance, and so the occurrence of an additional systematic error in the calibration is not terribly serious. Curve (a) has been used for the data analysis.

3. Application to Non-Stopping Tracks

a. Introductory Remark. The measurements required in applying the integral-gap-length method are very difficult and time consuming to carry out by hand. Therefore, the simpler and faster gap-length-distribution method was employed in the analysis of the possible K_2^o signatures.

b. Ideal, Constant Velocity Track. First consider an ideal track similar to the one discussed in Section D2aii, but with the added stipulation that n be constant over its whole length. The probability of a visible gap length being greater than ℓ_i is easily

Figure 43

Calibration for Gap-Length Measurements

The relationship between the mean gap-length, $1/n$, and the square of a particle's velocity, β^2, is shown for the measured value of n_o and the two guesses for n_m (see Fig. 42). Curves (a) and (b) correspond respectively to guesses (a) and (b) of Fig. 42. Curve (a) has been used for the data analysis. Note that this curve is a straight line for $\beta^2 < 0.88$, i.e., that $n = n_o/\beta^2$ for values of β up to 0.94.

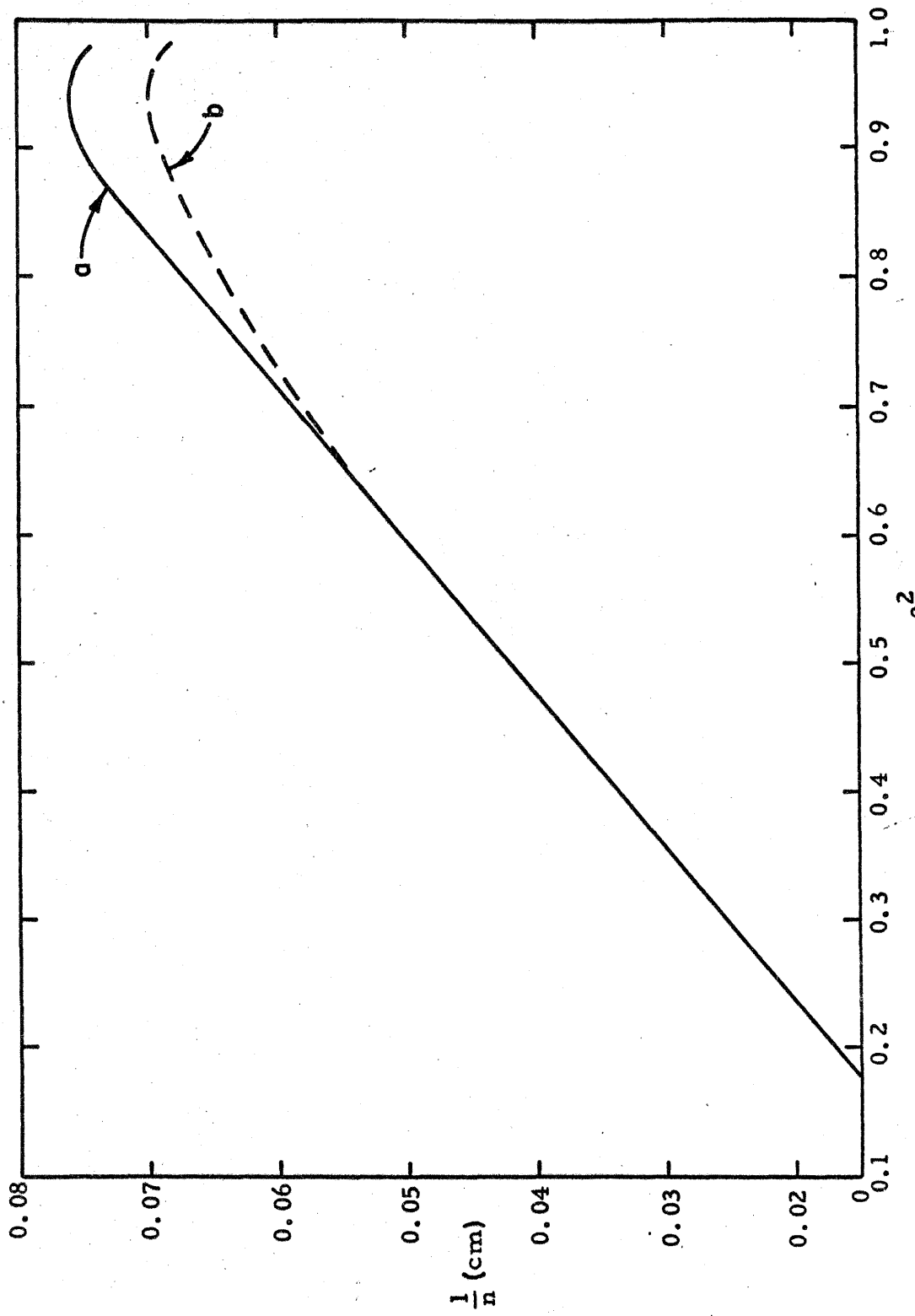
a
b
0.08
0.07
0.06
0.05
0.04
0.03
0.02
$\frac{1}{n}$ (cm)
0
0.1
0.2
0.3
0.4
0.5
0.6
0.7
0.8
0.9
1.0
β^2

Figure 43

found from equation AVII-14 to be:

$$P_1 (\ell > \ell_i) = e^{-n(d+\ell_i)} . \qquad \text{(AVII-27)}$$

This expression may be used to find n from measurements of the number of gaps greater than several values of ℓ_i. Fretwell[82] has shown that for r measurements the best fit for n is given by the solution of:

$$\sum_{i=1}^{r} \frac{(N_i - N_{i-1})(\ell_i e^{-n\ell_i} - \ell_{i-1} e^{-n\ell_{i-1}})}{(e^{-n\ell_i} - e^{-n\ell_{i-1}})} = 0 \qquad \text{(AVII-28)}$$

where N_i is the number of gaps longer than ℓ_i and $\ell_r = 0$. Fretwell has also calculated the optimum lengths for the ℓ_i functions of n and the resultant expected error as a function of r.

For ease of data reduction r was chosen to be 3. In this case, equation AVII-28 depends on only two parameters:

$$u_1 = N_1/N_3$$

$$u_2 = N_2/N_3 \qquad \text{(AVII-29)}$$

Curves of u_1 versus u_2 for constant n (or 1/n) are straight lines. With the aid of a family of these straight lines, n (or 1/n) is easily found graphically from the measured quantities u_1 and u_2.

Since the solution of equation AVII-27 for n (or 1/n) requires only two measurements (assuming d is unknown), n (or 1/n) is over-determined when three measurements are made. This extra degree of freedom may be used to make a chi-square test to check the

goodness of fit.

The expected fractional error (standard deviation) in (1/n) for the case r = 3 is

$$\epsilon = 1.1/\sqrt{N_3} \quad . \tag{AVII-30}$$

Thus 90 per cent of the statistically significant information in a track is obtained when three measurements are made.

c. Effect of Velocity Change. Application of the gap-length-distribution method to a track along which n changes because of gradual energy loss yields a value for n which is some weighted average for the track.

The importance of the difference between this weighted value and the value at the mid-point of the track has been investigated theoretically with the aid of the tables of F_1 and F_2 computed in conjunction with the integral-gap-length method. The use of the β^{-2} dependence of n in these calculations was appropriate because the largest effects of the variation of n along a track must occur for nearly stopping particles where the dependence of n is in fact β^{-2}. The expected number of gaps longer than ℓ_i for a particular track, including the variation of n, is easily found from equations AVII-16, AVII-17 and AVII-18:

$$N_i(R, L, n_o d_i') = n_o L F_1 F_2 (R, L, n_o d_i') \tag{AVII-31}$$

where

$$d_i' = d_{effective} + \ell_i \tag{AVII-32}$$

and the quantities in the parentheses after $F_1 F_2$ indicate the parameters on which both F_1 and F_2 depend. The expected value for u_j is, then:

$$u_j = F_1F_2(R, L, n_o d'_j)/F_1F_2(R, L, n_o d'_3) \qquad \text{(AVII-33)}$$

From these expected values of u_1 and u_2, one can follow through the graphic solution of equation AVII-28 to obtain the expected value of $\bar{n}$ for the gap-length-distribution method. Under the assumption that $\bar{n}$ is the value of n at the mid-point of the track, and with the help of range versus n and range-energy tables, one can find the expected measurement value of the kinetic energy at the beginning of the track. This kinetic energy is then to be compared with the true kinetic energy associated with the particular track under consideration.

Computations were carried out for pions over a wide variety of track lengths, ranges, track dips*, and bubble diameters. The particular ℓ_i of the measuring instrument were employed. In the worst cases, the error introduced by the mid-point assumption was found to be about 1/5 the statistical error (equation AVII-30). For a pseudo Λ^o decay with Q value close to 38 Mev, these worst-case errors from the mid-point assumption reflect as about 2 Mev in the Q value.

---

* Since the d'_i are constants in the projected image, tracks of various dips (or more accurately, various values of T/S) may be investigated by changing n_o; i.e., the projected value of n_o depends only on T/S.

The results for pions may be converted to those for protons through a scaling of R and L by the ratio of the proton to the pion mass. This was done for several cases and, as expected, the error from the mid-point assumption was found to be even less for protons than for pions.

The conclusion may be drawn that the error introduced into the gap-length-distribution method by the change of velocity along a track is negligible when the measured value of n is assumed to be that for the mid-point of the track.

d. Real Track. The comments made in the discussion of the integral-gap-length method about the length cutoff in useful gaps applies here, and the bubble diameter in equation AVII-27 must be the effective bubble diameter.

The projected image of a track displays an exponential distribution of gaps differing from the true-space distribution only through a magnification factor. The application of the gap-length-distribution method to the projected image, then, yields n_s (apparent) which is a superposition of n_s (real) and n_{bs} (see equation AVII-21):

$$n_s \text{ (apparent)} = n_s \text{ (real)} + n_{bs} \ . \qquad \text{(AVII-34)}$$

Background subtraction is achieved trivially by the solution of equation AVII-34 for n_s (real). Conversion to true space is also simple:

$$n \text{ (real)} = n_s \text{ (real)} \cdot (S/T) \ . \qquad \text{(AVII-35)}$$

e. Measurement Procedure and Errors. A track was first qualitatively classified into one of two categories and then the N_i for the appropriate set of ℓ_i were counted under magnification. The distances between edges of bubble images, t_i, and the ℓ_i for each category were:

	Category	
	low n	medium or high n
t_i (in 10^{-1} mm)	16,8,2	10,5,2
ℓ_i (in 10^{-1} mm)	14,6,0	8,3,0

The ℓ_i were approximations of Fretwell's optimum lengths for each category. The wedges on which the t_i were displayed are illustrated in Fig. 41b.

From the ratios, u_1 and u_2, graphical solutions were found first for 1/n and then for χ^2, which was used in the standard way to test the goodness of fit. In the infrequent case of an unsatisfactory χ^2, the measurement was redone.

The magnitude of the measurement error was investigated through the study of 100 typical tracks which were measured two independent times (usually by two different people). The fractional r.m.s. difference, Δ_{RMS}, was calculated from the formula:

$$\Delta_{RMS}^2 = \frac{1}{m-1} \sum_{i=1}^{m} \left(\frac{\Delta_i}{\epsilon_i}\right)^2 \qquad \text{(AVII-36)}$$

where ϵ_i is given in equation AVII-30 and Δ_i is the best approximation to the fractional measurement standard deviation:

$$\Delta_i = \frac{\left[\frac{1}{r-1}\sum_{j=1}^{r}\left(\frac{1}{n_i} - \left\langle\frac{1}{n}\right\rangle_{ave}\right)^2\right]^{\frac{1}{2}}}{\left\langle\frac{1}{n}\right\rangle_{ave}} = \frac{\left|\frac{1}{n_1} - \frac{1}{n_2}\right|}{\sqrt{2}\left\langle\frac{1}{n}\right\rangle_{ave}} \qquad \text{(AVII-37)}$$

For the 100 tracks, Δ_{RMS} was about 0.5. Noting that the measurement error and the statistical error are independent, one concludes that 90 per cent of the overall error was due to statistics while only 10 per cent was due to the measurement process.

The background measurement was made by counting the number of bubbles falling within a known area adjacent to or straddling the track. A simple multiplicative factor converted this number to the number expected to fall within the known width of the track. Although the magnitude of the background correction varied widely, it was seldom as large as 10 per cent. Thus a 20 per cent error in n_{bs} generally contributed an error of less than 2 per cent to $1/n$. This was negligible compared to the statistical error, ϵ, which had a minimum value of about 8 per cent.

E. ANGLE MEASUREMENT

The cosine of the angle between the pion and proton was calculated by taking the dot product of the vectors pointing in the directions of the pion and proton. Since scattering effects in the liquid alter particle directions, each direction vector was found by constructing in each projected view the tangent to the track at the origin and then measuring the true space vector joining the origin to a

point falling on these tangents at least 5 cm* from the origin (in true space). The method was not strictly correct because straight lines in true space transform into curved lines on the scanner. However, the curvature which depends on the true space direction is very slight and only produced an error between 0 and 0.5° in the true space direction.

It was, of course, necessary to establish a pair of corresponding points on the projected tangents. In most cases it was possible to make use of the fact that corresponding points are nearly equidistant from the 90° line on the scanner and that the analyst has memorized the small variations from equality. Often it was possible to establish the local variation by observing corresponding bubbles of the associated track which roughly paralleled the tangents.

Tracks nearly parallel to the 90° direction presented a serious problem because any set of points on the tangents were almost corresponding. In this case corresponding points were established by equating the z component of the direction vector to the difference in z of the origin and a carefully chosen bubble on the track. (The bubble was picked as far from the origin as possible under the condition that there were no large angle scatterings visible between the origin and the bubble.) Large errors were associated with such tracks. Luckily their occurrence was rare and they could be treated separately.

The error in judgement associated with determining the projected tangent direction tended to overshadow the effects of optical distortion and point measurement error discussed above. An

*The error due to point measurement inaccuracy was thus held to less than 0.3° (in true space).

experimental study of this type of error was carried out through the examination of 137 events in which two independent angle measurements were made. The qualitative appearance of each event was examined by means of the sketch made during scanning, the angle drawing and the analysis information on track lengths. Each angle was then classified good, fair, poor or impossible.

A large number of measurements of a single angle should exhibit a Gaussian distribution about the true angle. The standard deviation, σ, of the distribution represents the measurement error for the particular angle. All angles in one of the classifications listed above should exhibit roughly the same error distribution. The average distribution may be represented by $\bar{\sigma}$, which is the average of the standard deviations of the individual distributions. From only two measurements of the i^{th} angle, the best approximation to the i^{th} standard deviation, σ_i, is:

$$\sigma_i = \left[\frac{1}{m-1}\sum_{j=1}^{m}(\theta_j - \bar{\theta})^2\right]^{\frac{1}{2}} = |\theta_1 - \theta_2|/\sqrt{2} \qquad \text{(AVII-38)}$$

where θ_1 and θ_2 are the two independently measured angles. An estimate of how well $\bar{\sigma}$ represents all angles of a certain class may be secured by an examination of the distribution of the σ_i's about $\bar{\sigma}$. This distribution should also be Gaussian and may be designated by its standard deviation, S.D.(σ), which is given by:

$$\text{S.D.}(\sigma) = \left[\frac{1}{n-1}\sum_{i=1}^{n}(\sigma_i - \bar{\sigma})^2\right]^{\frac{1}{2}} \qquad \text{(AVII-39)}$$

Table 13 presents, for each classification, the number of

events, $\bar{\sigma}$ and S.D.(σ).

TABLE 13. Angle Measurement Error

Angle Classification	n	$\bar{\sigma}$	S.D.(σ)
Good	66	1.3^{o}	1.2^{o}
Fair	36	2.2^{o}	1.7^{o}
Poor	32	3.5^{o}	3.1^{o}
Impossible	3	12.3^{o}	9.9^{o}

APPENDIX VIII

K_2^o LOSS FACTOR

A. K_2^o LOSS IN LEAD ABSORBER

1. General. The 4 inches of lead placed in the sweeping magnet to reduce the low energy background also decreased the K_2^o meson intensity. The observed intensity must be corrected accordingly. The geometry of the K_2^o channel essentially confined the K_2^o beam to the cone defined by the boundaries of the target and the bubble chamber. Therefore, there is no need to consider the process in which K_2^o mesons, which normally would have missed the bubble chamber, were scattered into the chamber from this lead absorber.

Several authors[26,58,83-85] have theoretically treated the interaction of K_2^o mesons with matter in order to estimate the regeneration of K_1^o mesons. Since the diffraction regeneration of K_1^o mesons as measured in iron[25-27] accounts for only about 2 per cent of the total cross section of K_2^o mesons in copper[16], it may be neglected and the simplified approach of references (85) and (16) may be used for the rough calculation described below. Thus, the intensity, I(x), of the K_2^o beam directed towards the freon chamber at depth x in the lead is given by:

$$I(x) = I(o) \exp\left[- \frac{\rho N_o}{A} (\sigma_i + w\sigma_d) x \right] \qquad \text{(AVIII-1)}$$

where

ρ = density of lead

N_o = Avogadro's number

A = atomic weight of lead

σ_i = total "inelastic" cross section of K_2^o mesons on lead. "Inelastic" includes: elastic and inelastic scattering from, and interactions with, the individual nucleons within the nucleus.

σ_d = total diffraction scattering cross section of K_2^o mesons on lead nuclei.

w = fraction of diffraction scattered K_2^o mesons which scattered out of the solid angle subtended by the freon chamber.

No factor similar to w multiplies σ_i because the "inelastic" processes have wide angular distributions and the solid angle subtended by the freon chamber was small (0.015 ster.).

The evaluation of equation AVIII-1 consists of two parts: numerical values of σ_i and σ_d must be obtained; and w must be evaluated for the particular geometry of this experiment.

2. Values of σ_i and σ_d. Values for the cross sections, σ_i and σ_d, have been computed by Good et al.[27]. They find at T = 340 Mev:

	Iron	Lead
σ_i (mb)	597	1510
σ_d (mb)	289	996
πR^{2*} (mb)	776	1858

The cross sections in iron are also presented for several different

*Geometrical cross section included for comparison (R from equation AIV-6).

energies and input optical model parameters. The values obtained* imply that the cross sections probably do not vary more than 10% over the energy range of interest here. The values above agree reasonably well with an experim ent by Panofsky et al.[16] in which the average total cross section, $\sigma_i + \sigma_d$, in copper was found to be 1.12 ± 0.25 barns for a broad K_2^o energy spectrum extending from 0 to 450 Mev and peaking at 150 Mev. Constancy of the cross sections between 200 and 600 Mev is also implied by two facts: (a) the kaon-nucleon cross section[59] are nearly constant in this range; and (b) the difference between the propagation vector inside and outside the nucleus as given by equation AIV-5 changes by only 7% between these limits provided the nuclear potential remains constant. In any case, the values quoted above for the cross sections have been used throughout the energy range 100 to 600 Mev.

3. Evaluation of w.

a. Method. The fraction, $g(T, \vec{x})$, of diffraction-scattered K_2^o mesons of kinetic energy, T, which passed through the freon chamber after scattering from a particular point, $\vec{x}$, in the lead absorber is given by:

$$g(T, \vec{x}) = \frac{1}{\sigma_d (T)} \int_{C(\vec{x})} \frac{d\sigma_d}{d\Omega} (T)\, d\Omega \qquad \text{(AVIII-2)}$$

* The calculations do not cover the desired energy range, but the effect of greater absorption of the negative strangeness component is investigated.

where the integral is to be taken over the limits of the freon chamber, $C(\vec{x})$, as seen from point $\vec{x}$.

The fraction, w(T), is then:

$$w(T) = 1 - \frac{1}{V_o} \int_{V_o} g(T, \vec{x}) \, dV \qquad \text{(AVIII-3)}$$

where V_o is the volume of the lead absorber included in the cone of K_2^o mesons which passed through the freon chamber, and the integral is to be taken over this same volume. Variations of the K_2^o meson intensity within the cone have been neglected.

These expressions neglect second order processes by which particles are first scattered out of, and then back into, the beam.

b. Calculation of Differential Cross Section. The optical model of Fernbach, et al., described in Appendix IV, Section A, may be used to calculate the angular dependence of the diffraction scattering. Let the subscript + denote the positive-strangeness component, and - the negative-strangeness component, of the K_2^o wave. Since the mean lives of the K_1^o and K_2^o mesons are long compared to the transit time through the nucleus, one may utilize equation AIV-3 and the relationships in Appendix I to write the scattered amplitude of the K_2^o wave in the following way:

$$f_2(\theta) = k \int_0^R \left\{1 - \tfrac{1}{2} \left[\exp(-K_+ + 2ik_{1+})s + \exp(-K_- + 2ik_{1-})s \right] \right\} \times$$

$$\times J_o(q\rho) \, \rho \, d\rho \qquad \text{(AVIII-4)}$$

where $k = k_+ = k_-$ (mass difference of K^o and $\overline{K^o}$ ignored). k_{1+} and

k_{1-} may be calculated from equation AIV-5 using the charged K-meson nuclear potentials as measured in emulsion experiments:

$$V_+ = +12.5 \text{ Mev}^{(86)}$$

$$V_- = -16 \text{ Mev}^{(87)} \qquad \text{(AVIII-5)}$$

K_+ and K_- may be estimated from equation AIV-2 and the charged K-meson nucleon total cross sections[44,59] weighted according to the number of protons and neutrons in the lead nucleus. The effect of the Pauli principle as calculated by Sternheimer[88] may be included.

Following this procedure, hand calculations were carried out for six energies: 100, 200, 300, 400, 500 and 600 Mev. Within the errors of the calculation the function, $(d\sigma/d\Omega)/k^2 = |f_2(\theta)|^2/k^2$, when plotted against the variable q, has the same shape for all four energies. This shape is closely approximated by the function: $\exp(q^2/q_o^2)$ with $q_o = 0.26 \times 10^{13}/\text{cm}$. The total cross section required to calculate $g(T, \vec{x})$ from equation AVIII-2 was found by integrating the calculated differential cross section. Thus the optical model calculation was employed only to find the angular function, $(d\sigma/d\Omega)_d/\sigma_d$, which was subsequently integrated to obtain $g(T, \vec{x})$.

c. Results for w. The functions g(T,x) and w(T) were also computed by hand. The values found for w(T) are:

Kinetic Energy of K_2^o(Mev)	100	200	300	400	500	600
w(T).....	0.84	0.72	0.63	0.55	0.50	0.45

The errors in these values of w(T) are believed to be less than 10%.

4. Results for K_2^o Loss. The numerical results obtained from equation AVIII-1 for the loss in the K_2^o meson beam intensity due to the 4 inches of lead are:

Kinetic Energy of K_2^o (Mev)	100	200	300	400	500	600
I(after lead)/I(before lead)	0.46	0.47	0.49	0.50	0.51	0.52

A 20% error in the assumed cross sections transforms into something close to a 15% error in these factors. In the worst case the estimated error in w(T) reflects as a 2% error in the intensity ratio.

B. K_2^o LOSS IN BUBBLE CHAMBER WALLS AND LIQUIDS

The rather complicated layout of walls, beam ports, liquids, etc. at the entrance to the bubble chamber is illustrated in Figs. 5 and 6. In order to simplify matters, mean absorber thicknesses were computed by equating the total volume of each material to the volume of a uniform sheet spread across the K^o entrance channel. These thicknesses are presented in Table 14 together with the resulting reduction factors in the K_2^o beam intensity calculated from equations similar to AVIII-1. Several geometrical approximations were made for the various absorbers in order to compute the reduction factors.

1. Steel.

a) Support tank and expansion chamber. These walls were located within 4 inches of the illuminated volume of the freon chamber. For this reason all of the diffraction scattered, and one third of the inelastically scattered, K_2^o mesons were assumed to have continued through the freon chamber. From the K_2^o interaction cross

TABLE 14

K_2^o Loss in Bubble Chamber Walls and Liquids

Absorber	Absorption Coefficient α (1/cm)	Mean Thickness t (cm)	K_2^o Intensity Reduction Factor $e^{-\alpha t}$
1. Steel* a) support tank + expansion chamber.....	4.4×10^{-2}	3.34	0.86
b) safety tank + radiation shields	5.1×10^{-2}	1.45	0.93
2. FC-43 support liquid	0.76×10^{-2}	3.70	0.97
3. Polyethylene	0.49×10^{-2}	1.53	0.99
4. Neoprene	0.59×10^{-2}	0.16	1.00
5. CF_3Br (outside illuminated region).....	0.67×10^{-2}	1.88	0.99
Net effect from above sources.....			0.76

* Steel, stainless steel and inconel x are all grouped under "steel" and treated as iron.

section estimates made in conjunction with the selection of the best K_2^o signature (see Appendix IV) one finds that the K_2^o interaction cross section in iron accounts for about 61% of σ_i as calculated by Good et al. (see Section A2 above). This implies that the inelastic scattering cross section must be about 230 mb. Therefore, the cross section used to calculate the K_2^o meson loss in these walls was 520 mb.

b) Safety tank and radiation shields. These walls fell between 10 and 13 inches from the illuminated volume of the bubble chamber. The assumption was made that all of the diffraction scattered but none of the inelastically scattered K_2^o mesons passed through the freon chamber. Thus, 597 mb was used for the absorption cross section.

2 through 5. Liquids and plastics. These materials were all within $1\frac{1}{2}$ inches of the illuminated region of the bubble chamber. Only interaction processes were considered in the estimates of the absorption cross sections.

The net effect of these local absorbers was that the K_2^o meson beam intensity was reduced by a factor of 0.76. The largest and most important error in the mean thickness estimates occurs in that for the steel in the support tank and expansion chamber. This thickness estimate could be off by as much as 50%, leading to an 8% error in the intensity reduction factor. A 20% error in the absorption cross sections reflects as a 5% error in the intensity reduction factor.

C. K_2^o DECAYS IN FLIGHT

Decays in flight over the 242 cm path between the carbon target and the freon chamber reduced the K_2^o intensity by the following factors:

Kinetic Energy of K_2^o (Mev).....	100	200	300	400	500	600
I(at chamber)/ I(at target)	0.82	0.87	0.90	0.91	0.92	0.93

The errors in these factors range from 1% to 4%.

D. OVERALL K_2^o LOSS

The several K_2^o loss factors discussed in this appendix may be summarized in terms of the ratio, η_1, of the K_2^o beam intensity at the entrance to the visible volume of the freon chamber to that at the carbon target. As a function of K_2^o energy, the average of η_1 over the entrance window to the chamber is:

Kinetic Energy of K_2^o (Mev)	100	200	300	400	500	600
$\langle\eta_1\rangle$	0.29	0.31	0.33	0.35	0.36	0.37

In estimating the error in these ratios, one must take into account that the errors in the cross sections used are correlated, while the other errors are uncorrelated. One finds from the errors mentioned above that the net error is about $\pm$22%.

APPENDIX IX

K_2^o CONVERSION AND Λ^o DETECTION FACTOR

A. INTRODUCTORY REMARKS

$\overline{\eta}_2 d\Omega$ is the probability per unit K_2^o source intensity* that a Λ^o hyperon was produced in the element of solid angle $d\Omega$ and its decay was detected. In order to evaluate this quantity, the assumption will be made that the K_2^o beam had a constant intensity over a solid angle slightly larger than the visible volume of the bubble chamber. This constant intensity is given by the average quantities defined in Chapter VII. The effect of the finite aperture for the K_2^o beam will be discussed later in this appendix.

B. HYPOTHETICAL CASE

Consider the hypothetical case in which the visible volume is surrounded by a uniform sea of CF_3Br. If the small effects due to absorption≠ and spreading of the K_2^o beam are ignored, the number of Λ^o decays in an element of volume is constant and equal to the number of Λ^o hyperons produced there. Thus $\overline{\eta}_2 d\Omega$ may be considered the probability per unit K_2^o source intensity that in the element of solid angle $d\Omega$ a Λ^o decay would be detected.

Since the visible volume subtends a small solid angle at the carbon target, a rectangular coordinate system may be set up in the freon chamber with the y-axis parallel to the K_2^o beam and the z-axis in the vertical direction. In this coordinate system, $\overline{\eta}_2$

---

* Without losses between the source and freon chamber.

≠ Only 6 per cent of the K_2^o mesons are absorbed in traversing 10 cm of CF_3Br.

may be expressed as a function of x and z, and the integral over the solid angle becomes:

$$\int \overline{\eta_2}\, d\Omega = \int \frac{\overline{\eta_2}(x,z)}{L^2}\, dx\, dz \qquad \text{(AIX-1)}$$

where L is the mean distance from the carbon target to the volume in which the Λ^o decays are observed.

$\overline{\eta_2}\ (x,z)$ may be written as an integral over the y-coordinate in the visible region:

$$\overline{\eta_2}\ (x,z) = g_1 \int g_2(x,y,z)\, dy \qquad \text{(AIX-2)}$$

where g_1 dxdydz = constant probability per unit flux of K_2^o mesons that a Λ^o would decay in the element of volume at (x,y,z); and $g_2(x,y,z)$ = probability that a Λ^o decay at (x,y,z) would be detected.

g_1 may be expressed in terms of the cross section, $\sigma_f(K_2^o \rightarrow \Lambda^o)$, for the conversion of K_2^o mesons into Λ^o hyperons in CF_3Br.

$$g_1 = \sigma_f\ (K_2^o \rightarrow \Lambda^o)\ N_o \rho_f / M_f \qquad \text{(AIX-3)}$$

where

N_o = Avogadro's number = 6.02×10^{23}/mole

ρ_f = density of CF_3Br = 1.485 gm/cm^3

M_f = molecular weight of CF_3Br = 148.9 gm.

$g_2(x,y,z)$ is composed of several factors:

$$g_2(x,y,z) = \overset{+}{B}\ E_c C_\pi C_p C_s\ e(x,y,z) \qquad \text{(AIX-4)}$$

where

$B^{\pm}$ = branching ratio for charged mode of decay = 0.65

E_c = scanning efficiency = 0.95 ± 0.03

C_π = probability that decay pion has energy > cutoff (26.5 Mev), or has σ-star if energy < cutoff

C_p = probability that decay proton has energy > cutoff (8.7 Mev)

C_s = correction for Λ^o decay less than 0.05 cm from associated star

$e(x,y,z)$ = probability that Q-value measurement has error $\leq$ 14 Mev (i.e., measurement efficiency)

In terms of these quantities,

$$\int \overline{\eta_2}\, d\Omega = (g_1 B^{\pm} E_c C_\pi C_p C_s / L^2) \int e(x,y,z)\, dx\, dy\, dz \qquad \text{(AIX-5)}$$

C_π has been computed from the kinematics of Λ^o decay (assuming isotropic decay in the CM system) and the observed fact that 39 per cent of stopping negative pions exhibited σ stars (see p. 92). The dependence of C_π on the Λ^o kinetic energy is shown in Fig. 44. For the purposes of this experiment it may be considered constant. (The value 0.86 ± 0.03 will be used.) The variation of C_π with the pion range chosen for the cutoff is typically 0.003/mm for Λ^o energies above 50 Mev, i.e., it is small.

C_p and C_s are determined solely by kinematics. In Fig. 44 C_p is plotted as a function of the Λ^o energy. If all events were associated with stars, C_s would simply be an exponential function of the Λ^o momentum (in Mev/c): $C_s' = \exp(-7.4/p_\Lambda)$. At $T_\Lambda = 20$ Mev, $C_s' = 0.99$. Thus for the Λ^o energies of interest, both C_p and C_s are

Figure 44

Track-Length Cutoff Factors

The correction factors C_π and C_p, which are defined on p. 270, are plotted as functions of the Λ^o kinetic energy.

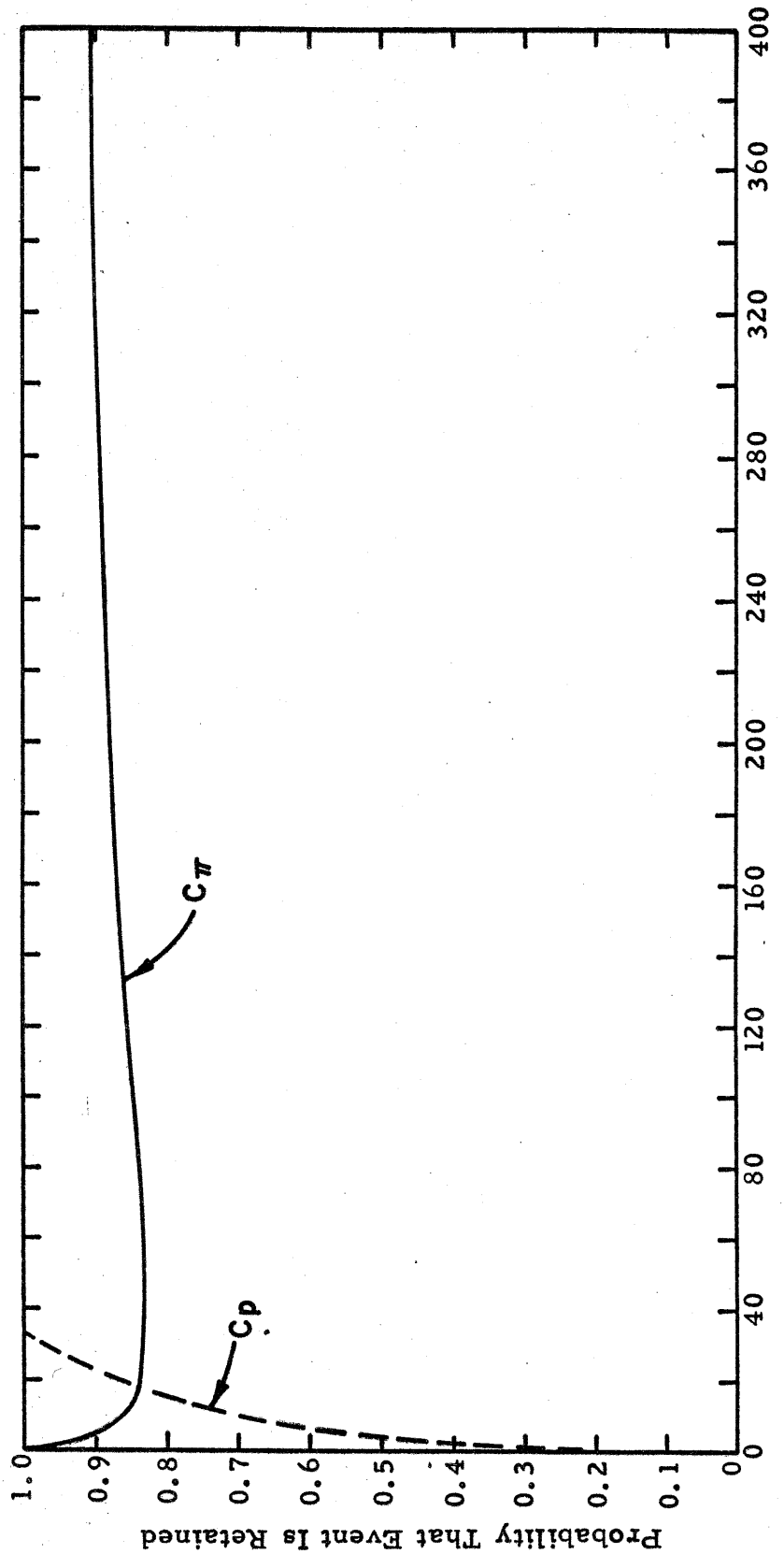
Probability That Event Is Retained
1.0
0.9
0.8
0.7
0.6
0.5
0.4
0.3
0.2
0.1
0
0
40
80
120
160
200
240
280
320
360
400
Λ° Kinetic Energy (Mev)
C_π
C_p

Figure 44

equal to 1.00.

The integral of $e(x,y,z)$ has been estimated from the observed distribution in position of all non-stopping events which fell in the Q-value interval $25 \leq Q \leq 50$ Mev and had Q-value errors ≤ 14 Mev. The assumption was made that this distribution adequately represents the distribution of true Λ^o decays. The computation was simplified by approximating $e(x,y,z)$ with a separated function*:

$$e(x,y,z) = e_1(x)e_2(y)e_3(z)$$

where $e_1(x)$, $e_2(y)$, and $e_3(z)$ are normalized histograms of the number of events versus x, y, and z. Since there was a region, ($x_1<x<x_2$, $y_1 < y < y_2$, $z_1 < z < z_2$), from which no events were discarded, normalization was accomplished through division by the average number of events satisfying:

for $e_1(x)$ ..... $x_1 < x < x_2$

for $e_2(y)$ ..... $y_1 < y < y_2$

for $e_3(z)$ ..... $z_1 < z < z_2$

The results of the calculation for several cutoffs in Λ^o energy are:

T (Mev)	Number of Events in Histograms	$\int e(x,y,z)dxdydz$ ** (cm^3)
> 0	91	4.4×10^3
> 50	80	4.0×10^3
> 100	63	3.6×10^3
> 150	44	3.4×10^3

*If the visible volume had been a rectangular parallelepiped, the separation would have been exact. Actually, the visible volume fell in between a rectangular parallelepiped and a right-circular cylinder.

** The total visible volume was 7.2×10^3 cc.

$(3.6 \pm 0.7) \times 10^3$ cm^3 is believed to be the best value applicable to the average true Λ^o decay.

C. APPLICATION TO ACTUAL CASE

1. Material Surrounding Freon Chamber.

a. The Difference System. The actual freon chamber was immersed in a conglomeration of materials. (See Figs. 5 and 6.) This situation may be treated as a superposition of the hypothetical uniform case discussed above and a difference system. The difference system is characterized by the number (positive or negative) of Λ^o hyperons in the visible volume which cannot be attributed to the uniform system. It will be shown below that this number, N_Λ(dif), is small compared to the number, N_Λ(unif), ascribable to the uniform system.

Most of the flux of Λ^o hyperons into and out of the visible volume occurred across the entrance and exit surfaces for the K_2^o beam. (The Λ^o hyperons generally traveled in directions close to that of the K_2^o beam.) Therefore, the following simpliciations are made in the estimate of the contribution from the difference system: (1) the thicknesses of the several layers of material outside the visible volume are taken to be those associated with the central ray of the K_2^o beam (normal to the layers); and (2) all Λ^o hyperons produced in a certain layer are assumed to travel radially towards the visible volume. Under these conditions the difference system may be thought of as a pseudo layer of CF_3Br of constant thickness, $S(T_\Lambda)$, extending across the entrance surface to the visible volume

and depending on the Λ^o kinetic energy, T_Λ. All Λ^o hyperons produced in this layer are considered to decay in the visible volume. Therefore, since $\int e_2(y)\,dy$ is the effective thickness in the uniform case,

$$N_\Lambda \text{ (dif)}/N_\Lambda \text{ (unif)} = S(T_\Lambda)/\int e_2(y)\,dy \ . \qquad \text{(AIX-6)}$$

Although this picture does not apply well near the boundaries of the entrance surface, it does account for the main contribution of the difference system.

b. Expression for and Numerical Values of $S(T_\Lambda)$. If λ_i is the reciprocal interaction length for Λ^o hyperon production in the i^{th} material, λ_o is the corresponding quantity in CF_3Br and $\rho_i(x)$ is the fractional volume occupied by the i^{th} material at distance, x, from the visible volume, then the mean reciprocal interaction length at x attributable to the difference system, in units of λ_o is:

$$\overline{\lambda_d(x)} = \sum_i (\lambda_i/\lambda_o)\,\rho_i(x) - 1$$

Account may be taken for the absorption of the K_2^o beam. The intensity of the beam at point x relative to the edge of the visible volume is: $\exp[\int_o^x \overline{\alpha(y)}\,dy]$ where $\overline{\alpha(y)}$ is the mean absorption coefficient at y: $\overline{\alpha(y)} = \sum_i \rho_i(y)\,\alpha_i$. The values of α_i are given in Table 14.

The fraction of the Λ^o hyperons produced at x which reach the useful volume before decaying is: $\exp[-x/x_o(T_\Lambda)]$ where $x_o(T_\Lambda)$

is the mean decay length for a Λ^o hyperon of kinetic energy T_Λ.

Combining these factors, one obtains $S(T_\Lambda)$, which has units of "centimeters of CF_3Br in the visible volume".

$$S(T_\Lambda) = \int_o^\infty S(T_\Lambda, x)\, dx$$

$$= \int_o^\infty \overline{\lambda_d(x)} \exp\left[\int_o^x \overline{\alpha(y)}\, dy\right] \exp\left[-x/x_o(T_\Lambda)\right] dx \qquad \text{(AIX-7)}$$

The values of λ_i/λ_o have been estimated from the data presented in Appendix IV, Section C:

Material	λ_i/λ_o
Steel*	4.63
FC-43	1.14
Polyethylene	0.74
Neoprene	0.89

In order to calculate $S(T_\Lambda)$, the distance from the useful volume was broken into 14 separate intervals which extended as far as, but not including, the radiation shields. In each interval mean values of $\rho_i(x)$ were evaluated for all materials present. The correction for K_2^o meson absorption never exceeded 1.2. As an example, Fig. 45 presents the quantity $S(T_\Lambda, x)$ from equation AIX-7 for the Λ^o hyperon kinetic energy of 200 Mev. The values found for S(T) are:

* Steel, stainless steel and inconel x were all grouped under "steel" and treated as iron.

Figure 45

Contributions to Pseudo Layer of CF_3Br

This figure illustrates the contribution of material outside the visible volume to the thickness of the "pseudo layer" of CF_3Br, which characterizes the difference system. $S(T_\Lambda, x)$ of equation AIX-7 is plotted as a function of x for $T_\Lambda = 200$ Mev. The variable x is the distance from the visible volume, and the integral of $S(T_\Lambda, x)$ over x is the thickness of the pseudo layer. (See text for details.)

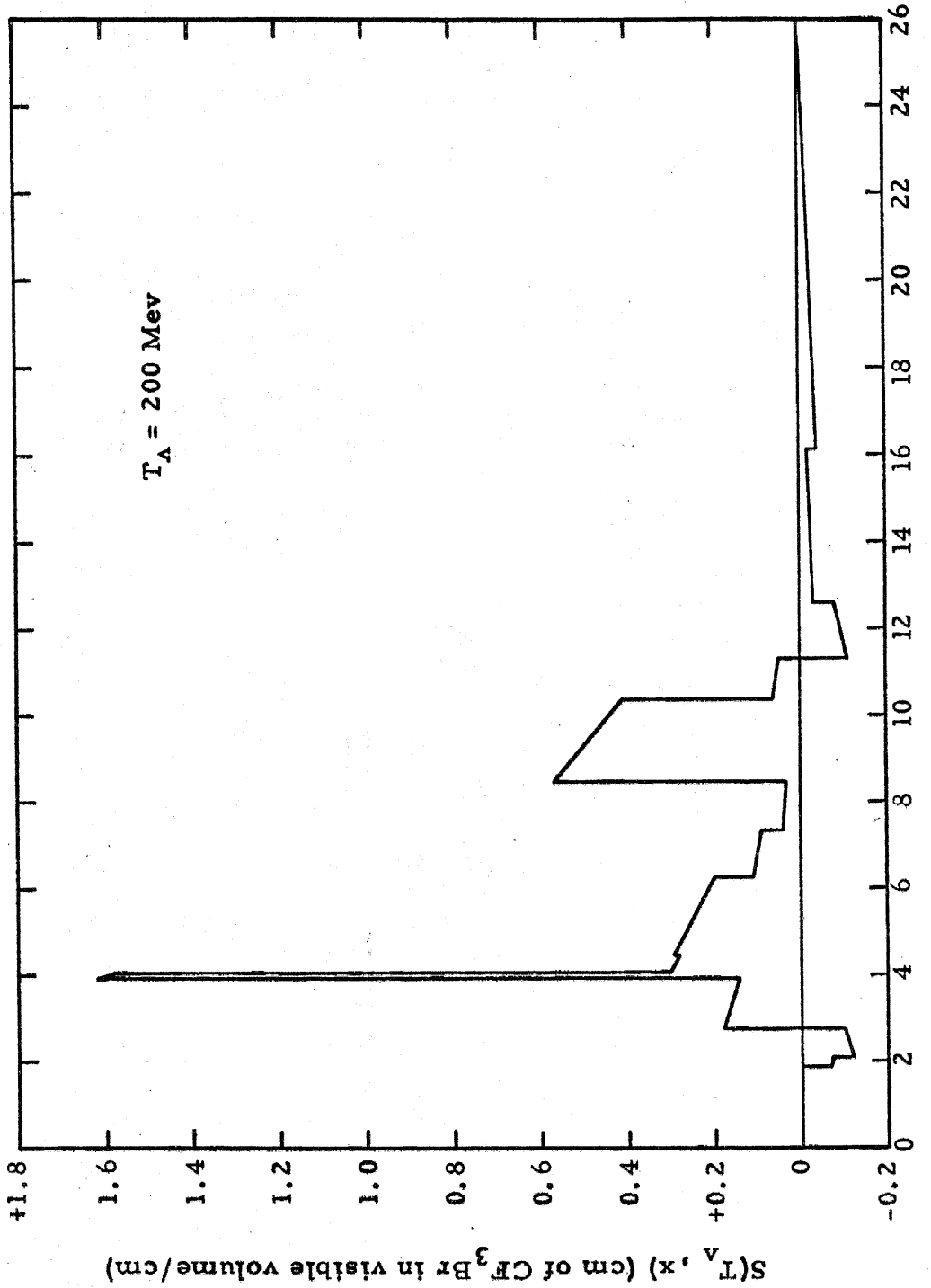
T_Δ = 200 Mev
$S(T_\Delta, x)$ (cm of CF_3Br in visible volume/cm)
x (cm)
+1.8
1.6
1.4
1.2
1.0
0.8
0.6
0.4
+0.2
0
-0.2
0
2
4
6
8
10
12
14
16
18
20
22
24
26

Figure 45

T_Λ (Mev)	20	50	100	200	300	400	500	600
$S(T_\Lambda)$ (cm)	0.14	0.43	0.91	1.58	1.90	2.16	2.28	2.34

c. Contribution to Observed Decays. Since $\int e_2(y)\,dy$ is about 16 cm*, N_Λ (dif)/N_Λ (unif) from equation AIX-6 is less than 1/10 for $T_\Lambda \leq 200$ Mev. The difference system, then, makes a relatively small contribution to the observed decays. Note that $S(T_\Lambda)$ is always positive and that the effect of the difference system is to add to rather than subtract from the Λ^o decays attributable to the uniform system. This tends to cancel the effect of the finite aperture for the K_2^o beam, which is discussed next.

2. Finite Aperture for K_2^o Beam. The transverse extent of the K_2^o beam was limited on the sides by lead shielding in the sweeping magnet, and on the top and bottom by the flanges of the support and safety tanks and by the steel pole tips of the sweeping magnet (see Fig. 2). The rectangular aperture thus formed had the following characteristics:

West side: Beam cutoff began about 2 cm outside the maximum extent of the visible volume. Cutoff was sharp - several millimeters wide.

East side: Cutoff began 4 cm outside the maximum extent of the visible volume. Cutoff was gradual - about 4 cm wide.

---

* The value associated with the "best" value of

$$\int e(x, y, z)\,dx\,dy\,dz.$$

Top: Cutoff began about 0.1 cm inside the top window. Roughly, the cutoff consisted of a sharp decrease to 1/3 the initial intensity in 1/2 cm, followed by 1/2 cm of constant intensity (at 1/3 the initial value), and then a gradual decrease over the next 3 cm to 1/10 the initial intensity.

Bottom: Cutoff began about 1 cm inside the bottom window. Structure was the same as at the top.

The important result of the finite aperture was a net flux of Λ^o hyperons out of the useful part of the visible volume. The estimate of the loss through each wall is influenced by two factors:

a) The lateral spread of the Λ^o hyperons tended to be small. For example, if Λ^o hyperons which originate in the reaction

$$\overline{K^o} + \text{nucleon} \rightarrow \Lambda^o + \pi$$

do not scatter before escaping from the nucleus, the lateral spread at a distance of one mean decay length is less than 3.2 cm for all K_2^o and Λ^o energies possible in this experiment.

b) The measurement efficiency, e(x,y,z), had very low values within 3 cm of the maximum extent of the east and west sides and within 1 cm of the top and bottom windows. The volume in which e(x,y,z) had an appreciable value is henceforth called the "useful" volume.

On the east and west sides the K_2^o beam extended at least 5 cm outside the useful volume, and no net loss of Λ^o hyperons through these sides should have occurred.

At the top the presence of the 1 cm thick vycor window helped to cancel the outward flux of Λ^o hyperons. Vycor has roughly twice the Λ^o production capacity per unit length as CF_3Br, and so, per unit length about the same number of Λ^o hyperons should have been produced in the vycor by the attenuated K_2^o beam as would have been produced in CF_3Br by the full intensity beam. Thus the upper effective edge of the K_2^o beam was about 2 cm outside the useful volume and the net flux of Λ^o hyperons out the top window was small.

At the bottom something like 2/3 of the Λ^o hyperons which were produced in the bottom 2 or 3 cm of the useful volume and traveled downward were not matched by Λ^o hyperons which were produced outside the useful volume and traveled upward. If one half of those produced are assumed to have traveled downwards, the number of Λ^o hyperons lost in this way equals the total number of Λ^o hyperons produced in a horizontal layer of CF_3Br, 2/3 to 1 cm thick. Since the area of this "effective" layer is 1.2 times the area of the entrance surface for the K_2^o beam, the actual situation is equivalent to the superposition of a system in which there is no limiting aperture and a negative pseudo layer of CF_3Br, 0.8 to 1.2 cm thick, extending across the entrance to the visible* volume. The effect of this pseudo layer is very nearly cancelled by the effect of the pseudo layer attributable to material outside the visible volume.

D. NUMERICAL VALUE OF $\int \overline{\eta_2}\, d\Omega$.

One may conclude from the foregoing discussion that the

* The useful volume and visible volume surfaces nearly coincided on the entrance side.

experimental situation is adequately approximated by the hypothetical case discussed at the beginning of this appendix. Insertion into equations AIX-3 and AIX-5 of the numerical values listed throughout this appendix and:

$$\sigma_f(K_2^o \rightarrow \Lambda^o) = (450 \pm 100) \times 10^{-27} \text{ cm}^2$$

$$L = 250 \text{ cm},$$

yields the following result for the integrated K_2^o conversion and Λ^o detection factor:

$$\int \overline{\eta_2}\, d\Omega = (0.83 \pm 0.25) \times 10^{-4} \text{ ster.} \quad . \qquad \text{(AIX-8)}$$

E. ESTIMATION OF $\int \overline{\eta_2}\, d\Omega$ FOR K_1^o DECAYS

Equations AIX-3 and AIX-5 may be used to obtain an estimate of the K_2^o conversion and K_1^o detection factor if the following assumptions are made:

a) The hypothetical case is also applicable to the regeneration of K_1^o mesons.

b) $\int e(x,y,z)dxdydz$ if the same for Λ^o production and K_1^o regeneration.

The numerical values of required quantities which differ from those listed previously in this appendix are:

$$\sigma_f(K_2^o \rightarrow K_1^o) = (290 \pm 230) \times 10^{-27} \text{ cm}^2$$

$$B^{+}_{-}(K_1^o) = 0.75$$

$$E_c = 0.65 \pm 0.13$$

$$C_\pi = C_p = 1.00$$

$$C_s > \exp(-8.3/p_{K_1^o}) = 0.96 \text{ for 50 Mev } K_1^o$$

Since the error in σ_f is so large, small error approximations cannot be used in computing the error in its reciprocal. For this reason the reciprocal of $\int \overline{\eta_2}\, d\Omega$ is quoted below and the effect of the error in σ_f is treated explicitly.

$$\left[\int \overline{\eta_2}\, d\Omega \right]^{-1}_{K_1^o} = (2^{+8}_{-1}) \times 10^4/\text{ster.} \qquad \text{(AIX-9)}$$

REFERENCES

1. Rochester and Butler, Nature 160, 855 (1947).
2. M. Gell-Mann, Sup. del Nuovo cimento 4, 848 (1956).
3. M. Kawaguchi and M. J. Moravcsik, Phys. Rev. 107, 563 (1957).
4. A. Fujii and R. E. Marshak, Phys. Rev. 107, 570 (1957).
5. D. Amati and B. Vitale, Nuovo cimento 6, 395 (1957).
6. B. T. Feld and G. Costa, Phys. Rev. 110, 968 (1958).
7. R. H. Capps, Phys. Rev. 114, 920 (1959).
8. M. J. Moravcsik, Phys. Rev. Letters 2, 352 (1959).
9. J. G. Taylor, Phys. Rev. 116, 768 (1959).
10. F. Turkot, Proc. 1960 Conf. on High Energy Physics at Rochester, Interscience Pub. (New York), p. 369.
11. Emery, Loebbaka, Maloy, McInturff, Mumseratt, Peterson, Prigen, and Roos; Private Communication.
12. K. Landé, E. T. Booth, J. Impeduglia, L. M. Lederman, and W. Chinowsky, Phys. Rev. 103, 1901 (1956).
13. K. Landé, L. M. Lederman, and W. Chinowsky, Phys. Rev. 105, 1925 (1957).
14. M. Bardon, K. Landé, L. M. Lederman, and W. Chinowsky, Ann. Phys. 5, 156 (1958).
15. D. Neagu, E. O. Okonov, N. I. Petrov, A. M. Rosanova, and V. A. Rosakov, Proc. 1960 Conf. on High Energy Physics at Rochester, Interscience Pub. (New York), p. 603; and Phys. Rev. Letters 6, 552 (1961).
16. W. K. H. Panofsky and W. G. Chesnut, Phys. Rev. 109, 1353 (1958).
17. R. Gomez; Private Communication.
18. W. F. Fry, J. Schneps, and M. S. Swami, Phys. Rev. 103, 1904 (1956).
19. R. G. Glasser, N. Seeman, and G. A. Snow, Phys. Rev. 107, 277 (1957).

20. R. Ammar, J. I. Friedman, R. Levi Setti, and V. L. Telegdi, Nuovo cimento 5, 1801 (1957).

21. M. Baldo-Ceolin, C. C. Dilworth, W. F. Fry, W. D. B. Greening, H. Huzita, S. Limentani, and A. E. Sichirollo, Nuovo cimento 6, 130 (1957).

22. V. Bisi, R. Cester, A. Debenedetti, C. M. Garelli, B. Quassiati, L. Tallone, and M. Vigone, Nuovo cimento 9, 864 (1958).

23. U. Camerini, W. F. Fry, M. Baldo-Ceolin, H. Huzita, and S. Natali, Phys. Rev. 115, 1048 (1959).

24. W. B. Fowler, R. L. Lander and W. M. Powell, Phys. Rev. 113, 928 (1959).

25. F. Muller, R. W. Birge, W. B. Fowler, R. H. Good, W. Hirsch, R. P. Matsen, L. Oswald, W. M. Powell, and H. S. White, Proc. 1960 Conf. on High Energy Physics at Rochester, Interscience Pub. (New York), p. 597.

26. F. Muller, R. W. Birge, W. B. Fowler, R. H. Good, W. Hirsch, R. P. Matsen, L. Oswald, W. M. Powell, H. S. White, and O. Piccioni, Phys. Rev. Letters 4, 418 (1960).

27. R. H. Good, R. P. Matsen, F. Muller, O. Piccioni, W. M. Powell, H. S. White, W. B. Fowler, and R. W. Birge, Phys. Rev. 124, 1223 (1961).

28. H. J. Martin, L. B. Leipuner, W. Chinowsky, F. T. Shively, and R. K. Adair, Phys. Rev. Letters 6, 283 (1961).

29. H. J. Martin; Private Communication.

30. J. A. Kaydk; Private Communication.

31. W. F. Fry; Private Communication.

32. M. Bloch, "A Low Energy Magnetic Spectrometer," CTSL (1957).

33. J. H. Mullins, Ph. D. Thesis, California Institute of Technology, (1959).

34. J. H. Mullins, E. D. Alyea, Jr., and J. M. Teem, Proc. Conf. Instrumentation for High-Energy Physics at Berkeley, Interscience Pub. (New York, 1960), p. 106.

35. L. W. Alvarez, Proc. Conf. Instrumentation for High-Energy Physics at Berkeley, Interscience Pub. (New York, 1960), p. 145.

36. B. Hahn, A. W. Knudsen, and E. Hugentobler, Sup. del Nuovo cimento 15, 236 (1960).

37. R. I. Louttit, Proc. Conf. Instrumentation for High-Energy Physics at Berkeley, Interscience Pub. (New York, 1960), p. 117.

38. B. Alfredsson and T. Johansson, Arkiv Fysik 19, 383 (1961).

39. C. Peyrou, Proc. Conf. Instrumentation for High-Energy Physics at Berkeley, Interscience Pub. (New York, 1960), p. 157.

40. California Institute of Technology Synchrotron Laboratory, Circuit Drawings: 16E 359, 16E 382, 10T 609A and 10T 577.

41. A. Pais and S. B. Treiman, Phys. Rev. 106, 1106 (1957).

42. C. Baglin, M. Bloch, V. Brisson, J. Hennessy, A. Lagarrigue, P. Mittner, P. Musset, A. Orkin-Lecourtois, P. Rançon, A. Rousset, A. M. Saruis, X. Sauteron, and J. Six, Proc. 1960 Conf. on High Energy Physics at Rochester, Interscience Pub. (New York, 1960), p. 594.

43. J. L. Brown, H. C. Bryant, R. A. Burnstein, D. A. Glaser, R. W. Hartung, J. A. Kadyk, D. Sinclair, G. H. Trilling, J. C. Vander Veld, and J. D. Van Putten, Proc. 1960 Conf. on High Energy Physics at Rochester, Interscience Pub. (New York, 1960), p. 613.

44. W. Chinowsky, G. Goldhaber, S. Goldhaber, W. Lee, T. O'Halloran, and T. Stubbs, Proc. 1960 Conf. on High Energy Physics at Rochester, Interscience Pub. (New York, 1960), p. 451.

45. T. H. Fields, G. B. Yodh, M. Derrick, and J. G. Fetkovich, Phys. Rev. Letters 5, 69 (1960).

46. J. Orear, "Notes on Statistics for Physicists," UCRL-8417 (1958).

47. T. D. Lee, R. Oehme, and C. N. Yang, Phys. Rev. 106, 340 (1957).

48. K. Aizu, Nuovo cimento 6, 1040 (1957).

49. M. Gell-Mann and A. Pais, Phys. Rev. 97, 1387 (1955).

50. S. Weinberg, Phys. Rev. 110, 782, (1957).

51. W. H. Barkas and A. H. Rosenfeld, UCRL-8030 (1960).

52. E. D. Alyea, Jr., "Bubble Chamber Lens Tests," CTSL (1957).

53. J. M. Teem and E. D. Alyea, Jr.; not published.

54. D. C. Gates, R. W. Kenney, D. A. McPherson, and W. P. Swanson, R. S. I. 31, 565 (1960).

55. J. H. Boyden, Ph. D. Thesis, California Institute of Technology, (1961).

56. R. M. Talman and R. L. Walker; Private Communication.

57. S. Fernbach, R. Serber, and T. B. Taylor, Phys. Rev. 75, 1352 (1949).

58. A. Pais and O. Piccioni, Phys. Rev. 100, 1487 (1955).

59. L. T. Kerth, Revs. Mod. Phys. 33, 389 (1961).

60. S. C. Freden, F. C. Gilbert, and R. S. White, Phys. Rev. 118, 564 (1960).

61. P. Eberhard, A. H. Rosenfeld, F. T. Solmitz, R. D. Tripp, and M. B. Watson, Phys. Rev. Letters 2, 312 (1959).

62. L. W. Alvarez, Proc. 1959 Conf. on High Energy Physics at Kiev, p. 471.

63. O. Dahl, N. Horwitz, D. Miller, J. Murray, and M. Watson, Proc. 1960 Conf. on High Energy Physics at Rochester, Interscience Pub. (New York, 1960), p. 415.

64. D. M. Ritson (ed.), Techniques of High Energy Physics, Interscience Pub. (New York, 1961).

65. H. A. Bethe, Z. Physik 76, 293 (1938).

66. R. M. Sternheimer, Phys. Rev. 115, 137 (1959); and Phys. Rev. 103, 511 (1956).

67. Proc. Informal Conf. at Gatlinburg, Tenn. (1958), E. A. Uehling, (ed.).

68. E. I. duPont de Nemours and Co., Inc., Freon Products Division, Report D-9.

69. B. B. Rossi, High-Energy Particles, Prentice-Hall (New York, 1952), pp. 63 ff.

70. K. R. Symon, Ph. D. Thesis, Harvard University (1948).

71. E. D. Alyea, Jr., A. B. Thesis, Princeton University (1953).

72. F. Seitz, Phys. of Fluids 1, 2 (1958).

73. G. A. Blinov, Iu. S. Krestinikov, and M. L. Lomanov, Zhur. Eksptl. i Teoret. Fiz. 31, 762 (1956). [Translation: Soviet Phys. J. E. T. P. 4, 661 (1957).]

74. W. J. Willis, E. C. Fowler, and D. C. Rahm, Phys. Rev. 108, 1046 (1957).

75. P. E. Argan, A. Gigle, E. Picasso, and G. Tomasini, Nuovo cimento 10, 177 (1958).

76. B. Hahn, E. Hugentobler, and F. Steinrisser, Proc. Conf. Instrumentation for High-Energy Physics at Berkeley, Interscience Pub. (New York, 1960), p. 143.

77. A. Ahmadzadeh and N. N. Biswas, Nuovo cimento 19, 958 (1961).

78. D. A. Glaser, D. C. Rahm, and C. Dodd, Phys. Rev. 102, 1653, (1956).

79. P. H. Fowler and D. H. Perkins, Phil. Mag. 46, 587 (1955).

80. V. P. Kenney, Phys. Rev. 119, 432 (1960).

81. T. Helliwell, Bull. Amer. Phys. Soc. 6, 524 (1961).

82. L. J. Fretwell, D. G. Coyne, and J. H. Mullins, Bull. Amer. Phys. Soc. 6, 524 (1961); and Private Communication.

83. K. M. Case, Phys. Rev. 103, 1449 (1956).

84. M. L. Good, Phys. Rev. 106, 591 (1957).

85. M. L. Good, Phys. Rev. 110, 550 (1958).

86. M. A. Melkanoff, O. R. Price, D. H. Stork, and H. K. Ticho, Phys. Rev. 113, 1303 (1959).

87. R. D. Hill, J. H. Hetherington, and D. G. Ravenhall, Phys. Rev. 122, 267 (1961).

88. R. M. Sternheimer, Phys. Rev. 106, 1027 (1957).